Cardiac electrophysiology and mechanoelectric feedback : modeling and simulation

Please check the document version of this publication:

• A submitted manuscript is the version of the article upon submission and before peer-review. There can be important differences between the submitted version and the official published version of record. People interested in the research are advised to contact the author for the final version of the publication, or visit the DOI to the publisher's website.
• The final author version and the galley proof are versions of the publication after peer review.
• The final published version features the final layout of the paper including the volume, issue and page numbers.

Link to publication

Download date: 16. Nov. 2023

Cardiac Electrophysiology and Mechanoelectric Feedback

Modeling and Simulation

Cover: Computer simulation of atrial fibrillation. The small pictures on the background represent 2 seconds of simulation in which a reentrant depolarization wave (atrial flutter) develops into atrial fibrillation. The color pictures on the foreground represent 4 successive simulation states during atrial fibrillation with a 50 ms interval. Yellow and red indicate depolarized tissue, green indicates refractory tissue, and blue indicates recovered tissue. The human atria are modeled by the triangular mesh shown on the back. The unstable arrhythmic behavior is caused by local changes in stretch due to the contraction of tissue in other parts of the atria (mechanoelectric feedback).

Cardiac Electrophysiology
and
Mechanoelectric Feedback

Modeling and Simulation

PROEFSCHRIFT

ter verkrijging van de graad van doctor aan de
Technische Universiteit Eindhoven, op gezag van de
Rector Magnificus, prof.dr.ir. C.J. van Duijn, voor een
commissie aangewezen door het College voor
Promoties in het openbaar te verdedigen op
woensdag 28 mei 2008 om 16.00 uur

door

Nicolaas Hendrikus Louis Kuijpers

geboren te Bergen op Zoom

Voor Heleen, Joris en Guus

Cardiac arrhythmia such as atrial and ventricular fibrillation are characterized by rapid and irregular electrical activity, which lead to asynchronous contraction and a reduced pump function. In addition to experimental and clinical studies, computer simulations are frequently applied to obtain insight in the onset and perpetuation of cardiac arrhythmia. In existing computer models, the excitable tissue is often modeled as a continuous two-phase medium, representing the intracellular and interstitial domains, respectively. A possible drawback of continuous models is the lack of flexibility when modeling discontinuities in the cardiac tissue.

In this thesis, we introduce a discrete bidomain model in which the cardiac tissue is subdivided in segments. Each of the segments represents a small number of cardiac cells. Ionic membrane currents as well as intracellular coupling and interstitial currents are described by this model. Compared with the well-known continuous bidomain equations, our Cellular Bidomain Model is more suitable when modeling the structure of cardiac tissue, in particular anisotropy, myofibers, fibrosis, and gap junction remodeling. To study mechanoelectric feedback, i.e., the effect of tissue deformation and mechanical load on the electrophysiology, the model describes stretch-activated ionic membrane currents and cardiomechanics. In our model, contractile forces generated by the sarcomeres are coupled to the intracellular concentration of free calcium and to the sarcomere length.

We apply the Cellular Bidomain Model in five simulation studies to cardiac electrophysiology and mechanoelectric feedback. In the first study, the effect of field stimulation on virtual electrode polarization is studied in uniform, decoupled, and nonuniform cardiac tissue. In the second study, the role of the hyperpolarization-activated inward current (I_f) is investigated in relation to ectopic foci and impulse propagation in normal and in pathological tissue. In the third study, the vulnerability to atrial fibrillation under stretch is investigated in relation to the stretch-activated current (I_sac). In the fourth study, it is investigated whether electrical remodeling, i.e., changes in ionic membrane currents that occur after ventricular pacing, is triggered by changes in mechanical load. Finally, in the fifth study, the vulnerability to atrial fibrillation under stretch is evaluated using a model of the human atria. Our simulation results are in agreement with experimental observations and provide insight in electrophysiological and mechanical behavior of the heart.

In conclusion, our model is capable of simulating cardiac electrophysiology and mechanoelectric feedback both at the cellular and at the organ level. Application of our model leads to more insight in the complex interaction between cardiac electrophysiology and cardiomechanics.

Introduction

The heart consists of two halves each functioning as a pump: the right half pumps blood through the lungs and the left half pumps blood through the remaining body parts. Each of the halves is a pulsatile two-chamber pump composed of an *atrium* and a *ventricle*. The atria function as a storage where blood is collected before it is pumped into the ventricles. Blood circulation is established by contraction of the ventricles. Malfunctioning of the heart leads to a decreased blood flow and may hamper oxygen supply, which is of vital importance for all body functions.

Contraction of the heart muscle is preceded by an electrical impulse, or *action potential* (AP), generated in the sino-atrial node (SA node). From the SA node, the impulse travels through the atria to the atrio-ventricular node (AV node), where it is delayed for about 0.1 s. In the ventricles, the impulse is first transported through the Bundle of His and then through the Purkinje system. The Purkinje fibers function as a fast conduction pathway to bring the impulse to the ventricular muscle mass (Figure 1.1).

Within the heart muscle, cardiac cells, also called *myocytes*, are capable of passing the action potential from one cell to another. Cell membranes of neighboring cells are fused with one another to form so-called *gap junctions* that allow relatively free diffusion of ions. Such a network of coupled cardiac myocytes is called a *syncytium* (Figure 1.2). After excitation of a group of cells, the action potential spreads rapidly through the syncytium so that all cells will be excited in short time.

Once cardiac muscle cells are excited, they start to contract. Contraction of the heart muscle cells is triggered by calcium ions (Ca^{2+}) that are released from the *sarcoplasmic reticulum* (SR), which functions as a buffer for calcium ions when the cell is at rest. Calcium release from the SR is triggered by the action potential. Normal propagation of the AP is thus important for efficient contraction of the heart muscle. In case impulse propagation hampers, this may lead to asynchronous contraction and a reduced pump function.

Under abnormal circumstances, impulses may be spontaneously generated in the heart muscle. In case an impulse re-excites cardiac tissue that
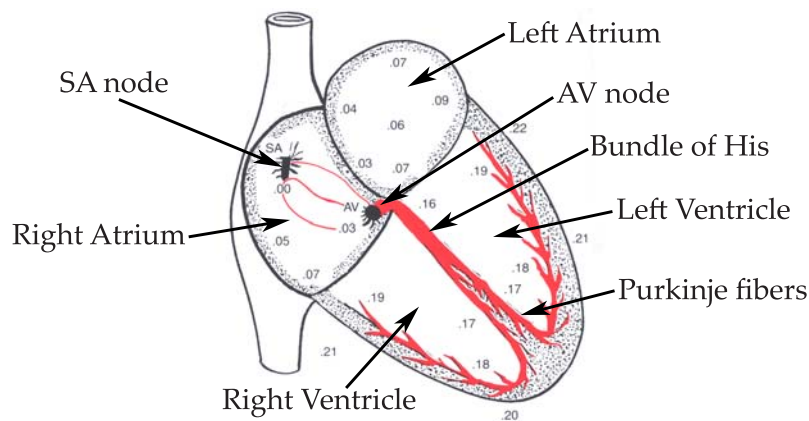
Figure 1.1: Propagation of the cardiac impulse. Times of excitation are indicated in s for different parts of the heart (Adapted from Guyton and Hall 1996, Fig. 10-4, p. 125).

was just recovered from the former impulse, a reentrant wave is established. Reentrant depolarization waves lead to arrhythmic electrical behavior and uncoordinated contraction. The most serious of all cardiac arrhythmia is *ventricular fibrillation* (VF), which is fatal if not treated immediately. In contrast, *atrial fibrillation* (AF) is not directly lethal. However, the pump function of the heart is reduced due to the loss of atrial contraction.

1.1 The Cellular Bidomain Model

To investigate normal and abnormal impulse propagation, we develop a mathematical model of cardiac electrophysiology and cardiomechanics. Models of cardiac electrophysiology usually comprise an accurate model of the ionic membrane currents of a single cell. Accurate simulation results can be obtained if the model also reflects the structure of cardiac tissue and distinguishes between the intracellular and interstitial domains. Mathematical models such as the bidomain equations describe the conductive properties of cardiac tissue by a continuous two-phase medium [69]. A possible drawback of continuous models is the lack of flexibility when modeling the discontinuities that characterize the pathological heart.

In this thesis, we introduce a discrete bidomain model, the Cellular Bidomain Model, in which the cardiac tissue is subdivided in segments. Each of the segments represents a small number of cardiac cells and the surrounding interstitial fluid. Active membrane behavior is simulated by considering a
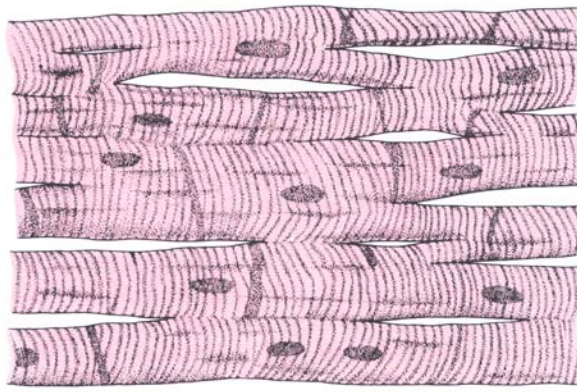
Figure 1.2: Interconnecting cardiac cells forming a syncytium (Guyton and Hall 1996, Fig. 9-2, p. 108).

number of ionic currents carrying sodium ions (Na^+), potassium ions (K^+), and calcium ions (Ca^{2+}) across the cell membrane. In our model, we apply the Courtemanche-Ramirez-Nattel model of the human atrial action potential [37] to describe the ionic membrane currents and intracellular calcium handling by the SR.

Mechanical behavior of a single segment is modeled by the classical three-element rheological scheme introduced by Hill in 1938 [71, 80]. Active force generated by the sarcomeres is represented by a contractile element together with a series elastic element. A parallel elastic element describes mechanical behavior when the segment is not electrically stimulated. Contractile force generated by the sarcomeres is related to the intracellular Ca^{2+} concentration, the sarcomere length, and the velocity of sarcomere shortening. To model the contractile force, we apply *model 4* from Rice *et al.* [158].

An important aspect of our model is the influence of mechanical deformation on electrophysiology, i.e., *mechanoelectric feedback*. In our model, we consider the immediate influence of stretch on the action potential by modeling a stretch-activated current as proposed by Zabel *et al.* [230]. In addition, we consider the adaptation of ionic membrane currents triggered by changes in mechanical load. The strong coupling between cardiac electrophysiology and cardiac mechanics is a unique property of our model, which is reflected by its application to obtain more insight in the cause and consequences of mechanical deformation on cardiac electrophysiology.

1.2 Applications of the Cellular Bidomain Model

We apply the Cellular Bidomain Model to investigate both physiological (normal) and pathological (abnormal) cardiac electrophysiology and mechano-electric feedback. In particular, we investigate the success and failure of defibrillation, the onset of atrial fibrillation in relation to ectopic activity and stretch, and the remodeling of ionic membrane currents due to changes in activation with ventricular pacing.

1.2.1 Defibrillation

Both atrial and ventricular fibrillation can be treated by the application of an electrical shock, which excites the entire muscle mass and stops any propagation of the impulse. If successful, normal sinus rhythm is restored when the heart muscle cells become excitable again. This procedure is called *defibrillation* and has been successfully applied for the first time to a human in 1947 [14].

Mathematical models describing the cardiac tissue as a uniform conductive bidomain do not predict successful defibrillation [136]. We simulate the fibrillating heart by inducing spiral waves in a sheet of cardiac tissue. By modeling the cardiac tissue as a nonuniform bidomain, we investigate whether nonconducting obstacles and nonuniform gap-junctional coupling may affect the formation of so-called virtual electrodes and explain the clinical success of defibrillation.

1.2.2 Atrial fibrillation

Once an atrial cell is excited, it remains refractory for a period of 0.2 to 0.3 s, during which the cell cannot be re-excited. If the wavefront continuously enters tissue that is just recovered from the previous excitation, we speak of a reentrant depolarization wave. The wavelength (WL) of a reentrant wave is defined as the product of the conduction velocity (CV) and the effective refractory period (ERP). The incidence of atrial arrhythmia is determined by the wave length and the size of the atria [155]. When stimulated at a higher frequency, the refractory period tends to shorten, so that the pathway of a reentrant depolarization wave may change [195], or the depolarization wave may break up in smaller reentrant circuits [196, 227]. In case a single depolarization wave circles around the atria, we speak of atrial flutter. If the depolarization wave breaks up in many reentrant circuits, we speak of atrial fibrillation.

Atrial fibrillation (AF) is the most common cardiac arrhythmia [133]. The prevalence of AF increases with age from 0.5 percent of people under the age of 60 to almost 10 percent of people over the age of 80 [92]. Procedures to prevent reoccurrence of AF once diagnosed have been developed for the treatment of patients [133]. Traditionally, cardiac arrhythmias are treated with antiarrhythmic drugs that control heart rhythm by changing electrical properties. These drugs not only influence atrial electrophysiology, but also ventricular electrophysiology. The effects on ventricular electrophysiology can lead to lifethreatening ventricular arrhythmia [132]. Nowadays, non-pharmacological therapies are under investigation. These therapies include controlled destruction of arrhythmia-generating tissue, the so-called *ablation therapy*, and implantable devices that can sense arrhythmias and terminate them with electrical shocks [131].

Related to the occurrence of AF are changes in the structural and electrical properties of the atrial tissue [5, 134]. *Structural remodeling* of the tissue includes the increase of cell size, interstitial fibrosis, and gap junction remodeling [11, 88, 183]. *Electrical remodeling* includes the change in number and morphology of ion channels, which affects the ionic membrane currents. In the atria, electrical remodeling is manifested through shorter refractory periods, greater dispersion of atrial refractoriness, and atrial conduction delay [18]. Since structural remodeling leads to a reduced conduction velocity and electrical remodeling leads to shorter refractory periods, both types of remodeling can influence the wavelength and thus the incidence of atrial arrhythmia. Besides structural and electrical remodeling, contractile remodeling [167], stretch [135], atrial dilatation [168], and atrial fibrillation itself ("AF begets AF") [221] are involved.

Although AF is facilitated by each of these mechanisms, a trigger is required to initiate an episode of AF [172]. Episodes of paroxysmal AF are often triggered by ectopic foci located in the pulmonary veins [39]. Possible mechanisms for focal activity include micro-reentry within the pulmonary veins [73] and spontaneous depolarization of cells located in the pulmonary veins [66]. Experimental data indicate a possible role of the pacemaker current I_f in the initiation of AF [76, 128]. By incorporating I_f in our model, we investigate the effect of I_f on impulse propagation and ectopic activity under normal and under pathological conditions.

1.2.3   Mechanoelectric feedback

Mechanoelectric feedback is a generic term to describe the influence of mechanical deformation of cardiac tissue on the electrophysiology [113, 114]. Mechanisms of mechanoelectric feedback include immediate influence on the

action potential through stretch-activated channels (SACs) [62, 78, 105], force-feedback on the intracellular Ca^{2+} concentration [115], and long-term effects involving cell signaling pathways [168].

Experimental studies show an increased vulnerability to AF in acutely dilated atria [54, 153, 166]. By application of a SAC blocker, vulnerability to AF decreases significantly [16, 17], indicating a role for SACs in the initiation of AF [152]. In this thesis, we investigate the effect of the stretch-activated current (I_{sac}) on impulse propagation in a homogeneous and in an inhomogeneous cardiac fiber. In addition, we investigate the effect of stretch on possible arrhythmic behavior in a model of the human atria.

1.2.4 Electrical remodeling in the ventricles

Changes in heart rate or activation sequence by means of pacing induces changes in AP morphology and duration [121]. Short-term rapid ventricular pacing results in APD shortening [121], while chronic rapid ventricular pacing results in APD prolongation [89]. Chronic epicardial pacing of the left ventricle results in APD prolongation near the pacing site and APD shortening in remote regions [36, 120]. These changes affect repolarization and appear as modulation of the T wave in the electrocardiogram (ECG) [160]. Experimental observations indicate that current density and kinetics of individual ionic membrane currents change over time in response to ventricular pacing [145, 164, 229]. In case these changes are persistent, we speak of electrical remodeling [36, 120]. The physiological mechanisms that trigger electrical remodeling are poorly understood. Based on experimental observations, Jeyaraj *et al.* [87] suggest mechanoelectric feedback as a mechanism for electrical remodeling. Recently, Sosunov *et al.* [178] showed that electrical remodeling can be inhibited by reducing mechanical load or by reducing contractility. These findings indicate that changes in mechanical load are involved in electrical remodeling with epicardial pacing. In this thesis, we investigate the relation between electrical remodeling and changes in mechanical load that occur with epicardial pacing.

1.3 Thesis outline

The thesis is organized as follows. In Chapter 2, the Cellular Bidomain Model is introduced. Simulation results of normal cardiac impulse propagation and arrhythmic behavior are presented. In addition, normal depolarization of the human atria is simulated using a triangular mesh created from MRI data. Numerical aspects of our model are discussed in Chapter 3. In particular,

our methods to save computation time and memory are introduced and verified. Next, in Chapter 4, the model is applied to study the origin and effect of virtual electrode polarization on 2D sheets of uniform and nonuniform cardiac tissue. We simulate defibrillation by the application of an electrical shock on a sheet of tissue in which a spiral wave has been initiated. With this model, we investigate whether nonconducting obstacles and nonuniform cellular coupling may explain the clinical success of defibrillation. In Chapter 5, we simulate pathology by extending the model with fibrosis and gap junction remodeling. The model is applied to investigate the effect of an increased expression of the pacemaker current I_f on impulse propagation and ectopic activity under normal and under pathological conditions. In Chapter 6, the model is extended with mechanical behavior and the stretch-activated current I_{sac} to investigate the effect of stretch on impulse propagation in a cardiac fiber model. In Chapter 7, the model from Chapter 6 is extended with a simulation of the cardiac cycle. Under the assumption that stroke work is homogeneously distributed after electrical remodeling, it is investigated whether remodeling of the L-type Ca^{2+} current $I_{Ca,L}$ is triggered by changes in mechanical load. In Chapter 8, we apply our model of cardiac electrophysiology and mechanoelectric feedback to evaluate the effect of stretch on the onset and perpetuation of atrial fibrillation. To initiate atrial arrhythmia, an ectopic focus is simulated by frequent stimulation of the tissue near the pulmonary veins. Acute atrial dilatation is simulated by applying overall stretch to the atria. In these simulations, we use the geometry of the human atria from Chapter 2 and the numerical approach described in Chapter 3. Finally, in Chapter 9, we discuss the model, its applications, and possible improvements.

2

Modeling and simulation of cardiac electrophysiology and arrhythmia: the Cellular Bidomain Model

Abstract

Origin and persistence of cardiac arrhythmia such as atrial fibrillation is studied by means of computer simulations. The excitable tissue is often modeled as a continuous two-phase medium, representing the intracellular and interstitial domains, respectively. A possible drawback of continuous models is the lack of flexibility when modeling discontinuities in the cardiac tissue. We introduce a discrete bidomain model in which the cardiac tissue is subdivided in segments, each representing a small number of cardiac cells. Active membrane behavior as well as intracellular coupling and interstitial currents are described by this model. Compared with the well-known continuous bidomain equations, our Cellular Bidomain Model is better aimed at modeling the structure of cardiac tissue, in particular anisotropy, myofibers, fibrosis, and gap junction remodeling. The model is applied to simulate propagation of the depolarization wave along a fiber, arrhythmic behavior on a sheet of tissue, and depolarization of the human atria. In conclusion, the Cellular Bidomain Model is well-suited to investigate cardiac electrophysiology under normal and under pathological conditions.

2.1 Introduction

Atrial fibrillation (AF) is characterized by rapid and irregular electrical activity, which results in irregular contraction of the atria [133]. Besides experimental and clinical studies, computer simulations are frequently applied to obtain insight in the onset and perpetuation of AF [67, 83, 84, 104, 214, 215]. In these simulation studies, the cardiac tissue is usually modeled as a continuous conductive medium. To investigate the effects of structural and electrical remodeling in relation to the onset and perpetuation of cardiac arrhythmia, we introduce the Cellular Bidomain Model. In this model, the cardiac tissue is subdivided in segments. Each segment represents a small number of cells with the same electrophysiological state. Active membrane behavior is modeled by a number of ion currents as well as storage and release of calcium (Ca^{2+}) from the sarcoplasmic reticulum (SR). Intracellular and interstitial currents flow between adjacent segments, and are related to the amount of cellular coupling. Local intercellular coupling may be varied to simulate structural remodeling. Electrical remodeling may be simulated by changing the ionic membrane currents.

We compare the Cellular Bidomain Model with the continuous bidomain equations and apply the model to study several aspects of cardiac electrophysiology. In particular, we investigate impulse propagation when the cardiac tissue is modeled as a square grid, a rectangular grid, or a brickwall. Furthermore, the dynamic behavior of the tissue over a longer period of time is studied by initiating a reentrant spiral wave. Finally, a depolarization wave over the atria is simulated using a 3D geometry representing the human atria.

2.2 Methods

2.2.1 Cellular Bidomain Model

The Cellular Bidomain Model describes active membrane behavior as well as intracellular coupling and interstitial currents. To abstract from the geometry and structure of the cardiac tissue, we introduce a *graph*, composed of nodes and edges, where a *node* represents a single cardiac cell or a group of cells and an *edge* the gap junctions between the cells. Such a graph is called a *simulation graph*. Within a simulation graph, different cell types may be distinguished, each having their own membrane behavior. The state of one node is characterized by the *intracellular potential* V_{int}, the *extracellular potential* V_{ext}, and the state of the cell membrane, which is expressed in gating variables and ion

concentrations. The *membrane potential* V_{mem} is defined by

$$V_{\text{mem}} = V_{\text{int}} - V_{\text{ext}}. \tag{2.1}$$

Edges are characterized by the conduction properties for intracellular and interstitial currents between two adjacent nodes. We call these electrical properties the *intracellular* and *extracellular* conductance, which are denoted by σ_{int} and σ_{ext}, respectively. It is assumed that for each edge it holds $\sigma_{\text{int}} > 0$ and $\sigma_{\text{ext}} > 0$.

Consider simulation graph $\mathcal{G}(\mathcal{N}, \mathcal{E})$, where $\mathcal{N}$ represents the set of nodes and $\mathcal{E}$ the edges between the nodes. It is assumed that $\mathcal{G}(\mathcal{N}, \mathcal{E})$ is connected, i.e., each node can be reached from all other nodes via a path consisting of one or more edges. The state of each node $n \in \mathcal{N}$ is described by intracellular potential V_{int}^n, extracellular potential V_{ext}^n, membrane potential $V_{\text{mem}}^n = V_{\text{int}}^n - V_{\text{ext}}^n$ (unit mV), and the state of the membrane. An edge between nodes $n, m \in \mathcal{N}$ exists when $(n, m) \in \mathcal{E}$. A simulation graph is not directed, thus $(n, m) \in \mathcal{E} \equiv (m, n) \in \mathcal{E}$. The intracellular conductance of edge $(n, m) \in \mathcal{E}$ is denoted by $\sigma_{\text{int}}^{(n,m)}$, and the extracellular conductance by $\sigma_{\text{ext}}^{(n,m)}$ (unit mS). For each edge $(n, m) \in \mathcal{E}$, it holds $\sigma_{\text{int}}^{(n,m)} = \sigma_{\text{int}}^{(m,n)}$ and $\sigma_{\text{ext}}^{(n,m)} = \sigma_{\text{ext}}^{(m,n)}$. The intracellular and extracellular currents flowing from node n to node m are denoted by $I_{\text{int}}^{n \to m}$ and $I_{\text{ext}}^{n \to m}$ (unit μA), and satisfy Ohm's law:

$$I_{\text{int}}^{n \to m} = (V_{\text{int}}^n - V_{\text{int}}^m)\sigma_{\text{int}}^{(n,m)}, \tag{2.2}$$

$$I_{\text{ext}}^{n \to m} = (V_{\text{ext}}^n - V_{\text{ext}}^m)\sigma_{\text{ext}}^{(n,m)}. \tag{2.3}$$

The intracellular current entering node n coming from adjacent nodes is denoted by I_{int}^n, and the extracellular current entering node n is denoted by I_{ext}^n, i.e.,

$$I_{\text{int}}^n = \sum_{(a,n) \in \mathcal{E}} I_{\text{int}}^{a \to n}, \tag{2.4}$$

$$I_{\text{ext}}^n = \sum_{(a,n) \in \mathcal{E}} I_{\text{ext}}^{a \to n}. \tag{2.5}$$

According to Kirchhoff's law, current entering a node as intracellular current must flow to the interstitial space as transmembrane current and leave the node as extracellular current. By choosing the transmembrane current (I_{trans}) flowing from the intracellular space to the interstitial space, we obtain for node n

$$I_{\text{trans}}^n = I_{\text{int}}^n = -I_{\text{ext}}^n. \tag{2.6}$$
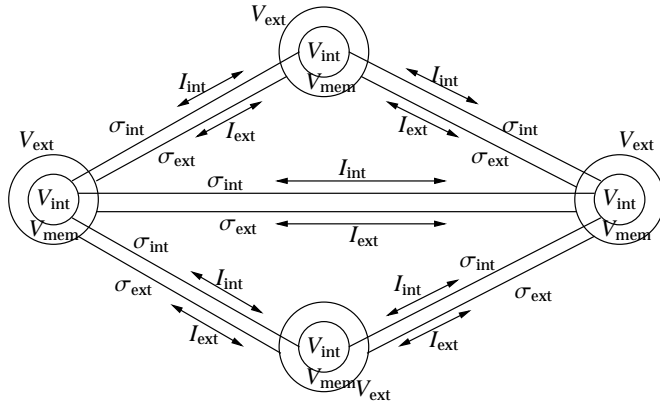
Figure 2.1: Graphical representation of a simulation graph. The state of each node is represented by the intracellular potential V_{int}, the extracellular potential V_{ext}, and the membrane potential V_{mem}. Electrical connections between the nodes are indicated by the intracellular and interstitial conductances, which are denoted by σ_{int} and σ_{ext}. The intracellular and interstitial currents flowing between the nodes are represented by the arrows labeled with I_{int} and I_{ext}.

The transmembrane current (unit μA) consists of capacitive and ionic currents, and is defined by

$$I_{\text{trans}}^n = C_{\text{mem}}^n \frac{\mathrm{d}V_{\text{mem}}^n}{\mathrm{d}t} + S_{\text{mem}}^n I_{\text{ion}}(V_{\text{mem}}^n, \mathbf{q}^n), \tag{2.7}$$

where C_{mem}^n is the membrane capacitance of node n (unit μF), t is time (unit ms), S_{mem}^n is the membrane surface (unit cm^2), and $I_{\text{ion}}(V_{\text{mem}}^n, \mathbf{q}^n)$ the ionic membrane current of node n expressed in μA per cm^2 membrane surface. The ionic current size depends on the membrane potential V_{mem}^n and the state of the membrane $\mathbf{q}^n$, which is usually expressed by a number of gating variables and ion concentrations. The Cellular Bidomain Model is defined by equations (2.6) and (2.7). A graphical representation of a simulation graph composed of four nodes and five edges is presented in Figure 2.1.

Although different membrane models can be applied for different nodes to model heterogeneous cell membrane behavior, we apply the Courtemanche-Ramirez-Nattel model of the human atrial action potential [37] for all nodes. In this model, the total ionic current is given by

$$I_{\text{ion}} = I_{\text{Na}} + I_{\text{K1}} + I_{\text{to}} + I_{\text{Kur}} + I_{\text{Kr}} + I_{\text{Ks}} + I_{\text{Ca,L}} + I_{\text{p,Ca}} + I_{\text{NaK}} + I_{\text{NaCa}} + I_{\text{b,Na}} + I_{\text{b,Ca}}, \tag{2.8}$$

where I_{Na} is fast inward Na$^+$ current, I_{K1} is inward rectifier K$^+$ current, I_{to} is transient outward K$^+$ current, I_{Kur} is ultrarapid delayed rectifier K$^+$ current, I_{Kr} is rapid delayed rectifier K$^+$ current, I_{Ks} is slow delayed rectifier K$^+$

current, $I_{\text{Ca,L}}$ is L-type Ca^{2+} current, $I_{\text{p,Ca}}$ is Ca^{2+} pump current, I_{NaK} is Na^+-K^+ pump current, I_{NaCa} is $\text{Na}^+/\text{Ca}^{2+}$ exchanger current, and $I_{\text{b,Na}}$ and $I_{\text{b,Ca}}$ are background Na^+ and Ca^{2+} currents [37]. The model keeps track of the intracellular concentrations of Na^+, K^+, and Ca^{2+}. The handling of intracellular Ca^{2+} by the sarcoplasmic reticulum (SR) is described by considering three intracellular compartments: myoplasm, sarcoplasmic reticulum (SR) release compartment (junctional SR), and SR uptake compartment (network SR). Furthermore, Ca^{2+} buffering within the cytoplasm mediated by troponin and calmodulin is described as well as Ca^{2+} buffering mediated by calsequestrin in the SR. An important characteristic of the Courtemanche-Ramirez-Nattel model is the rate-dependent adaptation of the action potential duration [37]. The equations defining the ion concentrations, ionic membrane currents, SR currents, and Ca^{2+} buffering are given in Appendix A.

2.2.2 Continuous bidomain equations

A generally accepted model which also distinguishes between the intracellular and interstitial space is described by the *bidomain equations* [69]. The bidomain model was first proposed by Tung and Geselowitz [203]. In this model, the microstructure of connected individual cells forming a syncytium in the extracellular space is homogenized in a three-dimensional domain. The cardiac tissue is then viewed as a two-phase medium, as if every point in space consists of a piece of intracellular space and a piece of interstitial space. At each point in space the two potentials V_{int} and V_{ext} are defined. As in the Cellular Bidomain Model, the total current defined by the sum of the intracellular and extracellular currents is conserved, which is denoted by

$$\nabla \cdot (\tilde{g}_{\text{int}} \nabla V_{\text{int}} + \tilde{g}_{\text{ext}} \nabla V_{\text{ext}}) = 0, \tag{2.9}$$

where $\tilde{g}_{\text{int}}$ and $\tilde{g}_{\text{ext}}$ are intracellular and extracellular conductivity tensors. The transmembrane current I_{trans} is the current flowing from the intracellular space to the interstitial space. I_{trans} is expressed per unit of tissue volume (unit $\mu\text{A}/\text{cm}^3$) and is defined by

$$I_{\text{trans}} = \nabla \cdot (\tilde{g}_{\text{int}} \nabla V_{\text{int}}) = -\nabla \cdot (\tilde{g}_{\text{ext}} \nabla V_{\text{ext}}). \tag{2.10}$$

As for the Cellular Bidomain Model, I_{trans} consists of capacitive and ionic currents, i.e.,

$$I_{\text{trans}} = \chi (C_{\text{mem}} \frac{\partial V_{\text{mem}}}{\partial t} + I_{\text{ion}}) = \nabla \cdot (\tilde{g}_{\text{int}} \nabla V_{\text{int}}), \tag{2.11}$$

where $V_{\text{mem}} = V_{\text{int}} - V_{\text{ext}}$ is the membrane potential, χ is the ratio of membrane surface to tissue volume (unit cm^{-1}), C_{mem} is the membrane capacitance (unit

μF/cm^2), and I_{ion} is the ionic membrane current (expressed in μA per cm^2 membrane surface).

The bidomain model is defined by equations (2.10) and (2.11). By eliminating V_{int}, the system of equations can be written as

$$\chi(C_{\text{mem}}\frac{\partial V_{\text{mem}}}{\partial t} + I_{\text{ion}}) = -\nabla \cdot (\tilde{g}_{\text{ext}}\nabla V_{\text{ext}}), \tag{2.12}$$

$$\nabla \cdot ((\tilde{g}_{\text{int}} + \tilde{g}_{\text{ext}})\nabla V_{\text{ext}}) = -\nabla \cdot (\tilde{g}_{\text{int}}\nabla V_{\text{mem}}). \tag{2.13}$$

Boundary conditions usually assume that there is no current across the boundary that directly enters the intracellular space. If a current is injected, it enters the cardiac tissue through the extracellular space. More explicit derivations of the bidomain equations are presented in Refs. [74, 97, 191].

2.2.3 Relation between bidomain equations and Cellular Bidomain Model

Consider a rectangular slab of cardiac tissue with anisotropy uniformly defined throughout the tissue. It is assumed that the intracellular and extracellular conductivities are homogeneous and are represented by tensors $\tilde{g}_{\text{int}}$ and $\tilde{g}_{\text{ext}}$ defined by

$$\tilde{g}_{\text{int}} = \begin{pmatrix} g_{\text{int}}^x & 0 & 0 \\ 0 & g_{\text{int}}^y & 0 \\ 0 & 0 & g_{\text{int}}^z \end{pmatrix}, \tag{2.14}$$

$$\tilde{g}_{\text{ext}} = \begin{pmatrix} g_{\text{ext}}^x & 0 & 0 \\ 0 & g_{\text{ext}}^y & 0 \\ 0 & 0 & g_{\text{ext}}^z \end{pmatrix}. \tag{2.15}$$

Using the definitions of tensors $\tilde{g}_{\text{int}}$ and $\tilde{g}_{\text{ext}}$, the continuous bidomain equations (2.10) and (2.11) become

$$g_{\text{int}}^x \frac{\partial^2 V_{\text{int}}}{\partial x^2} + g_{\text{int}}^y \frac{\partial^2 V_{\text{int}}}{\partial y^2} + g_{\text{int}}^z \frac{\partial^2 V_{\text{int}}}{\partial z^2} = -\left(g_{\text{ext}}^x \frac{\partial^2 V_{\text{ext}}}{\partial x^2} + g_{\text{ext}}^y \frac{\partial^2 V_{\text{ext}}}{\partial y^2} + g_{\text{ext}}^z \frac{\partial^2 V_{\text{ext}}}{\partial z^2}\right), \tag{2.16}$$

$$\chi(C_{\text{mem}}\frac{\partial V_{\text{mem}}}{\partial t} + I_{\text{ion}}) = g_{\text{int}}^x \frac{\partial^2 V_{\text{int}}}{\partial x^2} + g_{\text{int}}^y \frac{\partial^2 V_{\text{int}}}{\partial y^2} + g_{\text{int}}^z \frac{\partial^2 V_{\text{int}}}{\partial z^2}. \tag{2.17}$$

When solving the system of equations (2.16) and (2.17) by means of the finite difference method [198], the cardiac tissue must be discretized. Discretization gives a system of ordinary differential equations (ODEs) and linear equations. Under the assumption that the cardiac tissue is represented by a rectangular grid composed of segments of size $\Delta x \times \Delta y \times \Delta z$, we show

that the same system of ODEs and linear equations is obtained for a specific choice of conductances and capacitances in the Cellular Bidomain Model.

The conversion from the continuous bidomain equations to a simulation graph for the Cellular Bidomain Model is done by assuming that each node $n \in \mathcal{N}$ represents a segment of cardiac tissue of size $\Delta x \times \Delta y \times \Delta z$. The intracellular and extracellular conductances between two adjacent segments in the x-direction are defined by

$$\sigma_{\text{int}}^x = g_{\text{int}}^x \frac{\Delta y \Delta z}{\Delta x}, \tag{2.18}$$

$$\sigma_{\text{ext}}^x = g_{\text{ext}}^x \frac{\Delta y \Delta z}{\Delta x}, \tag{2.19}$$

the intracellular and extracellular conductances between two adjacent segments in the y-direction by

$$\sigma_{\text{int}}^y = g_{\text{int}}^y \frac{\Delta x \Delta z}{\Delta y}, \tag{2.20}$$

$$\sigma_{\text{ext}}^y = g_{\text{ext}}^y \frac{\Delta x \Delta z}{\Delta y}, \tag{2.21}$$

and the intracellular and extracellular conductances between two adjacent segments in the z-direction by

$$\sigma_{\text{int}}^z = g_{\text{int}}^z \frac{\Delta x \Delta y}{\Delta z}, \tag{2.22}$$

$$\sigma_{\text{ext}}^z = g_{\text{ext}}^z \frac{\Delta x \Delta y}{\Delta z}. \tag{2.23}$$

Furthermore, the membrane surface S_{mem}^n for node n is defined by

$$S_{\text{mem}}^n = \chi \Delta x \Delta y \Delta z, \tag{2.24}$$

and the membrane capacitance C_{mem}^n (expressed in μF) by

$$C_{\text{mem}}^n = S_{\text{mem}}^n C_{\text{mem}}, \tag{2.25}$$

where C_{mem} represents the membrane capacitance expressed in μF per cm^2 membrane surface.

Let $V_{\text{int}}(x, y, z)$ denote the intracellular potential of node n at position (x, y, z).

The intracellular current entering node n is then defined by

$$
\begin{aligned}
I_{\text{int}}^n &= \sum_{(a,n)\in\mathcal{E}} I_{\text{int}}^{a\to n} \\
&= (V_{\text{int}}(x-\Delta x,y,z)-V_{\text{int}}(x,y,z))\,\sigma_{\text{int}}^x + (V_{\text{int}}(x+\Delta x,y,z)-V_{\text{int}}(x,y,z))\,\sigma_{\text{int}}^x + \\
&\quad (V_{\text{int}}(x,y-\Delta y,z)-V_{\text{int}}(x,y,z))\,\sigma_{\text{int}}^y + (V_{\text{int}}(x,y+\Delta y,z)-V_{\text{int}}(x,y,z))\,\sigma_{\text{int}}^y + \\
&\quad (V_{\text{int}}(x,y,z-\Delta z)-V_{\text{int}}(x,y,z))\,\sigma_{\text{int}}^z + (V_{\text{int}}(x,y,z+\Delta z)-V_{\text{int}}(x,y,z))\,\sigma_{\text{int}}^z \\
&= (V_{\text{int}}(x-\Delta x,y,z)-2V_{\text{int}}(x,y,z)+V_{\text{int}}(x+\Delta x,y,z))\,\sigma_{\text{int}}^x + \\
&\quad (V_{\text{int}}(x,y-\Delta y,z)-2V_{\text{int}}(x,y,z)+V_{\text{int}}(x,y+\Delta y,z))\,\sigma_{\text{int}}^y + \\
&\quad (V_{\text{int}}(x,y,z-\Delta z)-2V_{\text{int}}(x,y,z)+V_{\text{int}}(x,y,z+\Delta z))\,\sigma_{\text{int}}^z.
\end{aligned}
$$

Using the definitions of σ_{int}^x, σ_{int}^y, and σ_{int}^z, we obtain

$$
\begin{aligned}
I_{\text{int}}^n &= \frac{V_{\text{int}}(x-\Delta x,y,z)-2V_{\text{int}}(x,y,z)+V_{\text{int}}(x+\Delta x,y,z)}{\Delta x^2}\Delta x\Delta y\Delta z\, g_{\text{int}}^x + \\
&\quad \frac{V_{\text{int}}(x,y-\Delta y,z)-2V_{\text{int}}(x,y,z)+V_{\text{int}}(x,y+\Delta y,z)}{\Delta y^2}\Delta x\Delta y\Delta z\, g_{\text{int}}^y + \\
&\quad \frac{V_{\text{int}}(x,y,z-\Delta z)-2V_{\text{int}}(x,y,z)+V_{\text{int}}(x,y,z+\Delta z)}{\Delta z^2}\Delta x\Delta y\Delta z\, g_{\text{int}}^z.
\end{aligned}
$$

A similar expression can be obtained for I_{ext}^n.

Equation (2.6) of the Cellular Bidomain Model states that $I_{\text{int}}^n = -I_{\text{ext}}^n$, which corresponds to the discretized form of equation (2.16) after division with $\Delta x\Delta y\Delta z$. Using $S_{\text{mem}}^n = \chi\Delta x\Delta y\Delta z$, and $C_{\text{mem}}^n = S_{\text{mem}}^n C_{\text{mem}}$, equation (2.7) of the Cellular Bidomain Model can be written as

$$
I_{\text{trans}}^n = \chi\Delta x\Delta y\Delta z(C_{\text{mem}}\frac{dV_{\text{mem}}^n}{dt} + I_{\text{ion}}(V_{\text{mem}}^n, \mathbf{q}^n)), \tag{2.26}
$$

which corresponds to the discretized form of equation (2.17) after division with $\Delta x\Delta y\Delta z$. Thus, by defining the conductivities, membrane surface, and membrane capacitance as described above, the simulation graph represents a discrete version of the continuous bidomain with surface-to-volume ratio χ, membrane capacitance C_{mem}, and conductivity properties defined by tensors $\tilde{g}_{\text{int}}$ and $\tilde{g}_{\text{ext}}$.

2.2.4   Brickwall configuration

An alternative way to segmentize the cardiac tissue is assuming that the segments are connected to one another in a brickwall fashion. Models in which the myocytes are interconnected in a brickwall fashion have been proposed by Leon and Roberge [118] and by Spach and Boineau [179]. In these models, a single myocyte is subdivided in segments. We introduce a brickwall
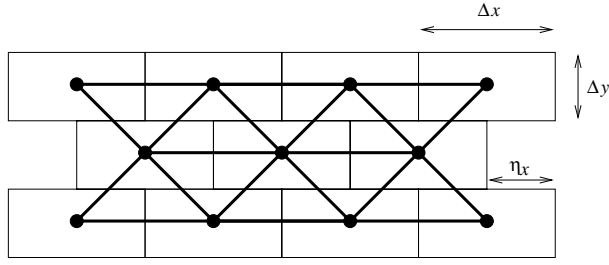
Figure 2.2: Graphical representation of brickwall configuration. The cardiac tissue is subdivided in rectangular segments of size $\Delta x \times \Delta y$. $\eta_x = \frac{1}{2}\Delta x$ is the length of the contact area between two segments in transverse direction. The simulation graph is represented by the dots (nodes) and the thick lines (edges).

configuration in which the segments of a rectangular grid are shifted in the longitudinal direction, such that each segment is connected to 6 other segments rather than 4 (Figure 2.2).

Conductivities in the x-direction are defined by equations (2.18) and (2.19). The intracellular and extracellular conductivities between two adjacent segments in the y-direction are defined by

$$\hat{\sigma}^y_{\text{int}} = g^y_{\text{int}} \frac{\eta_x \Delta z}{\Delta y}, \tag{2.27}$$

$$\hat{\sigma}^y_{\text{ext}} = g^y_{\text{ext}} \frac{\eta_x \Delta z}{\Delta y}, \tag{2.28}$$

where η_x represents the length of the contact area between the two segments in transverse direction. An irregular brickwall configuration is obtained when segment lengths are individually varied. Here, we consider a regular brickwall in which segments lengths are equal to Δx and $\eta_x = \frac{1}{2}\Delta x$. Using Taylor expansions, we derive a relation between the ratio $\Delta x/\Delta y$ and the effective conductivities that are approximated by a regular brickwall.

Consider a 2D brickwall and let $V_{\text{int}}(x, y)$ denote the intracellular potential of node n at position (x, y). Assuming $\eta_x = \frac{1}{2}\Delta x$, the intracellular current entering node n is defined by

$$
\begin{aligned}
I^n_{\text{int}} &= \sum_{(a,n)\in\mathcal{E}} I^{a\to n}_{\text{int}} \\
&= \left(V_{\text{int}}(x - \Delta x, y) - 2V_{\text{int}}(x, y) + V_{\text{int}}(x + \Delta x, y)\right) \sigma^x_{\text{int}} + \\
&\quad \left(V_{\text{int}}(x - \tfrac{1}{2}\Delta x, y - \Delta y) - 2V_{\text{int}}(x, y) + V_{\text{int}}(x + \tfrac{1}{2}\Delta x, y + \Delta y)\right) \hat{\sigma}^y_{\text{int}} + \\
&\quad \left(V_{\text{int}}(x - \tfrac{1}{2}\Delta x, y + \Delta y) - 2V_{\text{int}}(x, y) + V_{\text{int}}(x + \tfrac{1}{2}\Delta x, y - \Delta y)\right) \hat{\sigma}^y_{\text{int}}.
\end{aligned}
$$

Using Taylor expansions, it can be shown that

$$I_{int}^{n} \approx \Delta x^2 \frac{\partial^2 V_{int}}{\partial x^2} \sigma_{int}^x + \left(\frac{1}{2} \Delta x^2 \frac{\partial^2 V_{int}}{\partial x^2} + 2\Delta y^2 \frac{\partial^2 V_{int}}{\partial y^2} \right) \hat{\sigma}_{int}^y \qquad (2.29)$$

and using the definitions of σ_{int}^x and $\hat{\sigma}_{int}^y$ with $\eta_x = \frac{1}{2}\Delta x$, we obtain

$$I_{int}^{n} \approx \left(g_{int}^x \Delta x \Delta y \Delta z + g_{int}^y \frac{\Delta x^3 \Delta z}{4\Delta y} \right) \frac{\partial^2 V_{int}}{\partial x^2} + g_{int}^y \Delta x \Delta y \Delta z \frac{\partial^2 V_{int}}{\partial y^2}. \qquad (2.30)$$

For a rectangular grid, we obtain

$$I_{int}^{n} \approx \Delta x^2 \frac{\partial^2 V_{int}}{\partial x^2} \sigma_{int}^x + \Delta y^2 \frac{\partial^2 V_{int}}{\partial y^2} \sigma_{int}^y, \qquad (2.31)$$

where σ_{int}^x and σ_{int}^y are defined by equations (2.18) and (2.20). Using the definitions of σ_{int}^x and σ_{int}^y, we obtain for the rectangular grid

$$I_{int}^{n} \approx g_{int}^x \Delta x \Delta y \Delta z \frac{\partial^2 V_{int}}{\partial x^2} + g_{int}^y \Delta x \Delta y \Delta z \frac{\partial^2 V_{int}}{\partial y^2}. \qquad (2.32)$$

By dividing equations (2.30) and (2.32) with $\Delta x \Delta y \Delta z$ and inspecting the difference, we find that, when using a brickwall with $\eta_x = \frac{1}{2}\Delta x$, conductivity g_{int}^x changes to $g_{int}^x + \frac{1}{4}g_{int}^y(\frac{\Delta x}{\Delta y})^2$, while conductivity g_{int}^y remains the same. In a similar way, it can be shown that g_{ext}^x changes to $g_{ext}^x + \frac{1}{4}g_{ext}^y(\frac{\Delta x}{\Delta y})^2$, while g_{ext}^y remains the same. Thus, the ratio of anisotropy increases when the cardiac tissue is modeled by a brickwall.

2.2.5 Ionic membrane currents

When the cell is at rest, the membrane potential V_{mem} typically has a value between −80 and −90 mV. Consider ionic membrane current I_{ion} describing the current flow of ion species *ion* over the membrane. In case the charge of *ion* is positive (e.g., Na^+, K^+, or Ca^{2+}), $I_{ion} < 0$ means positive charge is flowing into the cell and the membrane depolarizes, i.e., the membrane potential V_{mem} becomes less negative. In case $I_{ion} > 0$, positive charge moves out of the cell and the membrane is repolarizing, i.e., V_{mem} returns to its resting value.

The current size of I_{ion} flowing into or out of the cell is related to the intracellular and extracellular concentrations of *ion* and, since *ion* is charged, on the membrane potential. The net force acting on the ion thus depends on the electrical and chemical gradients and is referred to as the *electrochemical*

gradient or *driving force* [19]. The driving force is defined as $(V_{\text{mem}} - E_{ion})$, where E_{ion} is the equilibrium potential of *ion*. E_{ion} is given by the Nernst equation

$$E_{ion} = \frac{RT}{z_{ion}F} \ln\left(\frac{[ion]_{\text{e}}}{[ion]_{\text{i}}}\right),\tag{2.33}$$

where R is the universal gas constant, T is the absolute temperature, z_{ion} is the valence of *ion*, F is Faraday's constant, and $[ion]_{\text{e}}$ and $[ion]_{\text{i}}$ are the extracellular and intracellular concentrations of *ion*.

The direction of I_{ion} across the membrane is determined by the sign of $(V_{\text{mem}} - E_{ion})$. The current size depends on the driving force as well as the conductance g_{ion} of the membrane to *ion*, i.e.,

$$I_{ion} = g_{ion}(V_{\text{mem}} - E_{ion}),\tag{2.34}$$

which is equivalent to Ohm's law. g_{ion} depends on the number and states of the ion channels. Let γ denote the conductance of a single channel, N the number of channels, and p the probability of a channel being in the open state, then

$$g_{ion} = \gamma N p.\tag{2.35}$$

The product of γ and N determines the maximum conductance $G_{ion} = \gamma N$ and equation (2.34) is usually written as

$$I_{ion} = G_{ion}\, p\, (V_{\text{mem}} - E_{ion}).\tag{2.36}$$

The probability p of a channel being in the open state corresponds to the fraction of channels in the open state in the cell. It is assumed that the channel is controlled by a gate that can be either open or closed. Let α_p denote the opening rate constant and β_p the closing rate constant. Since p is the fraction of channels in the open state, the rate of opening is equal to $\alpha_p(1 - p)$ and the rate of closing is equal to β_p. The dynamics of p are determined by the difference between the rates of opening and closing, i.e.,

$$\frac{dp}{dt} = \alpha_p(1 - p) - \beta_p\, p.\tag{2.37}$$

At steady-state, the rates of opening and closing are equal, i.e.,

$$\alpha_p(1 - p) = \beta_p\, p,\tag{2.38}$$

from which follows

$$p = p_\infty = \frac{\alpha_p}{\alpha_p + \beta_p}.\tag{2.39}$$

Let $p(t)$ denote the value of p at time t and p_0 the value of p at time t_0, then the solution of differential equation (2.37) is

$$p(t) = p_\infty - (p_\infty - p_0)\exp\left(-\frac{t - t_0}{\tau_p}\right), \tag{2.40}$$

where time constant τ_p is defined by

$$\tau_p = \frac{1}{\alpha_p + \beta_p}. \tag{2.41}$$

Opening rate constant α_p and closing rate constant β_p depend on V_{mem} and are usually fitted to experimental data using a Boltzmann-type equation [19]. All ionic membrane currents of the Courtemanche-Ramirez-Nattel model and similar membrane models are described in this way using one or more gating variables (Appendix A).

The current flow of ions through the membrane influences the intracellular and extracellular ion concentrations. In the Courtemanche-Ramirez-Nattel model, extracellular ion concentrations are assumed to be constant. Under the assumption that I_{ion} is expressed in pA/pF, the dynamics of the intracellular ion concentrations are described by

$$\frac{\mathrm{d}[ion]_{\mathrm{i}}}{\mathrm{d}t} = -\frac{C_{\mathrm{m}}}{z_{ion}F\,\mathrm{V_i}}I_{ion}, \tag{2.42}$$

where $[ion]_{\mathrm{i}}$ is the intracellular concentration of ion, C_{m} is the membrane capacitance of a single atrial cell (100 pF [37]), z_{ion} is the valence of ion, F is Faraday's constant, and $\mathrm{V_i}$ is the intracellular volume (13668 $\mu\mathrm{m}^3$ [37]).

2.2.6   Simulation set-up

Action potential propagation is related to the conductivity of the tissue and the membrane capacitance. In Table 2.1, the bidomain parameters used for the present simulation study are listed. These parameters are based on measurements by Clerc [33] and adjusted as described by Henriquez [69]. The numerical integration scheme is described in Chapter 3. With the exception of single-cell simulations, a simulation time step of 0.01 ms was used for all simulations.

2.3   Results

2.3.1   Single cell simulations

Rate-dependent adaptation of the action potential duration (APD) is an important aspect in the onset and perpetuation of atrial fibrillation. To investi-

Table 2.1: Bidomain parameters for cardiac tissue

Parameter	Definition	Value
g_{int}^x	Longitudinal intracellular conductivity	1.7422 mS/cm
g_{int}^y	Transverse intracellular conductivity	0.1934 mS/cm
g_{int}^z	Transmural intracellular conductivity	0.1934 mS/cm
g_{ext}^x	Longitudinal extracellular conductivity	6.2500 mS/cm
g_{ext}^y	Transverse extracellular conductivity	2.3641 mS/cm
g_{ext}^z	Transmural extracellular conductivity	2.3641 mS/cm
C_{mem}	Membrane capacitance	$1.0 \, \mu F/cm^2$
χ	Surface-to-volume ratio	$2000 \, cm^{-1}$
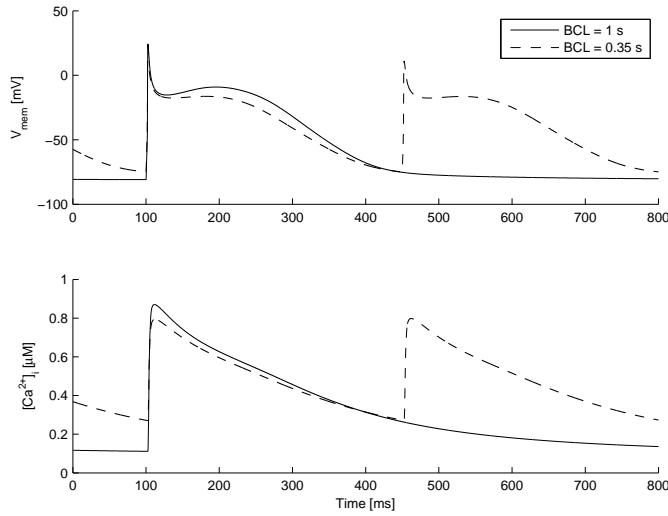
Figure 2.3: Effect of stimulation with different basic cycle length (BCL) on action potential and calcium transient. Membrane potential (V_{mem}) and intracellular calcium concentration ($[Ca^{2+}]_i$) for BCL = 1 s and BCL = 0.35 s. A stimulus current was applied at 100 ms (BCL = 1 s and BCL = 0.35 s) and at 450 ms (BCL = 0.35 s).
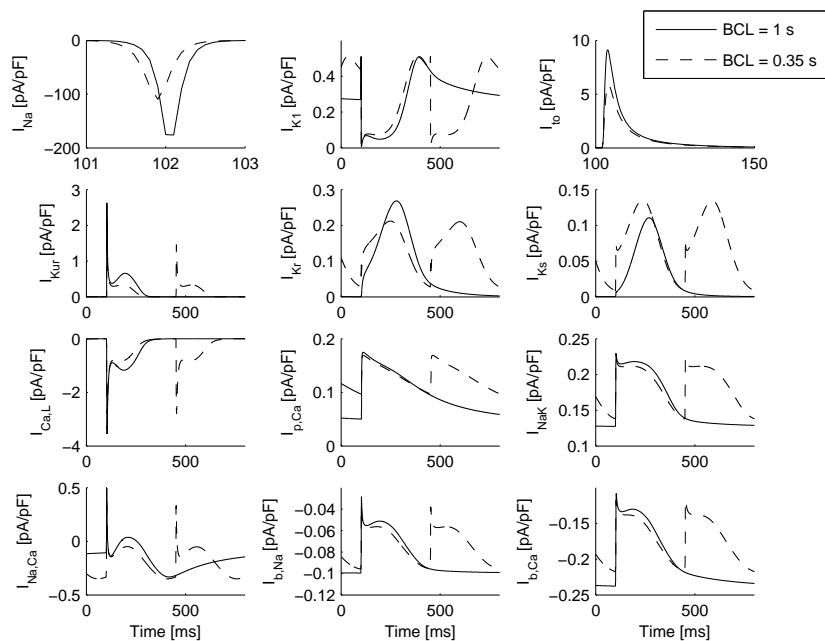
Figure 2.4: Effect of stimulation with different basic cycle length (BCL) on ionic currents. Fast inward Na$^+$ current (I_{Na}), inward rectifier K$^+$ current (I_{K1}), transient outward K$^+$ current (I_{to}), ultrarapid delayed rectifier K$^+$ current (I_{Kur}), rapid delayed rectifier K$^+$ current (I_{Kr}), slow delayed rectifier K$^+$ current (I_{Ks}), L-type Ca^{2+} current ($I_{Ca,L}$), Ca^{2+} pump current ($I_{p,Ca}$), Na$^+$-K$^+$ pump current (I_{NaK}), Na$^+$/Ca^{2+} exchanger current (I_{NaCa}), background Na$^+$ current ($I_{b,Na}$), and background Ca^{2+} current ($I_{b,Ca}$) for BCL = 1 s and BCL = 0.35 s. A stimulus current was applied at 100 ms (BCL = 1 s and BCL = 0.35 s) and at 450 ms (BCL = 0.35 s). Note the different time scales for I_{Na} and I_{to}.
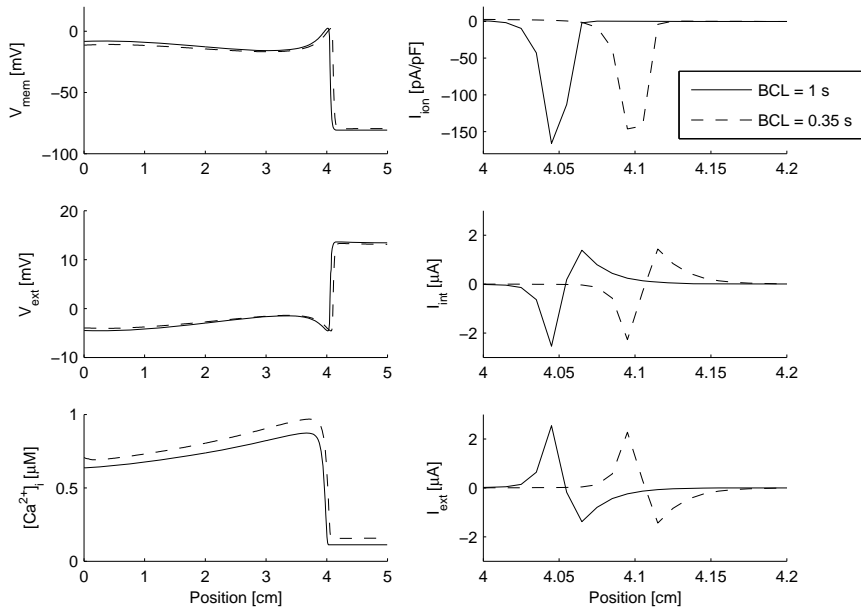
Figure 2.5: Depolarization wave along 5-cm-long fiber for BCL = 1 s and BCL = 0.35 s. Left: membrane potential (V_{mem}), extracellular potential (V_{ext}), and intracellular calcium concentration ($[\mathrm{Ca}^{2+}]_{\mathrm{i}}$). Right: ion current ($I_{\mathrm{ion}}$), intracellular current (I_{int}), and extracellular current (I_{ext}). Data plotted 0.1 s after stimulation of the segment at 0.0 cm. Note the different scales of the x-axis in the right column.

gate the effect of varying stimulation intervals, or basic cycle length (BCL), we performed a series of single cell simulations in which the cell was stimulated with a BCL of 1 s and 0.35 s, respectively. A simulation time step $\Delta t = 0.005$ ms was used and the cell was stimulated with a stimulus current of 20 pA/pF during 2 ms as in Ref. [37].

In Figure 2.3, the action potential and calcium transient are shown for BCL = 1 s and BCL = 0.35 s. The action potential duration (APD) decreases from 271 ms for BCL = 1 s to 258 ms for BCL = 0.35. In Figure 2.4, the ionic membrane currents are presented. The shorter APD for BCL = 0.35 s is mainly attributed to incomplete recovery of $I_{\mathrm{Ca,L}}$, I_{Kr}, and I_{Ks} (see Ref. [37] for details). Besides the currents involved in the plateau and repolarization phase, also the depolarizing I_{Na} current is affected by changes in BCL. I_{Na} current size decreases from 176 pA/pF (BCL = 1 s) to 110 pA/pF (BCL = 0.35 s).

2.3.2 Wave propagation along a fiber

To investigate the propagation of a depolarization wave, a 5-cm-long fiber was created that consisted of 0.01-cm-long segments. A depolarization wave was generated by stimulating the first segment with a stimulus current of 100 pA/pF until the membrane was depolarized. During twelve seconds, stimulation was repeated each 1 s or each 0.35 s to investigate the effect of varying BCL on wave propagation.

In Figure 2.5, the spatial distribution of V_{mem}, V_{ext}, $[Ca^{2+}]_i$ and of the currents I_{ion}, I_{int}, and I_{ext} are depicted 0.1 s after stimulation with BCL = 1 s and BCL = 0.35 s. The conduction velocity was 0.4103 m/s with BCL = 1 s and 0.4153 m/s with BCL = 0.35 s, such that approximately 0.1 s after stimulation of the first segment, the depolarization wave was ±4 cm from the stimulation site. Just before depolarization, V_{mem} = −80.8 mV for BCL = 1 s and V_{mem} = −79.6 mV for BCL = 0.35 s. Although I_{Na} is reduced for BCL = 0.35 s (Figure 2.4), the conduction velocity is not decreased, which is explained by the fact that V_{mem} was increased at the moment of depolarization and less current was needed to reach the excitation threshold.

2.3.3 Grid structure

The effect of using a square grid, a rectangular grid, or a brickwall was investigated using a 2×1 cm sheet of tissue in which a depolarization wave was generated in the center. The square grid was composed of segments of size 0.004×0.004 cm. Both the rectangular grid and the brickwall were composed of 0.01×0.004 cm segments. For the brickwall we used $\eta_x = \frac{1}{2}\Delta x$.

In Figure 2.6, the membrane potential V_{mem} is presented for the square grid, the rectangular grid, and the brickwall. It can be observed that a depolarization wave is generated in the center and spreads out over time. The shape of the depolarization front is ellipsoid, which is consistent with the anisotropy in the conductivity properties (Table 2.1). The shape of the depolarization fronts is similar for the square grid and the rectangular grid. In contrast, the depolarization front for the brickwall has a more elongated ellipsoidal shape, which is consistent with the larger effective conductivity in the x-direction (Section 2.2.4).

In the bidomain model [69], the conduction velocity in longitudinal direction (θ_L) is related to the tissue conductivities by

$$\theta_L \sim \sqrt{\frac{g_{int}^x \, g_{ext}^x}{g_{int}^x + g_{ext}^x}}, \tag{2.43}$$

time [ms]	square grid $\Delta x = 0.004$ cm $\Delta y = 0.004$ cm $\theta_L = 0.42$ m/s $\theta_T = 0.14$ m/s $\theta_L/\theta_T = 2.9$	rectangular grid $\Delta x = 0.01$ cm $\Delta y = 0.004$ cm $\theta_L = 0.40$ m/s $\theta_T = 0.14$ m/s $\theta_L/\theta_T = 2.8$	brickwall $\Delta x = 0.01$ cm $\Delta y = 0.004$ cm $\theta_L = 0.46$ m/s $\theta_T = 0.14$ m/s $\theta_L/\theta_T = 3.2$
5			
10			
15			
20			
25			
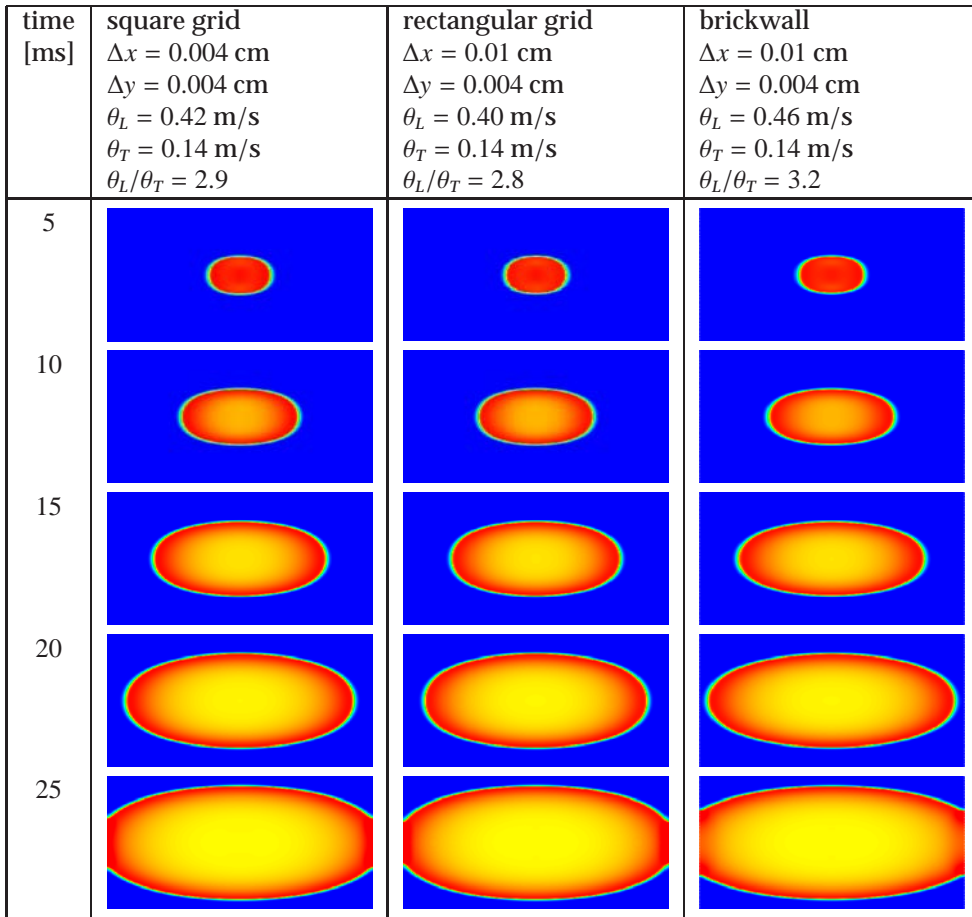
Figure 2.6: Membrane potential (V_{mem}) when cardiac tissue is represented by a square grid (left), a rectangular grid (center), or a brickwall (right). A depolarization front was generated by stimulating the center of the 2×1 cm tissue at 0 ms. Red/yellow indicates depolarized tissue and blue indicates resting tissue.

time [ms]	square grid $\Delta x = 0.004$ cm $\Delta y = 0.004$ cm $\theta_L = 0.42$ m/s $\theta_T = 0.14$ m/s $\theta_L/\theta_T = 2.9$	rectangular grid $\Delta x = 0.01$ cm $\Delta y = 0.004$ cm $\theta_L = 0.40$ m/s $\theta_T = 0.14$ m/s $\theta_L/\theta_T = 2.8$	brickwall $\Delta x = 0.01$ cm $\Delta y = 0.004$ cm $\theta_L = 0.46$ m/s $\theta_T = 0.14$ m/s $\theta_L/\theta_T = 3.2$
5			
10			
15			
20			
25			
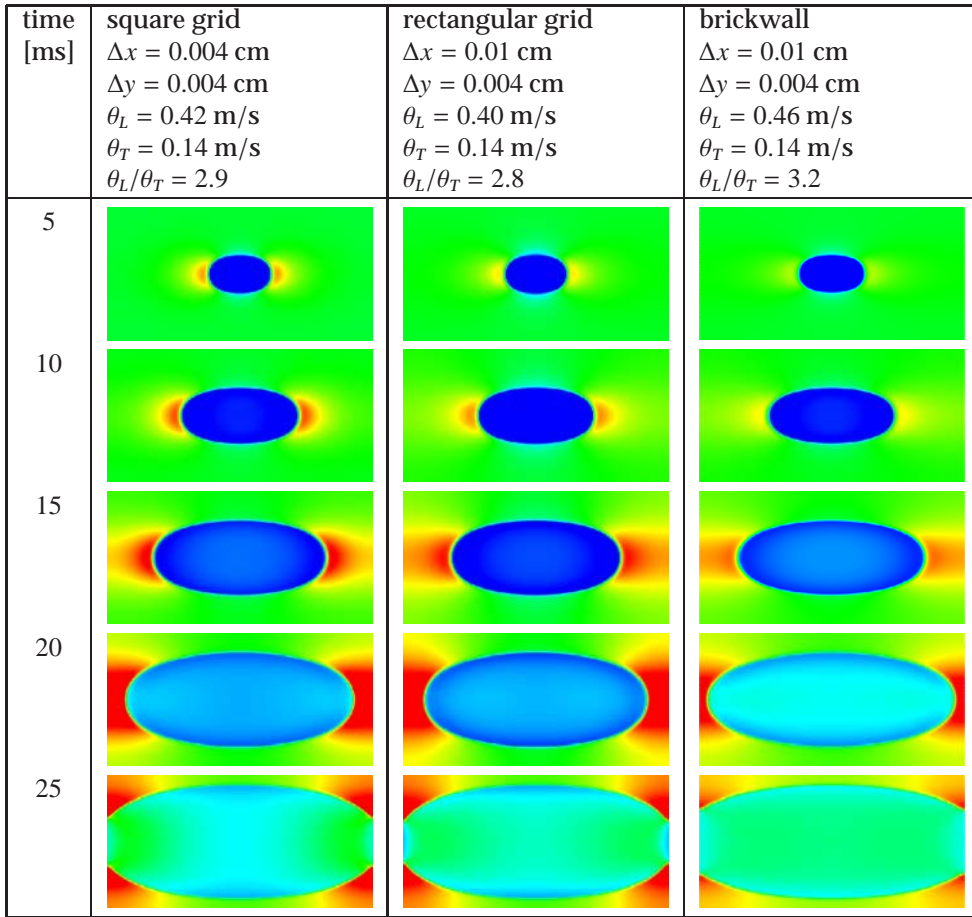
Figure 2.7: Extracellular potential (V_{ext}) when cardiac tissue is represented by a square grid (left), a rectangular grid (center), or a brickwall (right). A depolarization front was generated by stimulating the center of the 2×1 cm tissue at 0 ms. Red/yellow indicates positive V_{ext}, green indicates $V_{ext} = 0$ mV, and blue indicates negative V_{ext}.
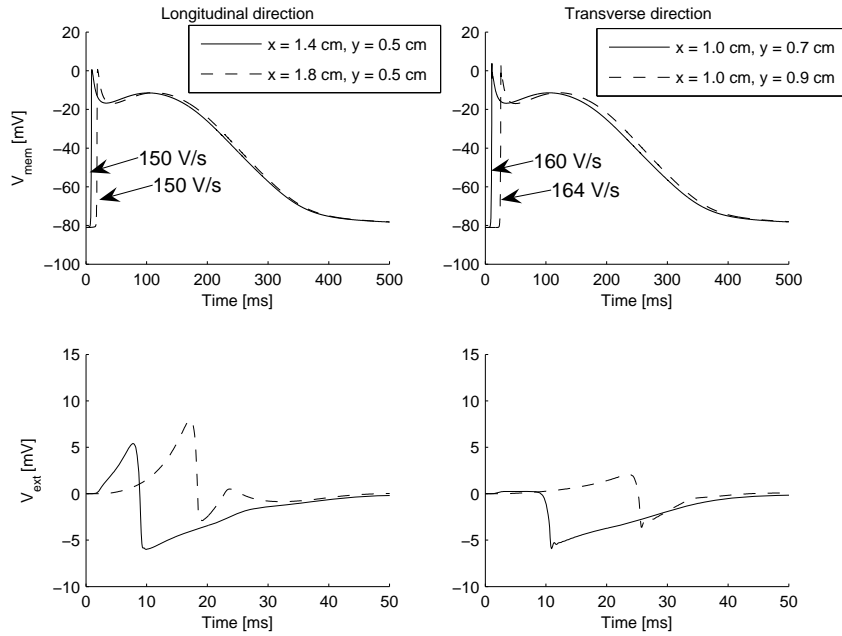
Figure 2.8: Membrane potential (V_{mem}) and extracellular potential (V_{ext}) for four segments of the 2×1 cm brickwall tissue. A depolarization wave was generated by stimulating the center ($x = 1.0$ cm, $y = 0.5$ cm) at 0 ms. Left: depolarization wave travels in longitudinal direction. Right: depolarization wave travels in transverse direction. Arrows indicate maximum upstroke velocity (($dV_{mem}/dt)_{max}$). Note the different time scale for V_{ext}.

and in transverse direction (θ_T) by

$$\theta_T \sim \sqrt{\frac{g^y_{\text{int}}\, g^y_{\text{ext}}}{g^y_{\text{int}} + g^y_{\text{ext}}}}. \tag{2.44}$$

For a regular brickwall ($\eta_x = \frac{1}{2}\Delta x$), the longitudinal intracellular conductivity is $g^x_{\text{int}} + \frac{1}{4}g^y_{\text{int}}(\frac{\Delta x}{\Delta y})^2$ and the longitudinal extracellular conductivity is $g^x_{\text{ext}} + \frac{1}{4}g^x_{\text{ext}}(\frac{\Delta x}{\Delta y})^2$ (Section 2.2.4). With the bidomain parameters defined in Table 2.1, the ratio of anisotropy θ_L/θ_T can be predicted. The predicted value of $\theta_L/\theta_T = 2.8$ for the square grid and the rectangular grid, and 3.1 for the brickwall. These values are in good agreement with the actual θ_L/θ_T in Figure 2.6.

In Figure 2.7, the extracellular potential V_{ext} is presented for the same three grids. In Figure 2.8, V_{mem} and V_{ext} are plotted for two segments of the brickwall when the depolarization wave travels in longitudinal direction and two segments when the wave travels in transverse direction. V_{mem} is similar for all segments. However, V_{ext} is more elevated before depolarization when the depolarization wave travels in longitudinal direction. This elevation in V_{ext} becomes more apparent when the segment is located further from the center. These differences in V_{ext} between longitudinal and transverse wave propagation are in agreement with the experimental results of Spach *et al.* [185] and the simulation results of Henriquez [69]. In Figure 2.8, the maximum upstroke velocity ($(dV_{\text{mem}}/dt)_{\text{max}}$) is indicated. The larger $(dV_{\text{mem}}/dt)_{\text{max}}$ for impulse propagation in transverse direction is in agreement with the experimental observations from Spach *et al.* [179, 184].

2.3.4 Arrhythmic behavior

Arrhythmic behavior was investigated by initiating a spiral wave in an 8×3 cm tissue using an S1S2 protocol [201]. First, the top of the tissue (S1) was stimulated. Next, a block of segments in the center of the left half (S2) was stimulated with a coupling interval of 325 ms. Since the bottom half of the tissue was still refractory, a depolarization front developed in one direction and a reentrant wave was established. The tissue was a brickwall structure composed of 0.02×0.008 cm segments with uniform conductivity properties. Arrhythmic behavior was studied during 6 s of simulation time.

In Figure 2.9, the onset of the spiral wave is presented. The spiral wave was unstable and after 6 s, the entire tissue was depolarized such that no re-entry could occur. The transition from arrhythmic behavior to depolarization of the entire tissue is shown in Figure 2.10. In Figure 2.11, V_{mem} is shown for three segments on the center row. The variation in AP morphology and
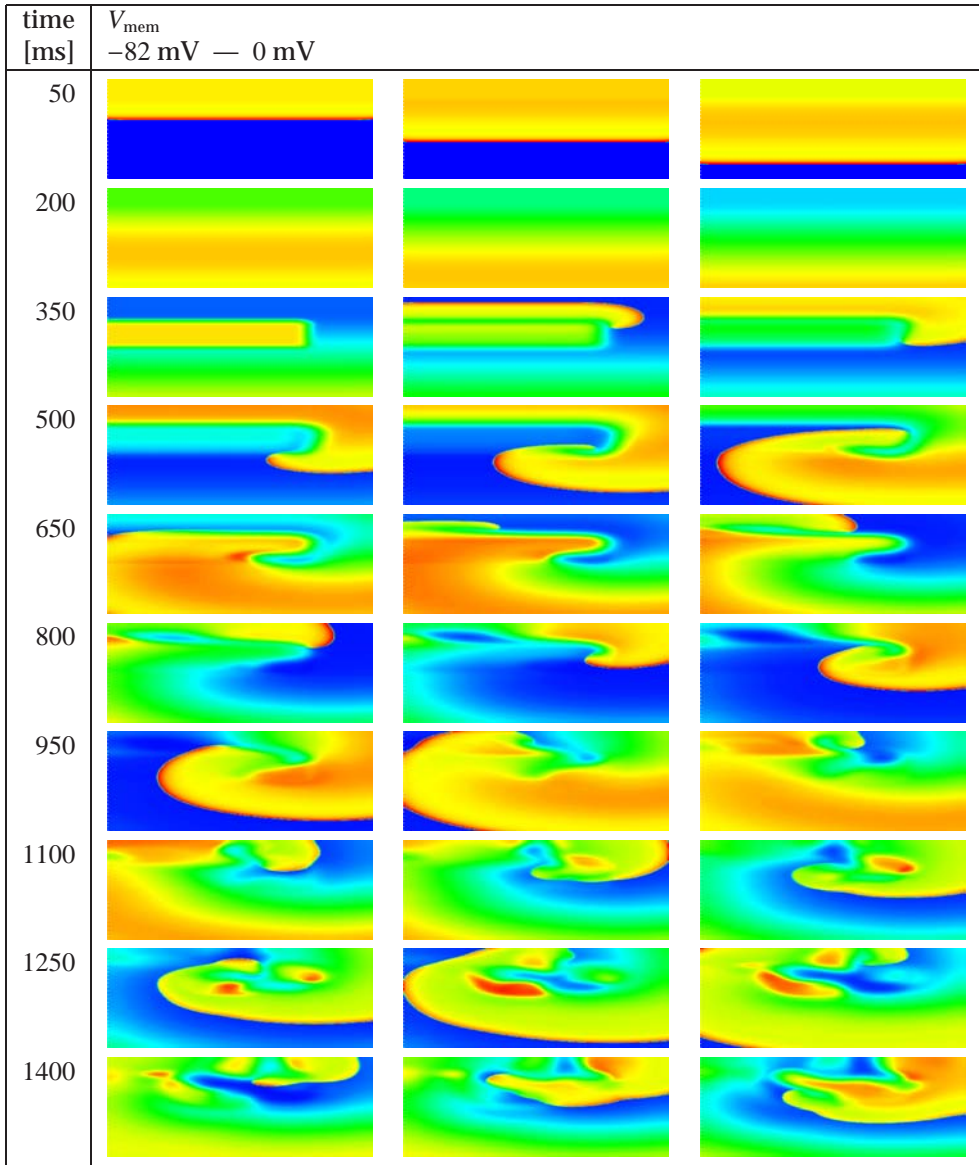
Figure 2.9: Membrane potential (V_{mem}) on an 8×3 cm tissue. An unstable spiral wave was generated using an S1S2 protocol with coupling interval 325 ms. Simulation state is shown between 50 and 1500 ms with intervals of 50 ms.
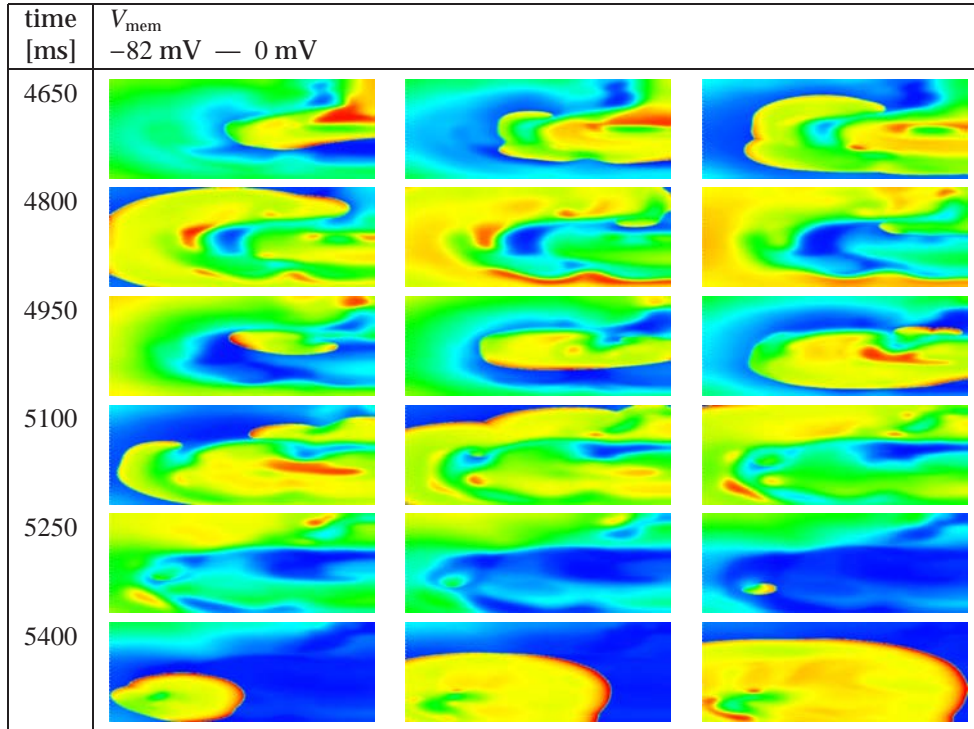
Figure 2.10: Membrane potential (V_mem) on an 8×3 cm tissue. An unstable spiral wave was generated using an S1S2 protocol with coupling interval 325 ms. Simulation state is shown between 4650 and 5500 ms with intervals of 50 ms.
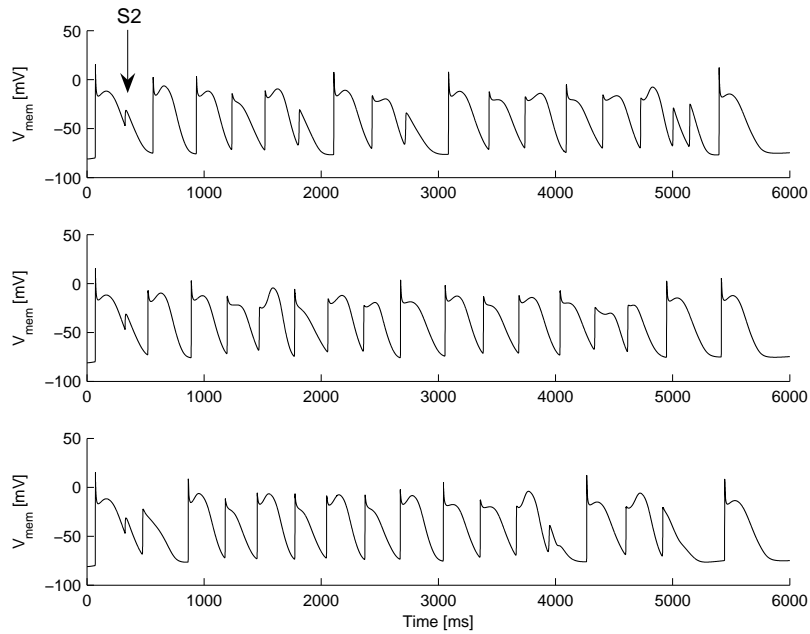
Figure 2.11: Membrane potential (V_{mem}) of three segments of the 8×3 cm tissue. Top: segment at $x = 2.0$ cm and $y = 1.5$ cm, center: segment at $x = 4.0$ cm and $y = 1.5$ cm, bottom: segment at $x = 6.0$ cm and $y = 1.5$ cm. An unstable spiral wave was generated using an S1S2 protocol with coupling interval 325 ms. Arrow indicates S2 stimulus.
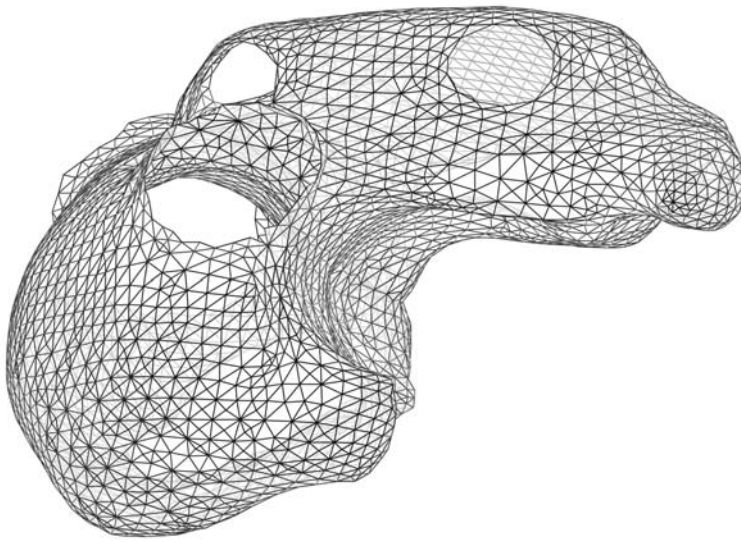
Figure 2.12: Triangular mesh representing the human atria. The mesh is created from MRI measurements and consists of 3800 nodes and 7446 triangles.

APD is a consequence of short diastolic intervals and explains the unstable behavior of the spiral wave.

2.3.5 Depolarization of the human atria

To simulate propagation of the depolarization wave on the human atria, we used a triangular mesh created from MRI data [207, 208]. The mesh was composed of 3800 nodes and 7446 triangles (Figure 2.12). The average distance between two connected nodes was 0.27 cm (standard deviation 0.07 cm), which was reduced to 0.03 cm by refining the mesh as described in Chapter 3. The tissue was assumed to be isotropic with $g_{int} = g_{ext} = 6.25$ mS/cm and segmentization was done as described by Virag *et al.* [215]. To obtain a conduction velocity of 0.9 m/s, maximum I_{Na} conductance (G_{Na}) was increased from 7.8 to 16 nS/pF as described by Jacquemet [82]. A depolarization wave was generated by electrical stimulation of the sino-atrial node.

In Figure 2.13, V_{mem} and V_{ext} are shown during 400 ms after stimulation of the sino-atrial node. All tissue was depolarized after 120 ms; after 400 ms, the atria were almost repolarized. The depolarization times obtained by our simulations are in agreement with the simulation results reported by Harrild and Henriquez [67] and by Virag *et al.* [215].

time [ms]	V_{mem} −82 mV — 0 mV	V_{ext} −8 mV — 8 mV
5		
50		
100		
200		
300		
400		
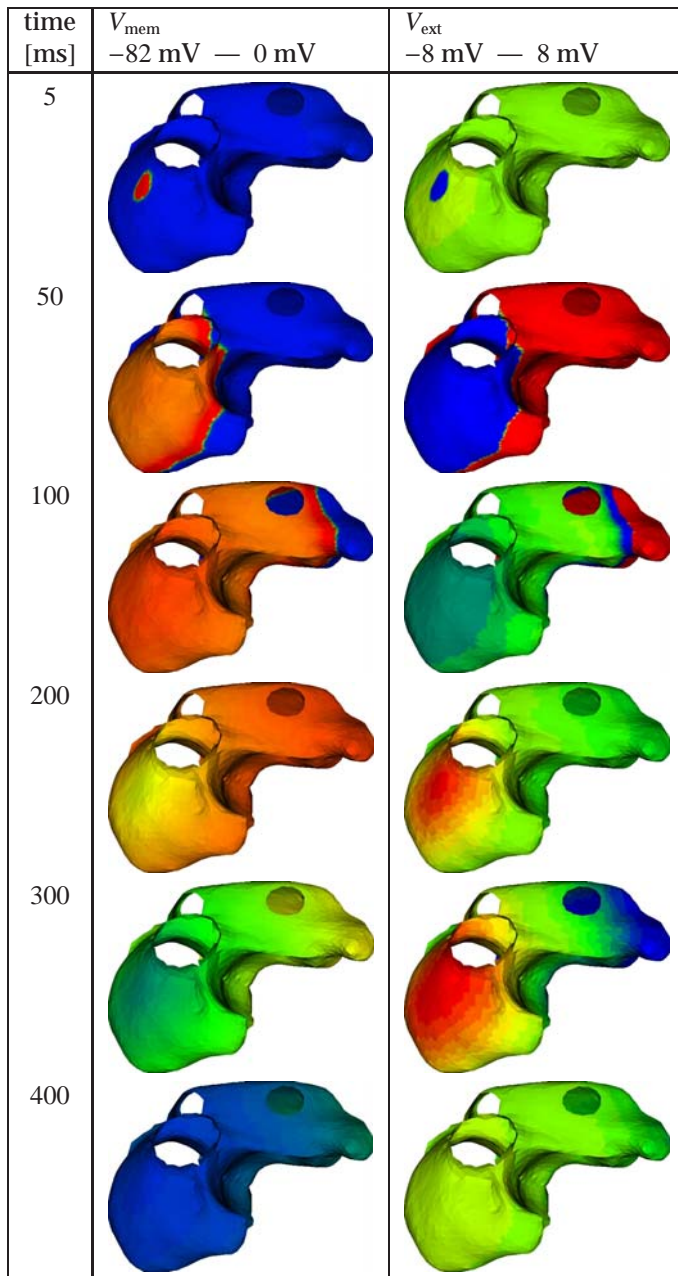
Figure 2.13: Membrane potential (V_{mem}) and extracellular potential (V_{ext}) on human atrial geometry. A depolarization wave was generated at 0 ms by stimulating the sino-atrial node.

2.4   Discussion

The Cellular Bidomain Model is aimed at modeling cardiac electrophysiology. Although the model is discrete by nature, we have mathematically proved that our model corresponds to the well-known continuous bidomain model under the assumption that the bidomain equations are solved with the finite difference method. By simulating impulse propagation, spiral waves, and depolarization of the human atria, we demonstrated that the model is capable of simulating normal as well as arrhythmic behavior.

To model the cardiac tissue, we compared a brickwall configuration with a square grid and a rectangular grid. We found that the effective conductivities are increased in longitudinal direction when a brickwall configuration is used. Since a brickwall better represents the way myocytes are connected, brickwall configurations are applied to model uniform and nonuniform cardiac tissue in Chapter 4 and pathological tissue in Chapter 5.

A possible extension of the Cellular Bidomain Model is to incorporate cardiomechanics and model the influence of mechanics on the ionic membrane currents, i.e., mechanoelectric feedback. In Chapter 6, we consider influence of local stretch on the membrane behavior through the stretch-activated current I_{sac}. In Chapter 7, the L-type Ca^{2+} current $I_{Ca,L}$ is regulated by the amount of local mechanical work during a cardiac cycle. Finally, in Chapter 8, the influence of stretch on the onset of atrial fibrillation is studied using the geometry of the human atria.

2.5   Conclusion

The Cellular Bidomain Model is well-suited to simulate cardiac impulse propagation, arrhythmia, and depolarization of the human atria. The model provides a research tool to investigate cardiac electrophysiology and mechano-electric feedback under normal and under pathological conditions.

3

Numerical aspects of the Cellular Bidomain Model

Abstract

Action potential propagation in normal and in pathological tissue can be modeled with the Cellular Bidomain Model. The model consists of a coupled system of nonlinear differential equations and linear equations. We introduce a forward Euler scheme to solve the differential equations and an iterative method to solve the system of linear equations. The gating variables of the ionic membrane currents are updated using the analytical solution of the differential equation, which allows for larger time steps when the membrane is repolarizing or at rest. Choices for segment size and simulation time steps are evaluated for both uniform and nonuniform cardiac tissue. By using different simulation time steps to update the state of the membrane, up to 70% of computational effort may be saved without significant loss of accuracy. On top of this reduction, computation time and memory usage can be reduced with another 85% by using a coarser mesh combined with a heuristic method to compute the transmembrane current.

35

3.1 Introduction

Cardiac electrophysiology can be modeled with the Cellular Bidomain Model, which is a coupled system of nonlinear differential equations and linear equations. We introduce an explicit numerical integration scheme to solve the coupled system of equations. Depending on local electrical activity, computational effort can be saved by using different simulation time steps to compute the ionic membrane currents. To quantify the effect of varying segment sizes and simulation time steps, we consider the simulation of wave propagation along a fiber and simulations of wave propagation and spiral waves on sheets of cardiac tissue. Furthermore, we introduce a multilevel numerical integration scheme to simulate wave propagation on a triangular mesh of the human atria. Finally, we investigate the effect of spatially "smoothing" the ionic membrane current to obtain accurate results with a coarse mesh of the human atria.

3.2 Methods

3.2.1 Cellular Bidomain Model in matrix notation

In Section 2.2.1, the Cellular Bidomain Model was introduced. Here, we formulate the model using matrices. Consider simulation graph $\mathcal{G}(\mathcal{N}, \mathcal{E})$ consisting of N nodes numbered 1 through N. We define the $N \times N$ matrices D_{int} and D_{ext} by

$$
D_{\text{int}}^{n,m} = \begin{cases} \sigma_{\text{int}}^{(n,m)}, & \text{if } (n,m) \in \mathcal{E} \\ -\sum_{(n,a) \in \mathcal{E}} \sigma_{\text{int}}^{(n,a)}, & \text{if } n = m \\ 0, & \text{otherwise} \end{cases} \tag{3.1}
$$

$$
D_{\text{ext}}^{n,m} = \begin{cases} \sigma_{\text{ext}}^{(n,m)}, & \text{if } (n,m) \in \mathcal{E} \\ -\sum_{(n,a) \in \mathcal{E}} \sigma_{\text{ext}}^{(n,a)}, & \text{if } n = m \\ 0, & \text{otherwise} \end{cases} \tag{3.2}
$$

It can be observed that the number of non-zero elements on each row of D_{int} and D_{ext} is equal to the number of adjacent nodes for each node plus one. Since, in general, the number of adjacent nodes is small compared with the total number of nodes, D_{int} and D_{ext} are sparse matrices. Furthermore, D_{int} and D_{ext} are singular, because they are constructed such that the sum of all elements in each row equals zero. Using definitions (3.1) and (3.2), we find

for each node n

$$I_{\text{int}}^n = \sum_{m \in \mathcal{N}} D_{\text{int}}^{n,m} V_{\text{int}}^m, \tag{3.3}$$

$$I_{\text{ext}}^n = \sum_{m \in \mathcal{N}} D_{\text{ext}}^{n,m} V_{\text{ext}}^m. \tag{3.4}$$

Using (3.3) and (3.4) to rewrite equations (2.6) and (2.7) defining the Cellular Bidomain Model, we obtain the system of equations

$$C_{\text{mem}} \frac{d\mathbf{V}_{\text{mem}}}{dt} + S_{\text{mem}} \mathbf{I}_{\text{ion}} = -D_{\text{ext}} \mathbf{V}_{\text{ext}}, \tag{3.5}$$

$$D_{\text{int}} \mathbf{V}_{\text{int}} + D_{\text{ext}} \mathbf{V}_{\text{ext}} = \mathbf{0}, \tag{3.6}$$

$$\mathbf{V}_{\text{mem}} = \mathbf{V}_{\text{int}} - \mathbf{V}_{\text{ext}}, \tag{3.7}$$

where $\mathbf{V}_{\text{int}}$, $\mathbf{V}_{\text{ext}}$, and $\mathbf{V}_{\text{mem}}$ are vectors of length N representing the intracellular, extracellular, and membrane potential of all nodes, and vector $\mathbf{I}_{\text{ion}}$ of length N represents the ionic membrane current of all nodes. Furthermore, C_{mem} and S_{mem} are diagonal matrices with elements C_{mem}^n and S_{mem}^n, respectively, on the diagonal.

The system of equations (3.5), (3.6), and (3.7) is a coupled system of non-linear differential equations and linear equations, which can be simplified by eliminating $\mathbf{V}_{\text{int}}$ as

$$C_{\text{mem}} \frac{d\mathbf{V}_{\text{mem}}}{dt} + S_{\text{mem}} \mathbf{I}_{\text{ion}} = -D_{\text{ext}} \mathbf{V}_{\text{ext}}, \tag{3.8}$$

$$(D_{\text{int}} + D_{\text{ext}}) \mathbf{V}_{\text{ext}} = -D_{\text{int}} \mathbf{V}_{\text{mem}}. \tag{3.9}$$

The system of differential equations (3.8) describes the time evolution of the membrane potentials $\mathbf{V}_{\text{mem}}$. The extracellular potentials $\mathbf{V}_{\text{ext}}$ occur in the right hand side of (3.8) and must be found by solving the linear system of equations (3.9). Since D_{int} and D_{ext} are singular, also matrix $D_{\text{int}} + D_{\text{ext}}$ is singular. Hence, it is not a priori clear that the system (3.9) has a unique solution for $\mathbf{V}_{\text{ext}}$. We discuss the consistency of the system of equations (3.8) and (3.9) in Appendix B.

3.2.2 Numerical integration scheme

Consider the Cellular Bidomain Model in matrix notation defined by equations (3.8) and (3.9). A forward Euler scheme to solve the system of equations is defined by

$$\mathbf{V}_{\text{mem}}^{k+1} = \mathbf{V}_{\text{mem}}^k - \Delta t \, C_{\text{mem}}^{-1} (D_{\text{ext}} \mathbf{V}_{\text{ext}}^k + S_{\text{mem}} \mathbf{I}_{\text{ion}}^k), \tag{3.10}$$

$$(D_{\text{int}} + D_{\text{ext}}) \mathbf{V}_{\text{ext}}^{k+1} = -D_{\text{int}} \mathbf{V}_{\text{mem}}^{k+1}, \tag{3.11}$$

where $\mathbf{V}^k_{\text{mem}}$ denotes the membrane potentials on time $k\Delta t$ and $\mathbf{I}^k_{\text{ion}}$ represents the ionic membrane currents computed with $\mathbf{V}^k_{\text{mem}}$. According to this scheme, $\mathbf{V}_{\text{mem}}$ is computed using a forward Euler step. Next, $\mathbf{V}_{\text{ext}}$ is found by solving the system of linear equations (3.11). Finally, $\mathbf{V}_{\text{int}}$ can be obtained from equation (3.7).

Since C_{mem} is a diagonal matrix, computation of $\mathbf{V}^{k+1}_{\text{mem}}$ from (3.10) requires only one matrix-vector multiplication with sparse matrix D_{ext}. Solving $\mathbf{V}^{k+1}_{\text{ext}}$ from (3.11) is, however, more complicated. Due to the singularity of the matrix $D_{\text{int}} + D_{\text{ext}}$, no unique solution of this system of equations exists. It can be shown that if the simulation graph is connected, the various solutions of (3.11) differ only by a constant shift of all extracellular potentials (Appendix B). To obtain a unique solution for (3.11), we introduce one additional equation stating that on each time the sum of extracellular potentials equals zero, i.e.,

$$\sum_{n \in \mathcal{N}} V^{n,k}_{\text{ext}} = 0, \tag{3.12}$$

where $V^{n,k}_{\text{ext}}$ denotes the extracellular potential of node n at time $k\Delta t$. Initially, this extra requirement can be satisfied by choosing $V^{n,0}_{\text{ext}} = 0$, for all nodes $n \in \mathcal{N}$. Since the number of equations is large, the system of linear equations (3.11) is solved with an iterative method. An iterative method has the advantage that the solution found during the former time step can be used to initialize the iteration process for the current time step. We discuss Jacobi's iteration method and the Conjugate Gradient (CG) method.

Jacobi's iteration method

Let $D = D_{\text{int}} + D_{\text{ext}}$, and let P be the diagonal part of D, with reversed sign. Hence, the elements of P are given by $P^{n,n} = \sum_{(n,a) \in \mathcal{E}} (\sigma^{(n,a)}_{\text{int}} + \sigma^{(n,a)}_{\text{ext}})$. Since the simulation graph is connected, each node n is connected to at least one other node, which implies that all elements $P^{n,n}$ are positive. Hence, the matrix P is not singular. Equation (3.11) can now be reformulated as

$$P \mathbf{V}^{k+1}_{\text{ext}} = (D + P)\mathbf{V}^{k+1}_{\text{ext}} + D_{\text{int}} \mathbf{V}^{k+1}_{\text{mem}}. \tag{3.13}$$

The solution of (3.13) can be approximated by iterating

$$\mathbf{V}^{k+1,i+1}_{\text{ext}} = P^{-1}(D + P)\mathbf{V}^{k+1,i}_{\text{ext}} + P^{-1}D_{\text{int}}\mathbf{V}^{k+1}_{\text{mem}}, \tag{3.14}$$

where $\mathbf{V}^{k+1,i}_{\text{ext}}$ denotes the approximation of $\mathbf{V}^{k+1}_{\text{ext}}$ after i iterations. This is Jacobi's iteration method for solving systems of linear equations [143, 147]. As

a first approximation of $\mathbf{V}_{\text{ext}}$ at time $(k+1)\Delta t$, the value of $\mathbf{V}_{\text{ext}}$ at time $k\Delta t$ is chosen, i.e.,

$$\mathbf{V}_{\text{ext}}^{k+1,0} = \mathbf{V}_{\text{ext}}^{k}. \tag{3.15}$$

The stop criterion is based on Kirchhoff's law stating that $I_{\text{int}}^{n} + I_{\text{ext}}^{n} = 0$ for all $n \in \mathcal{N}$ (equation (2.6)), and is defined by

$$|I_{\text{int}}^{n} + I_{\text{ext}}^{n}| < \epsilon, \tag{3.16}$$

for all nodes $n \in \mathcal{N}$. This is the ∞-norm of the residual [143]. We discuss the convergence of Jacobi's iteration method in Appendix B.

Conjugate Gradient method

Another method that can be used to solve the system of linear equations (3.11) is the Conjugate Gradient (CG) method [147]. Let $D = D_{\text{int}} + D_{\text{ext}}$, and let P be the diagonal part of D. Equation (3.11) can be reformulated as

$$P^{-1}D\,\mathbf{V}_{\text{ext}}^{k+1} = -P^{-1}D_{\text{int}}\mathbf{V}_{\text{mem}}^{k+1}, \tag{3.17}$$

where matrix P serves as a preconditioner. The solution of (3.17) can be approximated by the untransformed preconditioned conjugate gradient method [12] as follows:

$$\mathbf{r}^{(0)} \;=\; -D_{\text{int}}\mathbf{V}_{\text{mem}}^{k+1} - D\,\mathbf{V}_{\text{ext}}^{k+1,0} \tag{3.18}$$

$$\mathbf{d}^{(0)} \;=\; P^{-1}\,\mathbf{r}^{(0)} \tag{3.19}$$

$$\alpha^{(i)} \;=\; \frac{\mathbf{r}^{(i)^{\mathsf{T}}} P^{-1}\,\mathbf{r}^{(i)}}{\mathbf{d}^{(i)^{\mathsf{T}}} D\,\mathbf{d}^{(i)}} \tag{3.20}$$

$$\mathbf{V}_{\text{ext}}^{k+1,i+1} \;=\; \mathbf{V}_{\text{ext}}^{k+1,i} + \alpha^{(i)}\mathbf{d}^{(i)} \tag{3.21}$$

$$\mathbf{r}^{(i+1)} \;=\; \mathbf{r}^{(i)} - \alpha^{(i)} D\,\mathbf{d}^{(i)} \tag{3.22}$$

$$\beta^{(i+1)} \;=\; \frac{\mathbf{r}^{(i+1)^{\mathsf{T}}} P^{-1}\,\mathbf{r}^{(i+1)}}{\mathbf{r}^{(i)^{\mathsf{T}}} P^{-1}\,\mathbf{r}^{(i)}} \tag{3.23}$$

$$\mathbf{d}^{(i+1)} \;=\; P^{-1}\,\mathbf{r}^{(i+1)} + \beta^{(i+1)}\,\mathbf{d}^{(i)} \tag{3.24}$$

Here $\mathbf{r}^{(i)}$ and $\mathbf{d}^{(i)}$ represent the residual and the direction vectors at the ith iteration, and $\alpha^{(i)}$ and $\beta^{(i)}$ are scalars. The Conjugate Gradient method terminates after at most N iterations [147]. As before, we use the ∞-norm of the residual $\mathbf{r}^{(i)}$ as a stop criterion, which is equivalent to

$$|I_{\text{int}}^{n} + I_{\text{ext}}^{n}| < \epsilon, \tag{3.25}$$

for all nodes $n \in \mathcal{N}$.
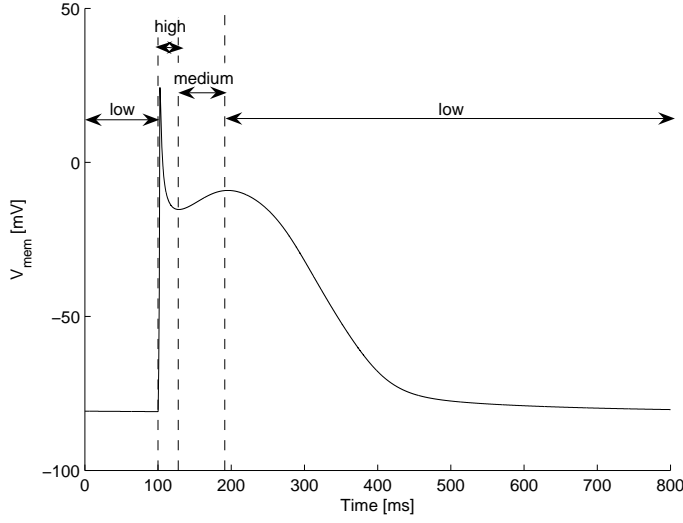
Figure 3.1: Action potential generated by the Courtemanche-Ramirez-Nattel model [37]. Accuracy levels *high*, *medium*, and *low* are indicated by arrows.

3.2.3 Computation of the membrane state

The membrane state, denoted by $\mathbf{q}^n$ for node $n \in \mathcal{N}$, is described by a large number of gating variables and intracellular ion concentrations. By reformulating equation (2.37) using definitions (2.39) and (2.41), the dynamics of gating variable p are described by

$$\frac{\mathrm{d}p}{\mathrm{d}t} = \frac{p_\infty - p}{\tau_p},$$

(3.26)

where p_∞ represents the steady-state value and τ_p the time constant. Let $p^{(k)}$ denote the solution of p at time $k\Delta t$, then $p^{(k+1)}$ can be computed by

$$p^{(k+1)} = p_\infty - (p_\infty - p^{(k)})\exp\left(-\frac{\Delta t}{\tau_p}\right).$$

(3.27)

Since p_∞ and τ_p are related to V_{mem}, larger simulation time steps can be used when V_{mem} changes little over time, i.e., during the plateau phase, repolarization, and rest.

The dynamics of the intracellular concentrations are described by equation (2.42). Let $[ion]_{\mathrm{i}}^{(k)}$ denote the intracellular ion concentration at time $k\Delta t$.

Using a forward Euler scheme, $[ion]_i^{(k+1)}$ is obtained by

$$[ion]_i^{(k+1)} = [ion]_i^{(k)} - \Delta t \frac{C_m}{z_{ion} F V_i} I_{ion}^k,$$

(3.28)

where I_{ion}^k is the ionic membrane current computed with V_{mem}^k. As before, larger simulation time steps can be used when the ion concentrations change little over time. This occurs when the ion currents are relatively small, which corresponds to small changes in V_{mem}.

Based on these observations, we introduce a simulation scheme to update the membrane state in which small time steps are used in areas near the depolarization wave front, and larger time steps in areas where the cells are in their plateau phase, repolarizing, or resting. During a simulation run, each node is in one of three distinctive levels of accuracy. The accuracy levels are named *high*, *medium*, and *low*. The simulation time steps to compute the membrane state are indicated by Δt_{high}^{mem}, Δt_{med}^{mem}, and Δt_{low}^{mem}, respectively. Nodes with depolarizing membranes have accuracy level *high*. A message passing mechanism is implemented to ensure that depolarizing nodes inform all other nodes in the simulation graph that can be reached by a path with length at most 10. These nodes also change their accuracy level to *high*. This mechanism ensures that all nodes located within a distance of approximately 1 mm of the depolarization front are updated with high accuracy. Nodes having repolarizing membranes change their accuracy level to *medium* during the notch (28 ms after depolarization), and to *low* during the plateau of the action potential (91 ms after depolarization; Figure 3.1). In this way, small time steps to compute the membrane state are only performed for a limited number of nodes during each time step.

3.2.4   Segment size and simulation time step size

Criteria for segment size and simulation step size are related to the model parameters. The bidomain parameters used for the simulations in Chapter 2 are listed in Table 2.1. To obtain criteria for the size of individual segments, we apply cable theory and consider subthreshold behavior along a fiber as described by Henriquez [69]. The application of a stimulus current produces a spatial change in the membrane potential along the fiber. For subthreshold behavior, the transmembrane current I_{trans} can be described by

$$I_{trans} = C_{mem} \frac{dV_{mem}}{dt} + \frac{V_{mem}}{R_{mem}},$$

(3.29)

where R_{mem} is the membrane resistance in $\Omega \cdot cm^2$ and C_{mem} the membrane capacitance in $\mu F/cm^2$ [69]. The *steady-state* response of V_{mem} along the fiber to a

subthreshold current at position $x = 0$ is exponential and can be described by

$$V_{\text{mem}}(x) = V_{\text{mem}}(0) \, \exp\left(-\frac{x}{\lambda}\right), \tag{3.30}$$

where $V_{\text{mem}}(x)$ is the membrane potential on distance x from the stimulus site, $V_{\text{mem}}(0)$ the membrane potential at the stimulus site ($x = 0$), and λ the length constant [69]. Using the bidomain parameters from Table 2.1, the length constants in longitudinal, transverse, and transmural direction, denoted by λ_x, λ_y, and λ_z, can be expressed as

$$\lambda_x = \sqrt{\frac{R_{\text{mem}} \, g_{\text{int}}^x \, g_{\text{ext}}^x}{\chi \, (g_{\text{int}}^x + g_{\text{ext}}^x)}} \tag{3.31}$$

$$\lambda_y = \sqrt{\frac{R_{\text{mem}} \, g_{\text{int}}^y \, g_{\text{ext}}^y}{\chi \, (g_{\text{int}}^y + g_{\text{ext}}^y)}} \tag{3.32}$$

$$\lambda_z = \sqrt{\frac{R_{\text{mem}} \, g_{\text{int}}^z \, g_{\text{ext}}^z}{\chi \, (g_{\text{int}}^z + g_{\text{ext}}^z)}} \tag{3.33}$$

Membrane resistance R_{mem} was estimated for the Courtemanche-Ramirez-Nattel model by applying a subthreshold stimulus current of 0.3 pA/pF during 300 ms using

$$\frac{V_{\text{mem}} - V_{\text{rest}}}{R_{\text{mem}}} = I_{\text{ion}}, \tag{3.34}$$

with $V_{\text{rest}} = -81$ mV and V_{mem} ranging from -80 mV to -70 mV. R_{mem} varied between 22 and 38 $\Omega \cdot \text{cm}^2$. For these values of R_{mem}, λ_x is in between 0.12 and 0.16 cm, and λ_y and λ_z are in between 0.04 cm and 0.06 cm. To obtain accurate simulation results, Δx should be at most 0.02 cm, while Δy and Δz should be at most 0.008 cm.

Explicit numerical methods are limited by a stability condition [147]. For an anisotropic, homogeneous, three-dimensional monodomain, this condition is formulated by

$$\Delta t < \frac{\chi \, C_{\text{mem}}}{2 \left(\frac{g^x}{\Delta x^2} + \frac{g^y}{\Delta y^2} + \frac{g^z}{\Delta z^2} \right)}, \tag{3.35}$$

where g^x, g^y, and g^z represent the conductivities in x-, y-, and z-direction, respectively [147].

A similar relation can be derived for an anisotropic, homogeneous, three-dimensional bidomain. Puwal and Roth [151] formulated the following stability condition for the three-dimensional bidomain:

$$\Delta t < \frac{\chi \, C_{\text{mem}} \left(\frac{g^x_{\text{int}} + g^x_{\text{ext}}}{\Delta x^2} + \frac{g^y_{\text{int}} + g^y_{\text{ext}}}{\Delta y^2} + \frac{g^z_{\text{int}} + g^z_{\text{ext}}}{\Delta z^2} \right)}{2 \left(\frac{g^x_{\text{int}}}{\Delta x^2} + \frac{g^y_{\text{int}}}{\Delta y^2} + \frac{g^z_{\text{int}}}{\Delta z^2} \right) \left(\frac{g^x_{\text{ext}}}{\Delta x^2} + \frac{g^y_{\text{ext}}}{\Delta y^2} + \frac{g^z_{\text{ext}}}{\Delta z^2} \right)}. \tag{3.36}$$

Using definitions (2.18) through (2.25) for conductances σ^x_{int}, σ^x_{ext}, σ^y_{int}, σ^y_{ext}, σ^z_{int}, σ^z_{ext}, membrane surface S^n_{mem}, and membrane capacitance C^n_{mem}, the stability condition for the Cellular Bidomain Model on a rectangular grid is formulated by

$$\Delta t < \frac{C^n_{\text{mem}} \left(\sigma^x_{\text{int}} + \sigma^x_{\text{ext}} + \sigma^y_{\text{int}} + \sigma^y_{\text{ext}} + \sigma^z_{\text{int}} + \sigma^z_{\text{ext}} \right)}{2 \left(\sigma^x_{\text{int}} + \sigma^y_{\text{int}} + \sigma^z_{\text{int}} \right) \left(\sigma^x_{\text{ext}} + \sigma^y_{\text{ext}} + \sigma^z_{\text{ext}} \right)}. \tag{3.37}$$

Puwal and Roth [151] proved that stability condition (3.36) holds under the assumption that $I_{\text{ion}} = 0$. To our knowledge, a proof has not been given for the more general assumption that $|I_{\text{ion}}| < A$, for some constant A. However, Puwal and Roth [151] did some numerical experiments in which they searched for the largest time step that did not lead to instability. They found similar results for $I_{\text{ion}} = 0$ and for I_{ion} modeled by the Fenton-Karma model [58]. In both cases, the maximum time step is close to the theoretical maximum time step, which indicates that the stability condition also holds when I_{ion} represents active membrane behavior.

3.2.5 Multilevel simulation graph

In Chapter 2, simulations were performed with a triangular mesh representing the human atria [207, 208]. The original mesh is composed of 3800 nodes and 7446 triangles. The average distance between two connected nodes in the mesh is 0.27 cm (standard deviation 0.07 cm). Under the assumption that the atria are isotropic with $g_{\text{int}} = g_{\text{ext}} = 6.25$ mS/cm, the length constant is in between 0.19 and 0.24 cm (R_{mem} between 22 and 38 $\Omega \cdot \text{cm}^2$). To obtain accurate simulation results, the distance between two connected nodes should be at most 0.03 cm, which is 9 times smaller than the average distance in the mesh.

An average distance of 0.09 cm can be obtained by refining the mesh such that each of the triangles is subdivided in 9 smaller triangles. By refining the mesh once more, the average distance becomes the desired 0.03 cm. The number of nodes increases from 3800 to 33754 after the first refinement and to 302320 after the second refinement. In this way, we obtain three levels

of coarseness. Since computation of V_{mem} and V_{ext} at the finest levels is only necessary near the depolarization wave front, we use a multilevel scheme to solve the system of equations as follows. In case the accuracy level is *high*, V_{mem} and V_{ext} are determined on the finest level. In case the accuracy level is *medium*, V_{mem} and V_{ext} are determined on the intermediate level, and in case the accuracy level is *low*, V_{mem} and V_{ext} are determined on the coarsest level. The state of the membrane is updated at all levels of the simulation graph. As before, the simulation time step to compute the membrane state depends on the accuracy level.

Using the multilevel approach to compute V_{mem} and V_{ext}, a considerable amount of computational effort can be saved. To further decrease the amount of computation time and memory usage, we introduce a heuristic method with which we use only two levels of the simulation graph in stead of all three. In the Cellular Bidomain Model, the transmembrane current I_{trans} of node n is defined by equation (2.7):

$$I_{\text{trans}}^n = C_{\text{mem}}^n \frac{\mathrm{d}V_{\text{mem}}^n}{\mathrm{d}t} + S_{\text{mem}}^n I_{\text{ion}}(V_{\text{mem}}^n, \mathbf{q}^n), \tag{3.38}$$

where C_{mem}^n is the membrane capacitance of node n, S_{mem}^n the membrane surface, and $I_{\text{ion}}(V_{\text{mem}}^n, \mathbf{q}^n)$ the ionic membrane current. The heuristic is defined by replacing $I_{\text{ion}}(V_{\text{mem}}^n, \mathbf{q}^n)$ in equation (3.38) with

$$(1 - \alpha)I_{\text{ion}}(V_{\text{mem}}^n, \mathbf{q}^n) + \frac{\alpha}{\#(n, a) \in \mathcal{E}} \sum_{(n,a)\in\mathcal{E}} I_{\text{ion}}(V_{\text{mem}}^a, \mathbf{q}^a), \tag{3.39}$$

where $0 \leq \alpha \leq 1$ indicates the influence of the ionic membrane current of the surrounding nodes on the transmembrane current. This method can be viewed as a way to "smooth" I_{ion} such that the spatial distribution of I_{ion} corresponds better to the coarser mesh.

3.2.6 Simulation set-up

The bidomain parameters used for the present study are the same as in Chapter 2 (Table 2.1). To investigate the effect of varying simulation time steps, segment sizes, and computational methods, the simulations of Chapter 2 were repeated with different choices for segmentization and numerical methods. Both computational effort and simulation results were compared with a reference simulation.

To compare simulation results, deviations in V_{mem}, V_{ext}, and time of excitation (t_{depol}) were computed as follows. The deviation in V_{mem} at simulation

time $k\Delta t$ is defined by

$$E_{V_{\text{mem}}}^k = \sqrt{\frac{1}{N}\sum_{n\in\mathcal{N}}(V_{\text{mem}}^{n,k} - \tilde{V}_{\text{mem}}^{n,k})^2},$$ (3.40)

where $V_{\text{mem}}^{n,k}$ is the membrane potential of segment n at time $k\Delta t$ and $\tilde{V}_{\text{mem}}^{n,k}$ the membrane potential of the same segment at the same time in the reference simulation. The deviation in V_{ext} is defined in the same way by

$$E_{V_{\text{ext}}}^k = \sqrt{\frac{1}{N}\sum_{n\in\mathcal{N}}(V_{\text{ext}}^{n,k} - \tilde{V}_{\text{ext}}^{n,k})^2}.$$ (3.41)

Furthermore, the deviation in t_{depol} is defined by

$$E_{\text{depol}} = \sqrt{\frac{1}{N}\sum_{n\in\mathcal{N}}(t_{\text{depol}}^n - \tilde{t}_{\text{depol}}^n)^2},$$ (3.42)

where t_{depol}^n represents the time of excitation of segment n and $\tilde{t}_{\text{depol}}^n$ the time of excitation of the same segment in the reference simulation. The time of excitation is defined by the moment V_{mem} exceeds -60 mV.

3.3 Results

3.3.1 Wave propagation along a fiber

To investigate the effect of varying simulation time steps on the propagation of a depolarization wave, a 5-cm-long fiber was created that consisted of 0.01-cm-long segments as in Chapter 2. A depolarization wave was generated by stimulating the first segment with a stimulus current of 100 pA/pF until the membrane was depolarized. During twelve seconds, stimulation was repeated each 1 s or each 0.35 s. To investigate the effect of larger time steps to update the membrane state on the simulation results and computation time, the simulations were performed with varying $\Delta t_{\text{high}}^{\text{mem}}$, $\Delta t_{\text{med}}^{\text{mem}}$, and $\Delta t_{\text{low}}^{\text{mem}}$.

In Table 3.1, the conduction velocity (θ), deviations in V_{mem}, V_{ext}, t_{depol}, number of iterations to compute V_{ext} (#iter), and computation time per ms simulation time (t_{comp}) are presented for BCL = 1 s and BCL = 0.35 s. Compared with a simulation time step of 0.005 ms, θ increases with 0.1% when using a simulation time step of 0.010 ms. This increase in conduction velocity explains the deviations in V_{mem}, V_{ext}, and t_{depol} for simulation time step 0.010 ms. When larger time steps for medium and low accuracy segments are used, the computation time can be reduced up to 70% for BCL = 1 s ($\Delta t_{\text{high}}^{\text{mem}}$ = 0.010

Table 3.1: Comparison of simulation time steps (depolarization wave)

BCL	Δt_{high}^{mem}	Δt_{med}^{mem}	Δt_{low}^{mem}	θ	$E_{V_{mem}}$	$E_{V_{ext}}$	E_{depol}	#iter	t_{comp}
[s]	[ms]	[ms]	[ms]	[m/s]	[mV]	[mV]	[ms]	[−]	[ms]
1.00	0.005	0.005	0.005	0.4098	0.00	0.00	0.000	8.4	1.61
1.00	0.010	0.010	0.010	0.4103	0.81	0.22	0.083	12.2	0.94
1.00	0.010	0.100	0.100	0.4103	0.80	0.22	0.082	12.2	0.33
1.00	0.010	0.100	0.500	0.4103	0.78	0.22	0.079	12.2	0.29
1.00	0.010	0.100	1.000	0.4103	0.75	0.21	0.075	12.2	0.27
0.35	0.005	0.005	0.005	0.4149	0.00	0.00	0.000	15.6	1.69
0.35	0.010	0.010	0.010	0.4153	0.75	0.21	0.075	24.2	1.11
0.35	0.010	0.100	0.100	0.4153	0.75	0.21	0.075	24.2	0.58
0.35	0.010	0.100	0.500	0.4156	1.21	0.28	0.136	24.9	0.56
0.35	0.010	0.100	1.000	0.4147	57.25	6.65	310.693	24.2	0.54

#iter$_{max}$ = 100, maximum number of iterations per time step; ϵ = 1.0E−3, iteration process stops when $|I_{int}^n + I_{ext}^n| < \epsilon$; θ, conduction velocity; $E_{V_{mem}}$, $E_{V_{ext}}$, w.r.t. first simulation after 100 ms; #iter, average number of iterations per time step; t_{comp}, computation time per ms simulation time.
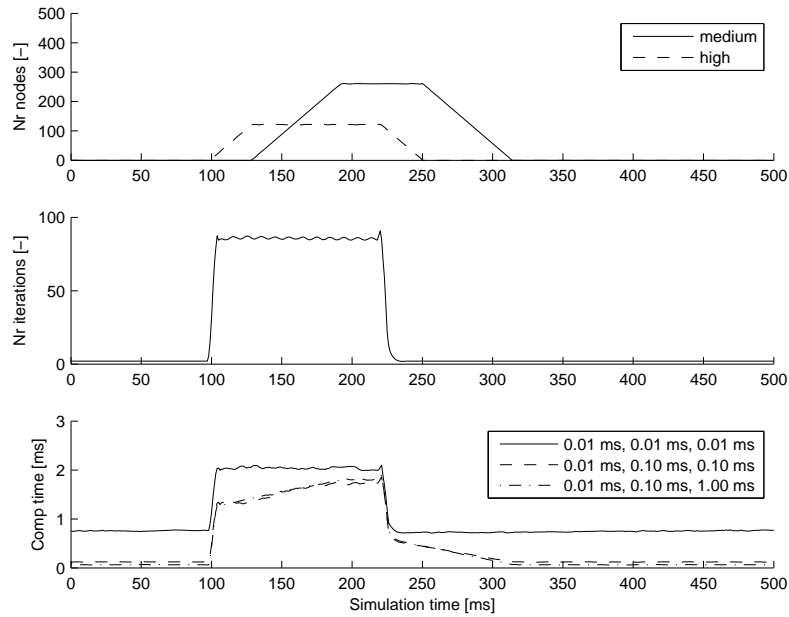
Figure 3.2: Computation data for depolarization wave along 5-cm-long fiber. Top: number of high and medium accuracy nodes. Center: number of iterations per simulation time step to compute V_{ext} using Jacobi's iteration method. Bottom: computation time per ms simulation time for $\Delta t_{\text{high}}^{\text{mem}} = 0.01$ ms and varying $\Delta t_{\text{med}}^{\text{mem}}$ and $\Delta t_{\text{low}}^{\text{mem}}$. A depolarization wave was generated at 100 ms by stimulating the first segment of the fiber.

Δy [cm]	square grid $\Delta x : \Delta y = 1 : 1$	rectangular grid $\Delta x : \Delta y = 2.5 : 1$	brickwall $\Delta x : \Delta y = 2.5 : 1$
0.004			
0.008			
0.016			
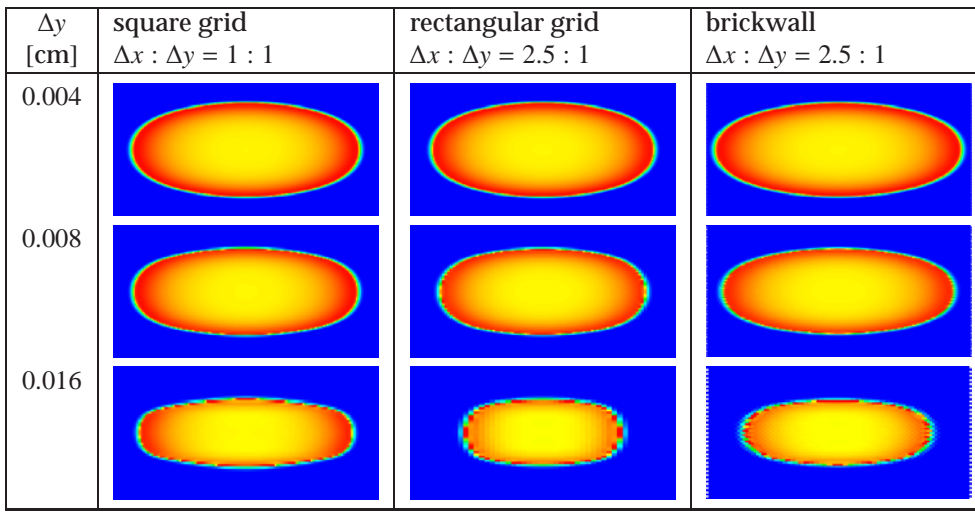
Figure 3.3: Membrane potential (V_{mem}) when cardiac tissue is represented by a square grid (left), rectangular grid (center), or brickwall (right). The coarseness of the grid is varied from fine (top) to coarse (bottom). A depolarization front was generated by stimulating the center of the 2×1 cm tissue. V_{mem} is shown 20 ms after stimulation. Red/yellow indicates depolarized tissue and blue indicates resting tissue.

ms, $\Delta t^{\mathrm{mem}}_{\mathrm{med}} = 0.100$ ms, and $\Delta t^{\mathrm{mem}}_{\mathrm{low}} = 1.000$ ms) and up to 47% for BCL $= 0.35$ s ($\Delta t^{\mathrm{mem}}_{\mathrm{high}} = 0.010$ ms and $\Delta t^{\mathrm{mem}}_{\mathrm{med}} = \Delta t^{\mathrm{mem}}_{\mathrm{low}} = 0.100$ ms), without significant loss of accuracy. In the simulation with BCL $= 0.35$ s and $\Delta t^{\mathrm{mem}}_{\mathrm{low}} = 1.000$ ms, propagation of the depolarization wave occurred every other stimulation, because the membrane was not fully recovered as a consequence of the larger $\Delta t^{\mathrm{mem}}_{\mathrm{low}}$ during repolarization and rest. This explains the large $E_{V_{\mathrm{mem}}}$, $E_{V_{\mathrm{ext}}}$, and E_{depol}. The conduction velocity was 0.15% smaller in case the wave did propagate.

In Figure 3.2, the number of high and medium accuracy nodes, number of Jacobi iteration steps to compute V_{ext}, and the computation time per ms simulation time are presented for a period of 0.5 s during the simulation. It can be observed that the reduction in computation time is largest when the fiber is repolarizing or resting.

3.3.2   Grid structure

In the Cellular Bidomain Model, the type of grid (i.e. square, rectangular or brickwall) as well as the coarseness of the grid (size of individual segments) may affect the simulation results. To quantify these effects on V_{mem}, V_{ext}, and t_{depol}, we performed nine simulations with the 2×1 cm tissue with maximum number of iterations $\#\mathrm{iter}_{\mathrm{max}} = 50$ and $\epsilon = 1.0\mathrm{E}{-}03$ μA. Simulation results
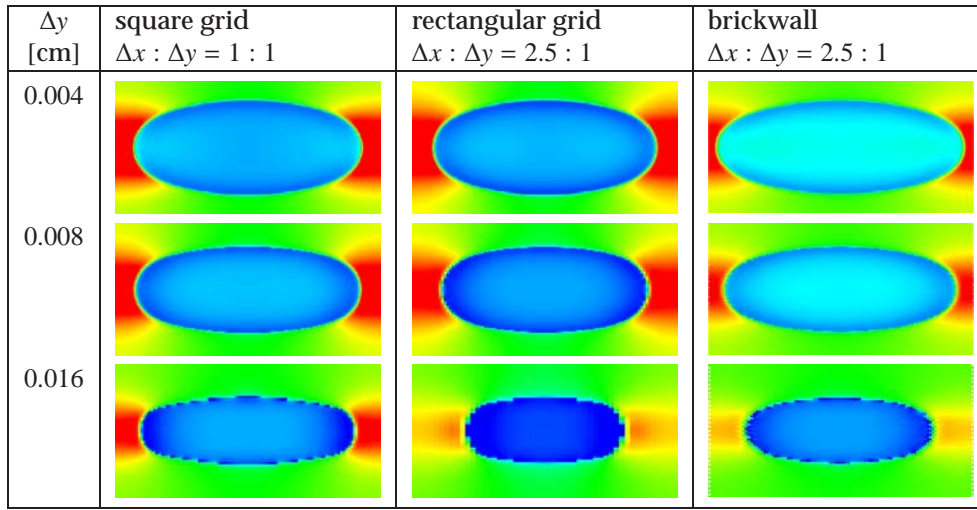
Figure 3.4: Extracellular potential (V_ext) when cardiac tissue is represented by a square grid (left), rectangular grid (center), or brickwall (right). The coarseness of the grid is varied from fine (top) to coarse (bottom). A depolarization front was generated by stimulating the center of the 2×1 cm tissue. V_ext is shown 20 ms after stimulation. Red/yellow indicates positive V_ext, green indicates $V_\text{ext} = 0$ mV, and blue indicates negative V_ext.

Table 3.2: Conduction velocity

Δx	Δy	brickwall	θ_L	θ_T	θ_L/θ_T†	θ_L/θ_T‡
[cm]	[cm]	[Y/N]	[m/s]	[m/s]	[−]	[−]
0.004	0.004	N	0.42	0.14	2.9	2.8
0.008	0.008	N	0.41	0.13	3.1	2.8
0.016	0.016	N	0.39	0.10	4.0	2.8
0.01	0.004	N	0.40	0.14	2.8	2.8
0.02	0.008	N	0.37	0.13	2.8	2.8
0.04	0.016	N	0.29	0.10	3.0	2.8
0.01	0.004	Y	0.46	0.14	3.2	3.1
0.02	0.008	Y	0.43	0.13	3.3	3.1
0.04	0.016	Y	0.34	0.10	3.6	3.1

θ_L, longitudinal conduction velocity; θ_T, transverse conduction velocity; θ_T/θ_L†, actual ratio of anisotropy; θ_T/θ_L‡, predicted ratio of anisotropy.

Table 3.3: Jacobi's iteration method vs Conjugate Gradient method (rectangular grid)

Method	Δt	#iter$_{max}$	ϵ	$E_{V_{mem}}$	$E_{V_{ext}}$	E_{depol}	#iter	t_{comp}
[−]	[ms]	[−]	[μA]	[mV]	[mV]	[ms]	[−]	[ms]
CG	0.01	500	1.0E−05	0.0000	0.0000	0.0000	199	442
CG	0.01	500	1.0E−04	0.0005	0.0017	0.0005	105	252
CG	0.01	500	1.0E−03	0.0064	0.0193	0.0019	40	112
CG	0.01	500	1.0E−02	0.0745	0.1039	0.0066	13	47
CG	0.01	500	1.0E−01	0.7036	0.6344	0.0446	3	23
CG	0.01	50	1.0E−03	0.0077	0.0193	0.0021	40	105
Jacobi	0.01	500	1.0E−05	0.0037	0.0061	0.0014	455	600
Jacobi	0.01	500	1.0E−04	0.0073	0.0120	0.0020	238	362
Jacobi	0.01	500	1.0E−03	0.0378	0.0490	0.0047	58	107
Jacobi	0.01	500	1.0E−02	0.2033	0.1949	0.0131	13	37
Jacobi	0.01	500	1.0E−01	0.8200	0.7783	0.0539	3	20
Jacobi	0.01	50	1.0E−03	0.0630	0.0701	0.0061	42	87

#iter$_{max}$, maximum number of iterations per time step; ϵ, iteration process stops when $|I_{int}^n + I_{ext}^n| < \epsilon$; $E_{V_{mem}}$, $E_{V_{ext}}$ (simulation time 20 ms), and E_{depol} w.r.t. Conjugate Gradient method, #iter$_{max} = 500$ and $\epsilon = 1.0E{-}05\ \mu$A; #iter, average number of iterations per time step; t_{comp}, computation time per ms simulation time.

were compared with accurate simulation results (0.004×0.004 cm segments, #iter$_{max} = 500$, $\epsilon = 1.0E{-}04\ \mu$A).

In Figure 3.3 and Figure 3.4, V_{mem} and V_{ext} are presented after 20 ms simulation for the square grid, rectangular grid, and brickwall with varying coarseness. It can be observed that, after 20 ms, the depolarization wave is less far from the center for the coarser grids, indicating that the conduction velocity decreases when the coarseness of the grid increases. In Table 3.2, longitudinal conduction velocity θ_L, transverse conduction velocity θ_T, and ratio of anisotropy θ_L/θ_T are presented for the square grid, rectangular grid, and brickwall with varying coarseness. The predicted values of θ_L/θ_T from Section 2.3.3 are added for comparison.

Table 3.4: Jacobi's iteration method vs Conjugate Gradient method (brickwall)

Method	Δt	#iter$_{max}$	ϵ	$E_{V\mathrm{mem}}$	$E_{V\mathrm{ext}}$	E_{depol}	#iter	t_{comp}
[−]	[ms]	[−]	[μA]	[mV]	[mV]	[ms]	[−]	[ms]
CG	0.01	500	1.0E−05	0.0000	0.0000	0.0000	177	502
CG	0.01	500	1.0E−04	0.0004	0.0010	0.0005	94	224
CG	0.01	500	1.0E−03	0.0049	0.0182	0.0018	37	113
CG	0.01	500	1.0E−02	0.0604	0.1448	0.0058	12	49
CG	0.01	500	1.0E−01	0.6119	0.7997	0.0378	3	24
CG	0.01	50	1.0E−03	0.0060	0.0174	0.0019	36	116
Jacobi	0.01	500	1.0E−05	0.0025	0.0051	0.0013	446	874
Jacobi	0.01	500	1.0E−04	0.0054	0.0091	0.0018	200	402
Jacobi	0.01	500	1.0E−03	0.0307	0.0641	0.0042	48	107
Jacobi	0.01	500	1.0E−02	0.1698	0.2704	0.0110	10	35
Jacobi	0.01	500	1.0E−01	0.7985	0.9633	0.0492	2	20
Jacobi	0.01	50	1.0E−03	0.0395	0.0709	0.0048	40	58

#iter$_{max}$, maximum number of iterations per time step; ϵ, iteration process stops when $|I_{\mathrm{int}}^n + I_{\mathrm{ext}}^n| < \epsilon$; $E_{V\mathrm{mem}}$, $E_{V\mathrm{ext}}$ (simulation time 20 ms), and E_{depol} w.r.t. Conjugate Gradient method, #iter$_{max}$ = 500 and ϵ = 1.0E−05 μA; #iter, average number of iterations per time step; t_{comp}, computation time per ms simulation time.

3.3.3 Jacobi's iteration method vs Conjugate Gradient method

To compare Jacobi's iteration method with the Conjugate Gradient method to solve the system of linear equations for V_{ext}, we consider the rectangular grid and brickwall with segments of size 0.02×0.008 cm. In Table 3.3, the deviations in V_{mem}, V_{ext} and t_{depol} are presented for the rectangular grid with respect to the most accurate CG simulation. Furthermore, the average number of iterations per time step (#iter) and the computation time per ms simulation time (t_{comp}) are given. In Table 3.4, the same information is presented for the brickwall. As expected, the number of iterations is smaller for CG compared with Jacobi's method. However, since one CG iteration requires more computational effort than one Jacobi iteration, Jacobi's method is faster for $\epsilon \geq 1.0\text{E}{-}03$ μA. For $\epsilon = 1.0\text{E}{-}03$ μA, the deviation in depolarization time (E_{depol}) is still smaller than the size of one simulation step ($\Delta t = 0.01$ ms). Despite the larger number of connections per segment (6 for the brickwall vs 4 for the rectangular grid), the amount of computation time per ms simulation is similar in all cases. This is related to the lower number of iterations required for the brickwall. Thus, although the connectivity matrices D_{int} and D_{ext} are less sparse for the brickwall, computation time is not increased.

3.3.4 Structural remodeling

To investigate the effect of nonuniform conductivity on the conduction velocity, we modeled structural remodeling on the 2×1 cm brickwall tissue with 0.01×0.004 cm segments (fine) and with 0.02×0.008 cm segments (coarse). Nonuniform tissue was modeled by changing the intracellular conductances in longitudinal direction (σ_{int}^x defined by equation (2.18)) and the intracellular conductances in transverse direction ($\hat{\sigma}_{\text{int}}^y$ defined by equation (2.27)). The σ_{int}^x were multiplied with a factor drawn from a normal distribution (μ, σ_L), with average $\mu = 1.0$ and standard deviation σ_L varying between 0.0 and 1.0. In a similar way, the $\hat{\sigma}_{\text{int}}^y$ were multiplied with a factor drawn from a normal distribution (μ, σ_T).

In Figure 3.5, the membrane potential is shown after 20 ms of simulation. It can be observed that for both the coarse and the fine brickwall, the conduction velocity decreases for increasing $\sigma_L = \sigma_T$.

In Figure 3.6, the effect of varying σ_L and σ_T on the conduction velocity is presented. It can be observed that for both the coarse and the fine brickwall, the conduction velocity decreases with the same amount for increasing σ_L and σ_T. Thus, regardless the coarseness of the brickwall, the effect of nonuniform structural remodeling on the conduction velocity is similar.
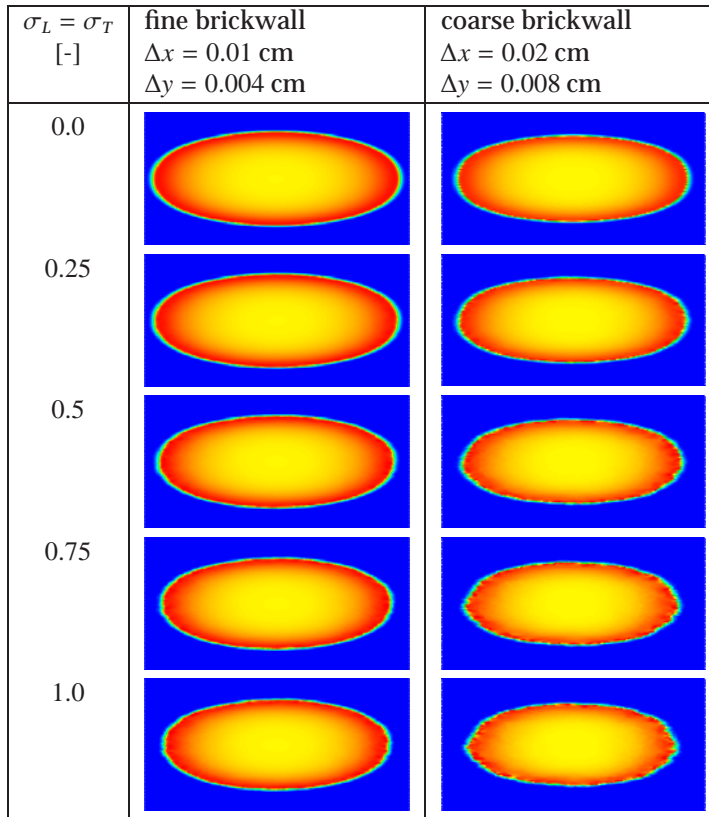
Figure 3.5: Effect of nonuniform distribution of conductivity for 0.01×0.004 cm segments (fine brickwall) and 0.02×0.008 cm segments (coarse brickwall). $\sigma_L = \sigma_T$ was varied between 0.0 (top) and 1.0 (bottom). A depolarization front was generated by stimulating the center of the 2×1 cm tissue. V_{mem} is shown 20 ms after stimulation. Red/yellow indicates depolarized tissue and blue indicates resting tissue.
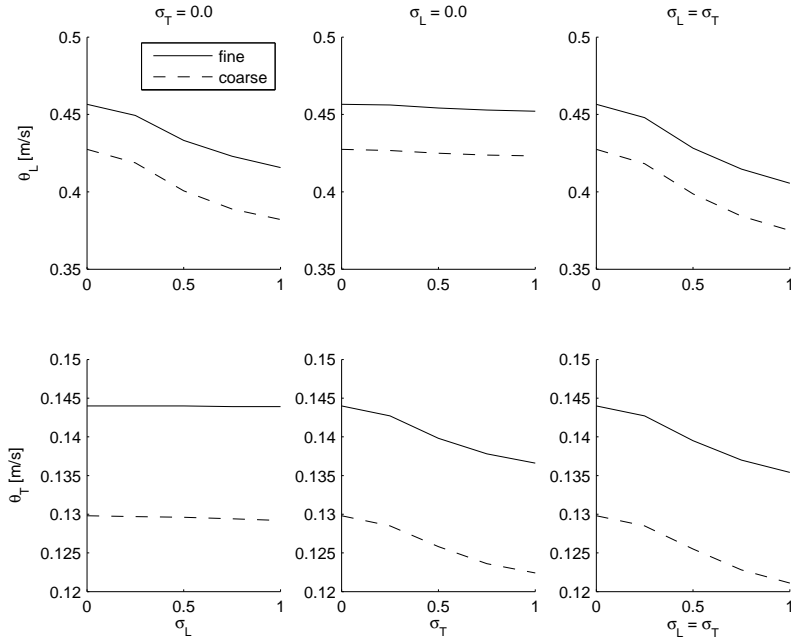
Figure 3.6: Effect of nonuniform distribution of conductivity for 0.01×0.004 cm segments (fine brickwall) and 0.02×0.008 cm segments (coarse brickwall). Top: conduction velocity in longitudinal direction (θ_L) for $0 \leq \sigma_L \leq 1$ and $\sigma_T = 0.0$ (left), $\sigma_L = 0.0$ and $0 \leq \sigma_T \leq 1$ (center), and $0 \leq \sigma_L = \sigma_T \leq 1$. Bottom: conduction velocity in transverse direction (θ_T).

time [ms]	V_{mem} −82 mV — 0 mV	V_{ext} −1 mV — 1 mV
0		
50		
100		
150		
200		
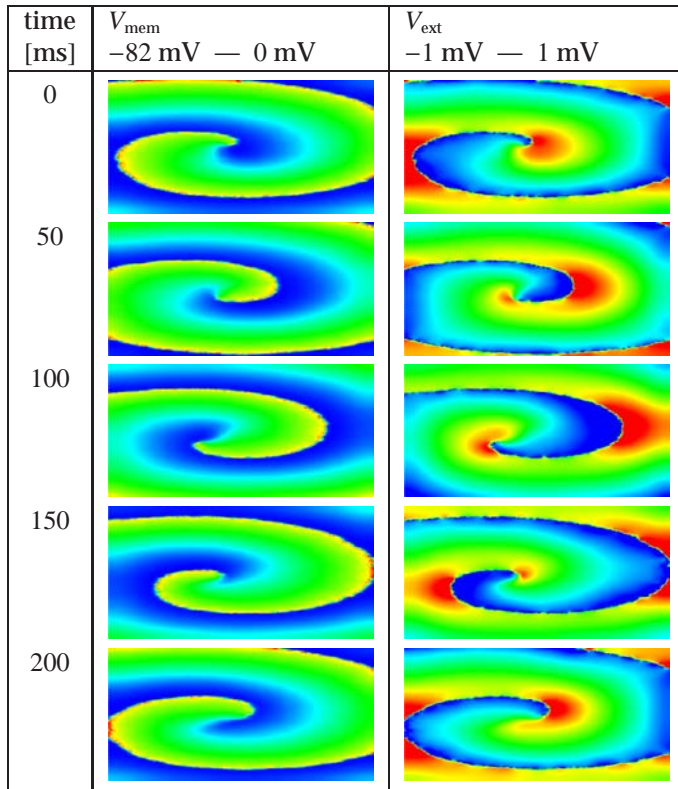
Figure 3.7: Membrane potential (V_{mem}) and extracellular potential (V_{ext}) on 4×2 cm nonuniform tissue. A spiral wave was generated using an S1S2 protocol with coupling interval 330 ms. Simulation state is shown during one rotation of the spiral wave (200 ms) with intervals of 50 ms.
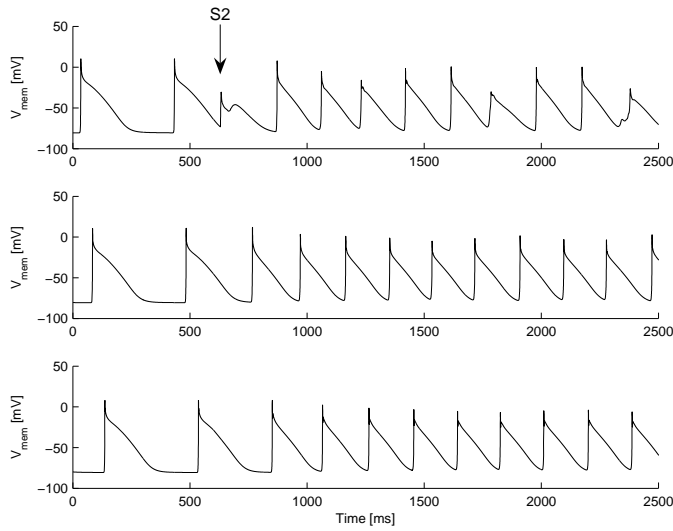
Figure 3.8: Membrane potential (V_{mem}) of three segments of the 4×2 cm tissue. Top: segment at $x = 2.0$ cm and $y = 1.0$ cm, center: segment at $x = 2.8$ cm and $y = 1.4$ cm, bottom: segment at $x = 3.6$ cm and $y = 1.8$ cm. A spiral wave was generated using an S1S2 protocol with coupling interval 330 ms. Arrow indicates S2 stimulus.

Table 3.5: Comparison of simulation time steps (spiral wave)

Δt_{high}^{mem}	Δt_{med}^{mem}	Δt_{low}^{mem}	$E_{V_{mem}}$	$E_{V_{ext}}$	E_{depol}	#iter	t_{comp}
[ms]	[ms]	[ms]	[mV]	[mV]	[ms]	[–]	[ms]
0.01	0.01	0.01	0.0000	0.0000	0.0000	18	211
0.01	0.02	0.20	0.0036	0.0001	0.0010	18	210
0.01	0.05	0.50	0.0072	0.0002	0.0030	18	212
0.01	0.10	1.00	0.0122	0.0003	0.0070	18	213
0.02	0.02	0.02	0.1187	0.0122	0.0472	28	143
0.05	0.05	0.05	0.6330	0.0380	0.2406	51	91
0.10	0.10	0.10	3.0235	0.1144	0.9613	76	64

#iter$_{max}$ = 100, maximum number of iterations per time step; ϵ = 1.0E−3, iteration process stops when $|I_{int}^n + I_{ext}^n| < \epsilon$; $E_{V_{mem}}$ and $E_{V_{ext}}$ computed for simulation time 200 ms w.r.t. first simulation; #iter, average number of iterations per time step; t_{comp}, computation time per ms simulation time.

3.3.5 Spiral wave

A spiral wave was initiated in a 4×2 cm sheet of tissue, which was a brickwall structure composed of 0.02×0.008 cm segments. Since the wavelength of a reentrant wave is too large for a 4×2 cm sheet of normal cardiac tissue, both the conduction velocity and the refractory period were reduced. The conduction velocity was reduced by simulating structural remodeling as follows: all intracellular conductivities were multiplied with a factor drawn from a normal distribution (μ, σ), with average $\mu = 0.3$ and standard deviation $\sigma = 1.0$. These factors were bound by a minimum value 0.1 and a maximum value 0.5. The refractory period was reduced by simulating electrical remodeling as follows: $I_{Ca,L}$ density was reduced with 80% and I_{to} density with 50%.

A spiral wave was initiated using an S1S2 stimulation protocol [201]. First, the top of the tissue (S1) was stimulated for 2 s with BCL $= 0.4$ s. After 2 s, a block of segments in the center of the left half (S2) was stimulated with a coupling interval of 330 ms. Since the bottom half of the tissue was still refractory, a depolarization front developed in one direction and a reentrant spiral wave was established. After one second of simulation time, the simulation state was stored and used as initial state to investigate the effect of varying simulation time steps. A number of simulations with varying simulation time steps were performed for a period of 200 ms using the same initial state. After 200 ms, deviations in V_{mem}, V_{ext}, and t_{depol} were computed with respect to the most accurate simulation. Furthermore, the number of iterations and the amount of computation time were measured during the simulation runs.

In Figure 3.7, one rotation of a spiral wave on the 4×2 cm tissue is presented. In Figure 3.8, V_{mem} is shown for the segment in the center (top) and for two segments in the right lower quarter of the tissue. Except for the center segment, little variation in action potential shape and APD can be observed, which is consistent with the stable behavior of the spiral wave.

In Table 3.5, deviations in V_{mem}, V_{ext}, and t_{depol} are presented for varying simulation time steps. Also the average number of iterations per time step (#iter) and the computation time per ms simulation time (t_{comp}) are given. As expected, the deviation in simulation results increases for increasing Δt. Furthermore, the number of iterations to compute V_{ext} increases for increasing Δt, which is explained by the larger change in V_{ext} over a longer time step. Interestingly, using larger time steps to update the membrane currents for medium and low accuracy has little influence on the computation time. This is explained by the fact that, on average, 12000 segments have high accuracy, 38000 have medium accuracy, while only few have low accuracy. Thus, a possible gain in computation time by differentiation in time steps as in the

Table 3.6: Comparison of conduction velocity

# levels	α	θ	θ/θ_0	t_{comp}
[−]	[−]	[m/s]	[−]	[ms]
3	0.0	0.90	1.00	519
2	0.0	0.57	0.64	65
2	0.2	0.76	0.84	55
2	0.3	0.89	0.99	79
2	0.4	1.06	1.18	80

levels, number of levels in simulation graph; α, value of α in heuristic (Section 3.2.5); θ, conduction velocity; θ/θ_0, relative conduction velocity; t_{comp}, computation time per ms simulation time.

5-cm-long fiber (Section 3.3.1) is lost due to the constant activity of the tissue and the bookkeeping of low, medium, and high accuracy.

3.3.6 Multilevel simulation graph

To quantify the effect of using the heuristic introduced in Section 3.2.5, we simulated depolarization of the human atria as in Chapter 2. One simulation was performed with all three levels of the simulation graph ($\alpha = 0.0$). Four simulations were performed with only two levels ($\alpha = 0.0$, 0.2, 0.3, and 0.4). In each of the simulations, a depolarization wave was generated by electrical stimulation of the sino-atrial node.

In Figure 3.9, V_{mem} is shown during 120 ms after stimulation of the sino-atrial node for the 2-level simulation graph with $\alpha = 0.0$ (left), the 2-level simulation graph with $\alpha = 0.3$ (center), and the 3-level simulation graph with $\alpha = 0.0$. It can be observed that, when $\alpha = 0.3$, the depolarization wave travels with approximately the same velocity as in the 3-level simulation graph, while for $\alpha = 0.0$, the conduction velocity is smaller.

In Table 3.6 the conduction velocity θ for various α on the 2-level simulation graph is compared with the conduction velocity θ_0 on the 3-level simulation graph. Best agreement is found for $\alpha = 0.3$. Compared with the 3-level simulation graph, the amount of computation time reduced with 85% when the heuristic is used on the 2-level simulation graph, without significant loss of accuracy.

time [ms]	2 levels ($\alpha = 0.0$) $\theta = 0.57$ m/s	2 levels ($\alpha = 0.3$) $\theta = 0.89$ m/s	3 levels ($\alpha = 0.0$) $\theta = 0.90$ m/s
20			
40			
60			
80			
100			
120			
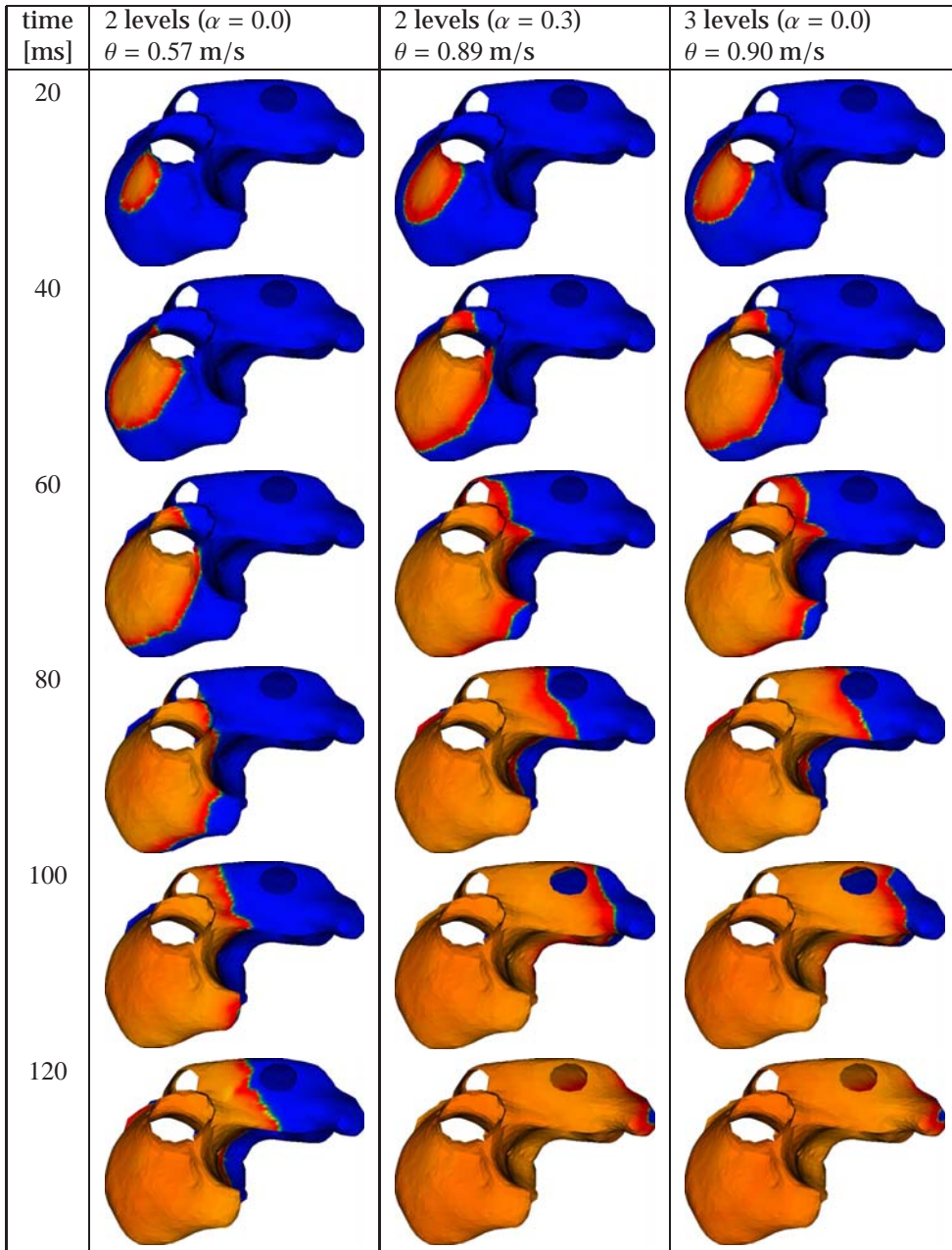
Figure 3.9: Membrane potential (V_{mem}) on multilevel atrial geometry. Left: two levels ($\alpha = 0.0$). Center: two levels ($\alpha = 0.3$). Right: three levels ($\alpha = 0.0$). A depolarization wave was generated at 0 ms by stimulating the sino-atrial node.

3.4 Discussion

3.4.1 Uniform and nonuniform cardiac tissue

To model the cardiac tissue, we compared a brickwall configuration with a square grid and a rectangular grid. Although segments of size 0.02×0.008 cm are larger than human atrial myocytes (0.01×0.002 cm), we obtain accurate simulation results when simulating normal impulse propagation. Therefore, we consider the brickwall composed of 0.02×0.008 cm segments a good representation of normal (uniform) cardiac tissue.

When simulating impulse propagation in structurally remodeled tissue, the conduction velocity is decreased as a consequence of the nonuniform distribution of intracellular conductivity between adjacent segments. The nominal decrease in conduction velocity in a brickwall of 0.02×0.008 cm segments is similar to the nominal decrease in conduction velocity when the brickwall is composed of 0.01×0.004 cm segments (Figure 3.6). Thus, although the nonuniformity induced by structural remodeling is simulated at a larger scale, this has little effect on the decrease in conduction velocity. We conclude that both uniform and nonuniform cardiac tissue may be represented by a brickwall composed of 0.02×0.008 cm segments. In Chapter 4 and in Chapter 5, uniform, nonuniform, and pathological tissue are represented by such a brickwall.

3.4.2 Numerical integration scheme

In the present study, we consider an explicit forward Euler scheme to solve the coupled system of nonlinear differential equations and linear equations. Keener and Bogar [94] state that, since solving a linear system of equations at each time step cannot be avoided, it is better to use a Crank-Nicolson step for the spatial discretization, and a multigrid inversion of the linear system at each time step. They argue that although this method is twice as costly per time step as the forward Euler method, it is potentially faster and more accurate when larger time steps are possible [94]. In our model, the Courtemanche-Ramirez-Nattel model requires small simulation time steps, which largely determines the time step that can be used to solve the coupled systems of equations. Since the advantage of having larger simulation time steps cannot be exploited, we decided to solve the system of equations using an explicit forward Euler scheme.

We also studied the differences between using Jacobi's iteration method and the Conjugate Gradient method to solve the system of linear equations for V_{ext}. As expected, CG converges faster than Jacobi's iteration method.

However, to solve V_{ext} in our model, Jacobi's iteration method can be faster than CG (Table 3.3 and Table 3.4). This is explained by the small simulation time step of 0.01 ms: V_{ext} of the former time step is a good first approximation to solve V_{ext} for the current time step. Indeed, the number of iterations increases for increasing simulation time step (Table 3.5). An advantage of Jacobi's iteration method over CG is that less communication per iteration is required when performing the simulation on a processor network. We used a parallel implementation of our simulation software on a cluster of 8 processors to perform the large-scale simulations of the 8×3 cm tissue (150000 segments) of arrhythmic behavior (Chapter 2), defibrillation (Chapter 4), and ectopic behavior (Chapter 5).

Furthermore, we studied the use of different simulation time steps to update the membrane state. When a depolarization wave is simulated along a fiber, up to 70% of computational effort may be saved without significant loss of accuracy (Table 3.1). However, in case a spiral wave is simulated, this advantage vanishes due to the large amount of activity present throughout the tissue at all times (Table 3.5). In Chapter 6 and in Chapter 7, mechano-electric feedback is studied by a depolarization wave through fibers of different lengths. When the fiber needs to be simulated for a long period of time (up to 150 s with BCL = 1.0 s in Chapter 7), the reduction in computational effort is considerable.

Finally, we investigated the effect of "smoothing" the ionic membrane current over the domain, such that the human atria can be represented with a coarser mesh. We found that, when applying the heuristic method introduced in Section 3.2.5 with $\alpha = 0.3$, accurate simulation results can be obtained with a mesh in which the average distance between two adjacent nodes is 0.09 cm, while normally this distance should be 0.03 cm. When simulating depolarization of the human atria, the number of nodes in the simulation graph may be reduced from over 300000 to approximately 34000. With this method, 89% less memory is required and about 85% of computational effort is saved on top of the 70% saved by using different simulation time steps to update the membrane behavior. We apply this method in Chapter 8 to investigate the role of stretch-activated channels in the onset of atrial fibrillation under stretch.

3.5   Conclusion

The equations of the Cellular Bidomain Model are solved using a forward Euler scheme for the nonlinear differential equations and an iterative method for the system of linear equations. To save computational effort, larger time steps

to update the membrane state can be applied when the membrane is repolarizing or resting. Both computation time and memory usage can be further reduced by using a coarser mesh in combination with a heuristic method to compute the transmembrane current.

4

Computer simulations of successful defibrillation in decoupled and nonuniform cardiac tissue

N.H.L. Kuijpers, R.H. Keldermann, T. Arts, and P.A.J. Hilbers

Abstract

Aim: The aim of the present study is to investigate the origin and effect of virtual electrode polarization in uniform, decoupled, and nonuniform cardiac tissue during field stimulation.

Methods: A discrete bidomain model with active membrane behavior was used to simulate normal cardiac tissue as well as cardiac tissue that is decoupled due to fibrosis and gap junction remodeling. Various uniform and nonuniform electric fields were applied to the extracellular domain of uniform, decoupled, and nonuniform resting cardiac tissue as well as cardiac tissue in which spiral waves were induced.

Results: Field stimulation applied to nonuniform tissue results in more virtual electrodes compared with uniform tissue. The spiral waves were terminated in decoupled tissue, but not in uniform, homogeneous tissue. By gradually increasing local differences in intracellular conductivities, the amount and spread of virtual electrodes increased and the spiral waves were terminated.

Conclusion: Fast depolarization of the tissue after field stimulation may be explained by intracellular decoupling and spatial heterogeneity present in normal and pathological cardiac tissue. We demonstrated that termination of spiral waves by means of field stimulation can be achieved when the tissue is modeled as a nonuniform, anisotropic bidomain with active membrane behavior.

4.1 Introduction

Defibrillation is a common clinical procedure to terminate atrial and ventricular fibrillation. An externally applied electric field leads to the development of so-called virtual electrode polarization, or VEP [49]. The VEP can affect the transmembrane potential: new action potentials can arise or existing action potentials can be prolonged or shortened [50]. When defibrillation is successful, the entire tissue depolarizes within a short time and after recovery sinus rhythm is restored [48]. In this study, we investigate the origin of the VEP in uniform, decoupled, and nonuniform cardiac tissue by means of computer simulations. Furthermore, we investigate the role of the VEP in relation to the termination of a spiral wave in normal as well as pathological tissue.

Computer simulations of defibrillation require a model that distinguishes between the intracellular and extracellular domains. If the rates of anisotropy for the intracellular and extracellular domains are modeled differently, virtual electrodes appear in the vicinity of both the cathode and the anode [161]. These observations have been verified experimentally [222]. However, in computer simulations using a continuous bidomain model, virtual electrodes do not appear in the bulk of the tissue and cannot explain depolarization of the entire tissue within short time.

Several groups have used discontinuous bidomain models to investigate the effect of structural nonuniformities in cardiac tissue when external electric fields are applied [136]. In some of these models, the effects of the gap junctions are incorporated by modeling periodic changes in the intracellular conductivities [96, 199]. In simulations using these models, so-called "sawtooth" patterns appear in spatial mappings of the transmembrane potential [108]. Although they have been searched for, these "sawtooth" patterns have not been observed experimentally [232]. Also in cultured layers of myocytes, no virtual electrodes were observed at the cell borders [64]. Later bidomain models focus on modeling fiber curvature both in 2D and 3D [202]. Using these models, virtual electrodes appeared further away from the physical electrodes and spiral waves have been terminated [201].

In a study by Fast *et al.* [56] using directed cell growth in cell cultures with intercellular clefts, large changes in the transmembrane potential have been observed at the boundaries of cell strands and at the intercellular clefts. Secondary sources of stimulation, i.e., depolarization of tissue not directly caused by the stimulating electrodes, have also been found near surgical incisions in dog hearts [220]. A bidomain model describing the laminar organization of myocytes has been used to investigate the effect of an external electric field applied to the ventricular wall of a rat [75]. In these simulations, the bulk of the tissue was depolarized in regions located near the interlami-

nar clefts [75].

In a simulation study by Fishler [60, 59], the effect of spatial heterogeneity during monophasic and biphasic shocks was investigated by varying the intracellular volume fraction randomly throughout the tissue. In another study by Krassowska [107], the effect of spatial heterogeneity was statistically investigated by varying cell length, cell diameter, thickness of the extracellular space and the junctional resistances in ten different random fibers. Both studies indicate a decrease in the field stimulation threshold as a consequence of spatial heterogeneity.

Keener and Cytrynbaum [95] investigated defibrillation in a 1D ring and a 2D sheet using dynamical systems theory. In their study, spatial heterogeneity was modeled at different scales. They concluded that spatial inhomogeneity, especially at smaller scales, leads to an increase in the success rate of defibrillation [95]. Very recently, Plank *et al.* [144] investigated the effect of spatial heterogeneity and the level of organization of fibrillating tissue in relation to the defibrillation shock strength. They concluded that the required shock strength for successful defibrillation increases with disorganization of the fibrillatory state [144]. Similar observations were also made by Hillebrenner *et al.* [72].

The aim of the present study is to obtain more insight in the role of decoupling and nonuniform conductivities in the clinical success of defibrillation. To simulate virtual electrode polarization as a consequence of field stimulation, we use a discrete bidomain model, which is aimed at irregular conductivity properties of cardiac tissue at the cellular level. To study the effects of decoupling and nonuniformity, conductivities between adjacent cells are randomly varied. In order to model the membrane behavior of individual atrial myocytes, we apply the Courtemanche-Ramirez-Nattel model of the human atrial action potential [37]. Electroporation is modeled as described by Aguel *et al.* [2]. Computer simulations of various rectangular sheets of atrial tissue have been performed to investigate the effect of nonuniformity and decoupling when an external electric field is applied. To investigate the success of defibrillation, spiral waves were induced on a sheet of $8 \text{ cm} \times 3 \text{ cm}$ cardiac tissue using an S1S2 protocol [201]. We hypothesize that fast depolarization of the entire tissue after field stimulation is related to the amount of decoupling and nonuniformity in the tissue.
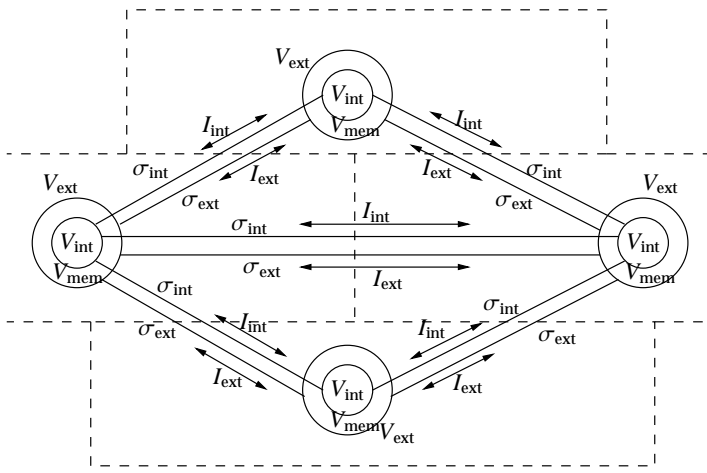
Figure 4.1: Graphical representation of a simulation graph. Each node represents a rectangular piece of cardiac tissue. The state of each node is represented by the intracellular potential V_{int}, the extracellular potential V_{ext}, and the membrane potential V_{mem}. Electrical connections between the nodes are indicated by the intracellular and interstitial conductances denoted by σ_{int} and σ_{ext}. The intracellular and interstitial currents flowing between the nodes are represented by the arrows labeled with I_{int} and I_{ext}.

4.2 Methods

4.2.1 Cellular Bidomain Model

The discrete bidomain model we use is called the Cellular Bidomain Model. Both the electrical behavior of the cell membrane and the propagation of the depolarization wave are described by this model. The structure of the cardiac tissue is represented by a *graph* consisting of nodes and edges, where a *node* represents a group of cells and an *edge* the electrical connections between the cells. Such a graph is called a *simulation graph* and is denoted by $\mathcal{G}(\mathcal{N}, \mathcal{E})$, where $\mathcal{N}$ is the set of nodes and $\mathcal{E}$ the set of edges connecting the nodes.

Within a simulation graph, a number of different cell types can be distinguished, e.g., sino-atrial node cells and atrial myocytes, each having their own membrane behavior. The state of each node $n \in \mathcal{N}$ is defined by the intracellular potential (V_{int}^n), the extracellular potential (V_{ext}^n), and the state of the cell membrane. The membrane potential (V_{mem}^n) is defined as the difference between V_{int}^n and V_{ext}^n. Edges define the conductance for intracellular and extracellular currents between two adjacent nodes. We distinguish the *intracellular* and *extracellular* conductance, which are denoted by σ_{int} and σ_{ext}, respectively. We assume that the simulation graph is not directed and for

edge $(n, m) \in \mathcal{E}$ connecting nodes n and m it is assumed that $\sigma_{\text{int}}^{(n,m)} > 0$ and $\sigma_{\text{ext}}^{(n,m)} > 0$. The intracellular and extracellular currents flowing from node n to node m are denoted by $I_{\text{int}}^{n \to m}$ and $I_{\text{ext}}^{n \to m}$, and are given by by Ohm's law:

$$I_{\text{int}}^{n \to m} = (V_{\text{int}}^n - V_{\text{int}}^m)\, \sigma_{\text{int}}^{(n,m)}, \tag{4.1}$$

$$I_{\text{ext}}^{n \to m} = (V_{\text{ext}}^n - V_{\text{ext}}^m)\, \sigma_{\text{ext}}^{(n,m)}. \tag{4.2}$$

The intracellular current entering node n coming from all adjacent nodes a, $(a, n) \in \mathcal{E}$, is denoted by I_{int}^n. The extracellular current entering node n is denoted by I_{ext}^n, i.e.,

$$I_{\text{int}}^n = \sum_{(a,n) \in \mathcal{E}} I_{\text{int}}^{a \to n}, \tag{4.3}$$

$$I_{\text{ext}}^n = \sum_{(a,n) \in \mathcal{E}} I_{\text{ext}}^{a \to n}. \tag{4.4}$$

According to Kirchhoff's law, current entering a node as intracellular current must leave as extracellular current, thus

$$I_{\text{int}}^n + I_{\text{ext}}^n = 0. \tag{4.5}$$

Furthermore, the transmembrane current for node n, denoted by I_{trans}^n, is the sum of capacitive and ionic currents, i.e.,

$$I_{\text{trans}}^n = C_{\text{mem}}^n \frac{dV_{\text{mem}}^n}{dt} + S_{\text{mem}}^n I_{\text{ion}}(V_{\text{mem}}^n, \mathbf{q}^n) = I_{\text{int}}^n, \tag{4.6}$$

where C_{mem}^n represents the membrane capacitance of node n in μF, and S_{mem}^n the membrane surface in cm^2. The ionic membrane current of node n is denoted by $I_{\text{ion}}(V_{\text{mem}}^n, \mathbf{q}^n)$ and is expressed in μA per cm^2 membrane surface. The ionic current depends on the membrane potential and the state of the membrane, which is usually described by a number of gating variables. The set of variables describing the membrane state is denoted by $\mathbf{q}^n$. The membrane state depends on the membrane potential:

$$\frac{d\mathbf{q}^n}{dt} = M_{\text{ion}}(V_{\text{mem}}^n, \mathbf{q}^n). \tag{4.7}$$

The ionic membrane current modeled by functions I_{ion} and M_{ion} can be implemented by any membrane model [15, 37, 125]. Different membrane models can be applied for different nodes to model heterogeneous cell membrane behavior of the cardiac tissue.

Table 4.1: Tissue parameters

Parameter	Definition	Value
g_{int}^x	Longitudinal intracellular conductivity	1.0440 mS/cm
g_{int}^y	Transverse intracellular conductivity	0.1158 mS/cm
g_{ext}^x	Longitudinal extracellular conductivity	3.7500 mS/cm
g_{ext}^y	Transverse extracellular conductivity	1.4160 mS/cm
C_{mem}	Membrane capacitance	$1.0\ \mu\text{F/cm}^2$
χ	Surface-to-volume ratio	$2000\ \text{cm}^{-1}$

In this study, we use a brickwall structure to model the cardiac myocytes. Each node represents a rectangular piece of tissue of length $200\ \mu$m and width $80\ \mu$m lying in the direction of the fibers (Figure 4.1). Note that the segments are not subdivided in smaller parts: the same state is assumed throughout the entire segment. In order to obtain conduction velocities within physiological range [179], we have rescaled the conductivity parameters as reported by Clerc [33] with a factor 0.6. The tissue parameters used in the present study are listed in Table 4.1. These parameters result in a conduction velocity of 0.41 m/s along the fiber direction and 0.13 m/s across the fiber direction.

The membrane behavior for each node is simulated by the model of Courtemanche *et al.* [37]. The equations of the Cellular Bidomain Model are solved using a forward Euler scheme with a simulation time step of 0.01 ms. We describe how electroporation, nonuniform conductivities, and field stimulation are modeled.

4.2.2 Electroporation

When applying a large electric field on cardiac tissue, the membrane of cells near the electrodes start to electroporate [106], i.e., the membrane conductance is increased by the formation of aqueous pores [3]. Electroporation prevents membrane potentials from reaching extreme values [106].

We model electroporation as described by Aguel *et al.* [2]. The membrane behavior of the Cellular Bidomain Model has been extended with an extra state variable G, denoting the pore generation in the membrane. Equation (4.6) is adapted as follows [175]:

$$I_{\text{trans}}^n = C_{\text{mem}}^n \frac{dV_{\text{mem}}^n}{dt} + S_{\text{mem}}^n (I_{\text{ion}}(V_{\text{mem}}^n, \mathbf{q}^n) + G V_{\text{mem}}^n) = I_{\text{int}}^n. \tag{4.8}$$

G is described by [175]:

$$\frac{dG}{dt} = \alpha \exp(\beta(V_{mem}^n - V_{rest}^n)^2)(1 - \exp(-\gamma(V_{mem}^n - V_{rest}^n)^2)), \tag{4.9}$$

where $\alpha = 2.5 \times 10^{-3}$ mS/cm²ms, $\beta = 2.5 \times 10^{-5}$ mV^{-2}, and $\gamma = 1.0 \times 10^{-9}$ mV^{-2} [175]. V_{rest} represents the resting membrane potential, which is near -81 mV for the Courtemanche-Ramirez-Nattel model [37]. Initially, G is set to 0 mS/cm².

4.2.3 Gap junctions

Gap junctions provide the pathways for intracellular current flow. The anisotropic conduction properties of the myocardium are dependent on the geometry of the intercalated disks and the number, size and location of the gap junctions in between them [88]. Changes in gap junction distribution are common in elderly people and are involved in the initiation and persistence of various cardiac arrhythmias [183].

In the Cellular Bidomain Model, a distinction is made between *longitudinal* edges and *transverse* edges. The intracellular conductances of the longitudinal edges represent the gap junctions between cells of the same fiber and the intracellular conductances of the transverse edges represent the gap junctions responsible for side-to-side coupling. The effects of gap junction remodeling are simulated by randomly changing the intracellular conductances. A normal distribution (μ, σ) is applied to determine the factor with which the standard values for the intracellular conductances are multiplied for each edge. In the sequel, the average and standard deviation of the gap junction remodeling factor in longitudinal direction are denoted by μ_L and σ_L, respectively, and the average and standard deviation in transverse direction by μ_T and σ_T, respectively.

4.2.4 Fibrosis

Fibrosis causes the loss of side-to-side cell coupling, which may result in a disturbed wavefront propagation and can isolate groups of myocytes [55]. The development of fibrosis is associated with changes in the topology and number of gap junctions [179]. Since side-to-side coupling is affected, fibrosis leads to a reduction of the conduction velocity, mainly in transverse direction [179].

In the Cellular Bidomain Model, diffuse fibrosis [93] is simulated by removing the intracellular conductances of some of the transverse edges. The so-called *fibrosis fraction* determines the number of affected transverse edges,

but which transverse edges are affected is randomly determined. In the sequel, the fibrosis fraction is denoted by FF.

4.2.5 Simulation protocol

To investigate virtual electrode polarization on uniform, decoupled, and non-uniform tissue, we modeled a 1 cm × 0.5 cm sheet of atrial tissue. A nonuniform electric field was established during 1 ms by placing the anode in the left upper quarter of the tissue and the cathode in the right lower quarter of the tissue. The strength of the electric field was varied using an anode voltage of +1, +5, and +10 V, respectively, and a cathode voltage of −1, −5, and −10 V, respectively. This protocol was applied to uniform, decoupled, and nonuniform tissue. Decoupled tissue was modeled as uniform tissue in which artificial obstacles were placed. These obstacles were either nonconductive in the intracellular domain only, or they were nonconductive in both domains. Nonuniform tissue was modeled by multiplying the intracellular conductances with a factor drawn from a normal distribution (μ, σ), with average $\mu = 1$ and standard deviation $\sigma = 0.5$, 1, and 1.5, respectively. These factors were bound with minimum 0.75, 0.5, and 0, respectively, and maximum 1.25, 1.5, and 2, respectively.

Two large-scale simulations of an 8 cm × 3 cm sheet of atrial tissue with and without fibrosis and gap junction remodeling were performed. In this case, the cardiac tissue was divided into 150,000 segments of size 200 μm × 80 μm. Pathological tissue was simulated with fibrosis fraction FF = 0.35 and average gap junction remodeling factor $\mu_L = \mu_T = 0.5$ and standard deviation $\sigma_L = \sigma_T = 1$. The conduction velocity in pathological tissue decreased from 0.41 to 0.19 m/s along the fiber direction and from 0.13 to 0.05 m/s across the fiber direction. To investigate the effect of nonuniform conductivity during defibrillation in normal tissue, the intracellular conductances were changed before the electric field was applied. All intracellular conductances were multiplied with a factor drawn from a normal distribution (μ, σ) with average $\mu = 1$ and standard deviation $\sigma = 0.5$ and 1, respectively. In both cases, the factors were bound with minimum 0.75 and 0.5, respectively, and maximum 1.25 and 1.5, respectively.

An electric field was established during 10 ms by placing the anode at the top row of the tissue and the cathode at the bottom. The anode voltage was +25 V and the cathode voltage −25 V, generating a uniform electric field of 16.7 V/cm in the direction across the fibers. A similar protocol was used by Trayanova and Skouibine [201]. Field stimulation was applied to uniform and nonuniform normal tissue as well as pathological tissue in the resting state. For the final series of simulations, a spiral wave was induced

in both normal and pathological tissue using an S1S2 stimulation protocol as described by Trayanova and Skouibine [201]. Each simulation lasted several seconds to let a spiral wave develop before field stimulation was applied.

4.3 Results

Anodal and cathodal point stimulation in uniform tissue results in the characteristic dog bones near the physical electrodes. For all three different strengths of the electric field, depolarization occurred near the cathode. Only in case of the two stronger electric fields, virtual electrodes near the anode lead to depolarization. No secondary sources were observed on larger distances from the physical electrodes. In Figure 4.2, the results are shown for anode voltage +10 V and cathode voltage −10 V in uniform and decoupled tissue. The dog bone is clearly visible in the left column (uniform tissue). Secondary sources appear near the artificial obstacles (center and right). Note that the location of the secondary sources is different for internally uncoupled tissue (center) and fully uncoupled tissue (right).

In Figure 4.3, the results are shown for anodal and cathodal point stimulation in nonuniform tissue. The results are shown for the simulation runs with anode voltage +10 V and cathode voltage −10 V. The dog bone is clearly visible in the left column, but less apparent in the center and right column. Furthermore, a larger number of virtual electrodes is present in the bulk of the tissue in the center and right column. Virtual electrode polarization facilitates faster depolarization of the entire tissue. This can be clearly observed in the center column of Figure 4.2 and in the center and right column of Figure 4.3.

In Figure 4.4, the results are shown when a uniform electric field is applied during 10 ms on normal, resting cardiac tissue. In uniform normal tissue (left) cells depolarize in the vicinity of the two electrodes, but not in the bulk of the tissue. In nonuniform normal tissue (center) more virtual electrodes are present in the bulk of the tissue. The virtual electrodes either depolarize or hyperpolarize cells in their vicinity. In the right column, more virtual electrodes originate that are better spread over the tissue. The result is that the entire tissue is more rapidly depolarized. In remodeled tissue (Figure 4.5), more virtual electrodes are created compared with normal, nonuniform tissue. However, since the velocity of the wavefront is lower compared with normal tissue, it takes more time to depolarize the entire tissue.

time [ms]	uniform	internally uncoupled	fully uncoupled
1			
2			
3			
5			
7			
9			
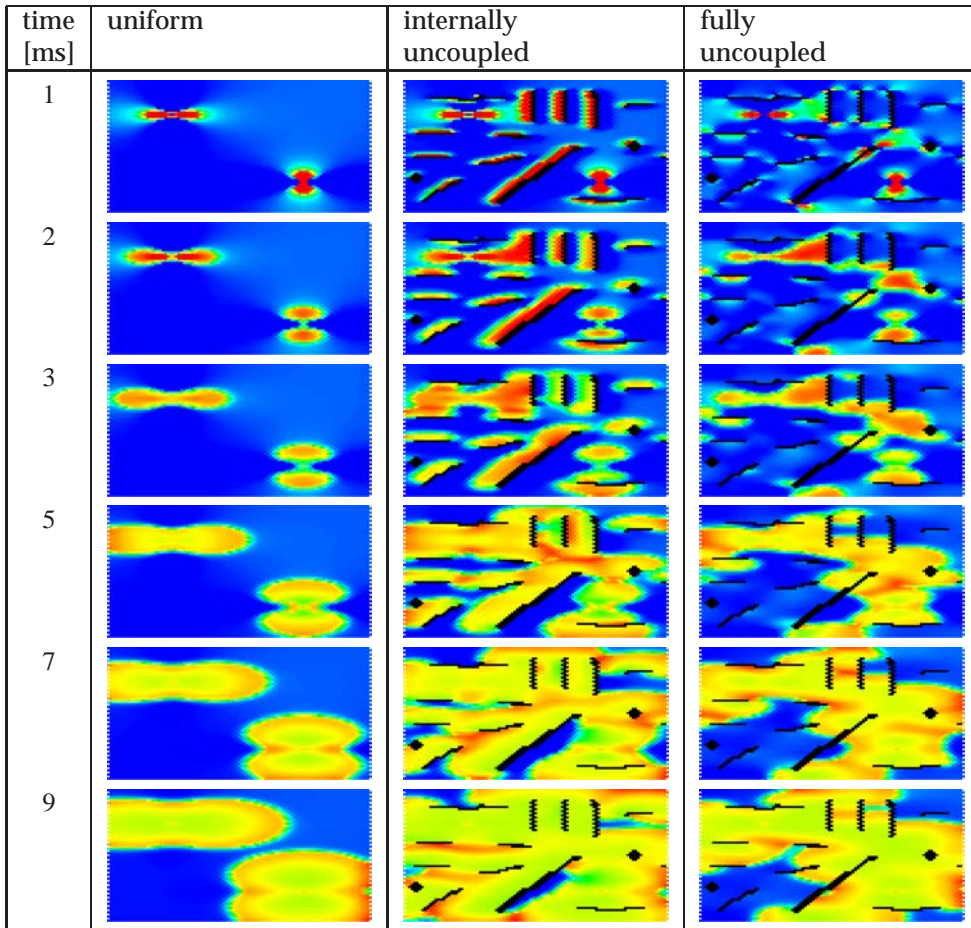
Figure 4.2: Anodal and cathodal point stimulation in uniform (left), internally uncoupled (center), and fully uncoupled (right) resting cardiac tissue. The anode is located in the upper left quarter and the cathode in the lower right quarter of the tissue. Artificial obstacles are created by (internally) uncoupling the black segments from the surrounding tissue. An electric field was applied during the first millisecond of the simulation. Shown are the membrane potentials for different simulation times after field stimulation. Depolarized tissue is red/yellow and hyperpolarized or resting tissue is blue.

time [ms]	$\mu_L = \mu_T = 1$ $\sigma_L = \sigma_T = 0.5$ FF = 0	$\mu_L = \mu_T = 1$ $\sigma_L = \sigma_T = 1$ FF = 0	$\mu_L = \mu_T = 1$ $\sigma_L = \sigma_T = 1.5$ FF = 0
1			
2			
3			
5			
7			
9			
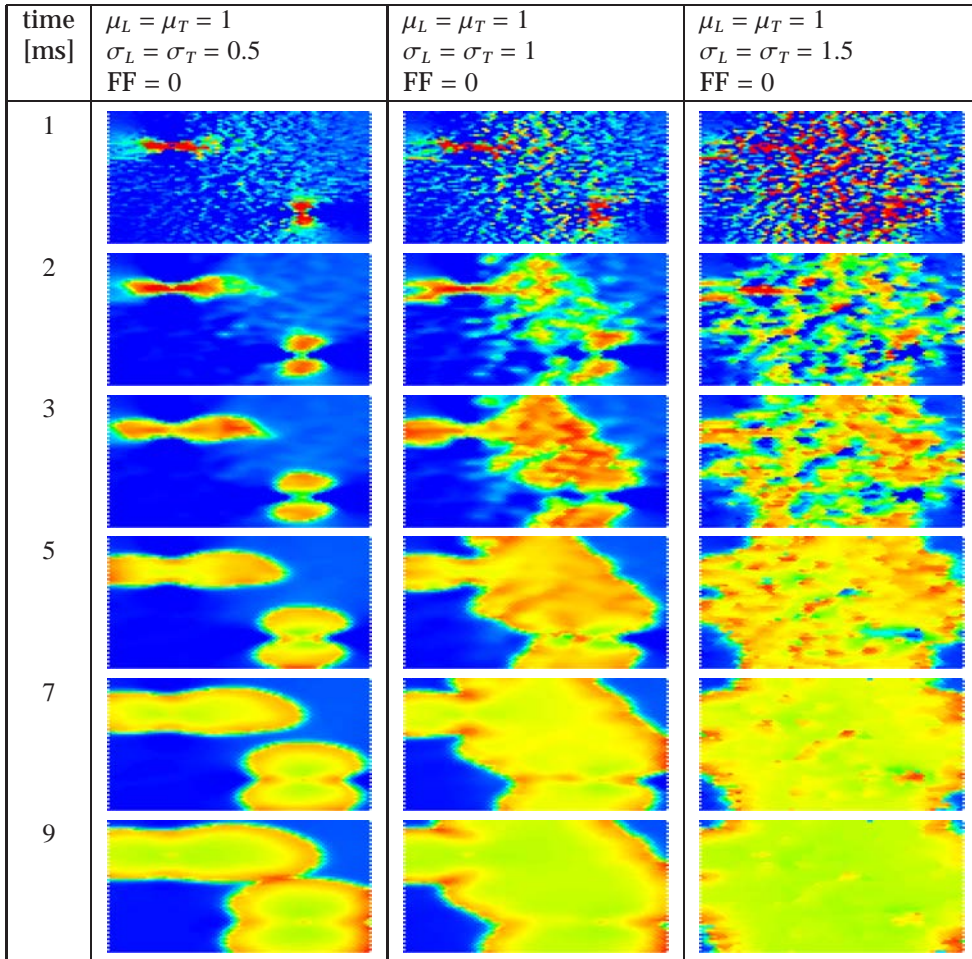
Figure 4.3: Anodal and cathodal point stimulation in resting cardiac tissue with nonuniform intracellular conductivity. The anode is located in the upper left quarter and the cathode in the lower right quarter of the tissue. An electric field was applied during the first millisecond of the simulation. Shown are the membrane potentials for different simulation times after field stimulation. Depolarized tissue is red/yellow and hyperpolarized or resting tissue is blue.

time [ms]	$\mu_L = \mu_T = 1$ $\sigma_L = \sigma_T = 0$ FF = 0	$\mu_L = \mu_T = 1$ $\sigma_L = \sigma_T = 0.5$ FF = 0	$\mu_L = \mu_T = 1$ $\sigma_L = \sigma_T = 1$ FF = 0
0			
1			
5			
10			
20			
50			
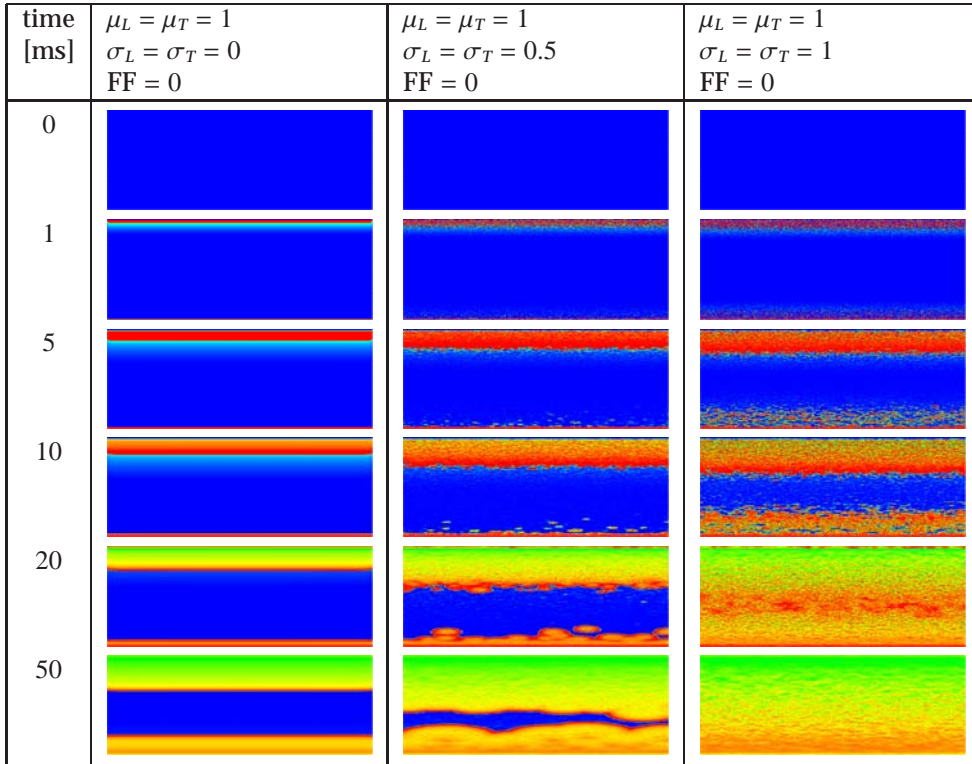
Figure 4.4: Virtual electrode polarization in uniform (left) and nonuniform (center and right) resting cardiac tissue. The anode was a line electrode at the top and the cathode a line electrode at the bottom of the tissue. A uniform electric field was applied during 10 ms. Shown are the membrane potentials for different simulation times during and after field stimulation. Depolarized tissue is red/yellow/green and hyperpolarized or resting tissue is blue.

$\mu_L = \mu_T = 0.5$ $\sigma_L = \sigma_T = 1$ FF $= 0.35$		
0 ms	1 ms	5 ms
10 ms	20 ms	50 ms
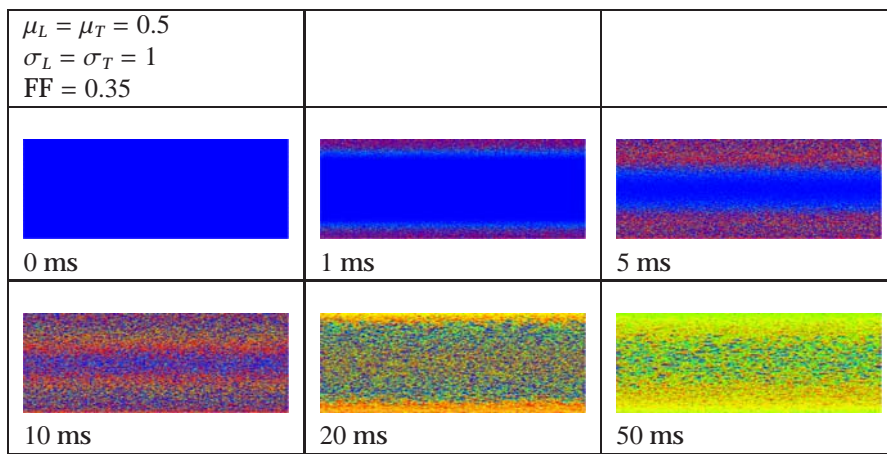
Figure 4.5: Virtual electrode polarization in resting remodeled tissue. The anode was a line electrode at the top and the cathode a line electrode at the bottom of the tissue. A uniform electric field was applied during 10 ms. Shown are the membrane potentials for different simulation times during and after field stimulation. Depolarized tissue is red/yellow/green and hyperpolarized or resting tissue is blue.

In Figure 4.6, the results are shown after application of an electric field in uniform and in nonuniform normal tissue in which a spiral wave was induced. The spiral wave is not terminated in uniform atrial tissue (left). As before, more virtual electrodes originate in the bulk of nonuniform tissue (center and right). Virtual electrodes can be observed in both the excitable gap and depolarized tissue. In the center column, the number of virtual electrodes in the excitable gap is too small to terminate the spiral wave. However, in the right column, more virtual electrodes are present in the excitable gap and the spiral wave is terminated. The entire tissue recovers and no activity is left to initiate new depolarization waves.

Also in Figure 4.7, virtual electrode polarization is clearly visible in remodeled tissue and the spiral wave is terminated. Compared with normal, nonuniform tissue more virtual electrodes are present. However, since the propagation of the action potential is slower in remodeled tissue, the time it takes to depolarize the entire tissue is longer compared with the time it takes to depolarize normal, nonuniform tissue. The membrane potentials of 10 different segments are shown in Figure 4.8. These segments are located in the same row in the center of the tissue, thus the distance to the anode and cathode is the same for each segment. The dashed lines represent the time when the cell recovers. All cells recover between approximately 180 and 320 ms after application of the electric field. Note the different shapes of the APs, as these are either prolonged or shortened due to the virtual electrodes.

time [ms]	$\mu_L = \mu_T = 1$ $\sigma_L = \sigma_T = 0$ FF $= 0$	$\mu_L = \mu_T = 1$ $\sigma_L = \sigma_T = 0.5$ FF $= 0$	$\mu_L = \mu_T = 1$ $\sigma_L = \sigma_T = 1$ FF $= 0$
0			
5			
10			
25			
50			
100			
200			
400			
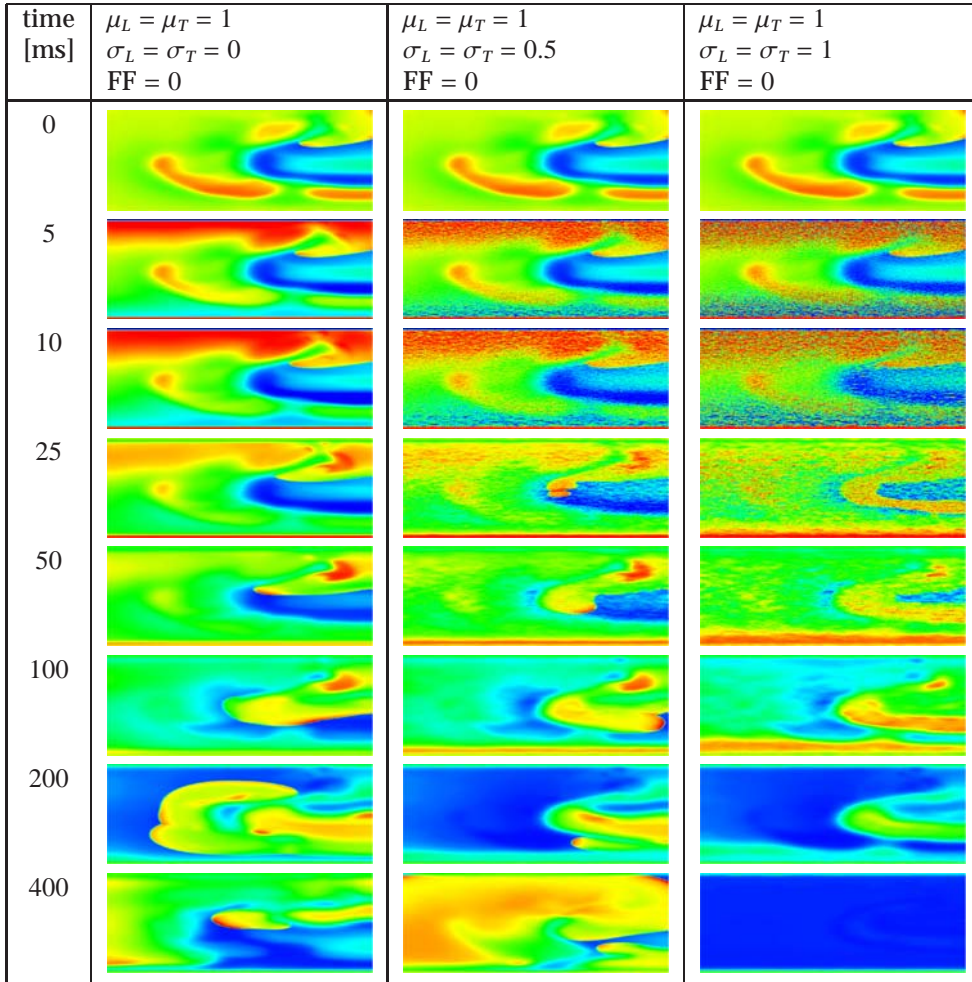
Figure 4.6: Unsuccessful and successful termination of a spiral wave in uniform (left) and nonuniform (center and right) tissue by means of defibrillation. The anode was a line electrode at the top and the cathode a line electrode at the bottom of the tissue. A uniform electric field was applied during 10 ms. Shown are the membrane potentials for different simulation times during and after field stimulation. Depolarized tissue is red/yellow/green and repolarized or hyperpolarized tissue is blue.

$\mu_L = \mu_T = 0.5$ $\sigma_L = \sigma_T = 1$ FF = 0.35		
1 ms	2 ms	3 ms
4 ms	5 ms	10 ms
25 ms	50 ms	100 ms
200 ms	300 ms	400 ms
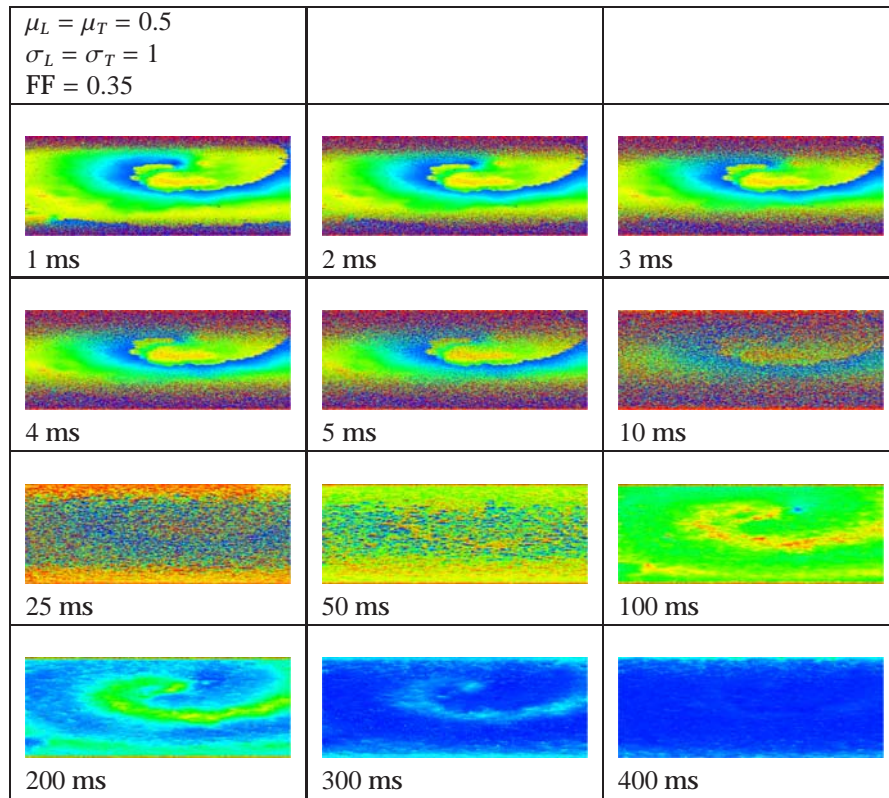
Figure 4.7: Termination of a spiral wave in remodeled tissue by means of defibrillation. The anode was a line electrode at the top and the cathode a line electrode at the bottom of the tissue. A uniform electric field was applied during 10 ms. Shown are the membrane potentials for different simulation times during and after field stimulation. Depolarized tissue is red/yellow/green and repolarized or hyperpolarized tissue is blue.
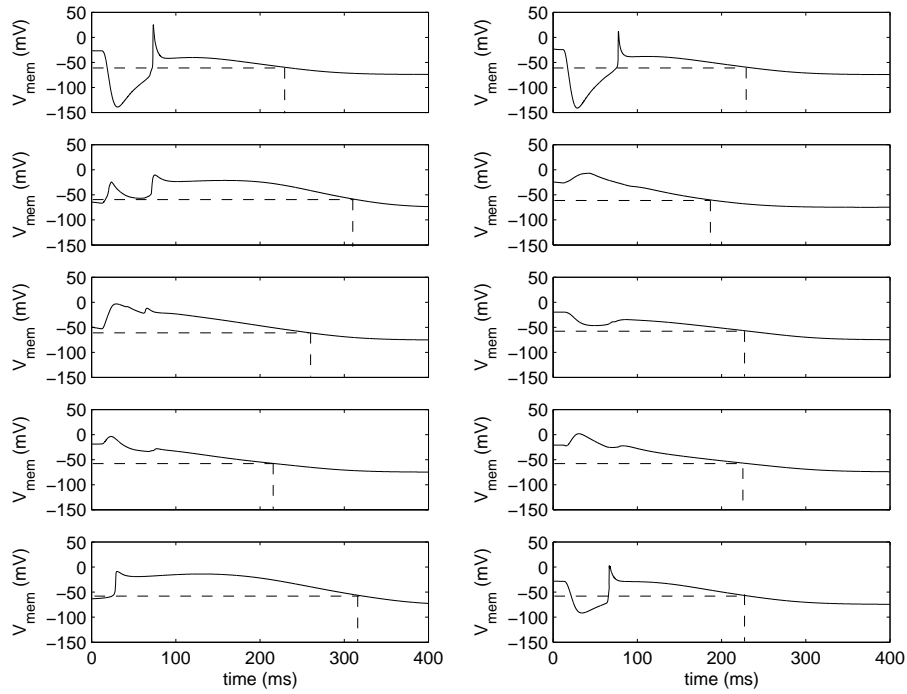
Figure 4.8: Prolonging and shortening of action potentials in remodeled tissue. Shown are the membrane potentials of 10 different segments lying on one line in the center of the tissue. The membrane potentials are shown starting 10 ms before application of the electric field. The dashed lines represent the recovery times.

This mechanism leads to total recovery of the tissue within a time window of approximately 140 ms, regardless of whether the nodes are depolarized or resting at the time the electric field is applied.

4.4 Discussion

4.4.1 Cellular Bidomain Model

To simulate cardiac electrical behavior the cardiac tissue is traditionally modeled either by a continuous model such as the bidomain equations [69] or a discontinuous model such as the parallel cable model [118]. The latter allows for the modeling of tissue at subcellular level. The parallel cables can be connected in a brickwall fashion as described in [118]. In recent studies to field stimulation, spatial heterogeneity is introduced in bidomain models in which the cells are subdivided and gap junctions are modeled explicitly [59, 60, 107]. In the Cellular Bidomain Model, the segments are not subdivided. Both the intracellular and extracellular domains can be viewed as a hexagonal grid of resistors. Nonuniformity is modeled by varying the intracellular resistances and decoupling is modeled by disconnecting some of the intracellular resistors randomly. Using a brickwall structure composed of segments of length 200 μm and width 80 μm and experimentally measured conductivities that are all scaled with the same factor, leads to conduction velocities that are in physiological range.

In the present study, the effects of a surrounding conductive bath and fiber curvature are not investigated. We expect that the results would not change qualitatively if the sheets of cardiac tissue were surrounded by a conductive bath (see e.g. the simulation study by Plank *et al.* [144]). The influence of fiber curvature when an electric field is applied has been thoroughly investigated in 2D and 3D by the group of Trayanova [46, 72, 159, 201, 202].

4.4.2 Virtual electrode polarization

By establishing an external electric field, virtual electrodes are formed which either depolarize or hyperpolarize regions in the cardiac tissue [222]. From our simulation results, we conclude that decoupling and nonuniform conductivity affects the virtual electrode polarization (VEP). In decoupled and nonuniform tissue virtual electrodes appear in the bulk of the tissue and depolarize all excitable parts of the tissue within short time. A spiral wave can be terminated when the excitable gap is depolarized and no excitable tissue is left.

4.4.3 Pathological tissue

We simulated pathological tissue by modeling diffuse fibrosis and remodeling of the gap junctions. An important difference between normal, nonuniform and remodeled tissue is the reduction in conduction velocity. Since the success of defibrillation depends on the fast depolarization of the entire tissue, a slower conduction velocity might lead to defibrillation failure. Virtual electrodes can occur near obstacles such as scars caused by infarction or surgical incisions [220]. If the virtual electrodes are not well-spread throughout the tissue, these obstacles might in fact form a substrate for arrhythmogenesis [220]. This mechanism can also be observed in Figure 4.2. The presence of virtual electrodes is determined by the location of non-conductive obstacles. Obstacles that are non-conductive in both domains lead to a different pattern of virtual electrode polarization compared with obstacles that are non-conductive in the intracellular domain only. In case of low conduction velocities, localized regions of depolarization might be a substrate for new fibrillating waves.

4.5 Conclusion

We have simulated sheets of normal and pathological atrial tissue to which an external electric field was applied. To introduce spatial heterogeneity and to simulate the effects of gap junction remodeling and diffuse fibrosis, local conductivities were varied throughout the tissue. Using this model, we investigated the role of nonuniform conductivities in relation to virtual electrode polarization on resting cardiac tissue as well as tissue in which spiral waves were induced. From the simulation results, we conclude that successful termination of spiral waves depends on the amount and spread of virtual electrodes. Compared with normal, nonuniform tissue, more virtual electrodes are present in the bulk of remodeled tissue. However, since the conduction velocity in remodeled tissue is lower, it takes more time to depolarize the entire tissue. We conclude that fast depolarization of the tissue after field stimulation may be explained by intracellular decoupling and spatial heterogeneity present in normal and pathological cardiac tissue. We demonstrated that termination of spiral waves by means of field stimulation can be achieved when the tissue is modeled as a nonuniform, anisotropic bidomain with active membrane behavior.

5

The role of the hyperpolarization-activated inward current I_f in arrhythmogenesis

N.H.L. Kuijpers, H.M.M. ten Eikelder, R.H. Keldermann,
T. Arts, and P.A.J. Hilbers

Abstract

Atrial fibrillation is the most common cardiac arrhythmia. Structural cardiac defects such as fibrosis and gap junction remodeling lead to a reduced cellular electrical coupling and are known to promote atrial fibrillation. It has been observed that the expression of the hyperpolarization-activated current I_f is increased under pathological conditions. Recent experimental data indicate a possible contribution of I_f to arrhythmogenesis. In this study, the role of I_f in impulse propagation in normal and in pathological tissue is investigated by means of computer simulations. The effect of diffuse fibrosis and gap junction remodeling is simulated by reducing cellular coupling nonuniformly. As expected, the conduction velocity decreases when cellular coupling is reduced. In the presence of I_f, the conduction velocity increases both in normal and in pathological tissue. In our simulations, ectopic activity is present in regions with increased expression of I_f and is facilitated by cellular uncoupling. We conclude that an increased I_f may facilitate propagation of the action potential. Hence, I_f may prevent conduction slowing and block. Overexpression of I_f may lead to ectopic activity, especially when cellular coupling is reduced under pathological conditions.

5.1 Introduction

Atrial fibrillation (AF) is the most common cardiac arrhythmia [133]. The prevalence of AF increases with age from 0.5% of people under the age of 60 to almost 10% of people over the age of 80 [92]. Related to the occurrence of AF is structural remodeling of the tissue, including increase of cell size, interstitial fibrosis, and gap junction remodeling [5]. These effects lead to the loss of electrical coupling between cardiac cells and are known to promote recurrence of AF episodes [6, 11]. Changes in gap junction distribution may be involved in the initiation and persistence of AF [88, 183, 209, 210].

Besides structural remodeling, electrophysiological remodeling is related to AF, including shorter atrial effective refractory periods (AERP), greater dispersion of atrial refractoriness, and atrial conduction delay [18]. However, even if AF initiation and AF perpetuation are facilitated by electrophysiological remodeling, the initiation of AF still requires a trigger [172]. Such a trigger may come from ectopic foci. Especially in the case of paroxysmal AF, episodes of atrial fibrillation are often triggered by ectopic foci that are located in the pulmonary veins [39]. The mechanism of focal activity leading to AF is, however, still unknown [39]. Two possible mechanisms are micro-reentry within the pulmonary veins [73] and spontaneous depolarization of cells located in the pulmonary veins [66].

The ionic current responsible for pacemaker activity of sino-atrial node cells and Purkinje fibers is the hyperpolarization-activated inward current I_f [42]. I_f channels are believed to be complexes of hyperpolarization-activated cyclic nucleotide-gated (HCN) channels [1]. I_f channels in atrial tissue are most likely heteromeric complexes composed of HCN4 and/or HCN2 [124, 128]. I_f conducts both K^+ and Na^+, with about a $3 : 1$ preference for K^+ [42]. It has some unusual features and is thereby known as the "funny" current [1, 42]. The first unusual feature is that I_f is activated by hyperpolarization with a threshold of approximately -40 to -50 mV in the sinus node [1] and about -65 mV in other myocardial cells [146]. The second unusual feature is that the fully activated current/voltage relation reverses near -10 to -20 mV in physiological solutions as a consequence of the channel's mixed permeability to Na^+ and K^+ [1]. The activation by hyperpolarization and permeability to Na^+ and K^+ are important properties with respect to the role of I_f in diastolic depolarization and spontaneous activity [1]. As opposed to earlier results [28, 76, 77, 228], it was recently observed by Michels *et al.* [128] that half-maximum activation of single-channel I_f is within the diastolic range of human atrial myocardium. These observations support a possible contribution of HCN-gated channels and I_f to arrhythmogenesis under pathological conditions [128].

I_f has been identified in cardiac tissue that is normally not capable of pacemaking, including human left ventricular myocytes [28, 77] and human atrial myocytes [25, 76, 146]. Interestingly, the expression of I_f in left ventricular myocytes of the rat increases with age [27]. Also, in ventricular myocytes of hypertrophied and failing hearts of the rat, the expression of I_f is increased and leads to diastolic depolarization in isolated myocytes [26, 27, 29]. Sartiani *et al.* [165] observed two action potentials of different HL-1 cells derived from the atria of a transgenic mouse. One of the action potentials showed spontaneous diastolic depolarization and the other a flat diastolic potential. A hyperpolarization-activated inward current was observed in the cell with a spontaneous diastolic depolarization phase, but not in the other cell [165]. Besides, they observed spontaneously beating cells in some regions of HL-1 cell cultures with a frequency varying between 1.3 and 5 Hz [165]. Since the beating stopped in the presence of I_f-blocker Cs^+, it is suggested that the spontaneous activity is caused by I_f [165]. However, whether I_f may favor spontaneous diastolic depolarization in individual human atrial myocytes remains to be determined [76].

Previous simulation studies to investigate conduction velocity and arrhythmia in structurally remodeled tissue did not include I_f. Fast and Kléber showed that conduction slowing and block may occur at an abrupt tissue expansion [55]. Shaw and Rudy applied a multicellular monodomain fiber model to investigate conduction slowing and block in relation to reduced membrane excitability and decreased gap junction coupling [170, 171]. Street and Plonsey applied a multi-fiber bidomain model to investigate conduction slowing and block in regions of passive, connective tissue representing infarcted regions [189]. Recent large-scale simulation studies to atrial arrhythmia apply detailed models of the ionic membrane currents, electrophysiological remodeling, anisotropy, and 3D geometry [67, 83, 84, 104, 213, 214, 215].

The aim of the present simulation study is to investigate the influence of I_f on impulse propagation and ectopic activity under normal and pathological conditions. We apply a discrete bidomain model with active membrane behavior to represent the cardiac tissue. Diffuse fibrosis and gap junction remodeling are modeled by decreasing intracellular coupling at random throughout the tissue. The amount of I_f current and of cellular uncoupling are varied to investigate their respective influence on the conduction velocity and ectopic activity.

5.2   Methods

We have developed a new discrete bidomain model, the Cellular Bidomain Model, which we previously applied to investigate virtual electrode polarization during external field stimulation under normal and pathological conditions [109]. Active membrane behavior as well as intracellular coupling and interstitial currents are described by this model. Similar to the volume averaging approach of the continuous bidomain model, each point in the tissue is assigned both an intracellular and an extracellular potential [69, 189]. In our model, the bidomain is subdivided in segments and the same state is assumed everywhere within a single segment, which is why we call it a discrete bidomain model, or Cellular Bidomain Model [109]. Although a segment may represent a single myocyte, we usually apply somewhat larger segments such that less computational power is required to simulate sheets of cardiac tissue. The segment sizes may vary as well as the electrical coupling between adjacent segments. Pathology such as fibrosis and gap junction remodeling can be modeled by reducing the intracellular coupling between the segments. Furthermore, active membrane behavior can be varied throughout the tissue by assigning different membrane properties to individual segments.

5.2.1   Cellular Bidomain Model

In the Cellular Bidomain Model, the structure of the cardiac tissue is represented by a *graph* consisting of nodes and edges, where a *node* represents a segment and an *edge* the electrical coupling between the segments. Let $\mathcal{N}$ represent the set of nodes and $\mathcal{E}$ the set of edges connecting the nodes. Each node has its own membrane model describing the ionic membrane currents. The state of each node $n \in \mathcal{N}$ is defined by the intracellular potential V_{int}^n and the extracellular potential V_{ext}^n. The membrane potential V_{mem} for node n is defined as $V_{mem}^n = V_{int}^n - V_{ext}^n$. Edges define the conductance for intracellular and extracellular currents between two adjacent nodes. We distinguish the *intracellular* and *extracellular* conductance, which are denoted by σ_{int} and σ_{ext}, respectively (Figure 5.1).

It is assumed that for each edge $(n, m) \in \mathcal{E}$ it holds $\sigma_{int}^{(n,m)} > 0$ and $\sigma_{ext}^{(n,m)} > 0$. The intracellular and extracellular currents flowing from node n to node m are denoted by $I_{int}^{n \to m}$ and $I_{ext}^{n \to m}$, and are given by Ohm's law:

$$I_{int}^{n \to m} = (V_{int}^n - V_{int}^m)\,\sigma_{int}^{(n,m)}, \qquad (5.1)$$
$$I_{ext}^{n \to m} = (V_{ext}^n - V_{ext}^m)\,\sigma_{ext}^{(n,m)}. \qquad (5.2)$$

The intracellular current entering node n coming from all adjacent nodes a, $(a, n) \in \mathcal{E}$, is denoted by I_{int}^n and the extracellular current by I_{ext}^n. These currents
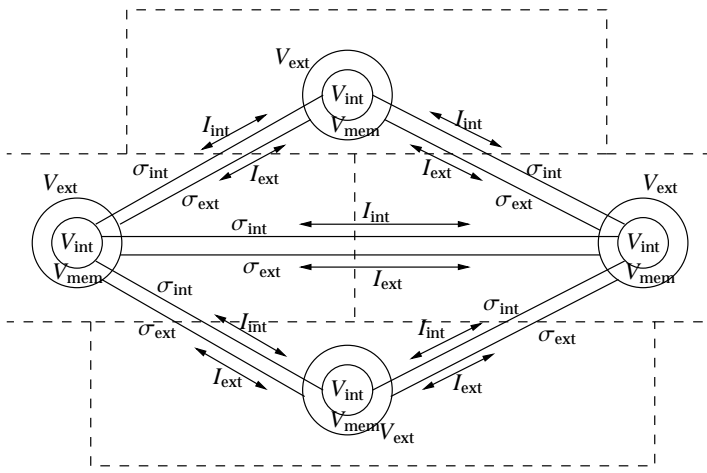
Figure 5.1: Graphical representation of a simulation graph. Each node represents a rectangular segment of cardiac tissue. The state of each node is represented by the intracellular potential V_{int}, the extracellular potential V_{ext}, and the membrane potential V_{mem}. Electrical coupling between the nodes is indicated by the intracellular and interstitial conductances denoted by σ_{int} and σ_{ext}. The intracellular and interstitial currents flowing between the nodes are represented by the arrows labeled with I_{int} and I_{ext}.

are defined by

$$I_{\text{int}}^n = \sum_{(a,n)\in\mathcal{E}} I_{\text{int}}^{a\to n}, \tag{5.3}$$

$$I_{\text{ext}}^n = \sum_{(a,n)\in\mathcal{E}} I_{\text{ext}}^{a\to n}. \tag{5.4}$$

According to Kirchhoff's law, current entering a node as intracellular current must flow to the interstitial space as transmembrane current and leave the node as extracellular current. By choosing the transmembrane current, denoted by I_{trans}, flowing from the intracellular space to the interstitial space, we obtain for node n

$$I_{\text{trans}}^n = I_{\text{int}}^n = -I_{\text{ext}}^n. \tag{5.5}$$

The transmembrane current is the sum of capacitive and ionic currents, i.e.,

$$I_{\text{trans}}^n = C_{\text{mem}}^n \frac{dV_{\text{mem}}^n}{dt} + S_{\text{mem}}^n I_{\text{ion}}(V_{\text{mem}}^n, \mathbf{q}^n), \tag{5.6}$$

where C_{mem}^n represents the membrane capacitance of node n in μF and S_{mem}^n the membrane surface in cm^2. The ionic membrane current of node n, denoted

by $I_{ion}(V_{mem}^n, \mathbf{q}^n)$, is expressed in μA per cm^2 membrane surface and depends on the membrane potential V_{mem} as well as gating variables and ionic concentrations denoted by the vector $\mathbf{q}^n$.

To model the ionic currents in the present study, we apply a modified version of the Courtemanche-Ramirez-Nattel model of the human atrial action potential [37]. We extended this model with the hyperpolarization-activated current I_f and adapted the I_{Na} kinetics as described below. The total ionic current is given by

$$I_{ion} = I_{Na} + I_{K1} + I_{to} + I_{Kur} + I_{Kr} + I_{Ks} + I_{Ca,L} + I_{p,Ca} + I_{NaK} + I_{NaCa} + I_{b,Na} + I_{b,Ca} + I_f. \quad (5.7)$$

The ionic and pump currents, including the handling of the intracellular Ca^{2+} concentration ($[Ca^{2+}]_i$) by the sarcoplasmic reticulum (SR), are described in Ref. [37]. The model keeps track of $[Ca^{2+}]_i$ as well as $[Na^+]_i$ and $[K^+]_i$, while the extracellular concentrations $[Ca^{2+}]_e$, $[Na^+]_e$, and $[K^+]_e$ are constant [37].

To solve the equations of the Cellular Bidomain Model, no-flux boundary conditions are assumed for both the intracellular and the interstitial domain. For the numerical integration scheme we refer to Chapter 2. Here, we describe how the pacemaker current I_f is modeled and the inward Na$^+$ current I_{Na} is modified. Next, it is described how normal and pathological atrial tissue is modeled. Furthermore, the simulation protocol for the present study is described.

5.2.2 Hyperpolarization-activated inward current I_f

The I_f current is expressed in pA/pF and is defined by

$$I_f = G_f \, p_o (V_{mem} - E_f), \quad (5.8)$$

where G_f is the maximum membrane conductance for I_f in nS/pF, p_o the fraction of channels in the open state, and E_f the reversal potential. The dynamics of p_o is defined by

$$\frac{dp_o}{dt} = \alpha_{p_o}(1 - p_o) - \beta_{p_o} \, p_o, \quad (5.9)$$

where α_{p_o} and β_{p_o} are defined as in DiFrancesco [43]:

$$\alpha_{p_o} = 2.83 \times 10^{-7} \, \exp\left(-\frac{V_{mem}}{15.08}\right) \quad (5.10)$$

$$\beta_{p_o} = 8.31 \times 10^{-2} \, \exp\left(\frac{V_{mem}}{15.08}\right). \quad (5.11)$$

Moroni *et al.* [129] describe human I_f kinetics based on HCN2 only. Ludwig *et al.* [124] concluded that pacemaker activity in the human heart is a

combined effect of HCN2 and HCN4 channels. Michels *et al.* [128] observed that single-channel characteristics of I_f in human atrial myocytes resemble those of HCN4 or HCN2 + HCN4. Since HCN4 kinetics are slower than HCN2 kinetics [124, 129], and the kinetics obtained by DiFrancesco [43] for rabbit sino-atrial nodal I_f are slower than the HCN2 kinetics obtained by Moroni *et al.* [129], we decided to model activation parameter p_o as described by DiFrancesco [43]. Using these parameters, the half activation potential is −95 mV and only a small fraction of I_f channels will be open in diastolic range (above −81 mV) [43].

The reversal potential E_f is defined as in Moroni *et al.* [129]:

$$E_f = \frac{RT}{F} \ln \left(\frac{[K^+]_e + (P_{Na}/P_K)[Na^+]_e}{[K^+]_i + (P_{Na}/P_K)[Na^+]_i} \right), \tag{5.12}$$

where P_{Na} and P_K are permeabilities to Na^+ and K^+, R is the universal gas constant, T is the temperature (310 K [37]), and F is Faraday's constant. The ratio (P_{Na}/P_K) is 0.41 [129]. In the model of Courtemanche *et al.*, the extra-cellular ion concentrations are constant ($[K^+]_e = 5.4$ mM and $[Na^+]_e = 140$ mM), while the intracellular ion concentrations are dynamic ($[K^+]_i = 139$ mM and $[Na^+]_i = 11.2$ mM when $V_{mem} = -81.2$ mV) [37]. We have adapted the model to take the influence of I_f on $[Na^+]_i$ and $[K^+]_i$ into account as described by DiFrancesco and Noble [45]. With the parameters defined in the Courtemanche-Ramirez-Nattel model, the reversal potential E_f is approximately −22 mV.

5.2.3 Fast inward Na^+ current I_{Na}

I_{Na} is modeled in the Courtemanche-Ramirez-Nattel model as in the Luo-Rudy phase-2 model [125], and is given by

$$I_{Na} = G_{Na} m^3 h j (V_{mem} - E_{Na}). \tag{5.13}$$

Here, G_{Na} is the maximum I_{Na} conductance (7.8 nS/pF) and E_{Na} is the equilibrium potential for Na^+ [37]. Further, m is the fast activation variable, and h and j are the fast and slow inactivation variables [37, 125]. To obtain diastolic action potentials, we adapted the I_{Na} kinetics by doubling the forward rates α_m and α_h of the fast gating variables m and h (Appendix A). With this change, the I_{Na} channels open and diastolic action potentials occur with a basic cycle length (BCL) of 1.5 s for $G_f = 0.27$ nS/pF. The action potential morphology and duration remain unchanged when a stimulus current of 20 pA/pF is applied during 2 ms as in Ref. [37].

5.2.4 Modeling normal atrial tissue

The modifications of the I_{Na} kinetics have effect on the maximum upstroke velocity $(dV_{mem}/dt)_{max}$ and, thus, on the conduction velocity. In our simulations, $(dV_{mem}/dt)_{max}$ increased from 167 V/s to 288 V/s. To obtain conduction velocities similar to those reported by Spach and Boineau (0.48 m/s longitudinal and 0.15 m/s transverse) [179], we have scaled the conductivity parameters as reported by Clerc [33, 69] with a factor 0.6. The bidomain parameters used in the present study for normal atrial tissue are listed in Table 5.1.

To obtain criteria for the size of individual segments, we apply cable theory and consider subthreshold behavior along a fiber as described in Ref. [69]. The application of a stimulus current produces a spatial change in the membrane potential along the fiber. For subthreshold behavior, the transmembrane current I_{trans} can be described by

$$I_{trans} = C_{mem} \frac{dV_{mem}}{dt} + \frac{V_{mem}}{R_{mem}}, \tag{5.14}$$

where R_{mem} is the membrane resistance in $\Omega \cdot cm^2$ and C_{mem} the membrane capacitance in $\mu F/cm^2$ [69]. The *steady-state* response of V_{mem} along the fiber to a subthreshold current at position $x = 0$ is exponential and can be described by

$$V_{mem}(x) = V_{mem}(0) \, \exp\left(-\frac{x}{\lambda}\right), \tag{5.15}$$

where $V_{mem}(x)$ is the membrane potential on distance x from the stimulus site, $V_{mem}(0)$ the membrane potential at the stimulus site ($x = 0$), and λ the length constant [69]. Using the bidomain parameters listed in Table 5.1, the length constants in longitudinal and transverse direction, denoted by λ_x and λ_y, can be expressed as

$$\lambda_x = \sqrt{\frac{R_{mem} \, g_{int}^x \, g_{ext}^x}{\chi \, (g_{int}^x + g_{ext}^x)}} \tag{5.16}$$

and

$$\lambda_y = \sqrt{\frac{R_{mem} \, g_{int}^y \, g_{ext}^y}{\chi \, (g_{int}^y + g_{ext}^y)}}, \tag{5.17}$$

where, as before, R_{mem} is the membrane resistance in $\Omega \cdot cm^2$ [69, 189]. We estimated R_{mem} for the modified Courtemanche-Ramirez-Nattel model by applying a subthreshold stimulus current of 0.3 pA/pF during 300 ms. R_{mem} was estimated using

$$\frac{V_{mem} - V_{rest}}{R_{mem}} = I_{ion} \tag{5.18}$$

Table 5.1: Bidomain parameters for atrial tissue

Parameter	Definition	Value
g_{int}^x	Longitudinal intracellular conductivity	1.0440 mS/cm
g_{int}^y	Transverse intracellular conductivity	0.1158 mS/cm
g_{ext}^x	Longitudinal extracellular conductivity	3.7500 mS/cm
g_{ext}^y	Transverse extracellular conductivity	1.4160 mS/cm
C_{mem}	Membrane capacitance	1.0 μF/cm^2
χ	Surface-to-volume ratio	2000 cm^{-1}

for $V_{\mathrm{rest}} = -81$ mV and V_{mem} ranging from -80 mV to -70 mV. We found values for R_{mem} between 22 and 38 $\Omega \cdot$cm^2. For these values of R_{mem}, λ_x is in between 0.095 and 0.125 cm, and λ_y is in between 0.034 cm and 0.045 cm. To obtain accurate simulation results, the tissue is modeled as a brickwall with segments of length 200 μm and width 80 μm. Hence, the segment sizes are approximately one fifth of the length constant in both directions.

5.2.5 Modeling pathological tissue

In the Cellular Bidomain Model, a distinction is made between *longitudinal* coupling (along the fiber direction) and *transverse* coupling (side-to-side). The effects of gap junction remodeling are simulated by varying the intracellular conductances nonuniformly throughout the tissue. A normal distribution with parameters (μ, σ) is applied to determine a factor by which the initial values for the intracellular conductances (σ_{int}) are multiplied for each edge. Negative factors and factors larger than one are replaced by zero and one, respectively. The average and standard deviation of the gap junction remodeling factor in longitudinal direction are denoted by μ_L and σ_L, respectively, and the average and standard deviation in transverse direction by μ_T and σ_T, respectively.

Fibrosis causes the loss of side-to-side cell coupling, which can result in a disturbed wavefront propagation and may isolate groups of myocytes [180]. Since side-to-side coupling is affected, the main effect of fibrosis is a reduction of the transverse conduction velocity [179]. We model the effect of diffuse fibrosis [93] by randomly removing some of the intracellular conductances in transverse direction, i.e., σ_{int} becomes zero for a fraction of the edges in transverse direction. This fraction is called *fibrosis fraction* and is abbreviated by FF.

5.2.6 Simulation protocol

Single cell simulations A series of single cell simulations over a period of 4 s was performed with varying expression of I_f (G_f = 0.08, 0.16, 0.31, and 0.55 nS/pF). Initially, the membrane state was equal to the resting state of a human atrial cell without I_f (V_{mem} = −81 mV) [37]. No stimulus current was applied in these simulations.

Gap junction remodeling and fibrosis To investigate the effect of gap junction remodeling and fibrosis on the longitudinal conduction velocity θ_L and the transverse conduction velocity θ_T, three series of simulations were performed on a 1 cm × 0.4 cm sheet of atrial tissue composed of uniform 200 μm × 80 μm segments. An action potential front was initiated by stimulating the left-most segments of each row (first series) or the upper row of segments (second and third series). The segments were stimulated by adding a stimulus current of 100 pA/pF to the ionic membrane currents until the membrane was depolarized. In the first series, μ_L ranged from 0.1 through 1, μ_T = 1, σ_L = 0, 0.5, and 1, and σ_T = 0. In the second series, μ_L = 1, μ_T ranged from 0.1 through 1, σ_L = 0, and σ_T = 0, 0.5, and 1. In the third series, fibrosis fraction FF ranged from 0 through 0.9. No gap junction remodeling was applied in the third series. θ_L and θ_T were determined by averaging the velocity of the action potential front along nine parallel tracks of length 0.8 cm in longitudinal direction and 0.32 cm in transverse direction.

Uniform expression of I_f To investigate the influence of a uniform expression of I_f on θ_L in normal, remodeled, and fibrotic tissue, five series of simulations were performed on a 2 cm × 0.5 cm sheet of atrial tissue with segment lengths varied randomly between 150 and 250 μm and width 80 μm. Two types of remodeled tissue were simulated by applying gap junction remodeling (μ_L = μ_T = 0.75 and σ_L = σ_T = 0.25, and μ_L = μ_T = 0.5 and σ_L = σ_T = 1). Two types of fibrotic tissue were simulated by applying both gap junction remodeling and fibrosis (FF = 0.35). The expression of I_f ranged from 0.0 through 0.6 nS/pF. The left-most segments of the center fibers were stimulated at the start of the simulation. Stimulation was repeated after 800 ms. Four independent measurements of θ_L were obtained by measuring over four consecutive tracks of length 0.4 cm along the central fiber.

Regional expression of I_f To investigate the critical size of an ectopic pacemaker in relation to cellular coupling, a series of simulations was performed on a 1 cm × 0.04 cm strip of tissue. I_f was present in the right part of the strip

($G_f = 0.3$ nS/pF), but not in the left part. The size of the region in which I_f was present was varied between 10% and 50% of the tissue. Uniform, reduced cellular coupling was simulated ($\mu_L = \mu_T$ ranged from 0.1 through 1, and $\sigma_L = \sigma_T = 0$). Each simulation lasted 5 s. No stimulus current was applied. In case ectopic activity occurred, the BCL was determined for each segment by averaging the interval times between consecutive depolarizations.

Nonuniform expression of I_f To compare ectopic activity in normal and in remodeled atrial tissue when the expression of I_f is nonuniform, two series, A and B, of 12 simulations were performed on a 1 cm $\times$ 0.4 cm sheet of tissue composed of uniform 200 μm $\times$ 80 μm segments. In series A, G_f was uniformly increased from 0.27 nS/pF (BCL 1.5 s) on the left to 0.58 nS/pF (BCL 0.75 s) on the right. In series B, G_f was randomly distributed throughout the tissue with average 0.42 nS/pF and standard deviation 0.19 nS/pF. G_f was bound by a minimum of 0.27 nS/pF (BCL 1.5 s) and a maximum of 0.58 nS/pF (BCL 0.75 s). Besides normal tissue, various types of remodeled tissue were simulated ($\mu_L = \mu_T = 0.5$ and 0.3, and $\sigma_L = \sigma_T = 0.0$, 0.5, 1.0, 1.5, and 2.0) as well as fully uncoupled tissue ($\mu_L = \mu_T = 0.0$ and $\sigma_L = \sigma_T = 0.0$). The distribution of G_f was exactly the same for all simulations of a series, thus, the simulations of one series only differ in cellular coupling. Each simulation lasted 5 s. No stimulus current was applied. The BCL was determined for each segment by averaging the interval times between consecutive depolarizations.

Large-scale simulations To investigate the effect of a nonuniform expression of I_f under normal and pathological conditions, three large-scale simulations were performed on an 8 cm $\times$ 3 cm sheet of atrial tissue with nonuniform expression of I_f. The width of the segments was 80 μm, while the length was varied using a normal distribution with average 200 μm and standard deviation 50 μm. The segment lengths were bound by a minimum of 150 μm and a maximum of 250 μm. G_f was 0.27 nS/pF in the leftmost 6.4 cm of tissue and G_f was varied in the rightmost 1.6 cm of the tissue with average 0.42 nS/pF and standard deviation 0.19 nS/pF. G_f was bound by a minimum of 0.27 nS/pF (BCL 1.5 s) and a maximum of 0.58 nS/pF (BCL 0.75 s). The leftmost segments of the center fibers were stimulated at the start of the simulation. Stimulation was repeated each 800 ms.

To simulate pathological tissue, two simulations were performed on the same 8 cm $\times$ 3 cm sheet of atrial tissue with the same distribution of I_f. The fibrosis fraction FF was 0.35. After the first stimulation, the action potential propagated from left to right such that the entire tissue was depolarized after

approximately 250 ms. Just before the second stimulation at simulation time 800 ms, the intracellular conductances were changed to simulate gap junction remodeling with average $\mu_L = \mu_T$ equal to 0.5 and 0.3, and standard deviation $\sigma_L = \sigma_T$ equal to 1 and 2, respectively. The second simulation of pathological tissue lasted 15 s of simulation time.

5.3 Results

5.3.1 Single cell simulations

In Figure 5.2, the membrane potential V_{mem}, the hyperpolarization-activated inward current I_f, the time-independent K^+ current I_{K1}, and conductance $g_f = G_f p_o$ are presented. for $G_f = 0.08, 0.16, 0.31,$ and 0.55 nS/pF. Spontaneous diastolic action potentials occurred for $G_f = 0.31$ and 0.55 nS/pF with BCL 1260 ms and 760 ms, respectively. $G_f = 0.08$ and 0.16 nS/pF resulted in a depolarized steady-state membrane potential of -74.4 mV and -70.8 mV, respectively. When comparing the ionic currents for $G_f = 0.08$ nS/pF with $G_f = 0.16$ nS/pF, the inward current I_f was increased from -0.24 to -0.29 pA/pF and the rectifier current I_{K1} was increased by the same magnitude from 0.45 to 0.50 pA/pF (Figure 5.2). The changes in the remaining currents were marginal (not shown). The change in I_{K1} is expected, because I_{K1} is voltage dependent with a maximum current size of 0.5 pA/pF for $V_{mem} = -67$ mV [37]. Thus, for increasing I_f, the membrane potential rises and I_{K1} increases. For G_f smaller than 0.27 nS/pF, a steady-state membrane potential is reached at which the depolarizing I_f current is compensated by the rectifying I_{K1} current. The fraction of I_f channels being in the open state $p_o = g_f/G_f$ is of the order of a few percent.

5.3.2 Gap junction remodeling and fibrosis

In Figure 5.3, the longitudinal and transverse conduction velocities θ_L and θ_T are presented for varying μ_L and $\mu_T = 1$ (top), $\mu_L = 1$ and varying μ_T (center) and varying FF (bottom). For larger values of σ_L and σ_T, the conduction velocities are smaller for large μ_L and μ_T, while larger conduction velocities are obtained for small μ_L and μ_T. This is caused by the requirement that the factors by which σ_{int} is multiplied must lie between 0 and 1. The average of these factors is, thus, smaller than μ_L or μ_T for $\mu_L, \mu_T > 0.5$ and larger than μ_L or μ_T for $\mu_L, \mu_T < 0.5$.

The solid lines indicate θ_L and θ_T predicted by cable theory. For noncurved action potential fronts, θ_L and θ_T are proportional to the length constants λ_x and λ_y (equations (5.16) and (5.17)) [69, 189]. The prediction of θ_L using cable
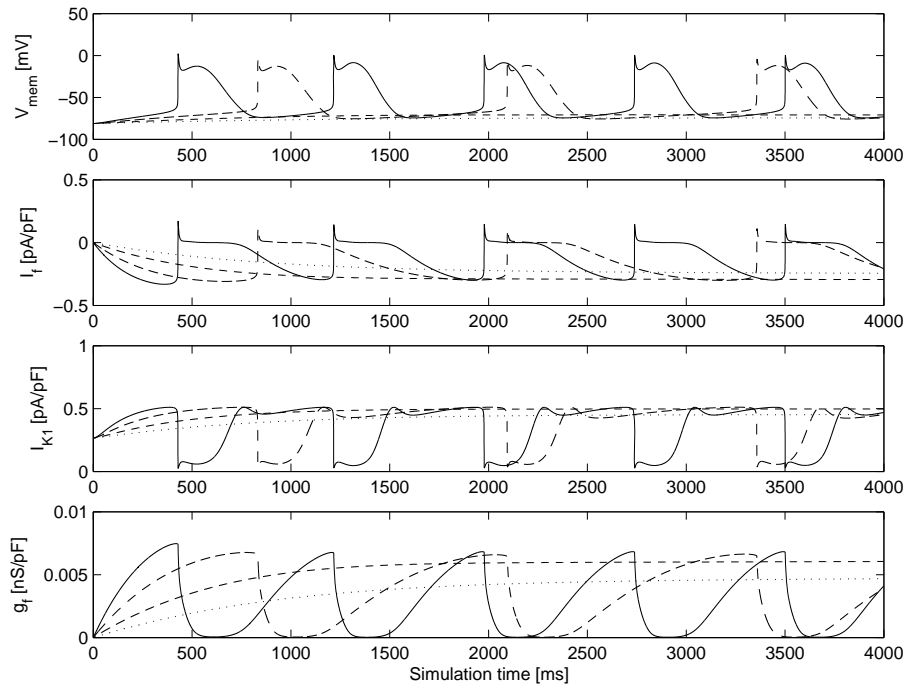
Figure 5.2: Membrane potential V_{mem} (mV), hyperpolarization-activated inward current I_f (pA/pF), time-independent rectifier K$^+$ current I_{K1} (pA/pF), and conductance $g_f = G_f\, p_o$ (nS/pF) for single cell simulations with different G_f values: dotted $G_f = 0.08$ nS/pF, short dash $G_f = 0.16$ nS/pF, long dash $G_f = 0.31$ nS/pF, solid $G_f = 0.55$ nS/pF. No stimulus current was applied. Initially, the membrane state was equal to the resting state of a human atrial cell without I_f ($V_{mem} = -81$ mV).
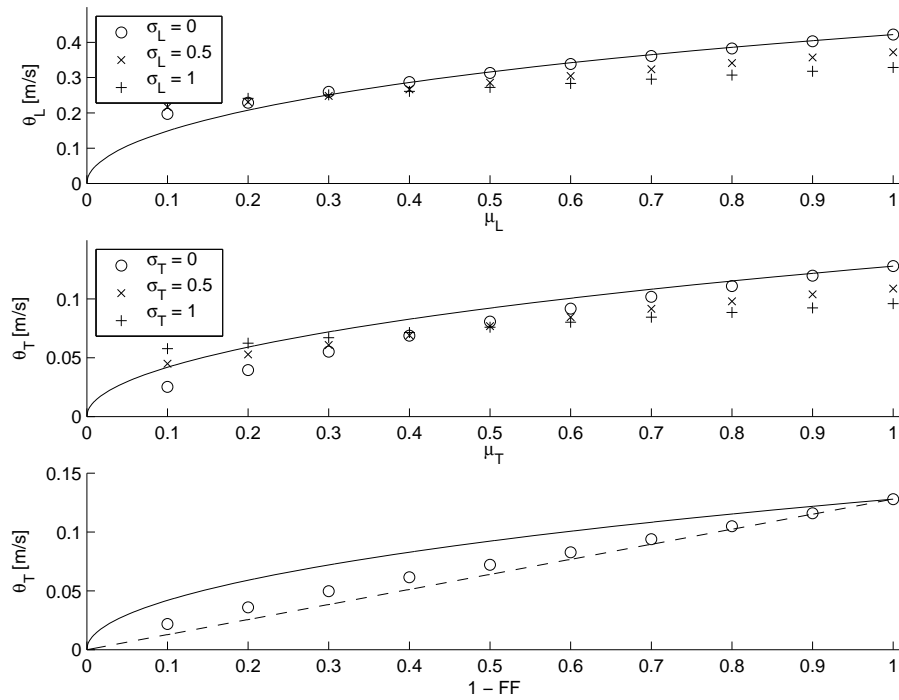
Figure 5.3: Effect of gap junction remodeling and fibrosis on the conduction velocity. Top: longitudinal conduction velocity θ_L for varying μ_L, $\mu_T = 1$, and $\sigma_T = 0$. Center: transverse conduction velocity θ_T for varying μ_T, $\mu_L = 1$, and $\sigma_L = 0$. Bottom: transverse conduction velocity θ_T for varying fibrosis fraction FF, $\mu_L = \mu_T = 1$, and $\sigma_L = \sigma_T = 0$. The solid lines represent θ_L and θ_T predicted by cable theory for the continuous bidomain model. The dashed line in the bottom figure represents θ_T for a linear descent.

theory is accurate for $\sigma_L = 0$ and $\mu_L \geq 0.3$. Cable theory overestimates θ_T for both transverse gap junction remodeling and fibrosis. As indicated by the dashed line, the effect of fibrosis is better estimated assuming a linear descent of θ_T.

A reduction of 30% in θ_L due to gap junction remodeling in rat ventricular tissue was reported by Uzzaman *et al.* [206]. A similar reduction of θ_L in our model is obtained for $\mu_L = 0.5$ and $\sigma_L = 0.5$. Spach and Dolber observed transverse conduction velocities related to uncoupling of side-to-side connections as low as 0.085 m/s in human cardiac tissue of adults over age 50 [180]. In Figure 5.3, it can be observed that such low values for θ_T in our model can be obtained for fibrosis fraction FF between 0.3 and 0.4.

5.3.3   Uniform expression of I_f

In Figure 5.4, the longitudinal conduction velocity θ_L versus G_f after the second stimulation is presented for five different types of tissue. The error bars indicate the standard deviation. A similar increase in θ_L is obtained for normal, remodeled, and fibrotic tissue. For G_f above 0.3 nS/pF, the increase in θ_L is approximately 0.04 m/s for all types of tissue. Compared with the conduction velocity in tissue without I_f, this increase is about 20% for remodeled tissue ($\mu_L = \mu_T = 0.5$ and $\sigma_L = \sigma_T = 1$, Figure 5.4). Note that, although for G_f above 0.27 nS/pF spontaneous diastolic action potentials can occur, the increase in conduction velocity for G_f below 0.5 nS/pF is caused by a more depolarized diastolic membrane potential. For values of G_f above 0.5 nS/pF ectopic pacemaking with BCL less than 800 ms occurred and the pacemaker at the stimulation site was captured (results not shown).

5.3.4   Regional expression of I_f

In Table 5.2, average BCLs for various $\mu_L = \mu_T$ and size of region with I_f are presented. Region size is indicated as a percentage of the total tissue. A dash means no ectopic activity occurred. In these simulations, the current generated by the I_f channels was spread over the entire tissue such that the threshold was not reached in any of the segments. For comparison, $G_f = 0.3$ nS/pF in single cell simulations leads to an average BCL of 1331.9 ms. In Table 5.2 it can be observed that when I_f is present in 50% of the tissue, ectopic activity occurs in normal atrial tissue. In tissue with reduced cellular coupling, smaller regions with expression of I_f lead to ectopic activity. Furthermore, the BCL decreases when cellular coupling decreases.
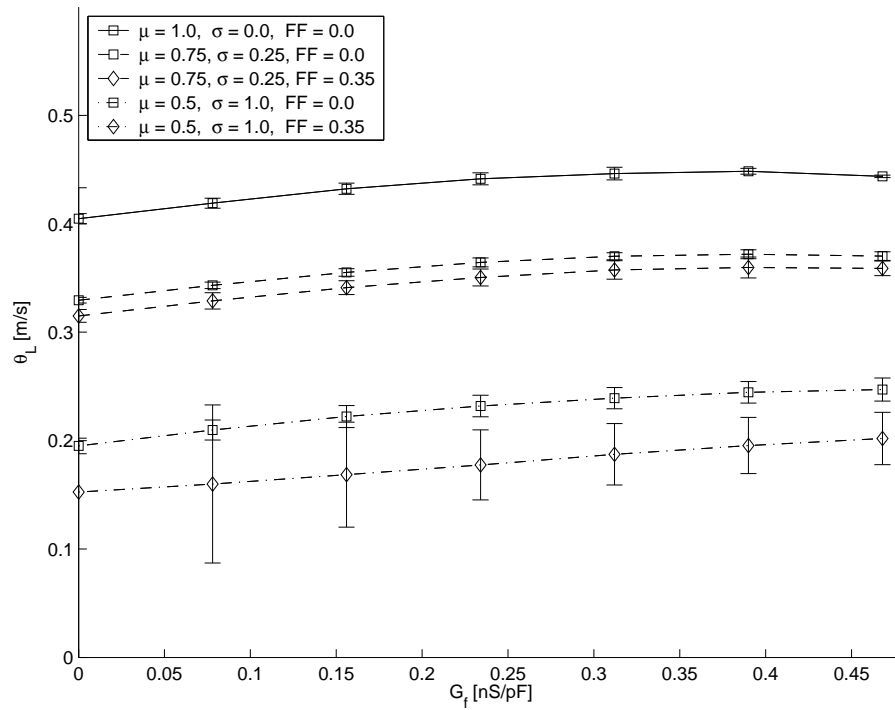
Figure 5.4: Longitudinal conduction velocity θ_L for normal, remodeled, and fibrotic atrial tissue. I_f is uniform and the expression of I_f is indicated by maximum conductance G_f. The error bars indicate the standard deviation of four independent measurements of θ_L along the same fiber.

Table 5.2: BCL in ms for regional expression of I_f

$\mu_L = \mu_T$	10%	20%	30%	40%	50%
0.1	-	1468.2	1365.3	1347.0	1341.2
0.2	-	-	1441.9	1372.0	1353.7
0.3	-	-	1566.8	1411.7	1367.9
0.4	-	-	-	1460.8	1390.5
0.5	-	-	-	1523.1	1416.1
0.6	-	-	-	1617.1	1444.7
0.7	-	-	-	2511.2	1476.8
0.8	-	-	-	-	1513.3
0.9	-	-	-	-	1557.2
1.0	-	-	-	-	1616.3

5.3.5 Nonuniform expression of I_f

In Table 5.3, the tissue properties, average BCLs and standard deviation of BCLs for the gradual increase of I_f (series A) and random distribution of I_f (series B) are presented. In both series, the average BCL decreases when coupling is reduced. In case coupling is nonuniformly reduced, the BCLs are even smaller. The standard deviation of the BCLs is smaller for coupled tissue compared with fully uncoupled tissue ($\mu_L = \mu_T = 0.0$). Due to coupling, the segments fire with similar frequencies (frequency entrainment [23]). By inspecting the times of activation we found that when coupling is increased, the segments not only fire with similar frequencies, but also at similar times (waveform entrainment [23]). The larger standard deviation of BCL in less coupled tissue is mainly caused by a few nonsynchronized segments that fire at their own BCL.

5.3.6 Large-scale simulations

In Figure 5.5 (left), the membrane potentials are presented for normal atrial tissue after the second stimulation. Note that, although the cardiac tissue is modeled as an irregular brickwall, the curvature of the wavefront is smooth and ellipsoidal, confirming that the segments are small enough to represent normal atrial tissue. The conduction velocities $\theta_L = 0.42$ m/s and $\theta_T = 0.13$ m/s as well as the anisotropy ratio $\theta_L/\theta_T = 3.3$ are similar to the results reported by Spach and Boineau ($\theta_L = 0.48$ m/s, $\theta_T = 0.15$ m/s, and $\theta_L/\theta_T = 3.2$) [179].

time [ms]	$\mu_L = \mu_T = 1$ $\sigma_L = \sigma_T = 0$ FF = 0 $\theta_L = 0.42$ m/s $\theta_T = 0.13$ m/s	$\mu_L = \mu_T = 0.5$ $\sigma_L = \sigma_T = 1$ FF = 0.35 $\theta_L = 0.19$ m/s $\theta_T = 0.05$ m/s	$\mu_L = \mu_T = 0.3$ $\sigma_L = \sigma_T = 2$ FF = 0.35 $\theta_L = 0.12$ m/s $\theta_T = 0.03$ m/s
800			
850			
900			
950			
1000			
1100			
1200			
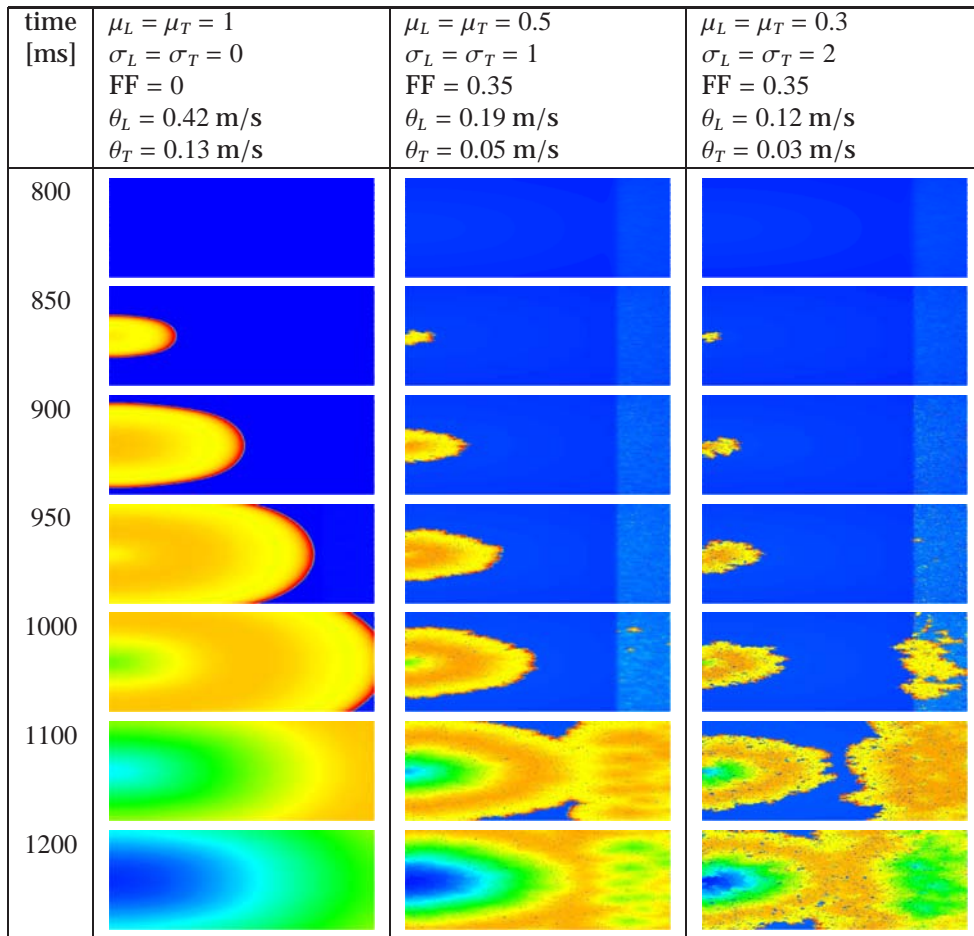
Figure 5.5: Simulation of normal (left) and pathological (center and right) atrial tissue with increased, nonuniform I_f in the right part of the tissue. The membrane potential is shown after the second stimulation at 800 ms. Just excited tissue is red, depolarized tissue is yellow or green, and repolarized tissue is blue.

time [ms]	$\mu_L = \mu_T = 0.3$ $\sigma_L = \sigma_T = 2$ FF = 0.35	time [ms]	$\mu_L = \mu_T = 0.3$ $\sigma_L = \sigma_T = 2$ FF = 0.35
1120		6810	
1950		8440	
2770		10060	
3580		11690	
4390		14980	
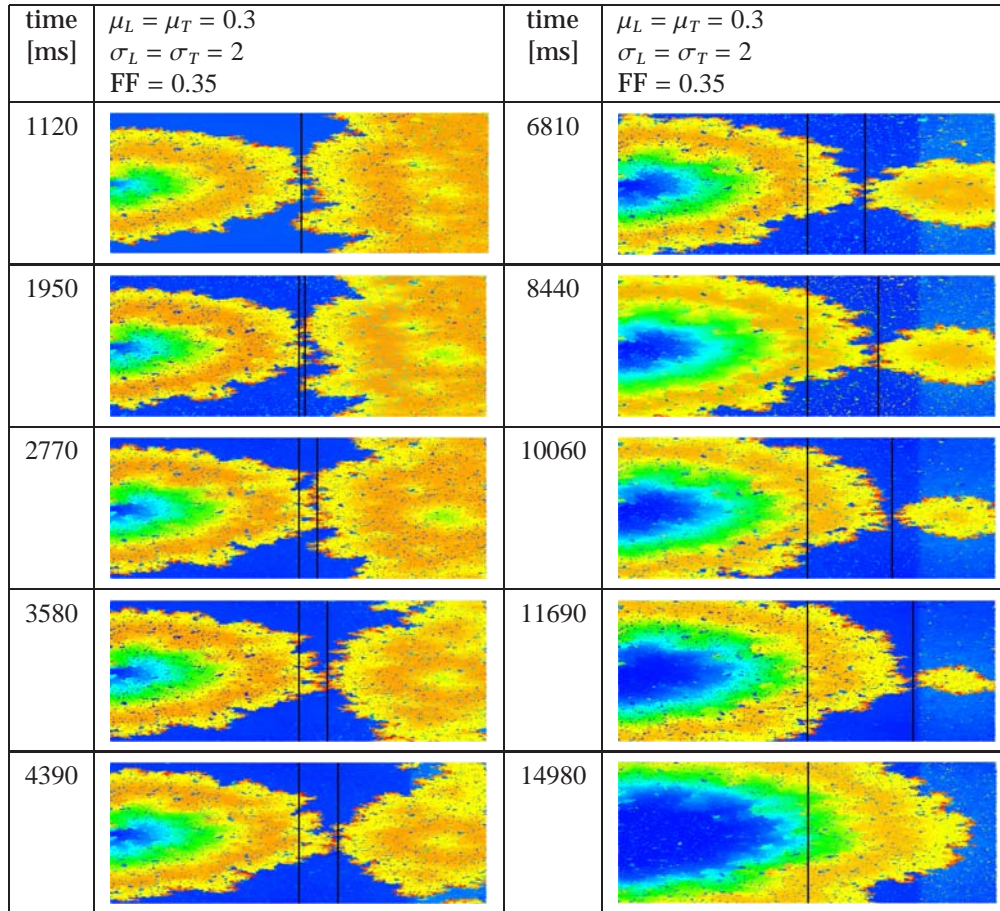
Figure 5.6: Capturing ectopic rhythm. An 8 cm × 3 cm sheet of atrial tissue is represented by an irregular brickwall structure. To simulate sinus rhythm, a stimulus current was applied each 800 ms to the left of the tissue. Ectopic activity occurs on the right due to an increased expression of I_f. The membrane potential is shown at different simulation times. Two black lines indicate how the collision front moves to the right over time. After 15 s, ectopic activity in the right is captured by the depolarization wave coming from the left. Just excited tissue is red, depolarized tissue is yellow or green, and repolarized tissue is blue.

Table 5.3: BCL in ms related to cellular coupling

μ_L	μ_T	σ_L	σ_T	series A mean	series A std	series B mean	seriesB std
1.0	1.0	0.0	0.0	807.1	0.1	931.7	0.2
0.5	0.5	0.0	0.0	789.9	0.1	931.6	0.6
0.5	0.5	0.5	0.5	781.6	0.4	930.8	1.1
0.5	0.5	1.0	1.0	776.0	3.4	929.3	4.3
0.5	0.5	1.5	1.5	773.9	20.1	928.2	19.0
0.5	0.5	2.0	2.0	774.1	38.0	924.1	24.2
0.3	0.3	0.0	0.0	780.1	0.1	930.3	1.1
0.3	0.3	0.5	0.5	771.6	3.2	927.0	4.2
0.3	0.3	1.0	1.0	770.3	23.5	919.6	22.9
0.3	0.3	1.5	1.5	770.8	38.3	911.2	31.2
0.3	0.3	2.0	2.0	771.0	40.2	909.7	36.8
0.0	0.0	0.0	0.0	985.0	208.8	1059.4	325.3

In Figure 5.5 (center and right), the membrane potentials are presented for pathological tissue after the second stimulation. Approximately 1000 ms after the start of the simulation, ectopic activity occurs on the right side of the tissue, which is related to the increased expression of I_f in that area. At 1000 ms, more ectopic activity is present in the right column than in the center column. Since cellular coupling is the only difference between the two simulations, and gap junction remodeling was applied just before the second stimulation at 800 ms, the state of the two stimulations was exactly the same till 800 ms. Thus, the increase in ectopic activity is explained by the decrease in cellular coupling.

In Figure 5.6, the membrane potentials are shown at several simulation times for the second simulation of pathological tissue. Each of the figures represents a moment of collision of the depolarization wavefront generated by the sinus node on the left-hand side and the wavefront generated by ectopic activity on the right-hand side. Note that the collision front moves to the right during the course of the simulation and eventually reaches the ectopic area before it can depolarize. After approximately 15 s, the ectopic pacemaker is captured by the normal pacemaker. The yellow and green spots indicate spontaneous action potentials from uncoupled segments that are not

activated by the depolarization wave. These segments are not capable of initiating new depolarization waves and, thus, no reentry will occur.

5.4 Discussion

5.4.1 Mechanisms leading to atrial arrhythmia

Many hypotheses have been proposed that may explain AF initiation and perpetuation, such as structural remodeling [88, 139, 183, 209, 210], electrophysiological remodeling [7, 18], stretch [135], atrial dilation [168], and atrial fibrillation itself ("AF begets AF") [221]. Recurrence of AF by late phase 3 early afterdepolarizations (EADs) shortly after termination of AF has been reported by Burashnikov and Antzelevitch [22]. Distinct electrophysiological properties between myocytes from the left atrial free wall and the pulmonary veins may contribute to the role of the pulmonary veins in atrial fibrillation [51, 85]. In the present study, we investigate the influence of I_f on the conduction velocity and ectopic activity triggered by diastolic action potentials.

5.4.2 Hyperpolarization-activated inward currents

I_f is not the only identified hyperpolarization-activated inward current. Ehrlich *et al.*[52] identified a hyperpolarization-activated time-dependent K^+ current I_{KH} in canine myocytes from the pulmonary veins. Chen *et al.* [31] observed pacemaker currents in canine PV myocytes which they believed to be I_f. It is suggested by Ehrlich *et al.*[52] that these currents may correspond to I_{KH}.

Hoppe and Beuckelmann found a considerable variability of I_f expression from cell to cell [76]. Based on a study by Wu *et al.* [226] identifying I_f and I_{K1} in atrial cells from the cat, Hoppe and Beuckelmann suggest that diastolic depolarization may not only depend on upregulation of I_f, but also on downregulation of I_{K1} [76]. We observed that for G_f smaller than 0.27 nS/pF, a steady-state membrane potential is reached at which the depolarizing I_f current is compensated by the rectifying I_{K1} current. Our findings support the suggestion by Hoppe and Beuckelmann that it is the combination of upregulation of I_f and downregulation of I_{K1} that may lead to diastolic depolarizations [76].

5.4.3 The role of I_f in structurally remodeled tissue

On the basis of our simulation results, we conclude that ectopic activity in regions with an increased expression of I_f is enhanced by a reduced cellular coupling. Similar observations have been reported by Wilders *et al.* [223] in a study on focal activity related to anisotropy. Cai *et al.* [23], Winslow *et al.* [224], and Cloherty *et al.* [34] observed in simulation studies that little cellular coupling is required for frequency entrainment of sino-atrial node cells. Frequency entrainment was also observed in our simulations of regional and distributed focal activity. However, we also observed that nonuniform uncoupling due to fibrosis and gap junction remodeling leads to lower BCLs of ectopic activity. We conclude that the combination of a distributed expression of I_f and uncoupling due to fibrosis and gap junction remodeling might lead to ectopic activity, contributing to arrhythmogenesis in diseases characterized by I_f overexpression such as heart failure, hypertrophy, and atrial fibrillation [28, 76, 77, 128].

From our simulation results, we also conclude that an increased expression of I_f leads to an increased conduction velocity. In the presence of I_f, the diastolic membrane potential rises, such that less current load is needed to reach the threshold. Especially in cases where few cells need to load a larger number of cells (current-to-load mismatch) this mechanism may prevent drastic slowing or even a total block of impulse propagation. We observed that the increase in conduction velocity is similar in normal, remodeled and fibrotic tissue. Compared with the conduction velocity in tissue without I_f, we observed an increase of up to 20% in remodeled and fibrotic tissue. Based on these findings, we propose that an increased expression of I_f in early stages of cellular uncoupling due to aging or pathology may be a mechanism to prevent conduction slowing and block. Michels *et al.* [128] hypothesize a therapeutic role for I_f blockers to modify pathological automaticity. On the basis of our simulation results, we conclude that blocking of I_f under pathological conditions might lead to slowing or block of impulse propagation.

5.4.4 Model validity and limitations

In the present study, structural remodeling and active membrane behavior extended with a hyperpolarization-activated inward current are brought together into one model. The aim of the model is to study impulse propagation and ectopic activity in normal and in structurally remodeled tissue. Although similar results would have been obtained by a monodomain formulation of the model, we think that, in order to model reduced intracellular coupling

caused by pathology, the interstitial space should explicitly be modeled as a possible conduction pathway. The validity of the model with respect to the cardiac tissue is discussed in Methods (see also Ref. [109]). We discuss the validity of our model of I_f, the modified I_{Na} kinetics, the ion concentrations, and the distribution of I_f.

I_f **kinetics**   We use large, nonphysiological, values for the maximum membrane conductance G_f to obtain significant diastolic depolarization and diastolic action potentials. I_f conductances of this size have not been observed experimentally [28, 76, 77, 228]. However, Michels *et al.* [128] recently observed that half-maximum activation of single-channel I_f is in fact within diastolic range of human atrial myocardium. These recent observations are most likely because cell dialysis was omitted in the new study [128]. The I_f channel availability in human atrial myocytes (p_o in our model) reported by Michels *et al.* [128] in diastolic range is much larger than the measurements reported by DiFrancesco [43], upon which p_o in our model is based. For example, $G_f = 0.16$ nS/pF in our model leads to a steady-state membrane potential $V_{mem} = -70.8$ mV, a conductance $g_f = G_f \, p_o = 0.006$ nS/pF, and $p_o = 0.0375$ (Figure 5.2). However, the channel availability reported by Michels *et al.* [128] would lead to $p_o = 0.26$ for $V_{mem} = -70.8$, giving a maximum conductance $G_f = g_f/p_o = 0.006/0.26 = 0.023$ nS/pF. Porciatti *et al.* [146] reported a current density of -3.77 pA/pF at $V_{mem} = -120$ mV for human atrial myocytes. For reversal potential $E_f = -13$ mV [146], the conductance $g_f = I_f/(V_{mem} - E_f) = 0.035$ nS/pF. Since $p_o = 1$ for $V_{mem} = -120$ mV [146], the maximum conductance G_f equals $g_f = 0.035$ nS/pF in that case. Although the values we have used for G_f are somewhat larger than the experimentally obtained values, the I_f current size in diastolic range is similar to the recent findings by Michels *et al.* [128]. The major findings of our study, namely the facilitation of impulse propagation and possible ectopic activity in badly coupled tissue, also hold for physiological G_f when the I_f kinetics are based on these recent findings.

I_{Na} **kinetics**   To obtain diastolic action potentials for large values of G_f, we adapted the kinetics of I_{Na} such that the I_{Na} channels open faster when the membrane depolarizes. In single cell simulations with the Courtemanche model, action potentials are generated by applying a stimulus current of 20 pA/pF for 2 ms [37]. When slowly depolarizing the membrane by applying a small stimulus current for a longer period of time, a minimum current of 0.5 pA/pF is required to generate an action potential. When smaller stimulus currents are applied, the threshold for the opening of the I_{Na} channels is never reached due to the increasing voltage dependent I_{K1} current. I_{K1} reaches a

maximum of approximately 0.5 pA/pF for membrane potential -67 mV [37]. By adapting the I_{Na} kinetics as described in Methods, action potentials can be generated when applying a stimulus current above 0.4 pA/pF. The changes of the I_{Na} kinetics have no effect on the action potential morphology and duration when the usual stimulus current is applied.

Ion concentrations   The ionic membrane currents of the Courtemanche-Ramirez-Nattel model interact with intracellular Na^+, K^+, and Ca^{2+} concentrations [37]. We adapted the model to take the influence of I_f on $[Na^+]_i$ and $[K^+]_i$ into account as described by DiFrancesco and Noble [45]. However, the effect on ion concentrations of the stimulus current and the intracellular currents responsible for loading of the cells are not taken into account. This may lead to a drift in ionic balance when simulating a longer period of time [37, 211]. Indeed, we observed some deviation in the ionic balance after several seconds of simulation time (not shown). However, the drift was marginal and since the longest simulation run lasted only 15 s, we do not expect any noticeable influence on our simulation results.

Distribution of I_f   An important aspect of our model is the nonuniform expression of I_f. Porciatti *et al.* [146] observed expression of I_f in 82% of human atrial cells. Hoppe and Beuckelmann found I_f in 95 to 100% of human atrial myocytes [76]. They report a considerable variability of I_f size from cell to cell [76]. Sartiani *et al.* [165] detected I_f in about 30% of cultured HL-1 cells (adult mouse atrial myocytes). Since little quantitative information is available on the distribution of I_f expression, we decided to model variability in the expression of I_f using a normal distribution of G_f.

5.5   Conclusion

In our model, an increased expression of I_f leads to a larger conduction velocity in normal, remodeled, and fibrotic tissue. The nominal increase in conduction velocity is similar for all types of tissue. Compared with tissue without I_f, the relative increase in conduction velocity is up to 20% in remodeled and fibrotic tissue. On the basis of these results, we propose that an increased expression of I_f in early stages of cellular uncoupling, due to aging or pathology, may be a mechanism to facilitate impulse propagation. Hence, I_f may prevent conduction slowing and block. We also found that in tissue with a nonuniform expression of I_f, the BCL of an ectopic pacemaker decreases due to cellular uncoupling. Thus, overexpression of I_f may lead to ectopic activity, especially in regions with a reduced cellular coupling.

6

Mechanoelectric feedback leads to conduction slowing and block in acutely dilated atria

N.H.L. Kuijpers, H.M.M. ten Eikelder, P.H.M. Bovendeerd,
S. Verheule, T. Arts, and P.A.J. Hilbers

Abstract

Atrial fibrillation, a common cardiac arrhythmia, is promoted by atrial dilatation. Acute atrial dilatation may play a role in atrial arrhythmogenesis through mechano-electric feedback. In experimental studies, conduction slowing and block have been observed in acutely dilated atria. In the present study, the influence of the stretch-activated current (I_{sac}) on impulse propagation is investigated by means of computer simulations. Homogeneous and inhomogeneous atrial tissues are modeled by cardiac fibers composed of segments that are electrically and mechanically coupled. Active force is related to free Ca^{2+} concentration and sarcomere length. Simulations of homogeneous and inhomogeneous cardiac fibers have been performed to quantify the relation between conduction velocity and I_{sac} under stretch. In our model, conduction slowing and block are related to the amount of stretch and are enhanced by contraction of early-activated segments. Conduction block can be unidirectional in an inhomogeneous fiber and is promoted by a shorter stimulation interval. Slowing of conduction is explained by inactivation of Na^+ channels and a lower maximum upstroke velocity due to a depolarized resting membrane potential. Conduction block at shorter stimulation intervals is explained by a longer effective refractory period under stretch. Our observations are in agreement with experimental results and explain the large differences in intra-atrial conduction, as well as the increased inducibility of atrial fibrillation in acutely dilated atria.

105

6.1 Introduction

Atrial fibrillation (AF) is a common cardiac arrhythmia [133]. An important risk factor for AF is chronic atrial dilatation [150, 212], whereas experimental studies indicate a role of acute atrial dilatation in the initiation of atrial arrhythmia [16, 135, 152, 174, 177]. Conduction slowing and shortening of the refractory period in acutely dilated atria have been reported [32, 79, 153]. Eijsbouts *et al.* [53, 54] found, in addition to conduction slowing, an increased occurrence of intra-atrial block. Hu and Sachs [78] and Kohl and Sachs [105] hypothesized that stretch-induced changes in electrophysiological behavior can be explained by stretch-activated channels (SACs). In the present simulation study, we investigate this hypothesis for atrial impulse propagation.

Several models have been proposed to describe SACs based on experimental observations [68, 163, 193, 230, 231]. Similar models have been applied in large-scale computer simulations to investigate the effect of stretch on defibrillation and the termination of ventricular tachycardia by means of precordial thump [119, 200]. Since cardiomechanics are not considered in these studies, the stretch-activated current (I_{sac}) is not influenced by contraction. Models of the ventricles in which contraction is triggered by electrical activation describe stimulation from the Purkinje system [99, 205] and epicardial stimulation [100, 204]. In these studies, mechanical deformation is triggered by electrical activation. However, mechanoelectric feedback, i.e., the effect of mechanical deformation on the electrophysiology, is not considered. To investigate the influence of mechanical deformation on impulse propagation, a strong coupling between cardiomechanics and electrophysiology is required, as proposed elsewhere [130, 137, 141]. In these studies, tissue conductivity is directly affected by mechanical deformation, and the amount of I_{sac} is related to local deformation of the cardiac tissue. Physiological details, such as ionic membrane currents, intracellular Ca^{2+} handling, and cross-bridge formation, are not considered in these models.

In the present study, we investigate the role of I_{sac} in conduction slowing and block as observed in acutely dilated atria. We apply a discrete bidomain model with strong coupling between cardiomechanics and cardiac electrophysiology. Our model describes ionic membrane currents, Ca^{2+} storage and release from the sarcoplasmic reticulum (SR), and cross-bridge formation. In contrast to all other multicellular models, contractile forces are directly coupled to free Ca^{2+} concentration, as well as sarcomere length. In our model, the amount of I_{sac} is related to local stretch and may change during contraction. We performed simulations of homogeneous and inhomogeneous cardiac fibers under stretch to quantify the conduction velocity in the presence of I_{sac}. We observed conduction slowing, a longer effective refractory period

(ERP), and (unidirectional) conduction block with increasing stretch. Further-more, we found that contraction of early-activated fiber segments can lead to conduction block in later-activated segments. The observed phenomena are in agreement with experimental observations and provide an explanation for the increased inducibility of atrial fibrillation in acutely dilated atria.

6.2 Methods

In the present study, we apply our discrete bidomain model, the Cellular Bidomain Model [109, 110], which describes active membrane behavior, as well as intercellular coupling and interstitial currents, and has been extended to model cardiac tissue mechanics and I_{sac}. We describe the extensions to our model of cardiac electrophysiology, in particular the influence of stretch on fiber conductivity, our model of I_{sac}, the Ca^{2+}-force relation, the mechanical behavior of a single segment, and the mechanical behavior of a cardiac fiber. Furthermore, the numerical integration scheme is described and an overview of the simulations is given.

6.2.1 Modeling cardiac electrophysiology

In the Cellular Bidomain Model, the cardiac tissue is subdivided in segments, each with its own membrane model describing the ionic membrane currents [109, 110]. The state of each segment is defined by the intracellular poten-tial (V_{int}), the extracellular potential (V_{ext}), and the state of the cell membrane, which is expressed in gating variables and ion concentrations. The membrane potential (V_{mem}) is defined by

$$V_{mem} = V_{int} - V_{ext}. \tag{6.1}$$

Intracellular and extracellular currents between adjacent segments are related to intracellular and extracellular conductivities and satisfy Ohm's law. Ex-change of current between the intracellular and extracellular space occurs as transmembrane current (I_{trans}), which is defined by

$$I_{trans} = \chi(C_{mem}\frac{dV_{mem}}{dt} + I_{ion}), \tag{6.2}$$

where χ is the surface-to-volume ratio needed to convert I_{trans} per unit mem-brane surface to I_{trans} per unit tissue volume, C_{mem} is the membrane capaci-tance, which is typically $1 \mu F/cm^2$ for biological membranes [15], and I_{ion} is ionic current (expressed in μA per cm^2 membrane surface or pA/pF when

$C_{\text{mem}} = 1\,\mu\text{F/cm}^2$). I_{ion} depends on V_{mem}, gating variables, and ion concentrations (see below). Impulse propagation is related to the longitudinal conductivity parameters g_{int} and g_{ext}. The bidomain parameters used for the present study are from Henriquez [69] and are based on measurements by Clerc [33] (Table 6.1).

To incorporate I_{sac}, we modified the model of the human atrial action potential (AP) of Courtemanche *et al.* [37]. The total ionic current is given by

$$I_{\text{ion}} = I_{\text{Na}} + I_{\text{K1}} + I_{\text{to}} + I_{\text{Kur}} + I_{\text{Kr}} + I_{\text{Ks}} + I_{\text{Ca,L}} + I_{\text{p,Ca}} + I_{\text{NaK}} + I_{\text{NaCa}} + I_{\text{b,Na}} + I_{\text{b,Ca}} + I_{\text{sac}}, \quad (6.3)$$

where I_{Na} is fast inward Na$^+$ current, I_{K1} is inward rectifier K$^+$ current, I_{to} is transient outward K$^+$ current, I_{Kur} is ultrarapid delayed rectifier K$^+$ current, I_{Kr} is rapid delayed rectifier K$^+$ current, I_{Ks} is slow delayed rectifier K$^+$ current, $I_{\text{Ca,L}}$ is L-type Ca^{2+} current, $I_{\text{p,Ca}}$ is Ca^{2+} pump current, I_{NaK} is Na$^+$-K$^+$ pump current, I_{NaCa} is Na$^+$/Ca^{2+} exchanger current, and $I_{\text{b,Na}}$ and $I_{\text{b,Ca}}$ are background Na$^+$ and Ca^{2+} currents [37]. The model for the ionic and pump currents, including handling of intracellular Ca^{2+} concentration ($[\text{Ca}^{2+}]_i$) by the SR, is adopted from the model of Courtemanche *et al.* [37].

6.2.2 Influence of stretch on fiber conductivity

The intracellular and extracellular conductivities (g_{int} and g_{ext}) may change during stretch or contraction of the fiber. Under stretch, the length of the cells increases and the cross-sectional area decreases, leading to a reduced fiber conductivity. To quantify the changes in g_{int} and g_{ext} (mS/cm), we assume that the resistivity of the intracellular space ($R_{\text{int}} = 1/g_{\text{int}}$, $\Omega{\cdot}\text{cm}$) is determined partly by the myoplasmic resistivity (R_{myo}) and partly by the gap-junctional resistivity (R_{junc}):

$$g_{\text{int}} = \frac{1}{R_{\text{int}}} = \frac{1}{R_{\text{myo}} + R_{\text{junc}}}. \quad (6.4)$$

For the nonstretched fiber, we define $g_{\text{int}} = g_{\text{int0}} = 1/R_{\text{int0}}$, $R_{\text{myo}} = R_{\text{myo0}}$, and $R_{\text{junc}} = R_{\text{junc0}}$. When the fiber is stretched with stretch ratio λ, cell length is increased and cross-sectional area is decreased (assuming that cell volume is conserved). Since R_{myo} is proportional to the length and inversely proportional to the cross-sectional area of the cell, we obtain

$$R_{\text{myo}} = R_{\text{myo0}}\,\lambda^2. \quad (6.5)$$

On the basis of the assumption that the total number of gap junctions in the fiber does not change under stretch, the number of gap junctions per length

unit decreases proportionally with λ, which leads to

$$R_{\text{junc}} = \frac{R_{\text{junc0}}}{\lambda}. \tag{6.6}$$

If equations (6.5) and (6.6) are combined, g_{int} is related to λ by

$$g_{\text{int}} = \frac{1}{R_{\text{myo}} + R_{\text{junc}}} = \frac{1}{R_{\text{myo0}}\lambda^2 + \frac{R_{\text{junc0}}}{\lambda}}. \tag{6.7}$$

For the extracellular domain, we assume that g_{ext} is related to g_{ext0} and λ by

$$g_{\text{ext}} = \frac{g_{\text{ext0}}}{\lambda^2}. \tag{6.8}$$

Chapman and Fry [30] determined that 52% of the total resistivity was attributed to gap-junctional resistance in frog myocardial cells ($R_{\text{junc0}}/R_{\text{int0}}$ = 0.52). Since these cells are longer (131 μm) [30] than human atrial cells (94 μm) [146], we estimate that $R_{\text{junc0}}/R_{\text{int0}}$ = 0.6 for human atrial myocardium (Table 6.1).

6.2.3 Stretch-activated current I_{sac}

On the basis of experimental observations, we assume that I_{sac} in atrial myocytes is a nonselective cation current with a near-linear current-voltage relation [101]. The reversal potential is -3.2 mV for rat atrial myocytes [101]. In our model, I_{sac} is permeable to Na$^+$, K$^+$, and Ca^{2+} and is defined by

$$I_{\text{sac}} = I_{\text{sac,Na}} + I_{\text{sac,K}} + I_{\text{sac,Ca}}, \tag{6.9}$$

where $I_{\text{sac,Na}}$, $I_{\text{sac,K}}$, and $I_{\text{sac,Ca}}$ represent the Na$^+$, K$^+$, and Ca^{2+} contributions, respectively, to I_{sac}. These currents are defined by the constant-field Goldman-Hodgkin-Katz current equation [97]:

$$I_{\text{sac,Na}} = P_{\text{Na}}\, g_{\text{sac}} \frac{z_{\text{Na}}^2 F^2 V_{\text{mem}}}{RT} \frac{[\text{Na}^+]_i - [\text{Na}^+]_e \exp(-\frac{z_{\text{Na}}F V_{\text{mem}}}{RT})}{1 - \exp(-\frac{z_{\text{Na}}F V_{\text{mem}}}{RT})}, \tag{6.10}$$

$$I_{\text{sac,K}} = P_{\text{K}}\, g_{\text{sac}} \frac{z_{\text{K}}^2 F^2 V_{\text{mem}}}{RT} \frac{[\text{K}^+]_i - [\text{K}^+]_e \exp(-\frac{z_{\text{K}}F V_{\text{mem}}}{RT})}{1 - \exp(-\frac{z_{\text{K}}F V_{\text{mem}}}{RT})}, \tag{6.11}$$

$$I_{\text{sac,Ca}} = P_{\text{Ca}}\, g_{\text{sac}} \frac{z_{\text{Ca}}^2 F^2 V_{\text{mem}}}{RT} \frac{[\text{Ca}^{2+}]_i - [\text{Ca}^{2+}]_e \exp(-\frac{z_{\text{Ca}}F V_{\text{mem}}}{RT})}{1 - \exp(-\frac{z_{\text{Ca}}F V_{\text{mem}}}{RT})}, \tag{6.12}$$

where, P_{Na}, P_K, and P_{Ca} denote the relative permeabilities to Na^+, K^+, and Ca^{2+}, z_{Na}, z_K, and z_{Ca} represent the ion valences, and F is Faraday's constant, R is the universal gas constant, and T is temperature (310 K) [37].

The conductance (g_{sac}) depends on λ as follows:

$$g_{sac} = \frac{G_{sac}}{1 + K_{sac}\exp(-\alpha_{sac}(\lambda - 1))}, \tag{6.13}$$

where G_{sac} is the maximum membrane conductance, K_{sac} a parameter to define the amount of current when the cell is not stretched ($\lambda = 1$, sarcomere length (l_s) = 1.78 μm), and α_{sac} is a parameter to describe the sensitivity to stretch. K_{sac} and α_{sac} are from Zabel $et\ al.$ [230] (Table 6.1).

The reversal potential (E_{sac}) can be obtained by solving the following equation for V_{mem}: $I_{sac,Na} + I_{sac,K} + I_{sac,Ca} = 0$. In the present study, we consider two cases: $P_{Na} : P_K : P_{Ca} = 1 : 1 : 1$, with $E_{sac} = -0.2$ mV, and $P_{Na} : P_K : P_{Ca} = 1 : 1 : 0$, with $E_{sac} = -0.9$ mV. In both cases, I_{sac} has a near-linear current-voltage relation (Figure 6.1).

To describe the influence of $I_{sac,Na}$, $I_{sac,K}$, and $I_{sac,Ca}$ on intracellular Na^+, K^+, and Ca^{2+} concentrations ($[Na^+]_i$, $[K^+]_i$, and $[Ca^{2+}]_i$), respectively, we replace equations (A.2)-(A.6) of the model of Courtemanche $et\ al.$ [37] (Appendix A) by

$$\frac{d[Na^+]_i}{dt} = C_m \frac{-3I_{NaK} - 3I_{NaCa} - I_{b,Na} - I_{Na} - I_{sac,Na}}{F\,V_i}, \tag{6.14}$$

$$\frac{d[K^+]_i}{dt} = C_m \frac{2I_{NaK} - I_{K1} - I_{to} - I_{Kur} - I_{Kr} - I_{Ks} - I_{sac,K}}{F\,V_i}, \tag{6.15}$$

$$\frac{d[Ca^{2+}]_i}{dt} = \frac{B1}{B2}, \tag{6.16}$$

$$B1 = C_m \frac{2I_{NaCa} - I_{p,Ca} - I_{Ca,L} - I_{b,Ca} - I_{sac,Ca}}{2F\,V_i} + \frac{V_{up}(I_{up,leak} - I_{up}) + I_{rel}V_{rel}}{V_i}, \tag{6.17}$$

$$B2 = 1 + \frac{[Trpn]_{max}\,K_{m,Trpn}}{([Ca^{2+}]_i + K_{m,Trpn})^2} + \frac{[Cmdn]_{max}\,K_{m,Cmdn}}{([Ca^{2+}]_i + K_{m,Cmdn})^2}, \tag{6.18}$$

where, C_m is the membrane capacitance of a single atrial myocyte (100 pF) [37], F is Faraday's constant, V_i is the intracellular volume (13668 μm^3) [37], V_{up} and V_{rel} are the volumes of the SR uptake and release compartments, respectively, $I_{up,leak}$, I_{up}, and I_{rel} represent the SR currents, [Trpn] is troponin concentration, [Cmdn] is calmodulin concentration, and K_m is the half-saturation constant. Equation (6.18) is equation (A.6) in the model of Courtemanche $et\ al.$ [37] and represents the influence of Ca^{2+} buffering in the cytoplasm mediated by troponin ($[Ca^{2+}]_{Trpn}$) and calmodulin ($[Ca^{2+}]_{Cmdn}$) on $[Ca^{2+}]_i$.

6.2.4 Modeling the Ca^{2+}-force relation

Rice *et al.* [157, 158] proposed five models of isometric force generation in cardiac myofilaments. To model the Ca^{2+}-force relation in the present study, we apply their *model 4*, which is based on a functional unit of troponin, tropomyosin, and actin. The binding of Ca^{2+} to troponin is described by two states: unbound troponin and Ca^{2+} bound to troponin. Tropomyosin can be in one of six states: nonpermissive with 0 and 1 cross bridges (*N0* and *N1*) and permissive with 0, 1, 2, and 3 cross bridges (*P0*, *P1*, *P2*, and *P3*). The permissive states refer to tropomyosin for which the accompanying actin binding sites are available for cross bridges to bind and generate force. Transitions between the states are governed by rate functions that depend on $[Ca^{2+}]_i$ and l_s. The entire model is presented in Appendix C.

In the model of Courtemanche *et al.* [37], Ca^{2+} buffering by troponin is modeled by

$$[Ca^{2+}]_{Trpn} = [Trpn]_{max} \frac{[Ca^{2+}]_i}{[Ca^{2+}]_i + K_{m,Trpn}}, \tag{6.19}$$

where $[Ca^{2+}]_{Trpn}$ is Ca^{2+}-bound troponin concentration, $[Trpn]_{max}$ is total troponin concentration ($70~\mu M$) [37], and $K_{m,Trpn}$ is half-saturation constant for troponin ($0.5~\mu M$) [37]. In the model of Rice *et al.* [157, 158], the concentration of Ca^{2+} bound to high-affinity troponin sites is [HTRPNCa], and the dynamics are governed by

$$\frac{d[HTRPNCa]}{dt} = k^+_{htrpn} [Ca^{2+}]_i ([HTRPN]_{tot} - [HTRPNCa]) - k^-_{htrpn} [HTRPNCa], \tag{6.20}$$

where $[HTRPN]_{tot}$ represents the total troponin high-affinity site concentration and k^+_{htrpn} and k^-_{htrpn} are the Ca^{2+} on- and off-rates for troponin high-affinity sites (Table 6.1). The concentration of Ca^{2+} bound to low-affinity troponin sites is [LTRPNCa], and the dynamics are governed by

$$\frac{d[LTRPNCa]}{dt} = k^+_{ltrpn} [Ca^{2+}]_i ([LTRPN]_{tot} - [LTRPNCa]) - k^-_{ltrpn} [LTRPNCa], \tag{6.21}$$

where $[LTRPN]_{tot}$ represents the total troponin low-affinity site concentration and k^+_{ltrpn} and k^-_{ltrpn} are the Ca^{2+} on- and off-rates for troponin low-affinity sites (Table 6.1).

In our model, the Ca^{2+} transient is computed by the model of Courtemanche *et al.* [37] using an immediate formulation of Ca^{2+} binding by troponin (equation (6.19)). The resulting Ca^{2+} transient is used to compute the Ca^{2+} binding to troponin by equations (6.20) and (6.21), and [LTRPNCa] is used to compute the tropomyosin rate from nonpermissive to permissive, as in the model of Rice *et al.* [157, 158]. In the present study, we do not consider a feedback mechanism that influences the Ca^{2+} transient through a change in the affinity of troponin for Ca^{2+} binding as in *model 5* [157, 158]. The choice between *model 4* and *model 5* is motivated in the Discussion (Section 6.4).

In *model 4*, the force generated by the sarcomeres depends on the fraction of tropomyosin in the force-generating states *N1*, *P1*, *P2*, and *P3*. We use the normalized force (F_{norm}), which is defined by

$$F_{norm} = \phi(l_s) \frac{P1 + N1 + 2\,P2 + 3\,P3}{P1_{max} + 2\,P2_{max} + 3\,P3_{max}}, \tag{6.22}$$

where $P1_{max}$, $P2_{max}$, and $P3_{max}$ are defined as in Ref. [158] and $\phi(l_s)$ describes the physical overlap structure of thick and thin filaments within a sarcomere [158]. When $\phi(l_s) = 1$, all myosin heads are able to interact with actin in the single overlap zone; when $\phi(l_s) < 1$, some of the filaments are in the double or nonoverlap zones. $\phi(l_s)$ is defined by

$$\phi(l_s) = \begin{cases} (l_s - 0.6\,\mu\mathrm{m})/1.4\,\mu\mathrm{m} & \text{if } 0.6\,\mu\mathrm{m} \leq l_s \leq 2.0\,\mu\mathrm{m} \\ 1 & \text{if } 2.0\,\mu\mathrm{m} < l_s \leq 2.2\,\mu\mathrm{m} \\ (3.6\,\mu\mathrm{m} - l_s)/1.4\,\mu\mathrm{m} & \text{if } 2.2\,\mu\mathrm{m} < l_s \leq 3.6\,\mu\mathrm{m} \end{cases} \tag{6.23}$$

In Figure 6.2, the steady-state Ca^{2+}-force relation is presented for *model 4* [158]. F_{norm} increases with increasing $[Ca^{2+}]_i$ and with increasing l_s, with a maximum at $l_s = 2.3\,\mu\mathrm{m}$. To emphasize the dependence on $[Ca^{2+}]_i$ and l_s, we will denote F_{norm} as a function: $F_{norm}([Ca^{2+}]_i, l_s)$.

Table 6.1: Model parameters

| Parameter	Definition	Value
g_{int0}	Intracellular conductivity ($\lambda = 1.0$)	1.7422 mS/cm
g_{ext0}	Extracellular conductivity ($\lambda = 1.0$)	6.2500 mS/cm
C_{mem}	Membrane capacitance	$1.0\,\mu\text{F/cm}^2$
χ	Surface-to-volume ratio	$2000\,\text{cm}^{-1}$
$R_{\text{junc0}}/R_{\text{int0}}$	Relative gap-junctional resistivity	0.6
K_{sac}	Parameter to define I_{sac} when not stretched	100
α_{sac}	Parameter to describe sensitivity to stretch	3
$[\text{LTRPN}]_{\text{tot}}$	Total troponin low-affinity site concentration	$70.0\,\mu\text{M}$
$[\text{HTRPN}]_{\text{tot}}$	Total troponin high-affinity site concentration	$140.0\,\mu\text{M}$
k_{ltrpn}^{+}	Ca^{2+} on-rate for troponin low-affinity sites	$20\,\text{M}^{-1}\cdot\text{s}^{-1}$
k_{ltrpn}^{-}	Ca^{2+} off-rate for troponin low-affinity sites	$40\,\text{s}^{-1}$
k_{htrpn}^{+}	Ca^{2+} on-rate for troponin high-affinity sites	$1.0\times 10^8\,\text{M}^{-1}\cdot\text{s}^{-1}$
k_{htrpn}^{-}	Ca^{2+} off-rate for troponin high-affinity sites	$0.33\,\text{s}^{-1}$
l_{s0}	Reference sarcomere length	$1.78\,\mu\text{m}$
f_{CE}	Scaling factor for contractile element	$100\,\text{mN/mm}^2$
l_{CE0}	Reference length of contractile element	$1.78\,\mu\text{m}$
v_{max}	Maximum velocity of sarcomere shortening	$0.0055\,\mu\text{m/ms}$
c_v	Constant describing shape of Hill relation	2
f_{SE}	Scaling factor for series elastic element	$2.8\,\text{mN/mm}^2$
k_{SE}	Material constant for series elastic element	$14.6\,\mu\text{m}^{-1}$
l_{SE0}	Reference length of series elastic element	$0\,\mu\text{m}$
f_{PE}	Scaling factor for parallel elastic element	$0.006\,\text{mN/mm}^2$
k_{PE}	Material constant for parallel elastic element	$14.6\,\mu\text{m}^{-1}$
l_{PE0}	Reference length of parallel elastic element	$1.78\,\mu\text{m}$
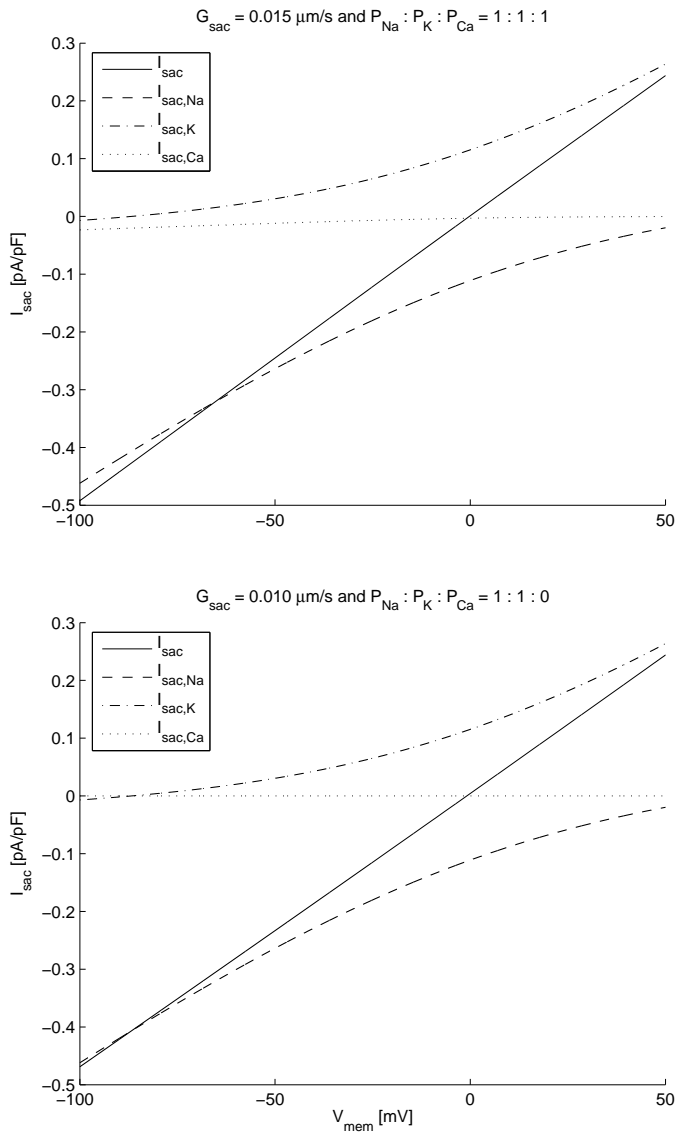
λ, stretch ratio.

Figure 6.1: Current-voltage relation for stretch-activated current (I_{sac}) and its Na^+, K^+, and Ca^{2+} components ($I_{sac,Na}$, $I_{sac,K}$, and $I_{sac,Ca}$); stretch ratio (λ) = 1.2. Top: I_{sac} permeable to Ca^{2+}. Bottom: I_{sac} not permeable to Ca^{2+}. G_{sac}, maximum membrane conductance; P_{Na}, P_{K}, and P_{Ca}, Na^+, K^+, and Ca^{2+} permeability; V_{mem}, membrane potential.
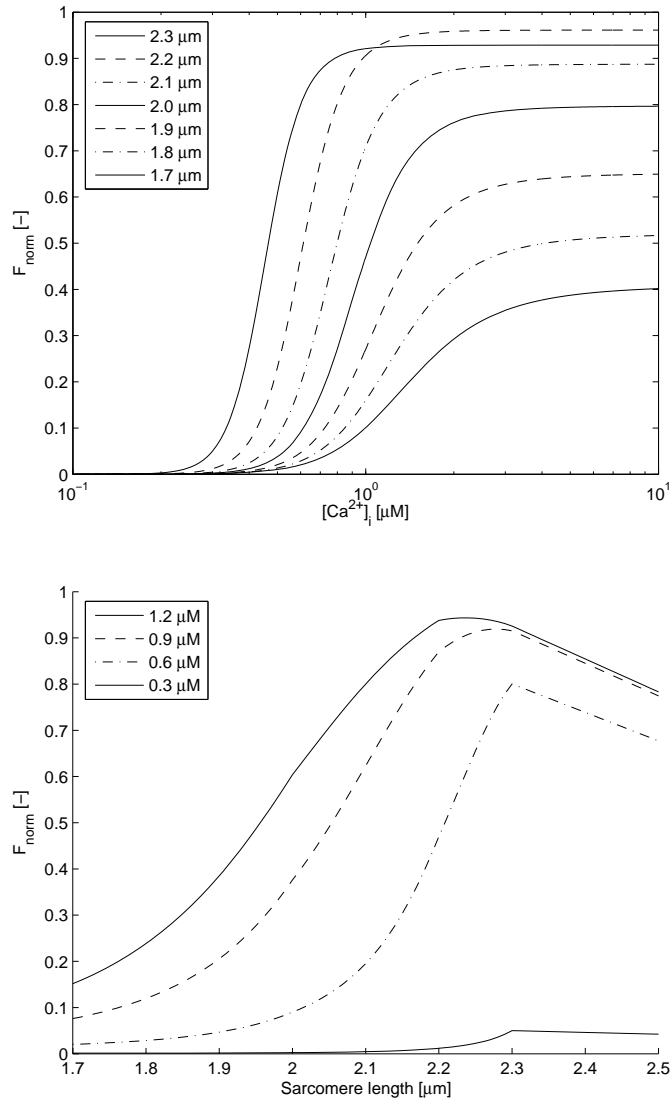
Figure 6.2: Steady-state Ca^{2+}-force relation for *model 4* from Rice *et al.* [158]. Top: normalized force (F_{norm}) vs. intracellular Ca^{2+} concentration ($[Ca^{2+}]_i$) for sarcomere length (l_s) = 1.7-2.3 μm. Bottom: F_{norm} vs. l_s for $[Ca^{2+}]_i$ = 0.3, 0.6, 0.9, and 1.2 μM.

6.2.5 Mechanical behavior of a single segment

The mechanical behavior of a single segment in our model is modeled as described by Solovyova *et al.* [176] by the classical three-element rheological scheme introduced by Hill in 1938 [71]. Active force is generated by the contractile element (CE), and passive forces are generated in a series elastic element (SE) and a parallel elastic element (PE; Figure 6.3). PE describes the force-length relation when the segment is not stimulated. CE and SE together describe the additional force generated on stimulation of the segment. The element lengths are l_{CE}, l_{SE}, and l_{PE}. The reference lengths, i.e., the lengths when the segment is at rest and no force is applied, are l_{CE0}, l_{SE0}, and l_{PE0}.

The force generated by the contractile element (F_{CE}) is defined by

$$F_{CE} = f_{CE}\, f_v(v)\, F_{norm}([Ca^{2+}]_i, l_s), \tag{6.24}$$

where f_{CE} is a scaling factor, $v = -\frac{dl_s}{dt}$ represents the sarcomere shortening velocity, and $F_{norm}([Ca^{2+}]_i, l_s)$ is F_{norm} generated by the sarcomeres. The relation between the generated force and v is Hill's force-velocity relation [71, 80] and appears to be hyperbolic for skeletal and cardiac muscle [21, 40]. We model the Hill relation by a function $f_v(v)$ as proposed by Hunter *et al.* [80]:

$$f_v(v) = \frac{1 - \frac{v}{v_{max}}}{1 + c_v \frac{v}{v_{max}}}, \tag{6.25}$$

where v_{max} is the maximum sarcomere shortening velocity and c_v is a constant describing the shape of the hyperbolic relationship.

The forces generated in SE and PE are nonlinearly dependent on their respective lengths l_{SE} and l_{PE} [176] and are defined by

$$F_{SE} = f_{SE}\, (\exp(k_{SE}\, (l_{SE} - l_{SE0})) - 1) \tag{6.26}$$

and

$$F_{PE} = f_{PE}\, (\exp(k_{PE}\, (l_{PE} - l_{PE0})) - 1), \tag{6.27}$$

where l_{SE0} and l_{PE0} denote the reference element lengths and f_{SE}, k_{SE}, f_{PE}, and k_{PE} are material constants describing the elasticity of the elements.

From mechanical equilibrium, it follows that F_{CE} must be equal to the force generated in the SE (F_{SE}). The total force generated by the segment ($F_{segment}$) is defined as $F_{SE} + F_{PE}$. Furthermore, l_{PE} must be equal to $l_{CE} + l_{SE}$ (Figure 6.3). Therefore, during mechanical equilibrium

$$F_{CE} = F_{SE}, \tag{6.28}$$
$$F_{segment} = F_{SE} + F_{PE}, \tag{6.29}$$
$$l_{PE} = l_{CE} + l_{SE}. \tag{6.30}$$
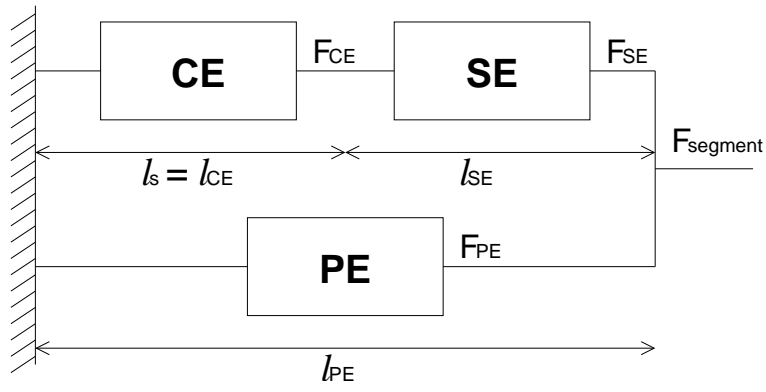
Figure 6.3: Three-element scheme to model the mechanical behavior of a single cell. Active force (F_{CE}) is generated by the contractile element (CE), and passive forces (F_{SE} and F_{PE}) are generated in the series elastic element (SE) and in the parallel elastic element (PE). $l_s = l_{CE}$ denotes sarcomere length, and l_{SE} and l_{PE} are SE and PE lengths. During mechanical equilibrium, $F_{CE} = F_{SE}$, $F_{segment} = F_{SE} + F_{PE}$, and $l_{PE} = l_{CE} + l_{SE}$.

l_{CE}, l_{SE}, and l_{PE} are related to physiological sarcomere length (l_s) and reference sarcomere length (l_{s0}) by $l_{CE} = l_s$ and $l_{CE0} = l_{s0}$ [176]. The reference length of a segment is 0.01 cm and is related to l_{PE0} by a scaling factor ξ. For segment n, we define the reference length l_{n0} by

$$l_{n0} = \xi_n \, l_{PE0}^n \tag{6.31}$$

and the actual length l_n by

$$l_n = \xi_n \, l_{PE}^n, \tag{6.32}$$

where l_{PE0}^n and l_{PE}^n represent the reference length and actual length of the PE of segment n. The stretch ratio (λ_n) for segment n is then defined by

$$\lambda_n = \frac{l_n}{l_{n0}} = \frac{l_{PE}^n}{l_{PE0}^n}. \tag{6.33}$$

The parameters for the three-element mechanical model are obtained from Solovyova *et al.* [176] (Table 6.1). In Figure 6.4, active force (F_{SE}), passive force (F_{PE}), and total force ($F_{segment}$) are presented for $l_s = 1.7\text{-}2.5$ μm and $[Ca^{2+}]_i = 1.2, 0.9, 0.6,$ and 0.3 μM. When the sarcomeres generate force, i.e., $l_{SE} > 0$, $l_{PE} = l_{CE} + l_{SE}$ is larger than $l_s = l_{CE}$. This results in a steeper increase of F_{PE} for increasing l_s and is in agreement with the passive force-length relation for intact cardiac muscle measured by Kentish *et al.* [98].
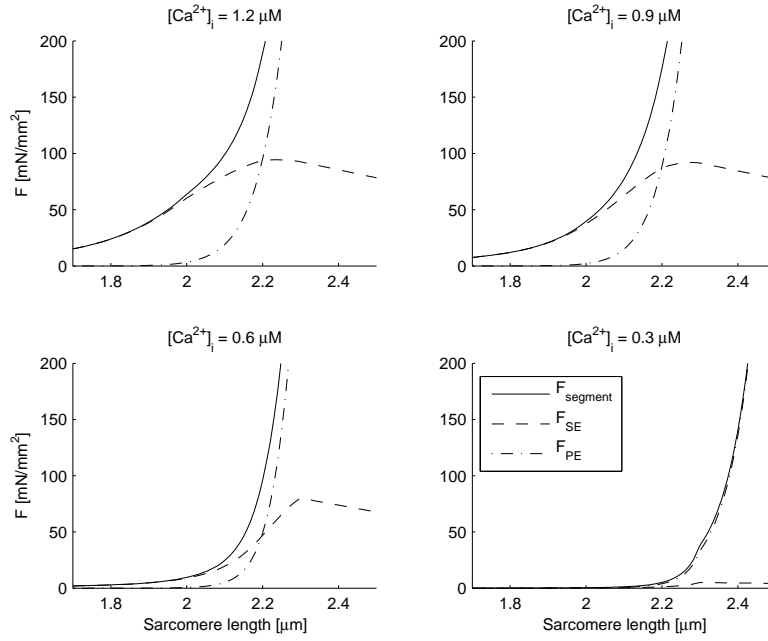
Figure 6.4: Active force (F_{SE}), passive force (F_{PE}), and total force ($F_{segment} = F_{SE} + F_{PE}$) vs. sarcomere length ($l_s$) for $[Ca^{2+}]_i = 1.2, 0.9, 0.6,$ and $0.3\ \mu M$.

6.2.6 Mechanical behavior of a cardiac fiber

A cardiac fiber is modeled as a string of segments that are coupled in series. From mechanical equilibrium, it follows that the force $F^n_{segment}$ generated by a single segment n, $n \in \mathcal{N}$, is equal to the force generated by the fiber (F_{fiber}), i.e.,

$$F^n_{segment} = F_{fiber}. \tag{6.34}$$

If we take into account that l_{n0} may be different for each segment n, $n \in \mathcal{N}$, the stretch ratio of the fiber (λ_{fiber}) is defined by

$$\lambda_{fiber} = \frac{L}{L_0} = \frac{\sum_{n \in \mathcal{N}} l_n}{\sum_{n \in \mathcal{N}} l_{n0}}, \tag{6.35}$$

where L denotes the actual fiber length and L_0 is the reference length.

In the present study, inhomogeneous cardiac tissue is represented by a 5-cm-long fiber with varying thickness and stiffness. The fiber is composed 0.01-cm-long segments with 0.01- to 0.1-mm^2 cross-sectional area. Tissue conductivity is related to stretch and may vary during the simulation. To enforce nonuniform stretch during the simulations, the diameter and stiffness of the

left half of the fiber are varied, while the diameter (0.01 mm^2) and stiffness of the right half are normal. Linear interpolation is applied in a 0.5-cm transitional zone in the center of the fiber. Thick tissue is modeled by increasing the diameter of the segments, which affects the electrophysiological and mechanical properties of the tissue. Conductances, membrane surface, and the mechanical parameters f_{CE}, f_{SE}, and f_{PE} are scaled with the increase of the cross-sectional area. To simulate stiff tissue, the mechanical parameter f_{PE} is scaled. Scaling factors for maximum and minimum thickness are denoted by t_{max} and t_{min}, respectively, and scaling factors for maximum and minimum stiffness by s_{max} and s_{min}, respectively.

6.2.7 Numerical integration scheme

To obtain criteria for the size of individual segments we apply cable theory and consider subthreshold behavior along a fiber as previously described [110]. For the bidomain parameters in Table 6.1, we obtain a length constant between 0.12 and 0.16 cm for $\lambda = 1.0$. When λ is increased to 1.4, the length constant decreases $\sim$15% for $R_{junc0}/R_{int0} = 0.6$. To obtain accurate simulation results, the fiber is modeled with segments that are 0.01 cm long, which is less than one-tenth of the length constant for $\lambda \leq 1.4$. To solve the equations of the Cellular Bidomain Model, we use a forward Euler scheme with a 0.01-ms time step to compute V_{mem} and an iterative method to solve the system of linear equations as described in Kuijpers *et al.* [110]. Our method does not require matrix inversions and, therefore, is well-suited to solve the system of equations when the conductivities change during the simulations as a result of stretch or contraction.

The ionic membrane currents are computed using a modified Euler method as described by Courtemanche *et al.* [37]. To reduce computation time, the time step changes during the simulation as follows: a 0.01-ms time step is used shortly before and during the upstroke of the AP, and a 0.1-ms time step is used during repolarization and rest. The Ca^{2+}-force relation is computed using a forward Euler method with a fixed 0.1-ms time step, which is also the time step used to compute the cardiac mechanics (Appendix D). Local conductivities are adjusted to the local λ whenever the mechanical state is updated.

To compare 0.1-ms (see above) with 0.01-ms time steps, we performed two simulations with the same parameter settings, but with different time steps. The differences in conduction velocity (θ), membrane currents, ionic concentrations, and mechanical forces were negligible, but computation time was reduced by 75%.

6.2.8 Simulation protocol

To illustrate the excitation-contraction coupling in our model, we performed single-cell simulations with constant l_s (isosarcometric contraction) and single-cell simulations with constant applied force (isotonic contraction). The influence of I_{sac} on the AP was investigated by application of a constant stretch to a single cell (isometric simulation). The cell was electrically stimulated with a frequency of 1 Hz. For investigation of spontaneous activity under stretch, simulations were performed with increasing stretch, but without electrical stimulation.

The influence of stretch on θ was investigated by stimulating the first segment of a 1-cm fiber. The fiber was short, such that contraction of early-activated segments did not affect impulse propagation in later-activated regions. λ_{fiber} was kept constant during the simulation (isometric fiber contraction). We used longer (5 cm) fibers to investigate the influence of contraction on impulse propagation. Simulations were performed with contraction enabled and with contraction disabled. Disabled contraction was implemented by assuming that $[Ca^{2+}]_i$ was equal to its resting value of $0.102\ \mu M$ [37] when $F_{norm}([Ca^{2+}]_i, l_s)$ was computed. Thickness and stiffness were varied to simulate inhomogeneous cardiac tissue.

All simulations were performed over a 12-s period. Electrical stimulation was performed each 1 s (1 Hz) or each 0.5 s (2 Hz) by application of a stimulus current. In the case of single-cell simulations, a stimulus current of 20 pA/pF was applied for 2 ms as described by Courtemanche *et al.* [37]. In the case of fiber simulations, the leftmost or the rightmost segment was stimulated by application of a stimulus current of 100 pA/pF until the membrane was depolarized. For the 1-cm fiber, the overall θ was measured by determination of the moment of excitation of two segments located 1 mm from each of the fiber ends. For the 5-cm (inhomogeneous) fiber, local θ was computed for each segment using the excitation time between two segments located 0.5 mm to the left and to the right in the nonstretched fiber.

6.3   Results

6.3.1   Isosarcometric contraction

Figure 6.5 illustrates the relation between the electrophysiology described by the model of Courtemanche *et al.* [37] and the force-producing states described by the model of Rice *et al.* [157, 158]. For the V_{mem} trace in Figure 6.5, AP duration (APD) at 50% repolarization (APD$_{50}$) and APD at 90% repolarization (APD$_{90}$) are 184 and 304 ms, respectively. The AP amplitude and AP
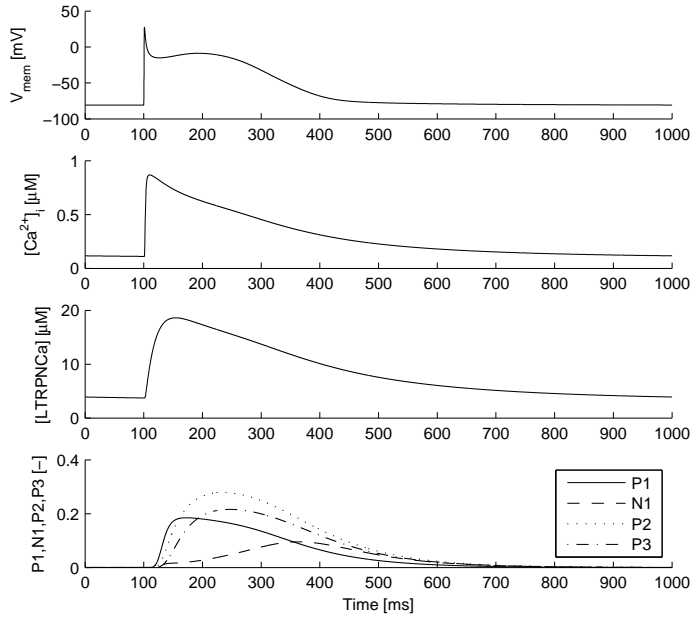
Figure 6.5: V_{mem}, $[Ca^{2+}]_i$, concentration of Ca^{2+} bound to low-affinity troponin sites [LTRPNCa], and fraction of functional units in force-producing state *P1, N1, P2,* or *P3* for $l_s = 2.3\ \mu m$. A stimulus current was applied at 100 ms. Traces from 12th action potential (AP) are shown for stimulation at 1 Hz. I_{sac} was disabled.

overshoot are 107 mV and 28 mV, respectively, and the maximum upstroke velocity $(dV_{mem}/dt)_{max}$ is 187 V/s. For the Ca^{2+} transient, resting $[Ca^{2+}]_i$ is 0.11 μM, peak $[Ca^{2+}]_i$ is 0.87 μM, and time required to return $[Ca^{2+}]_i$ to one-half of maximum $[Ca^{2+}]_i$ is 178 ms. Since the dynamics of the concentration of Ca^{2+} bound to low-affinity troponin sites ([LTRPNCa]) are governed by differential equation (6.21), the trace of [LTRPNCa] is smooth compared with that of $[Ca^{2+}]_i$.

From the traces of F_{norm} and individually normalized traces of F_{norm} for $l_s = 1.7\text{-}2.3\ \mu m$ in Figure 6.6, it can be observed that peak force, time to peak force, and relaxation time increase with increasing l_s, which is consistent with the experimental data measured by Janssen and Hunter [86].

6.3.2 Isotonic contraction

In Figure 6.7, traces of F_{norm}, F_{CE}, l_s, and l_{PE} are presented for simulations of isotonic contraction with applied force ($F_{segment}$) of 5-250 mN/mm². The AP

Table 6.2: AP characteristics when I_{sac} is permeable to Ca^{2+} ($G_{sac} = 0.015\ \mu m/s$)

λ	V_{rest}	$(dV_{mem}/dt)_{max}$	APA	APD$_{90}$	APD$_{50}$	$[Ca^{2+}]_{i,max}$	$\tau_{Ca^{2+}}$
[−]	[mV]	[V/s]	[mV]	[ms]	[ms]	[μM]	[ms]
1.00	−74.9	176	98.6	358	188	1.00	158
1.05	−73.7	170	95.6	370	190	1.02	155
1.10	−72.1	163	91.6	386	193	1.06	150
1.15	−69.9	148	84.9	410	200	1.11	144
1.20	−66.2	124	73.7	442	211	1.18	136
1.25	−56.7	88	57.7	388	205	1.31	123

AP, action potential; V_{rest}, resting potential; $(dV_{mem}/dt)_{max}$, maximum upstroke velocity; APA, AP amplitude; APD$_{90}$ and APD$_{50}$, AP duration at 90% and 50% repolarization; $[Ca^{2+}]_i$, intracellular Ca^{2+} concentration; $\tau_{Ca^{2+}}$, time required to return $[Ca^{2+}]_i$ to one-half of $[Ca^{2+}]_{i,max}$; G_{sac}, maximum I_{sac} conductance.

and Ca^{2+} transient are the same as in Figure 6.5. Less time is required to return F_{norm} to its resting value than in the case of isosarcometric contraction (Figure 6.6, top). This is explained by shortening of the sarcomeres during contraction: a shorter sarcomere yields a lower contractile force (Figure 6.2, bottom). The F_{CE} traces exhibit a plateau phase for $F_{segment} \leq 25$ mN/mm^2. For $F_{segment} = 250$ mN/mm^2, l_{PE} remains constant, indicating no shortening.

6.3.3 Effect of I_{sac} on action potential

Figure 6.8 illustrates the effect of I_{sac} on the AP. V_{mem}, I_{sac}, $I_{Ca,L}$, and $[Ca^{2+}]_i$ are presented for I_{sac} permeable to Ca^{2+} and I_{sac} not permeable to Ca^{2+} for $\lambda = 1.00$, 1.10, and 1.20. The cell was stimulated with a frequency of 1 Hz. With increasing λ, repolarization is prolonged and the resting V_{mem} is depolarized. I_{sac} is small during the plateau phase and larger during repolarization and rest, which is consistent with a reversal potential between 0 and −1 mV. $I_{Ca,L}$ is somewhat lowered under stretch, and the Ca^{2+} transient is increased. The lowered $I_{Ca,L}$ is explained by the Ca^{2+}-dependent inactivation of $I_{Ca,L}$ [37]. Interestingly, whether I_{sac} is permeable or not permeable to Ca^{2+}, the Ca^{2+} transient increases with increasing stretch. The characteristics for the AP and the Ca^{2+} transient are presented in Table 6.2 for I_{sac} permeable to Ca^{2+} and in Table 6.3 for I_{sac} not permeable to Ca^{2+}. For I_{sac} permeable to Ca^{2+}, peak $[Ca^{2+}]_i$ and the time required for return of $[Ca^{2+}]_i$ to one-half of maximum $[Ca^{2+}]_i$ is increased ~3%.

Table 6.3: AP characteristics when I_{sac} is not permeable to Ca^{2+} ($G_{sac} = 0.010\,\mu m/s$)

λ	V_{rest}	$(dV_{mem}/dt)_{max}$	APA	APD_{90}	APD_{50}	$[Ca^{2+}]_{i,max}$	$\tau_{Ca^{2+}}$
[−]	[mV]	[V/s]	[mV]	[ms]	[ms]	[μM]	[ms]
1.00	−75.3	176	99.3	353	188	0.98	161
1.05	−74.2	171	96.6	363	190	1.00	158
1.10	−72.7	166	93.3	377	192	1.03	154
1.15	−70.1	152	87.2	398	198	1.07	149
1.20	−67.8	132	77.9	428	207	1.12	142
1.25	−61.5	104	63.7	431	214	1.22	131

6.3.4 Stretch-induced action potentials

Figure 6.9 illustrates the effect of increasing λ in the presence of I_{sac}. V_{mem}, I_{sac}, $I_{Ca,L}$, and $[Ca^{2+}]_i$ are presented for λ linearly increasing from 1.00 at 0-ms simulation to 1.25, 1.35, and 1.45 at 200-ms simulation; λ is constant after 200 ms. In both cases, stretch-induced APs were elicited for $\lambda = 1.35$ and 1.45. The APs for $\lambda = 1.35$ have a low upstroke steepness and are mainly driven by $I_{Ca,L}$. $I_{Ca,L}$ increases faster for $\lambda = 1.35$ when I_{sac} is permeable to Ca^{2+}, which explains why V_{mem} reaches its maximum 50 ms earlier than when I_{sac} is not permeable to Ca^{2+}. For I_{sac} permeable to Ca^{2+} and for I_{sac} not permeable to Ca^{2+}, the sarcoplasmic Ca^{2+} flux signal for the Ca^{2+} release current (I_{rel}) is too small to trigger Ca^{2+} release from the SR. This explains why no Ca^{2+} transients are observed for $\lambda = 1.35$.

6.3.5 Effect of R_{junc0}/R_{int0} on conduction velocity

To investigate the influence of R_{junc0}/R_{int0} on θ, we simulated impulse propagation along a 1-cm fiber for various R_{junc0}/R_{int0} and λ_{fiber}. I_{sac} was disabled in these simulations ($G_{sac} = 0.0\,\mu m/s$). In Figure 6.10, the overall θ is presented for $R_{junc0}/R_{int0} = 0.0\text{-}1.0$, and $\lambda_{fiber} = 1.0\text{-}1.4$. For $R_{junc0}/R_{int0} = 1.0$, θ is little affected by increasing λ_{fiber}; for lower values of R_{junc0}/R_{int0}, θ decreases with increasing λ_{fiber}. The decrease in θ is almost linear for $R_{junc0}/R_{int0} = 0.4\text{-}0.8$.

6.3.6 Isometric fiber contraction

To investigate the influence of I_{sac} on impulse propagation, we simulated a series of isometric contractions in a 1-cm-long fiber. G_{sac} and λ_{fiber} were varied

(G_{sac} = 0.0-0.020 μm/s, λ_{fiber} = 1.0-1.4). The leftmost segment was electrically stimulated with a frequency of 1 Hz. In Figure 6.11, θ and $(dV_{mem}/dt)_{max}$ are presented for various G_{sac} and λ_{fiber}. With increasing G_{sac}, θ first increases and then decreases, while $(dV_{mem}/dt)_{max}$ decreases. The increase in θ is explained by the fact that, due to the increased resting V_{mem}, less charge is required by the downstream segments to reach the excitation threshold, whereas the decrease in θ is explained by the lower $(dV_{mem}/dt)_{max}$. When I_{sac} was permeable to Ca^{2+}, block of impulse propagation occurred for $\lambda_{fiber} \geq 1.35$ for G_{sac} = 0.010 μm/s, $\lambda_{fiber} \geq 1.25$ for G_{sac} = 0.015 μm/s, and $\lambda_{fiber} \geq 1.15$ for G_{sac} = 0.020 μm/s. When I_{sac} was not permeable to Ca^{2+}, block of impulse propagation occurred for $\lambda_{fiber} \geq 1.25$ for G_{sac} = 0.010 μm/s, $\lambda_{fiber} \geq 1.10$ for G_{sac} = 0.015 μm/s, and $\lambda_{fiber} \geq 1.05$ for G_{sac} = 0.020 μm/s.

In Figure 6.12, the APs and traces of I_{sac}, $I_{Ca,L}$, and $[Ca^{2+}]_i$ are presented for the center segment (λ_{fiber} = 1.00, 1.10, and 1.20). Traces of $I_{sac,Na}$, $I_{sac,K}$, and $I_{sac,Ca}$ are shown in Figure 6.13. As expected, I_{sac} increases with increasing λ during repolarization and rest. As in the single-cell simulations (Figure 6.8), $I_{Ca,L}$ decreases and $[Ca^{2+}]_i$ increases with increasing stretch. Since depolarization is mainly driven by I_{Na}, we further examine I_{Na} to investigate the cause of the decrease in θ and $(dV_{mem}/dt)_{max}$. The ionic current I_{Na} is defined by

$$I_{Na} = G_{Na}m^3hj(V_{mem} - E_{Na}), \tag{6.36}$$

where G_{Na} is the maximum I_{Na} conductance, E_{Na} is the equilibrium potential for Na$^+$, m is the fast activation variable, and h and j are the fast and slow inactivation variables [37] (Appendix A). In Figure 6.14, traces of m, h, j, and I_{Na} are presented for the center segment (λ_{fiber} = 1.00, 1.10, and 1.20). As λ_{fiber} increases, h and j are lower during rest and explain the lower I_{Na} current during depolarization; i.e., the membrane is less excitable. Except for I_{to} and I_{Kur}, all ionic currents were similar during the upstroke and shortly after the upstroke (not shown). I_{to} and I_{Kur} were smaller and caused the less prominent notch of the AP (Figure 6.12).

6.3.7 Impulse propagation along a homogeneous fiber

To investigate the effect of contraction of early-activated areas on θ in later-activated areas, we simulated impulse propagation along a 5-cm-long fiber with λ_{fiber} = 1.00, 1.05, 1.10, 1.15, and 1.20 (G_{sac} = 0.015 μm/s, $P_{Na} : P_K : P_{Ca}$ = 1 : 1 : 1). All simulations were performed with contraction enabled as well as with contraction disabled. Impulse propagation was initiated by application of a stimulus current to the leftmost segment.

In Figure 6.15, traces of V_{mem}, I_{sac}, $[Ca^{2+}]_i$, and λ are presented for segments located 1.0, 2.5, and 4.0 cm from the stimulation site (λ_{fiber} = 1.15). With con-

traction enabled, the early-activated segments start contracting, so that λ increases for the later-activated segments, which results in an increased I_{sac} and a depolarized resting V_{mem}. In Figure 6.16, θ and $(dV_{\text{mem}}/dt)_{\text{max}}$ are presented with contraction disabled ($t_{\text{max}} = 1$, $s_{\text{max}} = 1$) and contraction enabled ($t_{\text{max}} = 1$, $s_{\text{max}} = 1$).

6.3.8 Impulse propagation along an inhomogeneous fiber

To investigate the effect of inhomogeneity in tissue properties on the conduction velocity, we simulated impulse propagation along an inhomogeneous 5-cm-long fiber with $\lambda_{\text{fiber}} = 1.00$, 1.05, 1.10, 1.15, and 1.20 ($G_{\text{sac}} = 0.015$ μm/s, $P_{\text{Na}} : P_{\text{K}} : P_{\text{Ca}} = 1 : 1 : 1$). For the left half of the fiber, $t_{\text{max}} = 1$-10 and $s_{\text{max}} = 1$-10. For the right half of the fiber, $t_{\text{min}} = 1$ and $s_{\text{min}} = 1$. Linear interpolation was applied in the central 0.5 cm of the fiber. As described above, all simulations were performed with contraction enabled as well as with contraction disabled. Impulse propagation was initiated by application of a stimulus current to the leftmost or the rightmost segment.

In Figure 6.16, θ and $(dV_{\text{mem}}/dt)_{\text{max}}$ are presented for various simulations after stimulation of the leftmost segment ($\lambda_{\text{fiber}} = 1.15$) with contraction disabled (top panels) and with contraction enabled (bottom panels). In thick and/or stiff tissue (left half of the fiber), θ was larger; in the remaining, more stretched, parts, θ was smaller. In areas where the depolarization wave traveled from thick tissue to thin tissue ($t_{\text{max}} \geq 5$), θ was locally increased, which is explained by the smaller amount of charge required by the downstream segments to reach the excitation threshold. Decrease of $(dV_{\text{mem}}/dt)_{\text{max}}$ and block of impulse propagation occurred in the inhomogeneous fibers when contraction was enabled.

In Figure 6.17, θ and $(dV_{\text{mem}}/dt)_{\text{max}}$ are presented for various simulations after stimulation of the rightmost segment ($\lambda_{\text{fiber}} = 1.15$) with contraction disabled (top panels) and with contraction enabled (bottom panels). In thick and/or stiff tissue (left half of the fiber), θ was larger; in the remaining, more stretched, parts, θ was smaller. In areas where the depolarization wave traveled from thin tissue to thick tissue ($t_{\text{max}} \geq 5$), θ was locally decreased, which is explained by the larger amount of charge required by the downstream segments to reach the excitation threshold. Conduction block was not observed after stimulation from the right. Thus, for $\lambda_{\text{fiber}} = 1.15$, conduction block was unidirectional when contraction was enabled.

In Figure 6.18, traces of V_{mem}, I_{sac}, $[\text{Ca}^{2+}]_i$, and λ are presented for three segments of an inhomogeneous fiber ($\lambda_{\text{fiber}} = 1.15$, $t_{\text{max}} = 10$ and $s_{\text{max}} = 1$) with contraction enabled and with contraction disabled. As shown in Figure 6.15, the early-activated segments start contracting, causing λ to increase for the

later-activated segments, which leads to an increased resting V_{mem}. The AP of the segment at 4.0 cm had a low upstroke steepness and, similar to the AP for $\lambda = 1.35$ in Figure 6.9, the Ca^{2+} transient was absent, such that no contraction occurred. From the rapid decrease in $(dV_{mem}/dt)_{max}$ at ∼4.0 cm (Figure 6.16, bottom), it can be concluded that this type of AP cannot generate enough current to propagate.

6.3.9 Short stimulation intervals and unidirectional block

To investigate the effect of a shorter stimulation interval on impulse propagation, we stimulated the 5-cm fibers with an interval of 500 ms (2 Hz). In Table 6.4, θ for left stimulation at 1 Hz and at 2 Hz are presented for the left half (1.0 → 2.5 cm) and for the right half (2.5 → 4.0 cm) of the fiber. Since stimulation at 2 Hz can lead to alternating impulse propagation and conduction block, we distinguish between even (each 1 s) and odd (each 0.5 s) stimulation. The same data are presented in Table 6.5 for right stimulation.

From Tables 6.4 and 6.5, it can be concluded that stimulation at 2 Hz in general leads to slower conduction and conduction block at lower λ. This is explained by a longer ERP under stretch (Figure 6.14). Figure 6.19 illustrates the subtle transition from conduction block in the leftmost 0.5 cm every other stimulation to normal impulse propagation every stimulation ($\lambda_{fiber} = 1.05$, $t_{max} = 1$, $s_{max} = 1$). In this case, the ERP decreased after each stimulation, such that after stimulation at 2100 ms, the AP could propagate. The decrease in ERP is visible in Figure 6.19 as the increasing I_{Na} inactivation gating variables h and j at the moment of stimulation (segment at 0.1 cm). After 2100 ms, the cells in the fiber are stimulated at a higher frequency, which leads to a shorter APD and a more decreased ERP. Thus, impulse propagation at a higher frequency becomes a stable situation.

When an inhomogeneous fiber is stimulated from the right, conduction block may occur at lower λ. This can be explained by prolongation of the repolarization phase of the AP. Figure 6.20 illustrates this situation for $\lambda_{fiber} = 1.10$, $t_{max} = 10$, and $s_{max} = 1$. The extended repolarization phase of the segment at 4.0 cm (which is close to the stimulation site) is caused by contraction of the later-activated segments in the left half of the fiber.
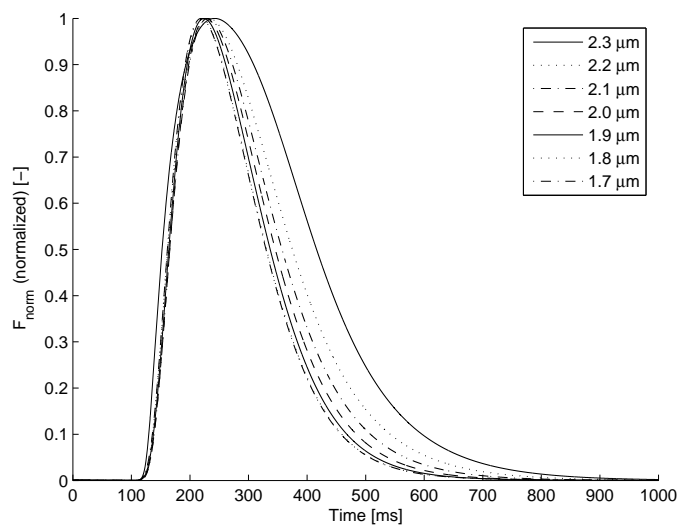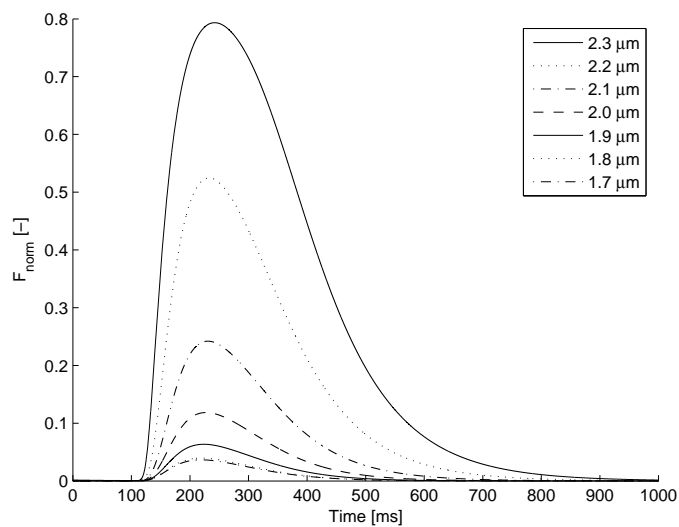
Figure 6.6: F_{norm} for $l_s = 1.7\text{-}2.3\,\mu$m (isosarcometric contraction). Top: F_{norm}. Bottom: F_{norm} individually normalized to maximum F_{norm}. A stimulus current was applied at 100 ms. Traces from 12th contraction are shown for stimulation at 1 Hz. I_{sac} was disabled.
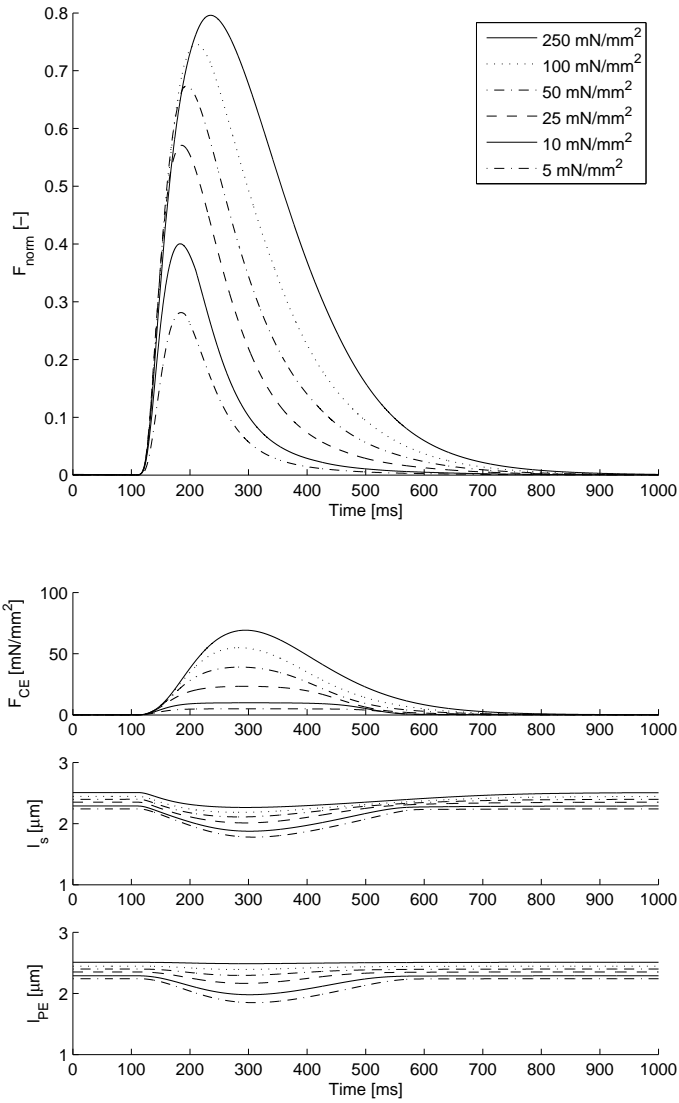
Figure 6.7: F_{norm}, F_{CE}, l_s, and segment length (l_{PE}) for isotonic contractions with applied force (F_{segment}) = 5-250 mN/mm^2. A stimulus current was applied at 100 ms. Traces from 12th contraction are shown for stimulation at 1 Hz. I_{sac} was disabled.
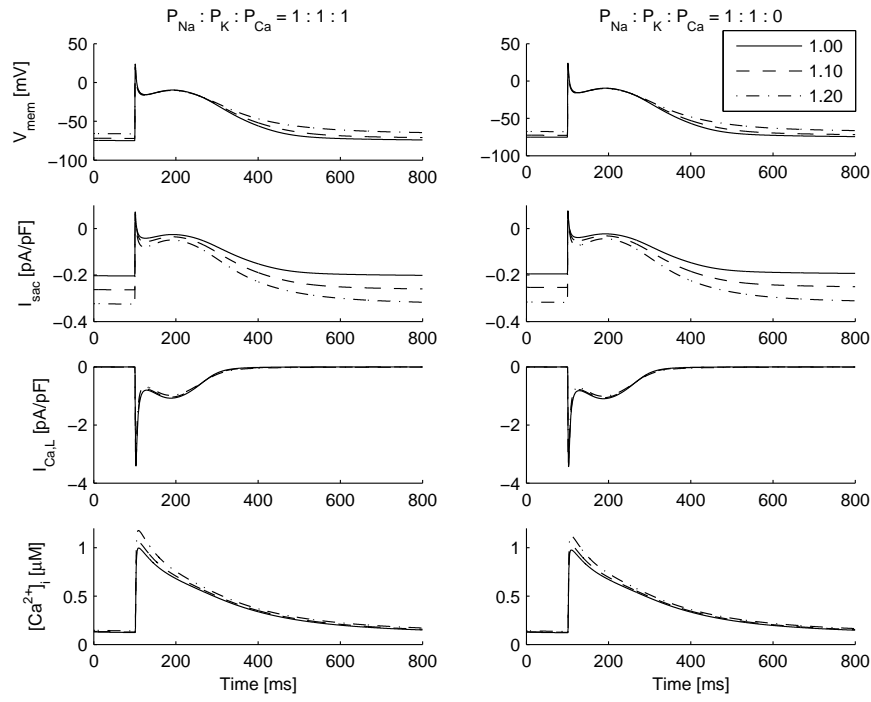
Figure 6.8: V_{mem}, I_{sac}, L-type inward Ca^{2+} current ($I_{Ca,L}$), and $[Ca^{2+}]_i$ for stretch applied to single cells at stretch ratio (λ) = 1.00, 1.10, and 1.20. Left: I_{sac} permeable to Ca^{2+} ($G_{sac} = 0.015\,\mu m/s$). Right: I_{sac} not permeable to Ca^{2+} ($G_{sac} = 0.010\,\mu m/s$). A stimulus current was applied at 100 ms.
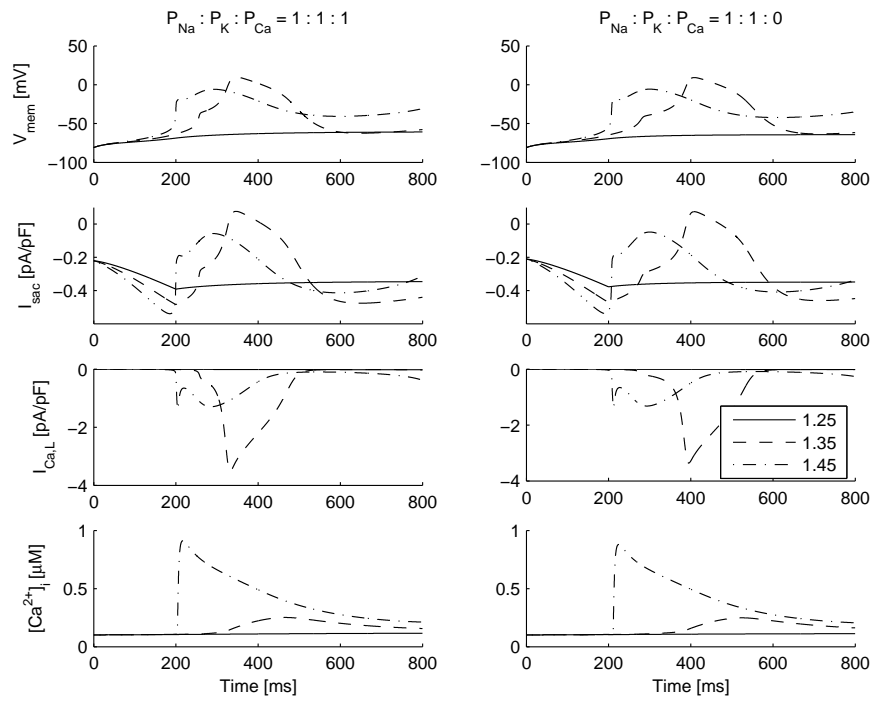
Figure 6.9: V_{mem}, I_{sac}, $I_{Ca,L}$, and $[Ca^{2+}]_i$ for stretch applied to single cells. λ was increased from 1.00 at 0-ms simulation to 1.25, 1.35, and 1.45 at 200 ms; λ was constant after 200 ms. Left: I_{sac} permeable to Ca^{2+} ($G_{sac} = 0.015\,\mu m/s$). Right: I_{sac} not permeable to Ca^{2+} ($G_{sac} = 0.010\,\mu m/s$). No stimulus current was applied.
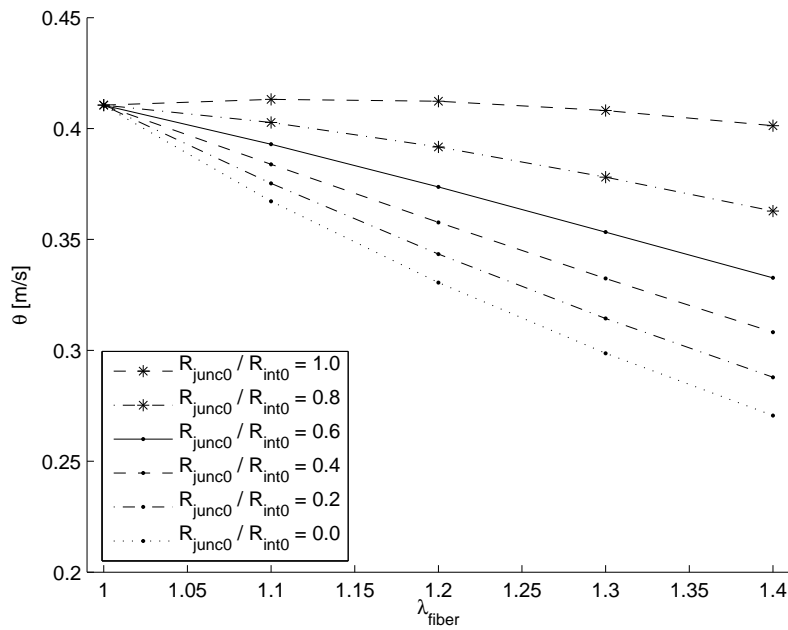
Figure 6.10: Overall conduction velocity (θ) for impulse propagation along a 1-cm fiber for relative gap-junctional resistivity (R_{junc0}/R_{int0}) = 0.0-1.0. Impulse propagation was initiated by application of a stimulus current to the 1st segment. I_{sac} was disabled.
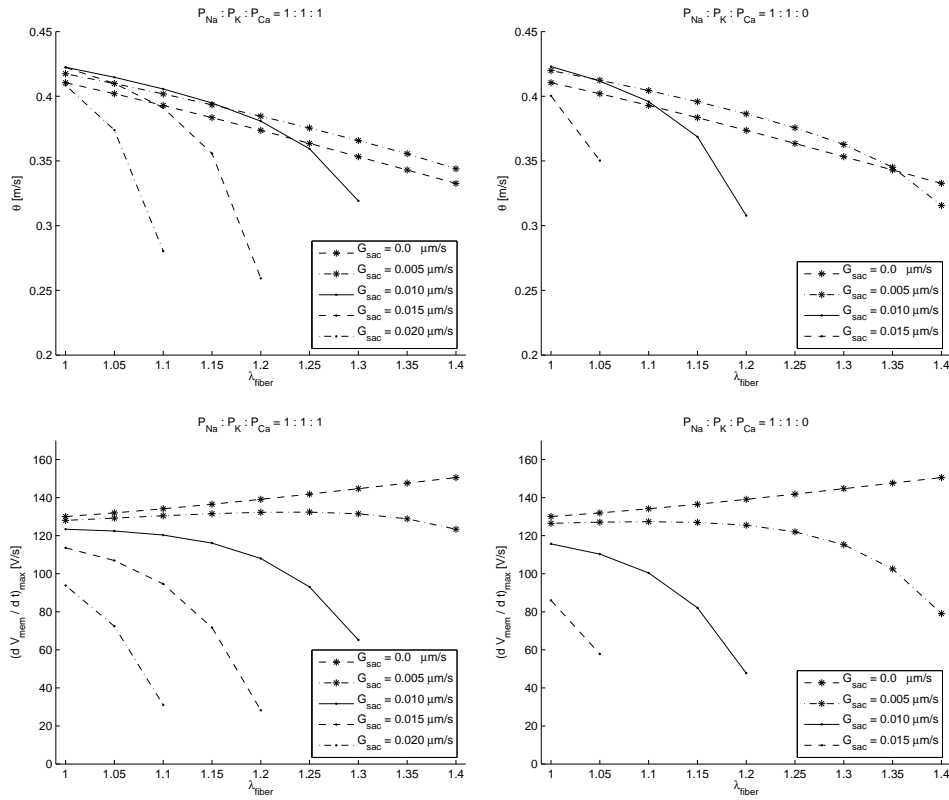
Figure 6.11: θ and maximum upstroke velocity $(dV_{mem}/dt)_{max}$ for impulse propagation along a 1-cm fiber ($R_{junc0}/R_{int0} = 0.6$). G_{sac} and λ_{fiber} were varied. Left: I_{sac} permeable to Ca^{2+}. Right: I_{sac} not permeable to Ca^{2+}. Impulse propagation was initiated by application of a stimulus current to the 1st segment.
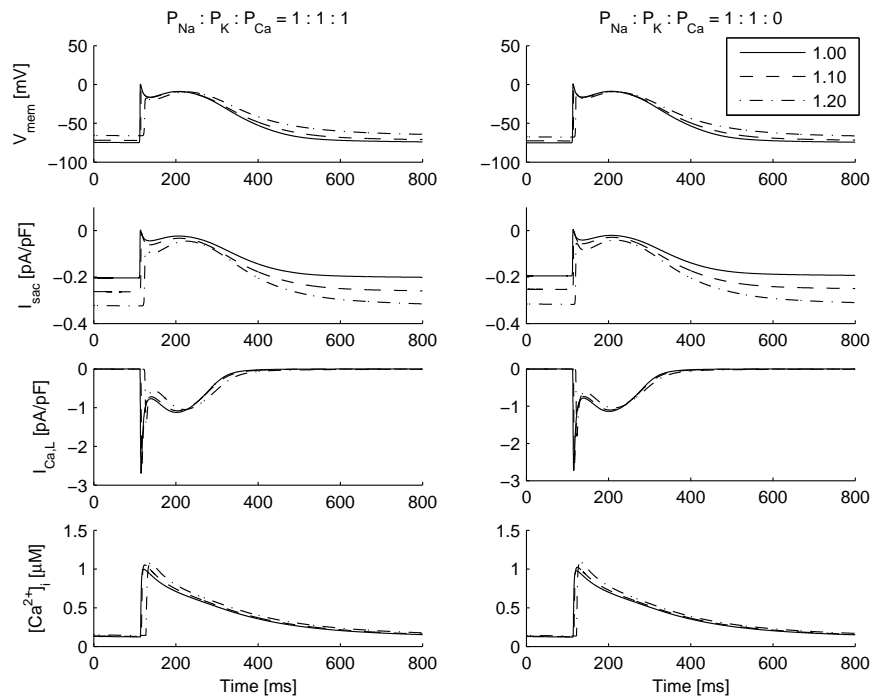
Figure 6.12: V_{mem}, I_{sac}, $I_{Ca,L}$, and $[Ca^{2+}]_i$ for the center segment of a 1-cm fiber ($\lambda_{fiber} =$ 1.00, 1.10, and 1.20). Left: I_{sac} permeable to Ca^{2+} ($G_{sac} = 0.015\ \mu m/s$). Right: I_{sac} not permeable to Ca^{2+} ($G_{sac} = 0.010\ \mu m/s$). A stimulus current was applied to the 1st segment at 100 ms.
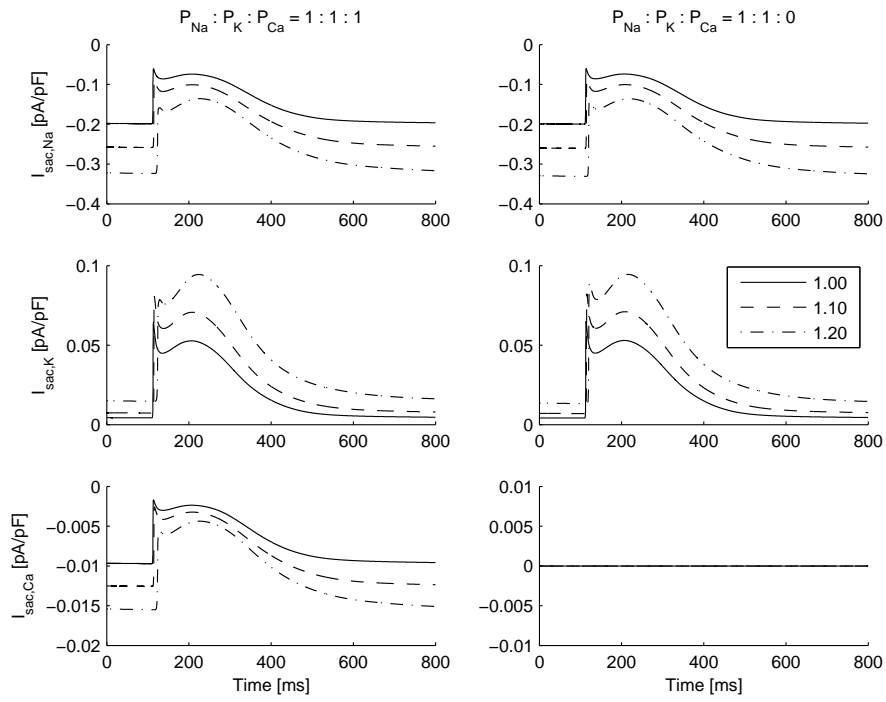
Figure 6.13: $I_{sac,Na}$, $I_{sac,K}$, and $I_{sac,Ca}$ for the center segment of a 1-cm fiber (λ_{fiber} = 1.00, 1.10, and 1.20). Left: I_{sac} permeable to Ca^{2+} (G_{sac} = 0.015 μm/s). Right: I_{sac} not permeable to Ca^{2+} (G_{sac} = 0.010 μm/s). A stimulus current was applied to the 1st segment at 100 ms.
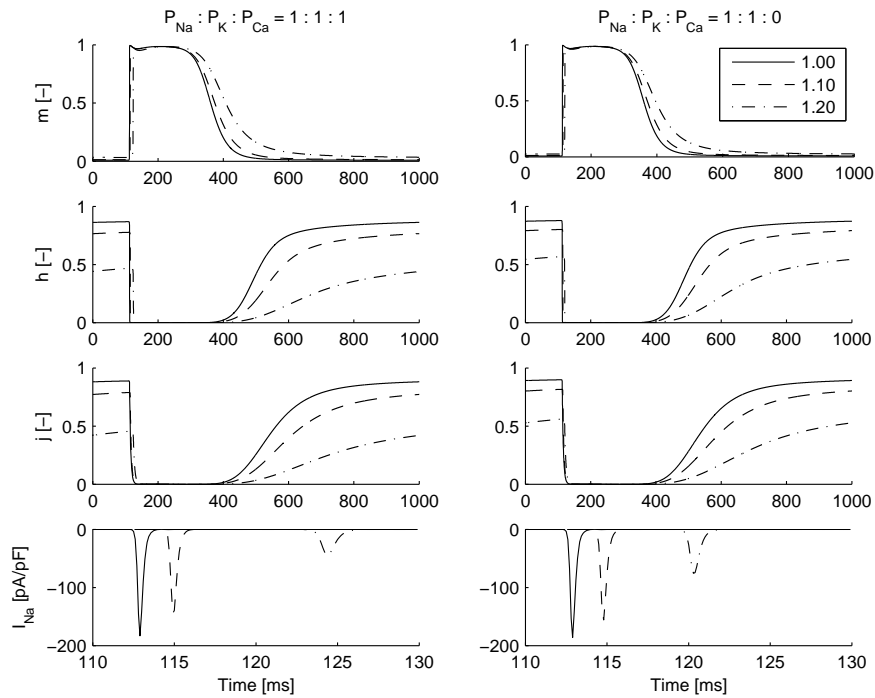
Figure 6.14: Activation gating variable (m), fast inactivation gating variable (h), and slow inactivation gating variable (j) for the fast inward Na$^+$ current I_{Na} of the center segment of a 1-cm fiber (λ_{fiber} = 1.00, 1.10, and 1.20). Left: I_{sac} permeable to Ca^{2+} (G_{sac} = 0.015 μm/s). Right: I_{sac} not permeable to Ca^{2+} (G_{sac} = 0.010 μm/s). A stimulus current was applied to the 1st segment at 100 ms. Note the different time scale for I_{Na}.
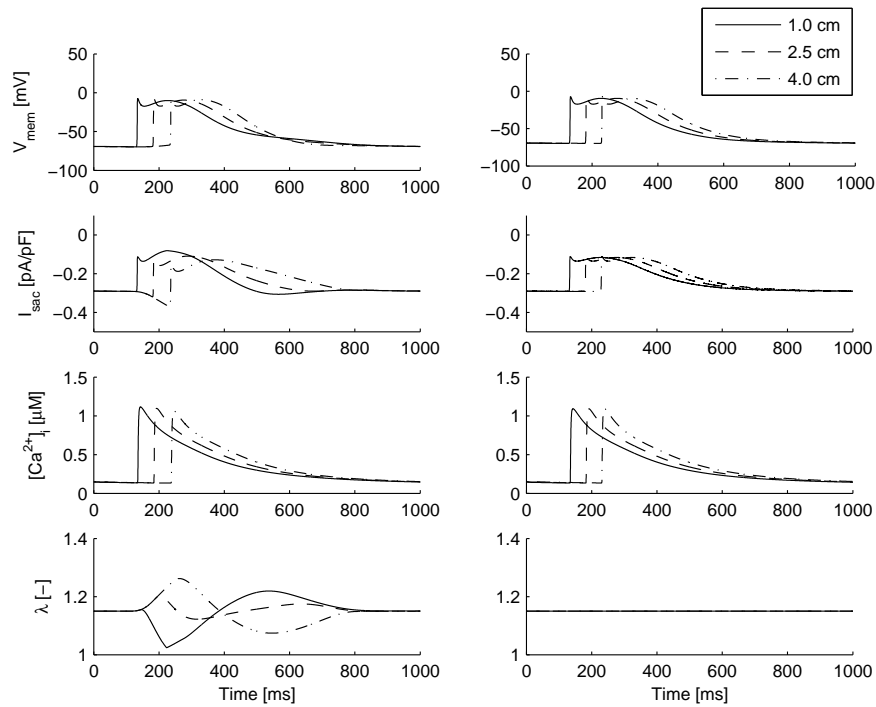
Figure 6.15: V_{mem}, I_{sac}, $[Ca^{2+}]_i$, and λ for 1.0-, 2.5-, and 4.0-cm segments of a homogeneous fiber with contraction enabled (left) and contraction disabled (right). Fiber length was 5 cm, I_{sac} was permeable to Ca^{2+} ($G_{sac} = 0.015\,\mu m/s$), and $\lambda_{fiber} = 1.15$. Impulse propagation was initiated by application of a stimulus current to the leftmost segment at 0 cm.
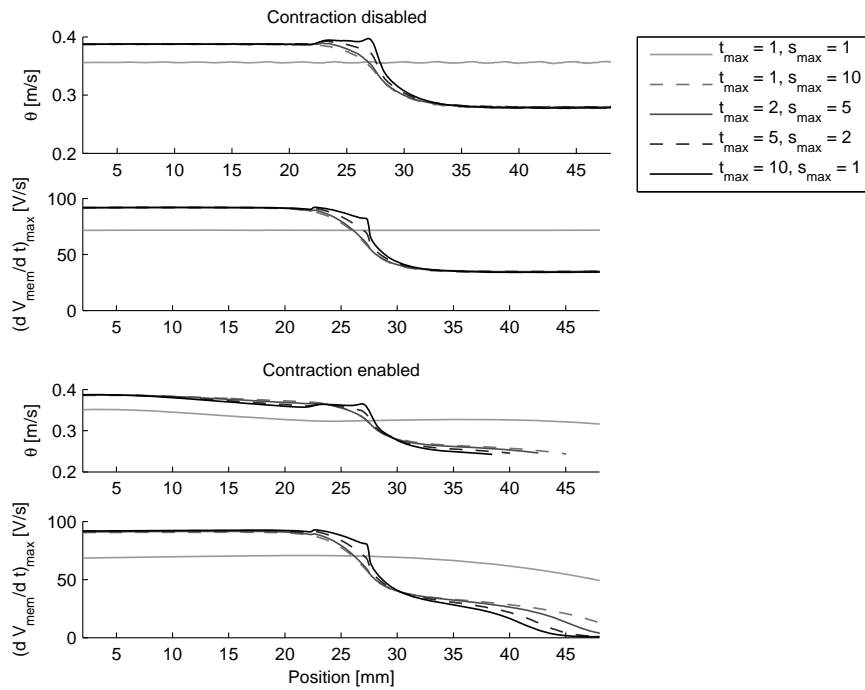
Figure 6.16: Left stimulation: θ and $(dV_{mem}/dt)_{max}$ for impulse propagation along a homogeneous fiber and various inhomogeneous fibers with contraction disabled (top panels) and enabled (bottom panels). I_{sac} was permeable to Ca^{2+} ($G_{sac} = 0.015$ $\mu m/s$). Fiber length = 5 cm, $\lambda_{fiber} = 1.15$. Impulse propagation was initiated by application of a stimulus current to the leftmost segment. t_{max} and s_{max}, scaling factors for thickness and stiffness, respectively.
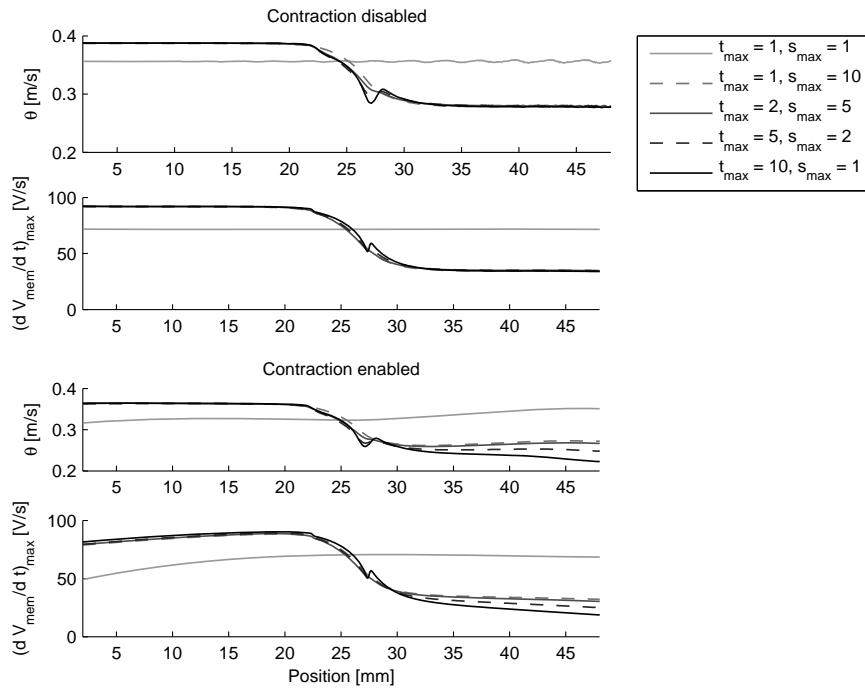
Figure 6.17: Right stimulation: θ and $(dV_{mem}/dt)_{max}$ for impulse propagation along a homogeneous fiber and various inhomogeneous fibers with contraction disabled (top panels) and enabled (bottom panels). I_{sac} was permeable to Ca^{2+} ($G_{sac} = 0.015$ μm/s). Fiber length = 5 cm, $\lambda_{fiber} = 1.15$. Impulse propagation was initiated by application of a stimulus current to the rightmost segment.
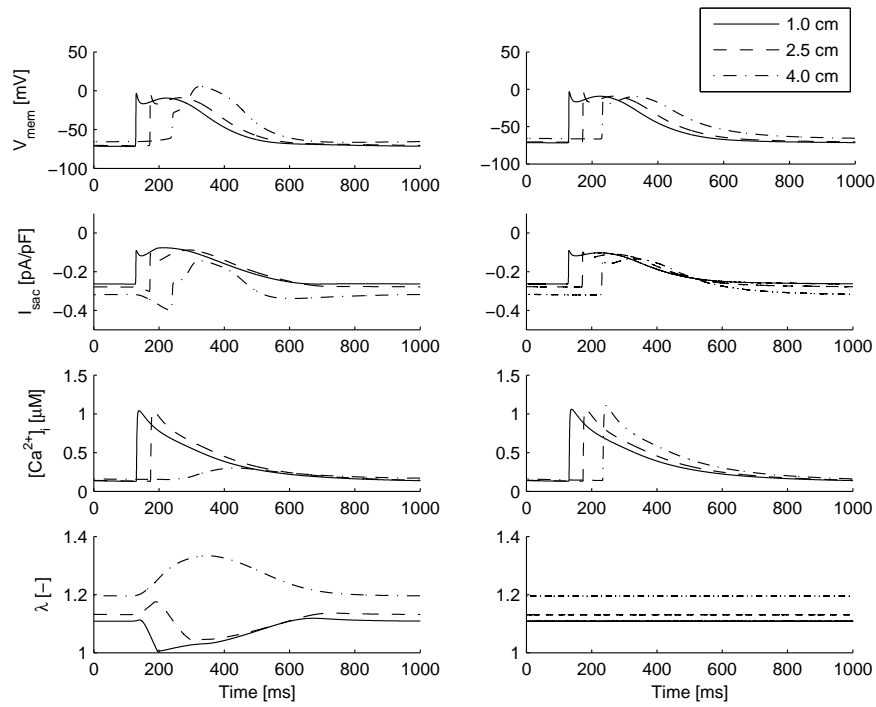
Figure 6.18: V_{mem}, I_{sac}, $[Ca^{2+}]_i$, and λ for 1.0-, 2.5-, and 4.0-cm segments of an inhomogeneous fiber ($t_{max} = 10$, $s_{max} = 1$) with contraction enabled (left) and disabled (right). Fiber length was 5 cm, I_{sac} was permeable to Ca^{2+} ($G_{sac} = 0.015$ μm/s), and $\lambda_{fiber} = 1.15$. Impulse propagation was initiated by application of a stimulus current to the leftmost segment at 0 cm.
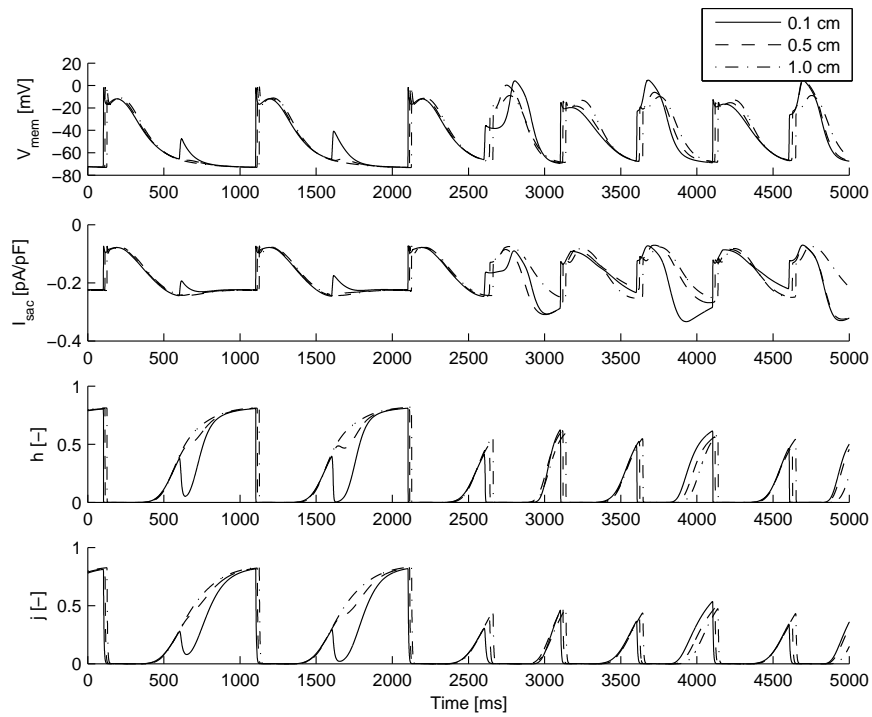
Figure 6.19: V_{mem}, I_{sac}, h, and j for 0.1-, 0.5-, and 1.0-cm segments of a homogeneous fiber stimulated with an interval of 500 ms. Fiber length was 5 cm ($t_{max} = 1$, $s_{max} = 1$), I_{sac} was permeable to Ca^{2+} ($G_{sac} = 0.015\,\mu$m/s), and $\lambda_{fiber} = 1.05$. Impulse propagation was initiated by application of a stimulus current to the leftmost segment at 0 cm.
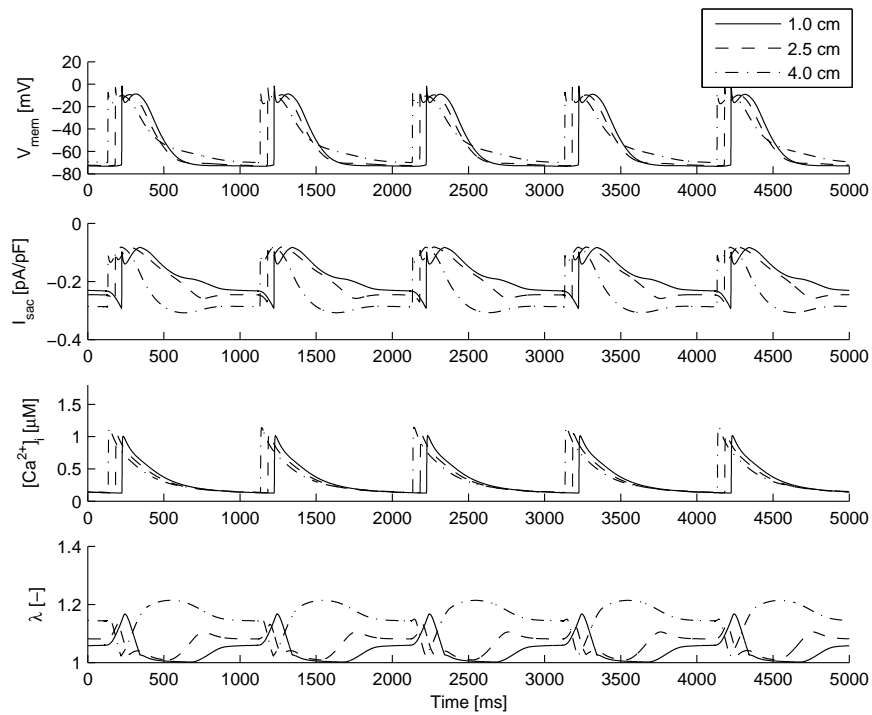
Figure 6.20: V_{mem}, I_{sac}, $[Ca^{2+}]_i$, and λ for 1.0-, 2.5-, and 4.0-cm segments of an inhomo-geneous fiber stimulated with an interval of 500 ms. Fiber length was 5 cm ($t_{max} = 10$, $s_{max} = 1$), I_{sac} was permeable to Ca^{2+} ($G_{sac} = 0.015$ μm/s), and $\lambda_{fiber} = 1.10$. Impulse propagation was initiated by application of a stimulus current to the rightmost seg-ment at 5.0 cm.

Table 6.4: Conduction velocity for left stimulation

λ_{fiber}	t_{max}	s_{max}	θ (1 Hz)	θ (1 Hz)	θ (2 Hz) Even	θ (2 Hz) Even	θ (2 Hz) Odd	θ (2 Hz) Odd
			$1 \to 2.5$	$2.5 \to 4$	$1 \to 2.5$	$2.5 \to 4$	$1 \to 2.5$	$2.5 \to 4$
[−]	[−]	[−]	[m/s]	[m/s]	[m/s]	[m/s]	[m/s]	[m/s]
1.00	1	1	0.42	0.42	0.34	0.35	0.34	0.35
1.00	1	10	0.42	0.42	0.34	0.35	0.34	0.35
1.00	2	5	0.42	0.42	0.35	0.35	0.35	0.35
1.00	5	2	0.42	0.42	0.35	0.35	0.35	0.35
1.00	10	1	0.42	0.42	0.35	0.35	0.35	0.35
1.05	1	1	0.39	0.39	0.29	0.35	0.29	0.36
1.05	1	10	0.41	0.39	0.27	0.31	0.29	0.32
1.05	2	5	0.41	0.39	0.28	0.25	0.31	0.28
1.05	5	2	0.41	0.39	0.33	0.31	0.31	0.24
1.05	10	1	0.42	0.40	0.34	0.34	0.34	bl
1.10	1	1	0.37	0.36	0.37	0.36	bl	bl
1.10	1	10	0.39	0.35	bl	bl	0.42	0.34
1.10	2	5	0.39	0.35	bl	bl	0.42	0.34
1.10	5	2	0.39	0.35	0.33	bl	0.33	bl
1.10	10	1	0.39	0.35	0.34	bl	0.34	bl
1.15	1	1	0.33	0.33	0.33	0.33	bl	bl
1.15	1	10	0.37	0.28	0.37	0.28	bl	bl
1.15	2	5	0.37	0.28	0.37	nc	bl	bl
1.15	5	2	0.37	0.27	bl	bl	0.34	nc
1.15	10	1	0.37	nc	0.29	bl	0.26	nc
1.20	1	1	0.23	nc	0.23	nc	bl	bl
1.20	1	10	0.33	nc	0.33	nc	bl	bl
1.20	2	5	0.33	nc	0.33	nc	bl	bl
1.20	5	2	0.33	nc	0.32	nc	bl	bl
1.20	10	1	0.33	nc	0.32	nc	bl	bl

θ, conduction velocity; Even, stimulation each 1 s; Odd, stimulation each 0.5 s; $1 \to 2.5$, θ from 1 cm to 2.5 cm; $2.5 \to 4$, θ from 2.5 cm to 4 cm; nc, no contraction: AP propagation without contraction; bl, block: no AP propagation.

Table 6.5: Conduction velocity for right stimulation

λ_{fiber}	t_{max}	s_{max}	θ (1 Hz)	θ (1 Hz)	θ (2 Hz) Even	θ (2 Hz) Even	θ (2 Hz) Odd	θ (2 Hz) Odd
			$1 \leftarrow 2.5$	$2.5 \leftarrow 4$	$1 \leftarrow 2.5$	$2.5 \leftarrow 4$	$1 \leftarrow 2.5$	$2.5 \leftarrow 4$
[−]	[−]	[−]	[m/s]	[m/s]	[m/s]	[m/s]	[m/s]	[m/s]
1.00	1	1	0.42	0.42	0.35	0.34	0.35	0.34
1.00	1	10	0.42	0.42	0.35	0.34	0.35	0.34
1.00	2	5	0.42	0.42	0.34	0.34	0.34	0.34
1.00	5	2	0.42	0.41	0.34	0.33	0.34	0.33
1.00	10	1	0.42	0.41	0.34	0.33	0.34	0.33
1.05	1	1	0.39	0.39	0.35	0.29	0.36	0.29
1.05	1	10	0.39	0.38	bl	bl	0.39	0.38
1.05	2	5	0.39	0.38	0.39	0.38	0.38	0.30
1.05	5	2	0.39	0.37	0.39	0.37	bl	bl
1.05	10	1	0.40	0.37	0.39	0.37	bl	bl
1.10	1	1	0.36	0.37	0.36	0.37	bl	bl
1.10	1	10	0.38	0.34	0.38	0.35	bl	bl
1.10	2	5	0.38	0.34	0.38	0.34	bl	bl
1.10	5	2	0.38	0.34	0.37	0.34	bl	bl
1.10	10	1	0.37	0.33	0.37	0.33	bl	bl
1.15	1	1	0.33	0.33	0.33	0.33	bl	bl
1.15	1	10	0.36	0.27	0.36	0.27	bl	bl
1.15	2	5	0.36	0.26	0.36	0.26	bl	bl
1.15	5	2	0.36	0.26	0.36	0.26	bl	bl
1.15	10	1	0.36	0.25	0.36	0.25	bl	bl
1.20	1	1	nc	0.23	nc	0.23	bl	bl
1.20	1	10	bl	bl	bl	bl	bl	bl
1.20	2	5	bl	bl	bl	bl	bl	bl
1.20	5	2	bl	bl	bl	bl	bl	bl
1.20	10	1	bl	bl	bl	bl	bl	bl

θ, conduction velocity; Even, stimulation each 1 s; Odd, stimulation each 0.5 s; $1 \leftarrow 2.5$, θ from 2.5 cm to 1 cm; $2.5 \leftarrow 4$, θ from 4 cm to 2.5 cm; nc, no contraction: AP propagation without contraction; bl, block: no AP propagation.

6.4 Discussion

In our model, contraction of the cardiac fiber is triggered by the Ca^{2+} transient, which occurs after depolarization of the membrane. By modeling I_{sac}, contraction of early-activated parts of the fiber leads to stretch in the later-activated parts and influences impulse propagation, APD, and ERP. For increasing levels of applied stretch, we observed conduction block, which can be unidirectional in an inhomogeneous fiber.

6.4.1 Conduction slowing and effective refractory period

Our model provides two mechanisms to explain conduction slowing as observed in acutely dilated atria [32, 53, 54, 79, 153]: 1) the decrease in tissue conductivity due to stretch and 2) a decreased membrane excitability caused by I_{sac} (Figure 6.11). In an experimental study, Eijsbouts *et al.* [54] reported a decreased θ and local conduction block when the right atrium of a rabbit was acutely dilated. They increased atrial pressure from 2 to 9 and 14 cmH_2O and measured λ as well as θ. With increasing pressure, θ first increases and then decreases for normal stimulation (240-ms interval). For fast stimulation (125-ms interval), θ decreases nonlinearly with increasing pressure [54]. In our model, θ decreases linearly with increasing λ when no I_{sac} is present (Figure 6.10). It is therefore likely that the nonlinear decrease in θ observed by Eijsbouts *et al.* is explained by a reduced excitability of the membrane, rather than a reduced tissue conductivity. Eijsbouts *et al.* [53, 54] also observed an increase in conduction block when the atrium was stimulated at a higher frequency, which is consistent with our findings (Tables 6.4 and 6.5).

Similar to our results, Shaw and Rudy [170] observed slowing of impulse propagation related to a reduced membrane excitability in a simulation study of impulse propagation in ischemic cardiac tissue. The extracellular K^+ concentration ($[K^+]_e$) was increased, which leads to a depolarized V_{mem} and a reduced $(dV_{mem}/dt)_{max}$. Their simulation results [170] correspond to experimental results [90]. Kléber and Rudy [103] explain the decreased θ in these experiments by a significant Na^+ channel inactivation. The result is a depressed membrane excitability (reduced $(dV_{mem}/dt)_{max}$), reduced θ, and, eventually, conduction block [103]. Thus their explanation for conduction slowing and block in ischemic tissue is similar to our explanation for conduction slowing and block under stretch.

In an experimental study, Sung *et al.* [192] observed a decrease in θ and an increase in APD when end-diastolic pressure was increased in the left ventricle of isolated rabbit hearts. Interestingly, the SAC blocker streptomycin had little effect on θ and APD [192]. Satoh and Zipes [166] measured differences

in ERP in the thin atrial free wall and the crista terminalis. Under stretch, the ERP of the thin free wall was increased more than that in the thicker crista terminalis. Satoh and Zipes explain this difference by assuming that the thin free wall is more stretched compared with the thicker parts. Huang *et al.* [79] observed slow conduction related to a shorter stimulation interval in dilated atria, but they did not measure a significant change in atrial ERP after dilatation. Conduction slowing in our model at a 500-ms stimulation interval is attributed to a longer ERP under stretch. From these observations, we conclude that experimentally observed changes in conduction and atrial ERP can be explained by I_{sac}.

6.4.2 Clinical relevance

AF is associated with hemodynamic or cardiomechanical disorders such as hypertension, mitral valve disease, and cardiac failure [92]. Ravelli *et al.* [154] found that atrial stretch caused by contraction of the ventricles influences atrial flutter cycle length in humans. Experimentally, it has been observed that acute atrial dilatation facilitates the induction and maintenance of AF in rabbit atria [16, 153] and in canine atria [79, 166]. Bode *et al.* [16] report that the SAC blocker Gd^{3+} reduces the stretch-induced vulnerability to AF, confirming that I_{sac} plays a significant role in the vulnerability to AF in acutely dilated atria.

In the present study, we observed conduction slowing, an increased ERP, and (unidirectional) conduction block with increasing stretch. These phenomena are attributed to I_{sac} and can lead to alternating impulse propagation and contractions at a stimulation frequency of 2 Hz. Conduction slowing [79], unidirectional block [103], and dispersion in atrial ERP [166] are related to the inducibility of AF. In the present study, these effects begin at $\lambda = 1.15$ and 1.05 for stimulation at 1 and 2 Hz, respectively. Bode *et al.* [16] gradually increased intra-atrial pressure in rabbit hearts up to 30 cmH$_2$O. They could not induce AF in the undilated atrium at 0 cmH$_2$O, but they observed a 50% probability of AF induction at 8.8 cmH$_2$O (baseline) and at 19.0 cmH$_2$O (after Gd^{3+}), which increased to 100% (baseline) and 90% (after Gd^{3+}) when pressure was further increased [16]. However, stretch was not measured in that study. Eijsbouts *et al.* [54] measured $\lambda = 1.16 \pm 0.14$ at 9 cmH$_2$O, confirming our model predictions that the vulnerability to AF is substantially increased when λ is ~1.15.

6.4.3 Model validity and limitations

To our best knowledge, our model is the first to integrate cardiac electrophysiology and cardiomechanics with physiological details such as ionic membrane currents, intracellular Ca^{2+} handling, and cross-bridge formation. In our model, changes in impulse propagation under stretch are related to I_{sac} and to a reduced conductivity. We do not consider other mechanisms that could influence impulse propagation, such as stretch-related function of other membrane channels, autonomic reflexes, and metabolic changes.

The validity of our model largely depends on the validity of the underlying models and parameters. Validity and limitations of the models for the ionic membrane currents, cross-bridge formation, and cardiomechanics are extensively discussed elsewhere [37, 158, 176, 230]. Here, we discuss the validity and limitations of the integrated model with respect to the Ca^{2+}-force relation, excitation-contraction coupling, stretch and fiber conductivity, I_{sac}, intracellular ion concentrations, Ca^{2+}-troponin binding, and the Ca^{2+} transient.

Ca^{2+}-force relation Rice *et al.* [158] proposed five models of isometric force generation in cardiac myofilaments. These are constructed assuming different subsets of three putative cooperative mechanisms [158]. *Model 4* assumes that the binding of a cross bridge increases the rate of formation of neighboring cross bridges and that multiple cross bridges can maintain activation of the thin filament in the absence of Ca^{2+}. The model also simulates end-to-end interactions between adjacent troponin and tropomyosin. The hypothesis that cross-bridge binding increases the affinity of troponin for Ca^{2+} is assumed by *model 5*, but not by *model 4*.

To choose between *model 4* and *model 5* for the present study, we studied the Ca^{2+}-force relation (see Figure 6.2 for *model 4*) and the isosarcometric twitches (see Figure 6.6 for *model 4*). We found better agreement between the Ca^{2+}-force relation obtained by *model 4* and the experimental results of Kentish *et al.* [98], in particular for $l_s > 1.9 \ \mu$m. When we compared the isosarcometric twitches, we found that, for *model 5*, the peak force was lower and the latency to peak force was increased for longer sarcomeres. Compared with the experimental data measured by Janssen and Hunter [86], the latency to peak force increased too much with sarcomere length. Our findings confirm the finding by Rice *et al.* [158] that the hypothesis that cross-bridge binding increases the affinity of troponin for Ca^{2+} is not crucial to reproduce the experimental results. Since the twitches obtained by *model 4* better resemble the experimental results from Janssen and Hunter, we have chosen *model 4* to describe the Ca^{2+}-force relation (see also Appendix C).

Excitation-contraction coupling   To compute F_{norm} during contraction, Rice *et al.* [158] used a Ca^{2+} transient with a peak $[Ca^{2+}]_i$ of 0.97 μM and 130 ms to return $[Ca^{2+}]_i$ to half of maximum $[Ca^{2+}]_i$. Our peak forces are smaller and the traces are less prolonged than those of Rice *et al.* [158]. This is explained by the lower peak value of $[Ca^{2+}]_i$ obtained from the model of Courtemanche *et al.* [37]. However, the main characteristics, i.e., increasing peak force, increasing time to peak force, and increasing relaxation time with increasing l_s, are observed in our model and are in agreement with experimental measurements [86]. These characteristics are important with respect to the Frank-Starling mechanism, which states that when the amount of blood flowing into the heart increases, the wall becomes more stretched and the cardiac muscle contracts with increased force. Furthermore, isosarcometric twitch duration (Figure 6.6, top) is longer than isotonic twitch duration (Figure 6.7, top). This is explained by shortening of the sarcomeres during isotonic contraction and is in agreement with experimental results [80].

Stretch and fiber conductivity   In our model, g_{int} and g_{ext} are determined by λ on the basis of the assumption that 60% of R_{int} is attributed to R_{junc}. The assumption that R_{int} is determined by R_{myo} only is equivalent to $R_{junc0}/R_{int0} = 0.0$ and would lead to a faster decrease in θ for increasing λ (Figure 6.10). Since intercellular coupling in cardiac tissue is through the gap junctions and since the number of gap junctions does not change when the tissue is acutely stretched, we believe that neglecting the distinction between R_{myo} and R_{junc} leads to overestimation of the effect of λ on conductivity.

Stretch-activated current I_{sac}   We model I_{sac} as a nonselective cation current with $E_{sac} = 0$ to -1 mV. Our model of I_{sac} has a near-linear current-voltage relation, which can be approximated by

$$I_{sac} = g_{sac}(V_{mem} - E_{sac}), \tag{6.37}$$

with $g_{sac} = 0.0027$ nS/pF for $\lambda = 1.0$, $g_{sac} = 0.0049$ nS/pF for $\lambda = 1.2$, and $g_{sac} = 0.0088$ nS/pF for $\lambda = 1.4$. Wagner *et al.* [218] used an externally applied current with $g_{sac} = 0.0083$ nS/pF and $E_{sac} = -10$ mV to elicit an AP in atrial cells from the rat. In our model, stretch-induced APs are elicited for $\lambda = 1.35$ (Figure 6.8), which corresponds to $g_{sac} = 0.0076$ nS/pF and is in a similar range.

Intracellular ion concentrations   The ionic currents of the model of Courtemanche *et al.* [37] interact with $[Na^+]_i$, $[K^+]_i$, and $[Ca^{2+}]_i$ [37]. To model the influence of I_{sac} on the intracellular ion concentrations, we assume that SACs

are permeable to Na^+, K^+, and Ca^{2+}. Whether SACs in human atrial cells are permeable to Ca^{2+} is still a matter of debate. To investigate the effect of permeability of SACs for Ca^{2+}, we performed simulations in which I_{sac} was permeable to Ca^{2+} and not permeable to Ca^{2+}. Our results show an increase in $[Ca^{2+}]_i$ under stretch, whether I_{sac} is permeable to Ca^{2+} or not permeable to Ca^{2+} (Figure 6.8). However, when I_{sac} is permeable to Ca^{2+}, $[Ca^{2+}]_i$ is increased $\sim 3\%$ compared with I_{sac} not permeable to Ca^{2+} (Tables 6.2 and 6.3). Our findings are in agreement with experimental observations that $[Ca^{2+}]_i$ increases in response to stretch [24, 193]. Kamkin et al. [91] observed that the behavior of SACs in isolated human atrial cells did not change when a Ca^{2+}-free external solution was used, suggesting that the current through the SACs was preferentially carried by Na^+, rather than by Ca^{2+} [218]. In Figure 6.13 (left), the current density of $I_{sac,Ca}$ is only 5% of the current density of $I_{sac,Na}$, which explains the finding by Kamkin et al. [91].

Ca^{2+}-troponin binding   Binding of Ca^{2+} to troponin is modeled in two different ways: in the model of Courtemanche et al. [37], a steady-state formulation (equation (6.19)) to describe Ca^{2+} binding to troponin is used; in the model of Rice et al. [158], binding of Ca^{2+} to troponin is modeled by differential equations (6.20) and (6.21). The resulting [LTRPNCa] is then used to compute the force generated by the sarcomeres. Although having two different ways to model binding of Ca^{2+} to troponin is not elegant, one cannot simply replace the formulation proposed by Courtemanche et al. with the formulation proposed by Rice et al. This would be a major modification of the model of Courtemanche et al. requiring adaptation of various parameters related to the Ca^{2+} fluxes and ionic currents, which is beyond the scope of the present study.

Calcium transient   As shown in Figures 6.9 and 6.18 (left), although there is an AP, the Ca^{2+} transient is absent. The APs for which no Ca^{2+} transient occurred are characterized by a low steepness of the AP upstroke (low $(dV_{mem}/dt)_{max}$) and were mainly driven by $I_{Ca,L}$. The absence of the Ca^{2+} transient is explained by the absence of Ca^{2+} release from the junctional SR, which may be caused by the lower $(dV_{mem}/dt)_{max}$. In our model, the effect of the intercellular currents on the ion concentrations is not taken into account. In case the AP is mainly driven by $I_{Ca,L}$, $[Ca^{2+}]_i$ in the downstream cell may slowly rise because of the Ca^{2+} in the current flow between the cells. This increase in $[Ca^{2+}]_i$ may then trigger buffered Ca^{2+} release. One may expect that a similar effect can be obtained when the SACs are permeable to Ca^{2+}. Although AP rises faster in the presence of $I_{sac,Ca}$ ($\lambda = 1.35$ in Figure 6.9), a Ca^{2+} tran-

sient was not observed. In simulations where Ca^{2+} transients did occur, the effect of $I_{sac,Ca}$ was limited to ~3% increase in $[Ca^{2+}]_i$ (Tables 6.2 and 6.3). On the basis of these observations, we conclude that the permeability of I_{sac} for Ca^{2+} contributes little to the changes in electrophysiological behavior under stretch.

6.5   Conclusion

In our model, conduction slowing and block are related to the amount of stretch and are enhanced by contraction of early-activated segments. Conduction block can be unidirectional in an inhomogeneous fiber and is promoted by a shorter stimulation interval. Our observations are in agreement with experimental results and provide an explanation for the increased inducibility of AF observed in acutely dilated atria.

7

Mechanoelectric feedback as a trigger mechanism for cardiac electrical remodeling

N.H.L. Kuijpers, H.M.M. ten Eikelder, P.H.M. Bovendeerd,
S. Verheule, T. Arts, and P.A.J. Hilbers

Submitted

Abstract

Regional variation in ionic membrane currents causes differences in action potential duration (APD) and is proarrhythmic. After several weeks of ventricular pacing, AP morphology and duration are changed due to electrical remodeling of the transient outward potassium current (I_{to}) and the L-type calcium current ($I_{Ca,L}$). It is not clear what mechanism drives electrical remodeling. By modeling the cardiac muscle as a string of segments that are electrically and mechanically coupled, we investigate the hypothesis that electrical remodeling is triggered by changes in mechanical load. In our model, contractile force generated by the sarcomeres depends on the calcium transient and on the sarcomere length. Stroke work is determined for each segment by simulating the cardiac cycle. Electrical remodeling is simulated by adapting $I_{Ca,L}$ kinetics such that a homogeneous distribution of stroke work is obtained. With electrical remodeling, a more homogeneous shortening of the fiber is obtained, while heterogeneity in APD increases and the repolarization wave reverses. Our results are in agreement with experimentally observed homogeneity in mechanics and heterogeneity in electrophysiology. In conclusion, electrical remodeling is a possible mechanism to reduce heterogeneity in cardiomechanics induced by ventricular pacing.

7.1 Introduction

Heterogeneity in action potential morphology and duration is an important factor in the initiation and persistence of reentrant arrhythmia such as atrial fibrillation (AF) [5, 18, 172]. An inverse relationship between action potential duration (APD) and activation time has been found both in the atria [181, 182, 217] and in the ventricles [63]. Differences in atrial action potential morphology are related to a regional variation in ionic membrane currents [57]. In the ventricles, differences in ionic membrane currents between the left ventricle (LV) and the right ventricle (RV) [216] and between the apex and base of the LV [13] have been observed. Cordeiro *et al.* [35] observed transmural heterogeneity in ionic currents, which was related to differences in mechanical function and is believed to help synchronize contraction in the ventricular wall.

Changing the activation sequence in the ventricles by pacing from a different site results in APD prolongation near the pacing site and APD shortening in remote regions [36, 120]. After several hours, these changes in electrophysiology lead to modulation of the T wave in the electrocardiogram (ECG). When normal activation is restored, the normal T wave reappears after several days. This phenomenon is known as "cardiac memory" and was first described by Rosenbaum *et al.* [160]. Herweg *et al.* [70] observed changes in the atrial T wave (Ta wave) after changing the activation sequence in canine atria, indicating that cardiac memory is possible in the atria. In contrast, no evidence for "atrial memory" has been found in the goat [217].

Experimental results indicate that both the transient outward potassium (K^+) current (I_{to}) [164] and the L-type calcium (Ca^{2+}) current ($I_{Ca,L}$) [20, 145] are involved in electrical remodeling after changing the activation sequence in the ventricles. Yu *et al.* [229] observed a reduction in I_{to} current size, which explains disappearance of the notch in the AP after remodeling. Plotnikov *et al.* [145] reversed the activation sequence in the canine heart from epicardium to endocardium by pacing the left ventricle. After 21 days, they isolated epicardial myocytes and compared $I_{Ca,L}$ current size and kinetics to $I_{Ca,L}$ in control (normally stimulated) epicardial myocytes. They found a similar $I_{Ca,L}$ current size, but observed a shift in activation towards a more positive membrane potential and slower inactivation after ventricular pacing. These changes in $I_{Ca,L}$ kinetics probably contribute to the increased APD and plateau height observed after pacing [145]. After 2 h of pacing the canine left ventricle, Patberg *et al.* [142] found a significant decrease in nuclear cAMP-responsive element binding protein (CREB) that did not occur in control dogs or in dogs treated with the $I_{Ca,L}$ blocker nifidipine. These observations indicate that changes in the $I_{Ca,L}$ current are related to modifications in the transcription of

the $I_{Ca,L}$ channel [20].

At present, it is unclear what mechanism drives electrical remodeling after changing the activation sequence. Based on experimental observations, Jeyaraj *et al.* [87] suggest mechanoelectric feedback as a mechanism for electrical remodeling. Recently, Sosunov *et al.* [178] found that electrical remodeling can be inhibited either by reducing mechanical load or by reducing contractility. These findings indicate that changes in mechanical load are involved in electrical remodeling after changing the activation sequence. Lab [113, 114] reviewed several mechanisms for mechanoelectric feedback in the heart. These mechanisms include direct influence on the action potential through stretch-activated channels (SACs) [62, 78, 105], force-feedback on the intracellular Ca^{2+} concentration ($[Ca^{2+}]_i$) [115], and long-term effects involving cell signaling pathways [168]. Prinzen *et al.* [148, 149] and Delhaas *et al.* [41] observed homogeneous strain and mechanical work when the heart was paced from the right atrium (normal stimulation). However, during ventricular pacing, systolic fiber strain and mechanical work were approximately zero near the stimulation site, and gradually increased to more than twice the normal value in remote regions [149]. We hypothesize that the deviation from normal mechanical work observed after ventricular pacing functions as a trigger for electrical remodeling.

In the present study, we investigate the effect of changing maximum I_{to} conductance, maximum $I_{Ca,L}$ conductance, and $I_{Ca,L}$ kinetics on AP morphology, Ca^{2+} dynamics, and mechanical behavior. To investigate the hypothesis that electrical remodeling is triggered by deviations from normal mechanical work, we apply our Cellular Bidomain Model [109, 110], which has been extended with cardiomechanics [111, 112]. The model describes ionic membrane currents, storage and release of Ca^{2+} from the sarcoplasmic reticulum (SR), Ca^{2+} buffering, and cross-bridge formation. Contractile forces are coupled to $[Ca^{2+}]_i$ and sarcomere length. With this model, ventricular electromechanics during the cardiac cycle is simulated in a cardiac fiber and stroke work is computed for each segment. Under the assumption that stroke work is homogeneously distributed after remodeling, we investigate the hypothesis that remodeling of $I_{Ca,L}$ is triggered by changes in mechanical load.

7.2 Methods

To investigate the effect of remodeling of ionic currents on cardiac electrophysiology and mechanics, we apply our discrete bidomain model, the Cellular Bidomain Model [109, 110]. The model describes active membrane behavior as well as intracellular coupling and interstitial currents, and has been

recently extended to describe cardiac mechanics [111, 112]. Here, we summarize our model of cardiac electrophysiology, the Ca^{2+}-force relation, and the mechanical behavior of a cardiac fiber. Furthermore, we describe the simulation of a cardiac cycle, adaptation of I_{to} and $I_{Ca,L}$, and the numerical integration scheme. Finally, an overview is given of the simulations performed.

7.2.1 Modeling cardiac electrophysiology

In the Cellular Bidomain Model, a distinction is made between the intracellular domain and the interstitium. The tissue is subdivided in segments. The electrophysiological state of each segment is defined by the intracellular potential (V_{int}), the extracellular potential (V_{ext}), and the state of the cell membrane, which is expressed in gating variables and ion concentrations. The membrane potential (V_{mem}) is defined by

$$V_{mem} = V_{int} - V_{ext}. \tag{7.1}$$

Exchange of current between the intracellular and extracellular domains occurs as transmembrane current (I_{trans}), which depends on ionic current (I_{ion}) and capacitive current according to

$$I_{trans} = \chi(C_{mem}\frac{dV_{mem}}{dt} + I_{ion}), \tag{7.2}$$

where χ is the ratio of membrane area to tissue volume and C_{mem} represents membrane capacitance per unit membrane surface. I_{trans} is expressed per unit of tissue volume in $\mu A/cm^3$. Assuming $C_{mem} = 1\ \mu F/cm^2$, I_{ion} is expressed in pA/pF and depends on V_{mem}, gating variables, and ion concentrations. To model I_{ion}, we apply the Courtemanche-Ramirez-Nattel model [37]. The total ionic current is given by

$$I_{ion} = I_{Na} + I_{K1} + I_{to} + I_{Kur} + I_{Kr} + I_{Ks} + I_{Ca,L} + I_{p,Ca} + I_{NaK} + I_{NaCa} + I_{b,Na} + I_{b,Ca}, \tag{7.3}$$

where I_{Na} is fast inward Na^+ current, I_{K1} is inward rectifier K^+ current, I_{to} is transient outward K^+ current, I_{Kur} is ultrarapid delayed rectifier K^+ current, I_{Kr} is rapid delayed rectifier K^+ current, I_{Ks} is slow delayed rectifier K^+ current, $I_{Ca,L}$ is L-type Ca^{2+} current, $I_{p,Ca}$ is Ca^{2+} pump current, I_{NaK} is Na^+-K^+ pump current, I_{NaCa} is Na^+/Ca^{2+} exchanger current, and $I_{b,Na}$ and $I_{b,Ca}$ are background Na^+ and Ca^{2+} currents [37]. Ca^{2+} handling by the sarcoplasmic reticulum (SR) is described by considering three compartments: myoplasm, SR release compartment (junctional SR), and SR uptake compartment (network SR). The model also describes Ca^{2+} buffering within the cytoplasm mediated by troponin and by calmodulin as well as Ca^{2+} buffering within the release compartment mediated by calsequestrin [37].

Table 7.1: Model parameters

Parameter	Definition	Value
g_{int}	Longitudinal intracellular conductivity ($\lambda = 1.0$)	1.7422 mS/cm
g_{ext}	Longitudinal extracellular conductivity ($\lambda = 1.0$)	6.2500 mS/cm
C_{mem}	Membrane capacitance	$1.0\,\mu\text{F/cm}^2$
χ	Surface-to-volume ratio	2000 cm^{-1}
f_{CE}	Scaling factor for contractile element	100 kPa
l_{CE0}	Reference length of contractile element	$1.78\,\mu\text{m}$
v_{max}	Maximum velocity of sarcomere shortening	$0.0055\,\mu\text{m/ms}$
c_v	Constant describing the shape of the Hill relation	2
f_{SE}	Scaling factor for series elastic element	28 kPa
k_{SE}	Material constant for series elastic element	$14.6\,\mu\text{m}^{-1}$
f_{PE}	Scaling factor for parallel elastic element	0.006 kPa
k_{PE}	Material constant for parallel elastic element	$14.6\,\mu\text{m}^{-1}$
l_{PE0}	Reference length of parallel elastic element	$1.78\,\mu\text{m}$

λ, stretch ratio.

Intracellular and extracellular currents between adjacent segments are related to intracellular and extracellular conductivities (g_{int} and g_{ext}) and satisfy Ohm's law. Conductivities are adjusted for changing stretch ratio (λ) as described previously [112] (Chapter 6). The bidomain parameters used for the present study are from Henriquez [69] and are based on measurements by Clerc [33] (Table 7.1).

7.2.2 Mechanical behavior of a cardiac fiber

The mechanical behavior of a single segment is modeled as described previously [112] by the classical three-element rheological scheme introduced by Hill in 1938 [71]. The model is formulated in terms of tension (first Piola Kirchhoff stress), defined as force per unit of fiber cross-sectional area in the undeformed state. Active tension is generated by the contractile element (CE) together with the series elastic element (SE) and passive tension is generated in the parallel elastic element (PE). The PE describes the tension-length relation when the segment is not stimulated. Contractile tension (T_{CE}) generated by the CE depends on $[\text{Ca}^{2+}]_{\text{i}}$, the length of the CE ($l_{\text{CE}}$), and the velocity of

sarcomere shortening $v = -\frac{\mathrm{d}l_{CE}}{\mathrm{d}t}$. T_{CE} is defined by

$$T_{CE} = f_{CE}\, f_v(v)\, F_{norm}([Ca^{2+}]_i, l_{CE}), \tag{7.4}$$

where f_{CE} is a scaling factor, $f_v(v)$ is Hill's force-velocity relation, and F_{norm} ($[Ca^{2+}]_i, l_{CE}$) is the normalized force generated by the sarcomeres. We model the Hill relation by a hyperbolic function as proposed by Hunter *et al.* [80]. Function $f_v(v)$ is defined by

$$f_v(v) = \frac{1 - \frac{v}{v_{max}}}{1 + c_v \frac{v}{v_{max}}}, \tag{7.5}$$

where v_{max} is the maximum velocity of sarcomere shortening and c_v is a constant describing the shape of the hyperbolic relationship [112] (Table 7.1).

$F_{norm}([Ca^{2+}]_i, l_{CE})$ is modeled by *model 4* from Rice *et al.* [158], which is based on a functional unit of troponin, tropomyosin, and actin. In our model, binding of Ca^{2+} to troponin is modeled in two different ways: the Ca^{2+} transient is computed by the model of Courtemanche *et al.* [37] using a steady-state formulation for Ca^{2+}-troponin binding; F_{norm} is computed by the model of Rice *et al.* [158] using differential equations for the Ca^{2+}-troponin binding and $[Ca^{2+}]_i$ obtained from the model of Courtemanche *et al.* [37] (see Chapter 6 for more detail). In the model of Rice *et al.* [158], troponin can be in one of two states, indicating whether it is unbound or bound to Ca^{2+}. Tropomyosin can be in one of six states of which two represent the non-permissive states with 0 and 1 cross bridges, and the other four the permissive states with 0, 1, 2, and 3 cross bridges [158]. Transitions between the states are governed by rate functions that depend on $[Ca^{2+}]_i$ and l_{CE}. The force generated by the sarcomeres depends on the fraction of tropomyosin in the states that represent cross-bridge formation. We do not consider a direct feedback mechanism that influences the Ca^{2+} transient through a change in the affinity of troponin for Ca^{2+} binding as in *model 5* of Rice *et al.* [157, 158]. The reader is referred to Rice *et al.* [158] or Kuijpers *et al.* [112] for a graphical representation of the steady-state Ca^{2+}-force relation (Figure 6.2).

Tensions generated in the SE and in the PE (T_{SE} and T_{PE}) are exponentially related to the length of the SE (l_{SE}) and the sarcomere length (l_{PE}), and are defined by

$$T_{SE} = f_{SE}\,(\exp(k_{SE}\, l_{SE}) - 1) \tag{7.6}$$

and

$$T_{PE} = f_{PE}\,(\exp(k_{PE}\,(l_{PE} - l_{PE0})) - 1), \tag{7.7}$$

where f_{SE}, k_{SE}, f_{PE}, and k_{PE} are material constants describing the elasticity of the elements, and l_{PE0} is the reference sarcomere length at which $T_{PE} = 0$ kPa. Total tension generated by the segment ($T_{segment}$) is the sum of passive tension (T_{PE}) and active tension (T_{SE}). In summary, it holds for the three-element model:

$$T_{CE} = T_{SE}, \tag{7.8}$$
$$T_{segment} = T_{SE} + T_{PE}, \tag{7.9}$$
$$l_{PE} = l_{CE} + l_{SE}. \tag{7.10}$$

Most parameters for the three-element mechanical model are from Solovy-ova *et al.* [176] and Kuijpers *et al.* [112] (Table 7.1). Parameter f_{SE} is changed from 2.8 kPa in [112] to 28 kPa to mimic the experimentally observed fiber shortening of 1% in a quick-release experiment [47, 80]. With these parameters, both the active and the passive tension-sarcomere length relation are in agreement with experimental data measured by Kentish *et al.* [98]. The reader is referred to Kuijpers *et al.* [112] for a graphical representation of active and passive tension-sarcomere length relations in our model (Figure 6.4).

7.2.3 Cardiac cycle simulation

The myofibers in the heart are represented by a single string of segments that are coupled in series. In the undeformed state, all segments have the same length (0.1 mm) and cross-sectional area (0.01 mm^2) [112]. The stretch ratio of a single segment ($\lambda_{segment}$) is defined by

$$\lambda_{segment} = \frac{l_{PE}}{l_{PE0}}, \tag{7.11}$$

and the stretch ratio of the fiber (λ_{fiber}) is defined as the average stretch ratio of the segments. From mechanical equilibrium, it follows that the tension generated by each segment, $T_{segment}$, must be equal to the tension applied to the fiber, T_{fiber}.

To simulate the cardiac cycle, we extend the preload-afterload experiment as described by Brutsaert and Sonnenblick [21]. We distinguish 5 phases as follows (Figure 7.1):

1. **Filling:**
   linear increase of T_{fiber} during 300 ms from $T_{fiber} = T_{rest}$ to $T_{fiber} = T_{preload}$;

2. **Isovolumic contraction:**
   isometric simulation (constant λ_{fiber}) until $T_{fiber} = T_{afterload}$;

3. **Ejection:**
   isotonic simulation (constant $T_{fiber} = T_{afterload}$) until λ_{fiber} stops decreasing;
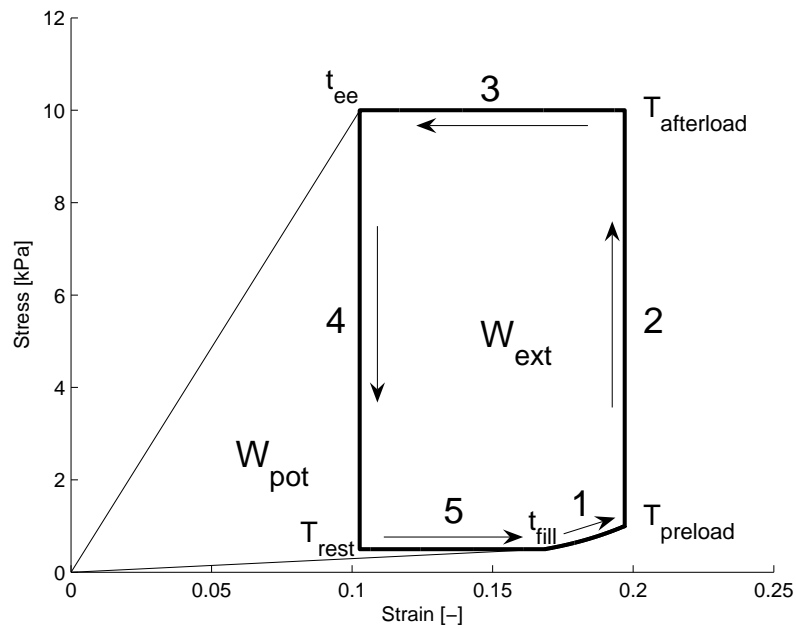
Figure 7.1: Overview of the preload-afterload experiment simulating the cardiac cycle. The 5 phases of the cardiac cycle are indicated by numbers as follows: 1 filling, 2 isovolumic contraction, 3 ejection, 4 isovolumic relaxation, and 5 isotonic relaxation. The arrows indicate the direction of time; t_{fill} indicates the time at which filling starts and t_{ee} the time of end ejection. A cardiac cycle was simulated with $T_{rest} = 0.5$ kPa, $T_{preload} = 1$ kPa, and $T_{afterload} = 10$ kPa. Strain is defined as $\lambda - 1$, where λ is the stretch ratio. External stroke work density (W_{ext}) is the area indicated by W_{ext} and potential work density (W_{pot}) is the area indicated by W_{pot}. Total stroke work density (W_{tot}) is the sum of W_{ext} and W_{pot}.

4. **Isovolumic relaxation:**
   isometric simulation (constant λ_{fiber}) until $T_{\text{fiber}} = T_{\text{rest}}$;

5. **Isotonic relaxation:**
   isotonic simulation (constant $T_{\text{fiber}} = T_{\text{rest}}$) until filling starts.

During filling, ejection, and isotonic relaxation, the load applied to the cardiac fiber (T_{fiber}) is set as a boundary condition, whereas during isovolumic contraction and isovolumic relaxation, the stretch ratio of the fiber (λ_{fiber}) is a boundary condition. To initiate contraction, the first segment is electrically stimulated at the beginning of isovolumic contraction.

In Figure 7.1, a stress-strain loop is presented. The five phases of the cardiac cycle are indicated by the numbers 1 through 5, and the direction of time is indicated by arrows. A cardiac cycle was simulated with $T_{\text{rest}} = 0.5$ kPa, $T_{\text{preload}} = 1$ kPa, and $T_{\text{afterload}} = 10$ kPa. These values are in agreement with the experiments by Iribe *et al.* [81].

7.2.4 Adaptation of I_{to} and $I_{\text{Ca,L}}$

To investigate the effect of changes in I_{to} and $I_{\text{Ca,L}}$ in relation to the calcium transient and cardiomechanics, we vary the maximum conductance of I_{to} and $I_{\text{Ca,L}}$. Furthermore, we model the changes in $I_{\text{Ca,L}}$ kinetics as observed by Plotnikov *et al.* [145] after ventricular pacing.

In the Courtemanche-Ramirez-Nattel model, I_{to} is defined by

$$I_{\text{to}} = G_{\text{to}}\, o_{\text{a}}^3\, o_{\text{i}}\, (V_{\text{mem}} - E_{\text{K}}), \tag{7.12}$$

where G_{to} is the maximum I_{to} conductance, o_{a} and o_{i} are the activation and inactivation gating variables, and E_{K} is the equilibrium potential for K^+ [37]. $I_{\text{Ca,L}}$ is defined by

$$I_{\text{Ca,L}} = G_{\text{Ca,L}}\, d\, f\, f_{\text{Ca}}\, (V_{\text{mem}} - 65), \tag{7.13}$$

where $G_{\text{Ca,L}}$ is the maximum $I_{\text{Ca,L}}$ conductance, d is the activation gating variable, f is the voltage-dependent inactivation gating variable, and f_{Ca} is the Ca^{2+}-dependent inactivation gating variable [37]. Changing the I_{to} and $I_{\text{Ca,L}}$ current size is realized by changing G_{to} and $G_{\text{Ca,L}}$, respectively.

To account for the shift in $I_{\text{Ca,L}}$ activation and slower inactivation observed by Plotnikov *et al.* [145], $I_{\text{Ca,L}}$ kinetics are changed by adaptation of the dynamics of gating variable d. In the Courtemanche-Ramirez-Nattel model, the dynamics of d are defined by

$$\frac{\mathrm{d}}{\mathrm{d}t}d = \frac{d_\infty - d}{\tau_d}, \tag{7.14}$$

where steady-state value d_∞ and time constant τ_d are defined by

$$d_\infty = \frac{1}{1 + \exp\left(-\frac{V_{\text{mem}}+V_{\text{shift}}}{8.0}\right)} \tag{7.15}$$

and

$$\tau_d = \frac{1 - \exp\left(-\frac{V_{\text{mem}}+V_{\text{shift}}}{6.24}\right)}{0.035(V_{\text{mem}} + V_{\text{shift}})\left(1 + \exp\left(-\frac{V_{\text{mem}}+V_{\text{shift}}}{6.24}\right)\right)}, \tag{7.16}$$

where $V_{\text{shift}} = 10$ mV.

We simulate remodeling of $I_{\text{Ca,L}}$ kinetics by replacing V_{shift} in (7.15) and (7.16) by

$$V_{\text{shift}} = V_{\text{shift,ref}}\,(\rho + 1), \tag{7.17}$$

where $V_{\text{shift,ref}} = 10$ mV and ρ is the *remodeling parameter*. Plotnikov *et al.* [145] observed a shift of 10 mV in $I_{\text{Ca,L}}$ activation in epicardial myocytes. Assuming a maximum shift of 10 mV, parameter ρ ranges between -1.0 and 1.0, where $\rho = 0.0$ represents the reference situation.

7.2.5 Mechanically induced remodeling of $I_{\text{Ca,L}}$

Based on the assumption that electrical remodeling is triggered by changes in mechanical load, we use stroke work per unit of tissue volume as a feedback signal to determine the remodeling parameter ρ. We distinguish between *external* stroke work density (W_{ext}) and *total* stroke work density (W_{tot}). W_{ext} is defined as the area enclosed by the stress-strain loop during the cardiac cycle (Figure 7.1):

$$W_{\text{ext}} = -\int_0^{t_{\text{cycle}}} T(t)\mathrm{d}\epsilon(t), \tag{7.18}$$

where t_{cycle} is the duration of one cardiac cycle (1 s), $T(t)$ represents T_{segment} at time t, and $\epsilon(t)$ the strain defined by $\epsilon = \lambda_{\text{segment}} - 1$. W_{tot} is the sum of W_{ext} and the so-called potential work density (W_{pot}), and is also referred to as the stress-strain area (SSA) [41, 190]. W_{tot} is computed as

$$W_{\text{tot}} = -\frac{T_{\text{rest}}\,\epsilon(t_{\text{fill}})}{2} - \int_{t_{\text{fill}}}^{t_{\text{ee}}} T(t)\mathrm{d}\epsilon(t) + \frac{T_{\text{afterload}}\,\epsilon(t_{\text{ee}})}{2}, \tag{7.19}$$

where t_{fill} denotes the time at which filling starts and t_{ee} the time at end of ejection (Figure 7.1).

For each segment n, the remodeling parameter is denoted by ρ_n. The parameters ρ_n are determined such that stroke work is homogeneously distributed over the fiber. The ρ_n are found by iteratively computing stroke work for each segment followed by adapting the ρ_n until the ρ_n no longer change. Stroke work generated by the segment in the center of the fiber is used as reference. This implicates that, although stroke work may change, the electrophysiology is not changed for the center segment. Initially, $\rho_n = 0.0$ for each segment n. Each time a new cardiac cycle starts, ρ_n is adapted by

$$
\rho_n \rightarrow \begin{cases}
\rho_n + 0.01 & \text{if } W_n < 0.99 \cdot W_{\text{ref}} \text{ and } \rho_n < 1.0 \\
\rho_n - 0.01 & \text{if } W_n > 1.01 \cdot W_{\text{ref}} \text{ and } \rho_n > -1.0 \\
\rho_n & \text{otherwise}
\end{cases}
\tag{7.20}
$$

Here, W_n represents either W_{ext} or W_{tot} of segment n, and W_{ref} represents either W_{ext} or W_{tot} of the reference segment.

7.2.6 Numerical integration scheme

The Cellular Bidomain Model can be written as a coupled system of differential equations and linear equations [110]. To compute V_{mem}, the differential equations are solved using a forward Euler scheme with a 0.01-ms time step. Each time step, the system of linear equations is solved by an iterative method to find V_{ext} as described in Kuijpers *et al.* [110]. The ionic currents are computed as described in Ref. [37]. Computation time is reduced by increasing the simulation time step for the ionic currents to 0.1 ms during repolarization and rest. This leads to a reduction of 70% in computation time, without significant loss of accuracy (Chapter 3). Both the Ca^{2+}-force relation and cardiomechanics are computed using a forward Euler method with a time step of 0.01 ms. Depending on the phase in the cardiac cycle, either T_{fiber} or λ_{fiber} is set as a boundary condition. The mechanical state of each segment is computed from the state obtained during the previous time step and the boundary condition. A numerical scheme that accounts for both boundary conditions is derived in Ref. [112] (Appendix D). Initially, $T_{\text{fiber}} = 0.0$ kPa and $\lambda_{\text{fiber}} = 1.0$. During the first 200 ms, T_{fiber} is increased until $T_{\text{fiber}} = T_{\text{rest}}$. The first cardiac cycle starts after 1 s.

7.2.7 Simulation protocol

To investigate the effect of changing maximum I_{to} conductance, maximum $I_{\text{Ca,L}}$ conductance, and $I_{\text{Ca,L}}$ kinetics on the action potential, calcium transient, and contractile force, a series of single-segment simulations was performed in which G_{to}, $G_{\text{Ca,L}}$, and ρ were varied. The segment was stimulated with a

stimulation rate of 1 Hz using a stimulus current of 20 pA/pF during 2 ms as in Ref. [37]. During the simulations, l_{CE} was kept constant (isosarcometric contraction). In another series of simulations, the effect of changing preload and afterload was investigated by single-segment simulations with $\rho = 0.0$, $\rho = 0.5$, and $\rho = 1.0$. In these simulations, $T_{rest} = 0.5$ kPa, $T_{preload}$ ranged between 0.75 and 2.5 kPa, and $T_{afterload}$ ranged between 5 and 20 kPa.

Electrical remodeling was simulated using cardiac fibers with reference length (L_0) of 1, 3, and 6 cm. All fibers have the same conductivity properties (Table 7.1). Normal activation during sinus rhythm is represented by the 1-cm-long fiber, whereas an increased duration of complete activation with epicardial pacing is represented by the longer fibers. With stimulation rate 1 Hz, a depolarization wave was generated by stimulating the first segment using a stimulus current of 100 pA/pF until the membrane was depolarized. Depolarization of the entire fiber took 32 ms for the 1-cm-long fiber, 98 ms for the 3-cm-long fiber, and 202 ms for the 6-cm-long fiber. 32 ms is comparable with normal ventricular depolarization and 98 ms is comparable with ventricular depolarization after epicardial pacing. The 6-cm-long fiber is included to compare our simulation results with the experimental results of Jeyaraj *et al.* [87], who report a dispersion in depolarization time of 180 ms. In all cases, the cardiac cycle was simulated with $T_{rest} = 0.5$ kPa, $T_{preload} = 1$ kPa, and $T_{afterload} = 10$ kPa.

To maintain steady-state, ρ_n can decrease or increase at most 0.01 each cardiac cycle. Thus, it takes at least 100 cardiac cycles to reach $\rho_n = 1.0$ or $\rho_n = -1.0$ for an individual segment n. In all cases, a final distribution of the ρ_n was reached in at most 140 cardiac cycles. By simulating 150 cardiac cycles, it was ensured that steady-state was reached. Since the effect of the stimulus current and the intracellular currents on the intracellular concentrations of Na^+ and K^+ ($[Na^+]_i$ and $[K^+]_i$) are not taken into account, a drift in the ionic balance between $[Na^+]_i$ and $[K^+]_i$ may occur during longer simulation runs [37, 110]. To avoid such drift, $[Na^+]_i$ and $[K^+]_i$ were kept constant during the entire simulation. By performing single-cell simulations with and without fixed $[Na^+]_i$ and $[K^+]_i$, we found that the effect of assuming constant $[Na^+]_i$ and $[K^+]_i$ on the AP morphology, Ca^{2+} transient, and ionic currents is marginal and can be neglected.

7.3 Results

7.3.1 Isosarcometric contraction

In Figure 7.2, the effect of parameter ρ on electrophysiology and F_{norm} is compared with the effect of scaling G_{to} and $G_{Ca,L}$ with a factor 0.3 - 1.7. Increasing G_{to} results in a lower plateau phase, a prolonged APD, a reduced Ca^{2+} transient, and a lower F_{norm}. Decreasing G_{to} leads to disappearance of the notch and a shorter APD, but has no significant influence on the Ca^{2+} transient and F_{norm} (Figure 7.2, left). Increasing $G_{Ca,L}$ does not affect the APD, but results in an increased Ca^{2+} transient and F_{norm}. Decreasing $G_{Ca,L}$ leads to a shorter APD, a reduced Ca^{2+} transient, and a lower F_{norm} (Figure 7.2, center). Interestingly, increasing G_{to} with a factor larger than 2.5 also leads to a shorter APD and a reduced Ca^{2+} transient (results not shown). In that case, peak I_{to} exceeds 14 pA/pF, which results in early deactivation of $I_{Ca,L}$. Similar observations have been reported by Greenstein et $al.$ [65] with models of ventricular membrane behavior.

Parameter ρ and scaling $G_{Ca,L}$ have similar effects on the Ca^{2+} transient and F_{norm} (Figure 7.2, center and right). In contrast with increasing $G_{Ca,L}$, increasing parameter ρ results in a slower inactivation of $I_{Ca,L}$ and an increased APD, which is in agreement with the measurements by Plotnikov et $al.$ [145]. Peak $[Ca^{2+}]_i$ increases for positive ρ and decreases for negative ρ. Larger peak $[Ca^{2+}]_i$ corresponds to larger and more prolonged contractions. The traces of F_{norm} are in agreement with experimental data obtained by Janssen and Hunter [86] (see also Kuijpers et $al.$ [112]).

In experiments, disappearance of the notch in epicardial cells was observed with epicardial pacing, which was related to a reduction in I_{to} [121, 122, 229]. Since reducing G_{to} has no significant influence on the Ca^{2+} transient and on F_{norm} in our model, scaling G_{to} is not further considered in the present study. With increasing $G_{Ca,L}$, the Ca^{2+} transient and F_{norm} increase, but APD is not affected. Thus, the increase in APD observed in experiments cannot be reproduced by increasing $G_{Ca,L}$ alone. Since no changes in peak $I_{Ca,L}$ current size have been observed in experiments after ventricular pacing [20, 89, 145], also scaling $G_{Ca,L}$ is not considered further.

In Table 7.2, AP characteristics, peak $[Ca^{2+}]_i$, and peak F_{norm} (l_{CE} = 2.3 μm) are presented for various values of ρ. With increasing ρ, APD$_{90}$, APD$_{50}$, peak $[Ca^{2+}]_i$, and peak F_{norm} all increase. Resting membrane potential (V_{rest}), maximum upstroke velocity $((dV_{mem}/dt)_{max})$, and AP amplitude (APA) are not significantly different for different values of ρ.

In Figure 7.3, the twelve ionic membrane currents of the Courtemanche-Ramirez-Nattel model are plotted for parameter ρ = −1.0, 0.5, 0.0, 0.5, and
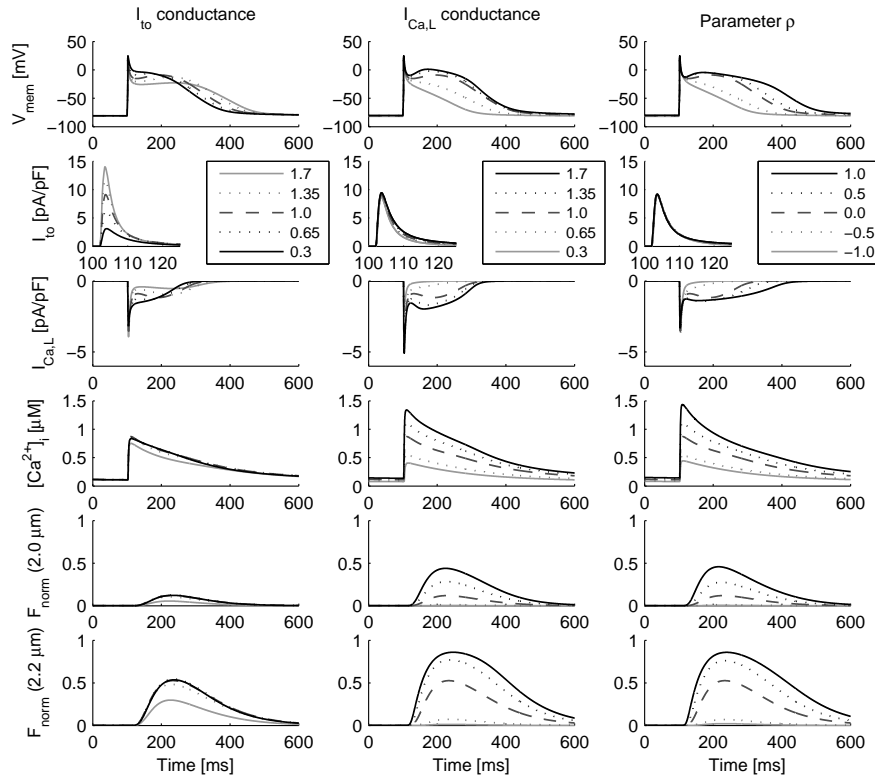
Figure 7.2: Comparison of scaling maximum I_{to} conductance (G_{to}, factor 0.3 - 1.7) and maximum $I_{Ca,L}$ conductance ($G_{Ca,L}$, factor 0.3 - 1.7) with parameter ρ. From top to bottom: membrane potential (V_{mem}), transient outward K$^+$ current (I_{to}), L-type Ca^{2+} current ($I_{Ca,L}$), intracellular Ca^{2+} concentration ([Ca^{2+}]$_i$), normalized contractile force (F_{norm}) for l_{CE} = 2.0 μm, and F_{norm} for l_{CE} = 2.2 μm. A stimulus current was applied at 100 ms. Note the different time scale for I_{to}.
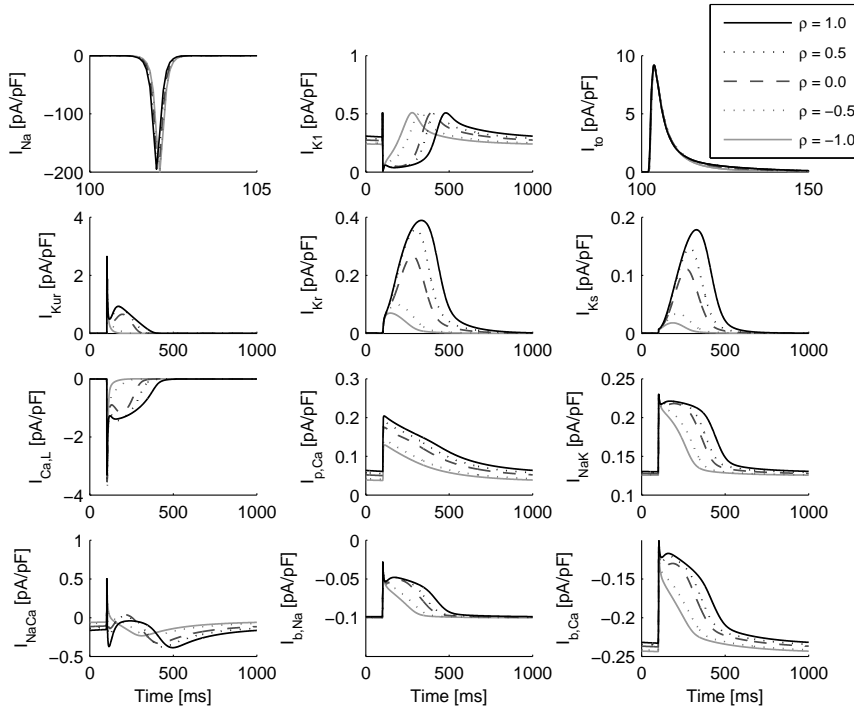
Figure 7.3: Effect of parameter ρ on ionic membrane currents. Fast inward Na^+ current (I_{Na}), inward rectifier K^+ current (I_{K1}), transient outward K^+ current (I_{to}), ultrarapid delayed rectifier K^+ current (I_{Kur}), rapid delayed rectifier K^+ current (I_{Kr}), slow delayed rectifier K^+ current (I_{Ks}), L-type Ca^{2+} current ($I_{Ca,L}$), Ca^{2+} pump current ($I_{p,Ca}$), Na^+-K^+ pump current (I_{NaK}), Na^+/Ca^{2+} exchanger current (I_{NaCa}), background Na^+ current ($I_{b,Na}$), and background Ca^{2+} current ($I_{b,Ca}$) for $\rho = 1.0, 0.5, 0.0, -0.5$, and -1.0. A stimulus current was applied at 100 ms. Corresponding APs are presented in the top-right panel of Figure 7.2. Note the different time scales for I_{Na} and I_{to}.

Table 7.2: Effect of parameter ρ on electrophysiology and contractile force

ρ	V_{rest}	$(dV_{mem}/dt)_{max}$	APA	APD_{90}	APD_{50}	$[Ca^{2+}]_{i,max}$	$F_{norm,max}$
[−]	[mV]	[V/s]	[mV]	[ms]	[ms]	[μM]	[−]
−1.0	−81.7	161	105.8	197	43	0.44	0.09
−0.5	−81.5	162	105.7	244	91	0.54	0.27
0.0	−80.9	163	105.2	311	190	0.87	0.79
0.5	−80.5	161	104.8	336	217	1.11	0.87
1.0	−80.0	156	104.4	393	264	1.44	0.90

AP, action potential; V_{rest}, resting potential; $(dV_{mem}/dt)_{max}$, maximum upstroke velocity; APA, AP amplitude; APD_{90} and APD_{50}, AP duration at 90% and 50% repolarization; $[Ca^{2+}]_{i,max}$, maximum intracellular Ca^{2+} concentration; $F_{norm,max}$, maximum normalized contractile force ($l_{CE} = 2.3\ \mu$m).

1.0. Except for I_{Na} and I_{to}, all currents are changed in response to changes in parameter ρ. I_{Na} and I_{to} are affected little, because they mainly play a role during depolarization and early repolarization. All other currents contribute to the plateau and repolarization phases and are affected by changes in $I_{Ca,L}$ kinetics.

7.3.2 Single cell cardiac cycle simulation

In Figure 7.4, F_{norm}, T_{CE}, $T_{segment}$, l_{CE}, strain, and the stress-strain loop are shown for $\rho = 0.0$, $\rho = 0.5$, and $\rho = 1.0$ ($T_{rest} = 0.5$ kPa, $T_{preload} = 1$ kPa, and $T_{afterload} = 10$ kPa). F_{norm} is larger for larger values of ρ, which results in an increased shortening during ejection and more stroke work.

To investigate the effect of applied load on mechanical behavior, we performed a series of single cell simulations with various combinations of $T_{preload}$ and $T_{afterload}$. In Figure 7.5, the effect of varying $T_{preload}$ and $T_{afterload}$ on the stress-strain loop is shown for $\rho = 0.0$, $\rho = 0.5$, and $\rho = 1.0$. Shortening increases for larger values of $T_{preload}$, because the segment is more stretched prior to contraction (Frank-Starling mechanism). On the other hand, shortening decreases for increasing $T_{afterload}$, which is explained by the fact that the sarcomeres need to generate more force to be able to shorten. These results are in agreement with the work-loop style contractions in the experiments by Iribe *et al.* [81].
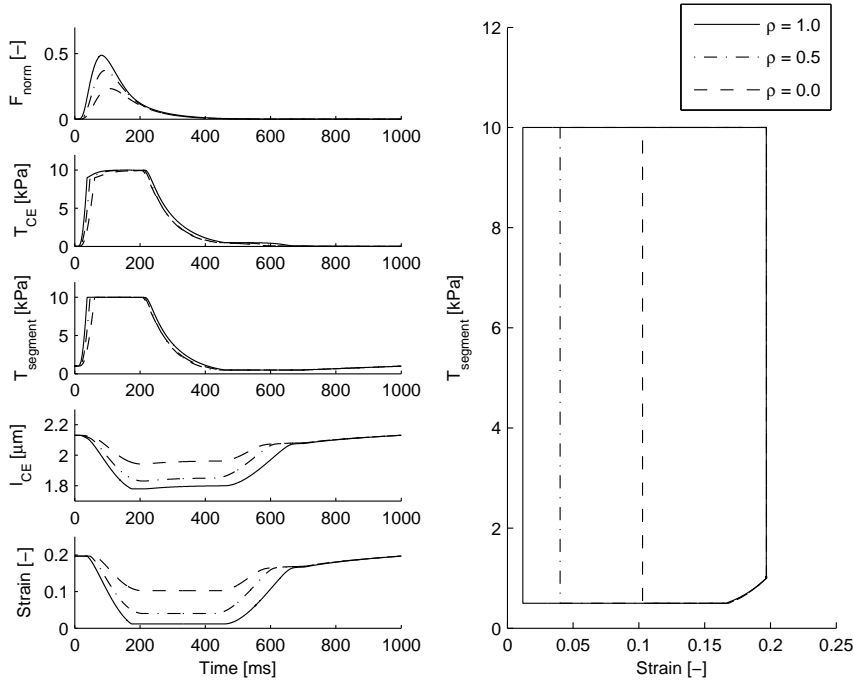
Figure 7.4: Effect of parameter ρ on mechanical behavior during cardiac cycle (single segment). $T_{rest} = 0.5$ kPa, $T_{preload} = 1$ kPa, and $T_{afterload} = 10$ kPa; $\rho = 0.0$, 0.5, and 1.0. Left: F_{norm}, active tension (T_{CE}), $T_{segment}$, l_{CE}, and strain. Right: stress-strain loop. The cell was electrically stimulated at the beginning of isovolumic contraction at simulation time $t = 0$ ms.
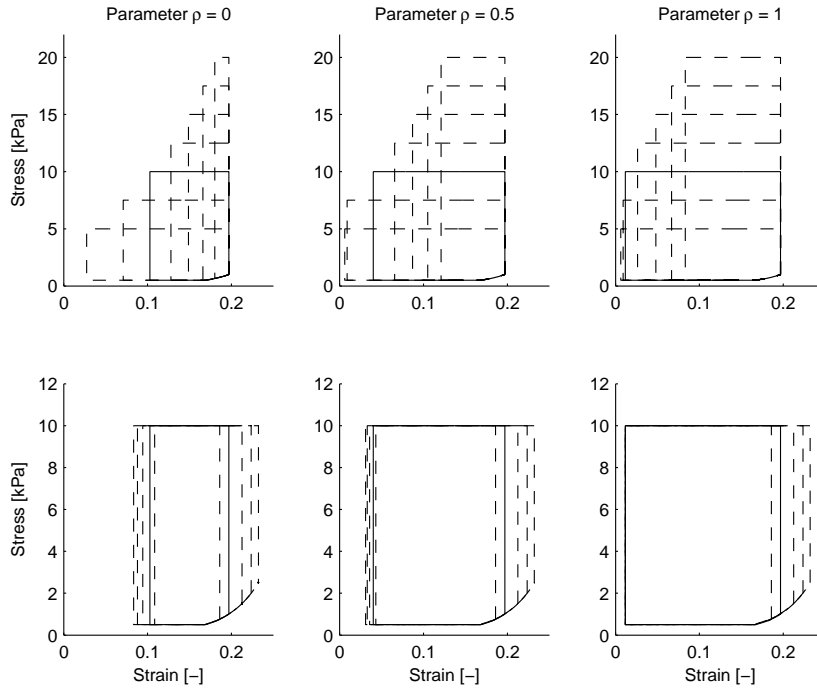
Figure 7.5: Effect of varying T_{preload} and $T_{\text{afterload}}$ for $\rho = 0$, $\rho = 0.5$, and $\rho = 1$. Top: $T_{\text{rest}} = 0.5$ kPa, $T_{\text{preload}} = 1$ kPa, and $T_{\text{afterload}}$ ranges between 5 and 20 kPa. Bottom: $T_{\text{rest}} = 0.5$ kPa, $T_{\text{afterload}} = 10$ kPa, and T_{preload} ranges between 0.75 and 2.5 kPa. Solid lines indicate $T_{\text{preload}} = 1$ kPa and $T_{\text{afterload}} = 10$ kPa.

7.3.3 Remodeling of $I_{Ca,L}$ in a cardiac fiber

To investigate the effect of remodeling of $I_{Ca,L}$ on electrical and mechanical behavior, we consider the 1-cm-long, 3-cm-long, and 6-cm-long fibers with $T_{rest} = 0.5$ kPa, $T_{preload} = 1$ kPa, and $T_{afterload} = 10$ kPa. In Figure 7.6, W_{ext}, W_{tot}, parameter ρ, action potential duration (APD$_{100}$), and time of repolarization (t_{repol}) are shown for each location along the fibers without remodeling, with remodeling controlled by W_{ext}, and with remodeling controlled by W_{tot}. Without remodeling, W_{ext} is small for early-activated segments in the short fiber and negative for early-activated segments in the longer fibers. With remodeling, W_{ext} and W_{tot} are increased for early-activated segments and decreased for later-activated segments. Although W_{ext} is positive for the early-activated segments in the longer fibers, the reference value (W_{ext} in the center) is not reached, since ρ reaches its maximum value of 1.0. Electrical remodeling has no effect on the conduction velocity; the time of depolarization is the same with and without remodeling (not shown).

As expected, remodeling affects the APD. APD$_{100}$ increases for early-activated segments and decreases for later-activated segments. In the 6-cm-long fiber, APD$_{100}$ also increases for later-activated segments in case remodeling is controlled by W_{tot}. These changes in APD result in a decreased dispersion of repolarization in the longer fibers. In Figure 7.6 (bottom) it can be observed that without remodeling, the repolarization wave starts at the stimulation site and travels in the same direction as the depolarization wave to the other end. With remodeling in the 1-cm-long fiber, repolarization starts at the other end, and hence the repolarization wave travels in the opposite direction from the depolarization wave. With remodeling in the longer fibers, the repolarization wave starts near the center and travels in both directions, partly in opposite direction from the depolarization wave.

Figure 7.7 illustrates the effect of $I_{Ca,L}$ remodeling on V_{mem}, $[Ca^{2+}]_i$, F_{norm}, T_{CE}, T_{PE}, and strain for three segments of the 1-cm-long fiber. Without remodeling, the APs of the three segments have similar morphology and duration. However, with remodeling the AP of the segment at 0.2 cm envelops the APs of the other two segments. This is also the case for the Ca^{2+} transient. With remodeling, F_{norm} is increased for early-activated segments such that these segments are able to shorten more during ejection. On the other hand, F_{norm} is decreased for later-activated segments, which results in a decreased T_{CE}. During ejection, T_{PE} is larger to compensate for the decrease in T_{CE}, and thus the strain is increased for these segments. The overall result is that later-activated segments exhibit less shortening, while early-activated segments shorten more. To quantify shortening during ejection, we compare the stretch at end of ejection (λ_{ee}) with the stretch at begin of ejection (λ_{be})

for each segment. Without remodeling $\lambda_{ee}/\lambda_{be} = 0.95$, 0.92, and 0.89 for the segments located at 0.2, 0.5, and 0.8 cm, respectively, while with remodeling $\lambda_{ee}/\lambda_{be}$ is between 0.89 and 0.90 for all segments. Thus, a homogeneous shortening of the 1-cm-long fiber is obtained with remodeling.

In Figures 7.8 and 7.9, V_{mem}, $[Ca^{2+}]_i$, F_{norm}, T_{CE}, T_{PE}, and strain for three segments of the 3-cm-long and 6-cm-long fibers are presented. Without remodeling, the early-activated segments stretch the later-activated segments, which leads to an inhomogeneous contraction. With remodeling of the 3-cm-long fiber, the AP and Ca^{2+} transient of the early-activated segments envelops the AP and Ca^{2+} transient of the later-activated segments and a more homogeneous shortening is obtained during ejection. For the 6-cm-long fiber, depolarization of the later-activated segments is delayed so that part of the shortening occurs after ejection and does not contribute to the shortening of the fiber. In case electrical remodeling is controlled by W_{tot}, the ρ_n are increased for the later-activated segments, which results in more shortening during ejection. The large differences in strain during ejection between early and later-activated segments are in agreement with the large differences in peak systolic strains measured by Jeyaraj *et al.* [87] after 4 weeks of ventricular pacing. Prolongation of the APD occurs for both early and later-activated segments, but not for intermediate segments (Figure 7.6), which is also in agreement with the experimental observations by Jeyaraj *et al.* [87].

In Figure 7.10, the stress-strain loops with and without remodeling are presented for the same segments of the three fibers. Without remodeling, W_{ext}, which is by definition the area enclosed by the stress-strain loop, is small or negative for the early-activated segments. However, with remodeling the area enclosed by the stress-strain loop is enlarged, indicating that these segments shorten more during ejection. On the other hand, the shortening of the later-activated segments is decreased with remodeling. An exception is the later-activated segment of the 6-cm-long fiber, which shortens more during ejection when remodeling is controlled by W_{tot}.

Finally, in Figure 7.11, stress, strain, and the stress-strain loop for the entire fiber are presented without and with remodeling. Relative to the fiber length at begin of ejection, fiber shortening increases from 8% without remodeling to 10-12% with remodeling.
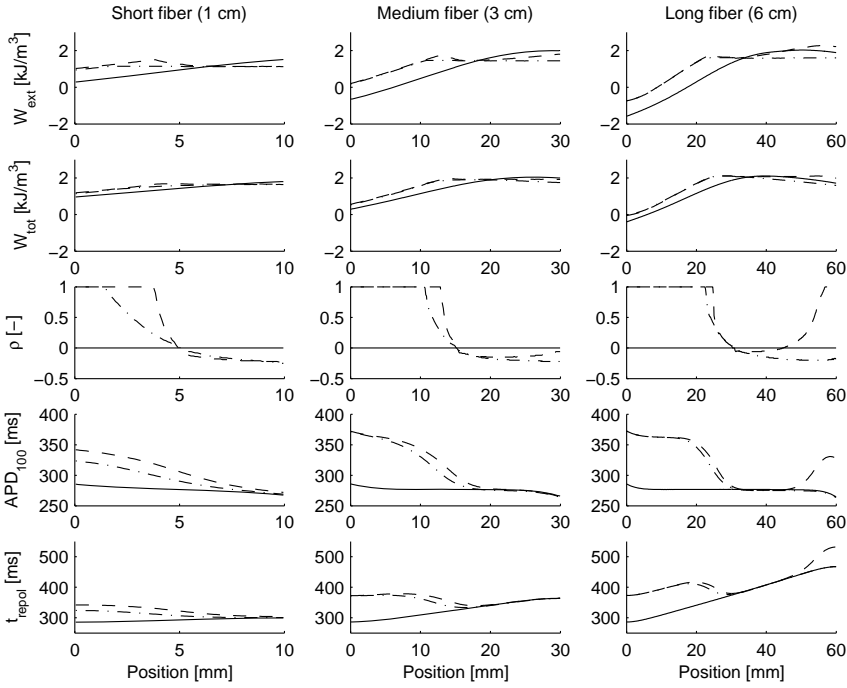
Figure 7.6: Effect of electrical remodeling of $I_{Ca,L}$ on cardiac fibers of length 1 cm, 3 cm, and 6 cm ($T_{rest} = 0.5$ kPa, $T_{preload} = 1$ kPa, $T_{afterload} = 10$ kPa). From top to bottom: external stroke work density (W_{ext}), total stroke work density (W_{tot}), parameter ρ, action potential duration (APD$_{100}$), and repolarization time (t_{repol}). APD$_{100}$ is defined as the time during which V_{mem} is larger than -60 mV and t_{repol} is the time at which V_{mem} becomes lower than -60 mV. Data are plotted without remodeling (solid line), with remodeling controlled by W_{ext} (dash-dotted line), and with remodeling controlled by W_{tot} (dashed line). A stimulus current was applied to the segment at 0 mm at 0 ms.
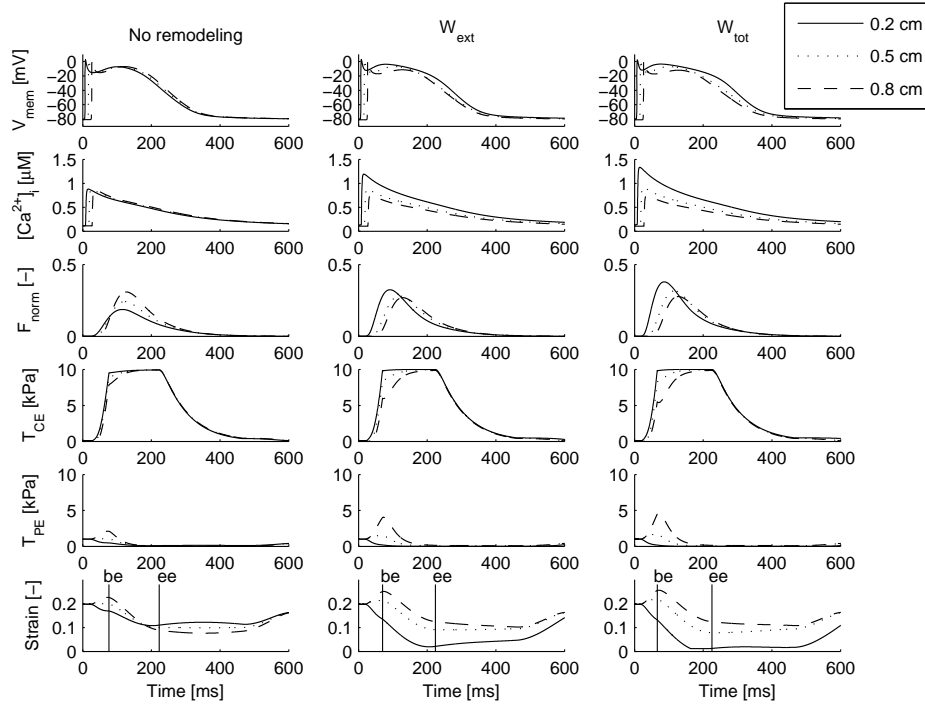
Figure 7.7: Effect of electrical remodeling of $I_{Ca,L}$ controlled by W_{ext} and by W_{tot} on individual segments in 1-cm-long cardiac fiber (T_{rest} = 0.5 kPa, $T_{preload}$ = 1 kPa, and $T_{afterload}$ = 10 kPa). V_{mem}, $[Ca^{2+}]_i$, F_{norm}, T_{CE}, T_{PE}, and strain are plotted for segments located at 0.2, 0.5, and 0.8 cm. Left: without remodeling. Center: remodeling controlled by W_{ext}. Right: remodeling controlled by W_{tot}. The vertical lines in the lower panels indicate begin of ejection (be) and end of ejection (ee). A stimulus current was applied to the segment at 0.0 cm at 0 ms.
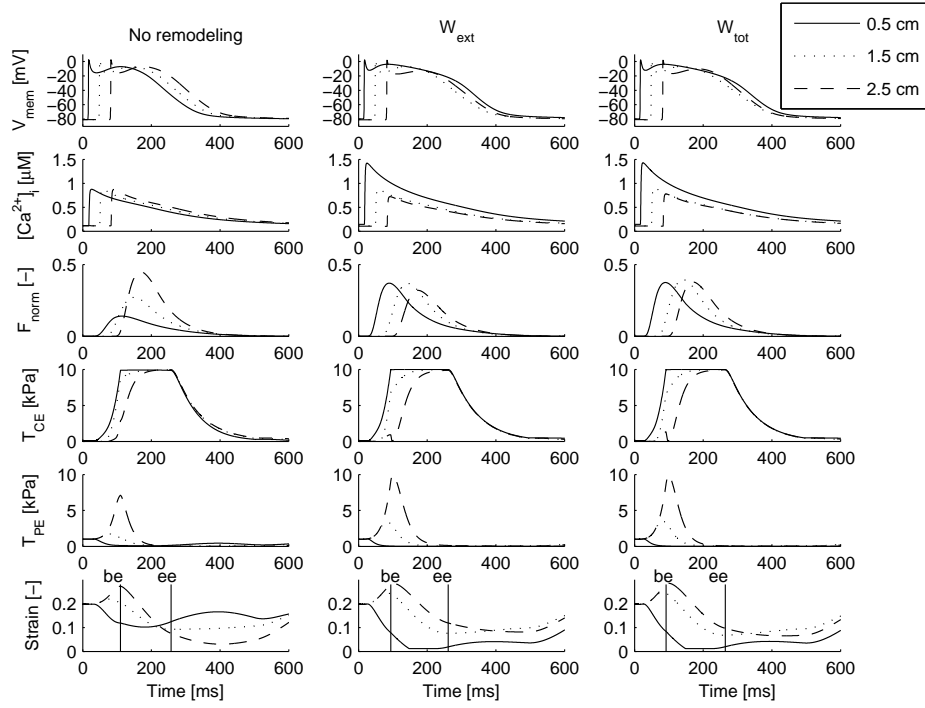
Figure 7.8: Effect of electrical remodeling of $I_{Ca,L}$ controlled by W_{ext} and by W_{tot} on individual segments in 3-cm-long cardiac fiber (T_{rest} = 0.5 kPa, $T_{preload}$ = 1 kPa, and $T_{afterload}$ = 10 kPa). V_{mem}, $[Ca^{2+}]_i$, F_{norm}, T_{CE}, T_{PE}, and strain are plotted for segments located at 0.5, 1.5, and 2.5 cm. Left: without remodeling. Center: remodeling controlled by W_{ext}. Right: remodeling controlled by W_{tot}. The vertical lines in the lower panels indicate begin of ejection (be) and end of ejection (ee). A stimulus current was applied to the segment at 0.0 cm at 0 ms.
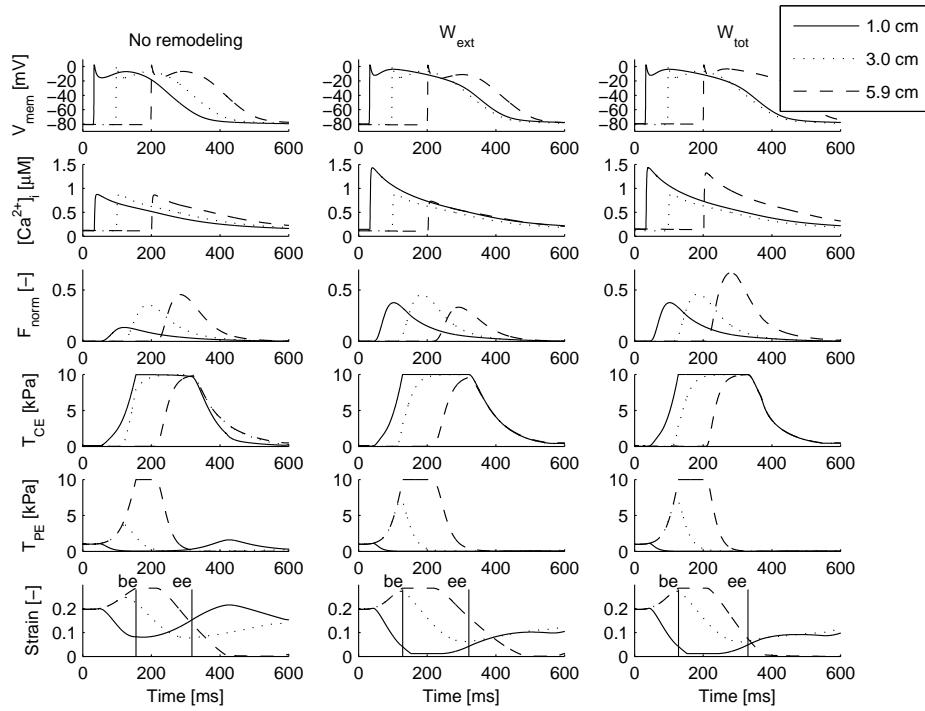
Figure 7.9: Effect of electrical remodeling of $I_{Ca,L}$ controlled by W_{ext} and by W_{tot} on individual segments in 6-cm-long cardiac fiber ($T_{rest} = 0.5$ kPa, $T_{preload} = 1$ kPa, and $T_{afterload} = 10$ kPa). V_{mem}, $[Ca^{2+}]_i$, F_{norm}, T_{CE}, T_{PE}, and strain are plotted for segments located at 1.0, 3.0, and 5.9 cm. Left: without remodeling. Center: remodeling controlled by W_{ext}. Right: remodeling controlled by W_{tot}. The vertical lines in the lower panels indicate begin of ejection (be) and end of ejection (ee). A stimulus current was applied to the segment at 0.0 cm at 0 ms.
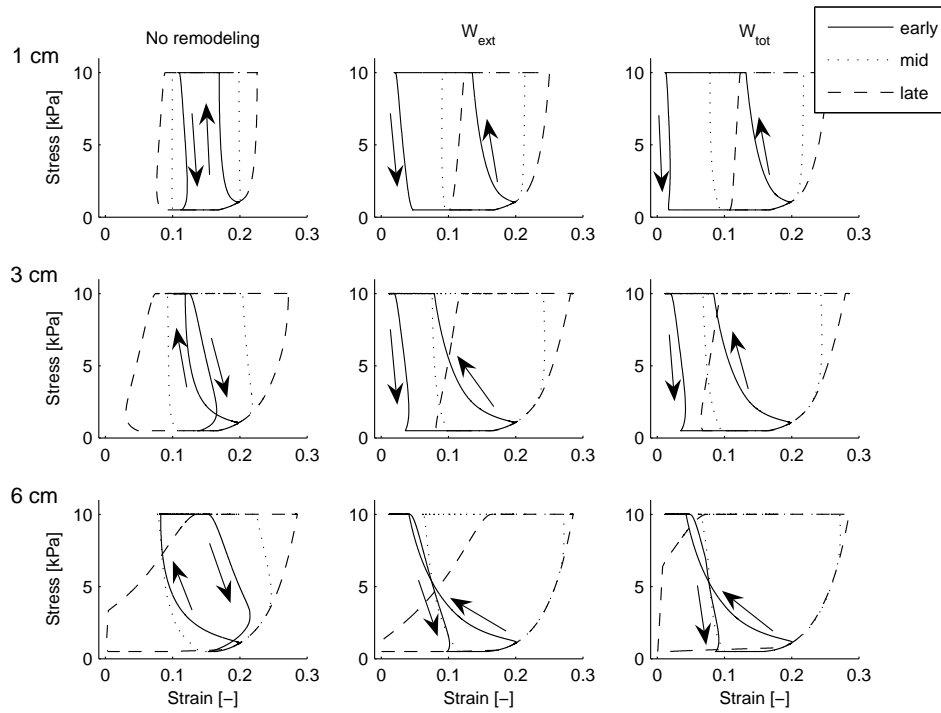
Figure 7.10: Effect of electrical remodeling of $I_{Ca,L}$ controlled by W_{ext} and by W_{tot} on the stress-strain loop for individual segments in cardiac fibers with length 1 cm, 3 cm, and 6 cm ($T_{rest} = 0.5$ kPa, $T_{preload} = 1$ kPa, and $T_{afterload} = 10$ kPa). Stress-strain loops are plotted for early-activated segments (solid), intermediate-activated segments (dotted), and later-activated segments (dashed). Left: without remodeling. Center: remodeling controlled by W_{ext}. Right: remodeling controlled by W_{tot}. A stimulus current was applied to the segment at 0.0 cm. The arrows indicate the direction of time for the early-activated segments (solid lines).
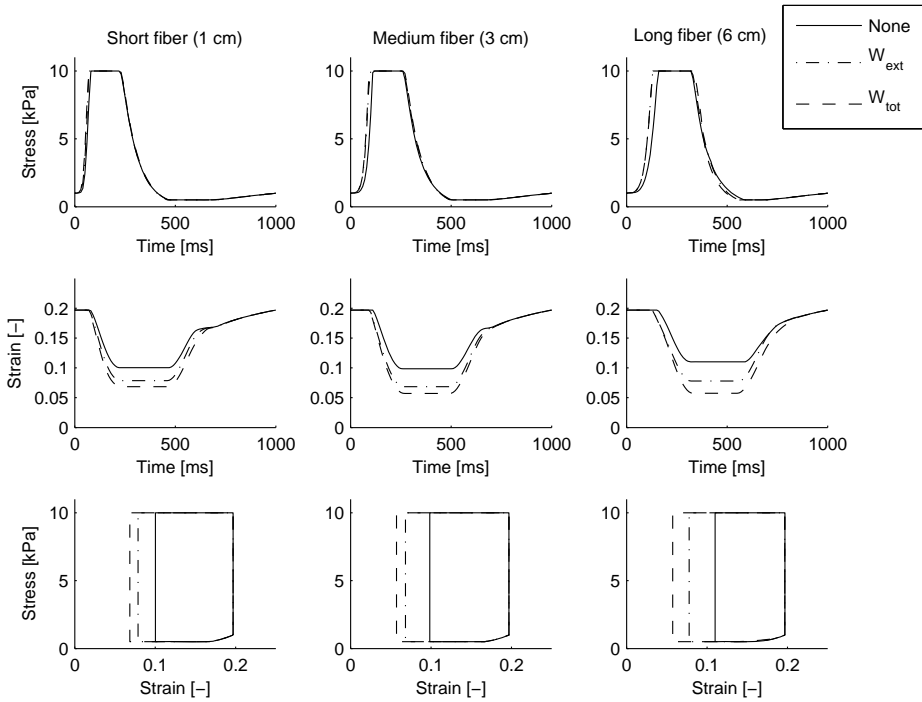
Figure 7.11: Effect of electrical remodeling of $I_{Ca,L}$ controlled by W_{ext} and W_{tot} on the stress-strain loop for cardiac fibers with length 1 cm, 3 cm, and 6 cm ($T_{rest} = 0.5$ kPa, $T_{preload} = 1$ kPa, and $T_{afterload} = 10$ kPa). A stimulus current was applied to the segment at 0.0 cm at 0 ms.

7.4 Discussion

7.4.1 What triggers electrical remodeling?

Libbus and Rosenbaum [121] showed that electrical remodeling can be triggered by changing the stimulation rate as well as by changing the activation sequence. The observed changes in APD and AP morphology are, however, different. Increasing the stimulation rate leads to a shortening of the APD, while changing the activation sequence leads to prolongation of the APD. In both cases, the notch of the AP is reduced, indicating a reduction in I_{to} [121]. Libbus *et al.* [122] suggest that remodeling of I_{to} may be explained by changes in electrotonic load. Jeyaraj *et al.* [87] recently proposed mechano-electric feedback as a mechanism for electrical remodeling. Based on their observation that APD is prolonged near the site of stimulation and also in remote regions, it is unlikely that electrical remodeling is explained by electrotonic interactions [87]. Based on their measurements of circumferential strain, Jeyaraj *et al.* [87] propose that electrical remodeling is related to the distribution of strain. Sosunov *et al.* [178] found that electrical remodeling can be inhibited either by reducing mechanical load or by reducing contractility, indicating that changes in mechanical load are involved. Patberg *et al.* [142] suggest that angiotensin II is a likely candidate to trigger $I_{Ca,L}$ remodeling, since its release is altered by changes in stretch and it affects $I_{Ca,L}$. Local changes in the stress-strain loop may lead to changes in angiotensin II release and eventually affect $I_{Ca,L}$ and calcium homeostasis [20, 142, 168].

In our model, reduction of G_{to} leads to disappearance of the notch in the action potential as well as a reduced APD (Figure 7.2). After changing the activation sequence for 20 days, Yu *et al.* [229] observed disappearance of the notch and APD prolongation. Jeyaraj *et al.* [87] observed APD prolongation without disappearance of the notch, indicating that I_{to} may not be the only ionic current that changes when the activation sequence is changed. Kääb *et al.* [89] found a reduced notch and prolonged APD after 3 to 4 weeks of ventricular pacing. They also found a reduction in I_{to}, but did not find any differences in $I_{Ca,L}$. Kääb *et al.* [89] hypothesized that downregulation of I_{to} is at least partially responsible for the prolongation of the APD. Shvilkin *et al.* [173] observed APD prolongation in both epicardium (which has large I_{to}) and endocardium (which has small I_{to}), and no change in APD in midmyocardium (which has prominent I_{to}). These results suggest that other ionic currents play an important role in electrical remodeling [173]. Rubart *et al.* [162] reported a prolonged APD and a reduced notch after one hour of ventricular pacing in dogs. They found a reduction in I_{to} and as well as an increase in peak $I_{Ca,L}$ [162]. After 21 days of ventricular pacing, Plotnikov *et al.* [145] observed

a more positive $I_{Ca,L}$ activation threshold and slower inactivation in epicardial myocytes, but $I_{Ca,L}$ current size was not changed. Based on these observations, we hypothesized that I_{to} conductance (G_{to}) and $I_{Ca,L}$ kinetics, but not $I_{Ca,L}$ conductance ($G_{Ca,L}$), are affected after changing the activation sequence. Although I_{to} remodeling is probably related to changes in $I_{Ca,L}$, the relation between I_{to} and $I_{Ca,L}$ during electrical remodeling is not clear. Since reducing G_{to} has little effect on the calcium transient in our model, we decided to adapt $I_{Ca,L}$ kinetics, but not I_{to} conductance, when simulating electrical remodeling.

7.4.2 Effect of electrical remodeling on Ca^{2+} and mechanics

In our model, a more positive $I_{Ca,L}$ activation threshold and slower inactivation is represented by a positive value of remodeling parameter ρ and leads to an increased intracellular Ca^{2+} concentration and APD prolongation (Figure 7.2). Plotnikov et al. [145] observed a shift of 10 mV in $I_{Ca,L}$ activation and an increase in APD$_{90}$ of 65 ms. In our model, a shift of 10 mV in $I_{Ca,L}$ activation corresponds to an increase of 82 ms in APD$_{90}$ (Table 7.2). Changing $I_{Ca,L}$ kinetics in our model affects the calcium transient and thus the amount of stroke work. The increase in $I_{Ca,L}$ results in an increased [Ca^{2+}]$_i$ during the AP and in an increased steady-state concentration of Ca^{2+} in the SR uptake compartment, which leads to an increased Ca^{2+} release and explains the increased Ca^{2+} transient.

The effect of electrical remodeling on the 1-cm-long and 3-cm-long fibers can be characterized as follows. Early-activated segments are less stretched than later-activated segments before they start to contract. According to the Frank-Starling law, the tension generated by the early-activated segments is small. With remodeling, the early-activated segments generate more active tension and are able to shorten. On the other hand, the later-activated segments generate less active tension (Figures 7.7 and 7.8). The overall effect is that an increased and more homogeneous shortening of the fiber is obtained with electrical remodeling. Furthermore, the APD is increased in early-activated areas and decreased in later-activated areas, which results in an inverse relationship between APD and activation time, and is in agreement with the results of Costard-Jäckle et al. [36].

Jeyaraj et al. [87] observed an increase in APD in areas close to the pacing site as well as in remote areas, while the APD was either normal or decreased in intermediate areas. We observed a similar distribution of the APD in the 6-cm-long fiber when remodeling was controlled by W_{tot}, but not when remodeling was controlled by W_{ext}. This difference in behavior is explained by the fact that W_{ext} in the later-activated areas is larger than in the center of the fiber, whereas W_{tot} is smaller than in the center. In both cases, the segments

in the later-activated areas exhibit the same amount of shortening. However, only in case remodeling is controlled by W_{tot}, most of the shortening occurs during ejection. We conclude that electrical remodeling of the 6-cm-long fiber controlled by W_{tot} is in agreement with experimentally observed distributions of APD and may lead to homogeneous shortening during ejection.

7.4.3 Transmural heterogeneity in excitation-contraction coupling

Wang and Cohen [219] investigated transmural heterogeneity in the L-type Ca^{2+} channel in the canine left ventricle. Although the kinetic properties of the L-type Ca^{2+} current in epicardial and endocardial myocytes were not significantly different, they found a larger $I_{Ca,L}$ current in endocardial than in epicardial myocytes [219]. Laurita *et al.* [117] observed a longer duration of the Ca^{2+} transient in endocardial compared with epicardial myocytes from the canine left ventricle. In our model, normal transmural activation is represented by the 1-cm-long fiber, in which the early-activated segments represent the endocardial myocytes and the later-activated segments the epicardial myocytes. With remodeling, a larger $I_{Ca,L}$ current and slower inactivation during the plateau phase is obtained for early-activated segments, which is in agreement with the experimental observations. However, to date, no experimental evidence exists for a transmural gradient in L-type Ca^{2+} kinetics in the normal heart.

Cordeiro *et al.* [35] examined unloaded cell shortening of endocardial, midwall, and epicardial cells that were isolated from the canine left ventricle. Time to peak and latency to onset of contraction were shortest in epicardial and longest in endocardial cells, while an intermediate time to peak was observed in midwall cells [35]. These differences in excitation-contraction coupling (ECC) are related to differences in time to peak and decay of the Ca^{2+} transient [35]. In our model, time to peak of the Ca^{2+} transient is not significantly different when $I_{Ca,L}$ kinetics is changed (Figure 7.2), which explains why the heterogeneity in ECC observed by Cordeiro *et al.* [35] is not reproduced by our model.

7.4.4 T wave concordance and cardiac memory

Remodeling of $I_{Ca,L}$ kinetics in our model leads to significant changes in repolarization. In the 1-cm-long fiber, the repolarization wave travels in the opposite direction from the depolarization wave. In the longer fibers, the repolarization wave starts near the center and travels in both directions along the fiber, partly in opposite direction from the depolarization wave. The changes in repolarization are explained by changes in APD and are in agreement with

experimental observations [36, 87]. In the ventricles, the repolarization path is different from the depolarization path, which explains T wave concordance in the normal electrocardiogram (ECG) [63]. During ventricular pacing, the T wave changes, but T wave concordance reappears after several days when normal activation is restored ("cardiac memory") [160]. Our model provides a possible explanation for this phenomenon by assuming that electrical remodeling of cardiomyocytes is triggered by changes in mechanical work.

7.4.5 Ventricular electromechanics

Our simulation results show large differences in shortening of individual segments with and without remodeling. Without remodeling, early-activated segments shorten, then stretch and finally shorten again. Later-activated segments are first stretched, followed by a pronounced shortening (Figures 7.7 - 7.9, left). With remodeling, a more homogeneous shortening of the segments is obtained (Figures 7.7 - 7.9, center and right). Similar results were obtained by Nickerson *et al.* [137] when they compared simulation results of ventricular electromechanics in the case that electrophysiology was modeled differently for endocardial, midwall, and epicardial myocytes to simulation results in the case that electrophysiology was modeled homogeneously. When electrophysiology was modeled homogeneously, a significant heterogeneity in strain was observed at the end of isovolumic contraction. However, when electrophysiology was modeled inhomogeneously, a reduction in transmural sarcomere length variation was observed during repolarization.

Prinzen *et al.* [149] measured systolic fiber strain and external work at different locations in the left ventricle during right atrial pacing (RA pacing) and during left ventricular pacing (LV pacing). Compared with the normal values (RA pacing), strain and external work during LV pacing were approximately zero in regions near the pacing site, and gradually increased to more than twice the normal value in remote regions [149]. These results are similar to our results for the 3-cm-long fiber without remodeling. With remodeling, we found a more homogeneous distribution of shortening and external work for the 1-cm-long and 3-cm-long fibers. In the 1-cm-long fiber, external work was almost homogeneous with remodeling (Figure 7.6), which is in agreement with the measurements during RA pacing (normal stimulation) of Prinzen *et al.* [149].

Ashikaga *et al.* [10] investigated transmural dispersion of mechanics in vivo. They found that the onset of myofiber shortening was earliest in the endocardial layers, while the onset of myofiber relaxation was latest in the endocardial layers. In our model, the onset of relaxation in early-activated segments was delayed with remodeling, such that both onset and relaxation

of segment shortening were in agreement with the experimental results of Ashikaga *et al.* [10]. Thus, cardiomechanics in the ventricles during normal sinus rhythm or RA pacing is better approximated by our model with electrical remodeling of $I_{Ca,L}$. We conclude that adaptation of electrophysiology as proposed here may lead to better predictions of ventricular mechanics in coupled models of cardiac electromechanics.

7.4.6 Model validity and limitations

To our knowledge, the model presented here is the first model in which adaptation of electrophysiology is triggered by heterogeneity in mechanical work. Validity and limitations of the models for the ionic currents, cross-bridge formation, and cardiomechanics are extensively discussed elsewhere [37, 112, 158, 176]. Here, we discuss the validity and limitations of our choices for the cardiac fiber model, the ionic membrane currents, the Ca^{2+}-force relation, the cardiac cycle, and electrical remodeling.

Cardiac fiber model In the present study, a three-dimensional heart is represented by a single fiber. Regarding cardiomechanics, a basic assumption in our fiber model is that the stress applied to each segment is equal at all times during the cardiac cycle. In the real heart, this is related to the assumption that local stress in the direction of the myofibers is uniformly distributed. It is thus assumed that myofiber orientation in the normal heart is adapted such that myofiber stress and strain are about uniform, which is a valid assumption for the normal heart [8]. Regarding electrophysiology, our fiber model assumes a uniform distribution of excitation times along the fiber. In the three-dimensional heart this assumption does not hold. Despite this deviation, we found relations between excitation and mechanics that are comparable with the modeling results of Kerckhoffs *et al.* [99, 100] and the experimental results of Prinzen *et al.* [149].

Ionic membrane currents To describe the membrane currents and calcium handling, we apply the Courtemanche-Ramirez-Nattel model of the human atrial action potential [37]. In this model, calcium handling is based on the ventricular model by Luo and Rudy [125, 126]. Since the model is capable of reproducing the complex interaction between I_{to} and $I_{Ca,L}$ as described by Greenstein *et al.* [65] for ventricular models, we conclude that the model is representative for cardiomyocytes in general. By adjusting $I_{Ca,L}$ gating variable d, our model is capable of reproducing a larger $I_{Ca,L}$ current and slower inactivation during the plateau phase, which is in agreement with the increased

APD and plateau height observed by Plotnikov *et al.* [145]. Although we obtain qualitative agreement, fitting $I_{Ca,L}$ kinetics to the data provided by Plotnikov *et al.* [145] may require a recent ventricular model such as the Winslow-Rice-Jafri model of the canine ventricle [225] (including the new formulation of I_{to1} by Greenstein *et al.* [65]) or the model by Ten Tusscher *et al.* [197].

Ca^{2+}-force relation   To date, no model describing the Ca^{2+}-force relation of human atrial myocytes exists. In the present study, we apply *model 4* of Rice *et al.* [157, 158], which approximates the contractile force measured during isosarcometric twitches from RV rat trabeculae [86]. In *model 4*, the affinity of troponin for Ca^{2+} does not increase in the presence of strongly bound cross bridges. Incorporation of the crossbridge-troponin cooperativity mechanism [4] as in *model 5* would lead to an increasing steepness in the Ca^{2+}-force relation, especially in the midlevel ranges of force [158]. In our model, the increased intracellular Ca^{2+} concentration in early-activated segments would have a more prominent effect on F_{norm}, which leads to a more homogeneous distribution of work.

The choice between *model 4* and *model 5* is motivated by the fact that we found better agreement between the Ca^{2+}-force relation obtained by *model 4* and the experimental results of Kentish *et al.* [98], in particular for sarcomere lengths above 1.9 μm. When we compared the isosarcometric twitches, we found that, for *model 5*, the peak force was lower and the latency to peak force was increased for longer sarcomeres. Compared with the experimental data measured by Janssen and Hunter [86], the latency to peak force increased too much with sarcomere length [112]. Since the twitches obtained by *model 4* better resemble the experimental results from Janssen and Hunter, we have chosen *model 4* to describe the Ca^{2+}-force relation. Lab *et al.* [115] observed in experiments that a decreased mechanical load during shortening leads to an increased $[Ca^{2+}]_i$ and a longer APD. These observations are acute and are not related to electrical remodeling. Although direct force feedback may result in a more uniform contraction, we do not consider acute mechanoelectric feedback in the present simulation study.

Cardiac cycle   In our model, the cardiac cycle is simulated by an extended preload-afterload experiment. Although the work loops obtained with our values for $T_{preload}$ and $T_{afterload}$ are in agreement with the work loops used in the experiments by Iribe *et al.* [81], our value of $T_{afterload}$ is low compared with the afterload of 35 kPa computed by Kerckhoffs *et al.* [100] when simulating ventricular work loops. We decided not to increase $T_{afterload}$, because that would lead to too little shortening for $\rho = 0.0$ (Figure 7.5).

Electrical remodeling   Electrical remodeling is simulated by changing $I_{Ca,L}$ kinetics based on the experiments by Plotnikov *et al.* [145]. With respect to electrophysiology, our model predicts changes in AP morphology and duration similar to the changes observed after ventricular pacing [36, 87]. A less prominent notch of the AP as observed in experiments [121, 229] would occur if not only $I_{Ca,L}$ kinetics was adapted, but also I_{to} conductance was reduced. In addition to $I_{Ca,L}$ and I_{to}, transmural heterogeneity was found in I_{Ks} [123] and in I_{NaCa} [233]. Obreztchikova *et al.* [138] observed remodeling of I_{Kr} and I_{Ks} after three weeks of epicardial pacing. Although these currents influence AP morphology and excitation-contraction coupling, we do not consider remodeling of I_{Kr}, I_{Ks}, and I_{NaCa} in our model.

With respect to cardiomechanics, our model predicts homogeneous shortening and mechanical work in the normal heart (represented by the 1-cm-long fiber) when $I_{Ca,L}$ is adapted. The homogeneous mechanical behavior is in agreement with experimental observations [41, 149]. Without $I_{Ca,L}$ adaptation, the model predicts inhomogeneous shortening and mechanical work during ventricular pacing (represented by the 3-cm-long fiber), which is in agreement with experimental observations after 15 minutes of ventricular pacing [41, 149]. With $I_{Ca,L}$ adaptation, our model predicts large differences in strain during ejection between early and later-activated segments in the 6-cm-long fiber. These large differences in strain are in agreement with the large differences in peak systolic strains between early and later-activated regions observed by Jeyaraj *et al.* [87] after 4 weeks of ventricular pacing.

7.4.7   Clinical relevance

Models of cardiac electromechanics have been applied to investigate medical interventions such as cardiac resynchronization therapy (CRT) [100, 204]. Extension of models for cardiac electromechanics with adaptation of ionic currents in response to changes in mechanical load may lead to more accurate predictions of regional electrical, mechanical, and metabolic properties of cardiac tissue in the healthy heart, during pathology, and during pacing. Application of such models in cardiovascular research may improve our understanding of the interaction between electrophysiology and cardiomechanics.

7.5   Conclusion

Experimentally observed heterogeneity in APD and homogeneity in fiber shortening are reproduced by adaptation of $I_{Ca,L}$ kinetics triggered by changes

in mechanical work. Thus, adaptation of $I_{Ca,L}$ is a possible mechanism to reduce heterogeneity in mechanics induced by heterogeneity in activation.

8

Vulnerability to atrial fibrillation under stretch can be explained by stretch-activated channels

N.H.L. Kuijpers, R.J. Rijken, H.M.M. ten Eikelder, and P.A.J. Hilbers

Abstract

Experimental studies show an increased vulnerability to atrial fibrillation (AF) in acutely dilated atria. By application of a stretch-activated channel (SAC) blocker, vulnerability to AF decreases significantly, indicating a role for SACs in the initiation of AF. Using a computer model of cardiac electromechanics, we investigate the hypothesis that increased vulnerability to AF may be attributed to SACs. In our model, the human atria are represented by a triangular mesh obtained from MRI data. In this geometry, thickness is varied to model the bundles that are located in the atrial wall. Electrophysiology is modeled by the Courtemanche-Ramirez-Nattel model of the human atrial action potential extended with the stretch-activated current I_{sac}. Mechanical behavior is modeled by a series elastic, a contractile, and a parallel elastic element. The contractile force is related to the intracellular concentration of free calcium as well as to the sarcomere length. To simulate acute dilatation, overall stretch is applied to the atria. Due to contraction of some areas, stretch increases in other areas, leading to a variation in I_{sac}. In the presence of I_{sac}, the membrane potential depolarizes, which causes inactivation of the sodium channels and results in conduction slowing or block. Inducibility of AF increases under stretch, which is explained by an increased dispersion in effective refractory period (ERP), conduction slowing, and local conduction block. Our observations explain the large differences in intraatrial conduction measured in experiments and provide insight in the vulnerability to AF in dilated atria.

185

Table 8.1: Model parameters

Parameter	Definition	Value
g_{int}	Intracellular conductivity	6.25 mS/cm
g_{ext}	Extracellular conductivity	6.25 mS/cm
C_{mem}	Membrane capacitance	$1.0\,\mu\text{F/cm}^2$
χ	Surface-to-volume ratio	$2000\,\text{cm}^{-1}$
G_{sac}	Maximum I_{sac} conductance	0.5 nS/pF
E_{sac}	Reversal potential for I_{sac}	0 mV
K_{sac}	Parameter for I_{sac}	100
α_{sac}	Parameter for I_{sac}	3

8.1   Introduction

Atrial fibrillation (AF) is characterized by rapid and irregular electrical activity, which results in irregular contraction of the atria [133]. Experimental studies indicate an increased vulnerability to AF in acutely dilated atria [16, 54, 152, 166]. Stretch-induced changes in electrophysiology are explained by the stretch-activated channel (SAC) hypothesis [78, 105]. In the present simulation study, we investigate the effect of the stretch-activated current (I_{sac}) on impulse propagation and arrhythmic behavior in the human atria.

8.2   Methods

To investigate the effect of stretch on atrial electrophysiology, we apply our discrete bidomain model, the Cellular Bidomain Model [109, 110]. The model describes active membrane behavior as well as intracellular coupling and interstitial currents, and has been extended to describe cardiac mechanics [112]. The human atria are modeled by a triangular mesh composed of 7446 triangles created from MRI data [207, 208].

8.2.1   Atrial electrophysiology

In the Cellular Bidomain Model, a distinction is made between the intracellular domain and the interstitium. The triangular mesh is refined by subdividing each of the triangles in nine smaller triangles (Chapter 3). The electrophysiological state of each node in the refined mesh is defined by the intracel-

lular potential (V_{int}), the extracellular potential (V_{ext}), and the state of the cell membrane, which is expressed in gating variables and ion concentrations. The membrane potential (V_{mem}) is defined by

$$V_{mem} = V_{int} - V_{ext}. \tag{8.1}$$

Intracellular and extracellular currents between adjacent segments are related to intracellular and extracellular conductivities (g_{int} and g_{ext}). In the present study, we assume equal g_{int} and g_{ext} in all directions, i.e., the atrial tissue is assumed to be isotropic (Table 8.1). Conductivities are locally adjusted for changing stretch ratio as described in Section 6.2.2.

Exchange of current between the intracellular and extracellular domains occurs as transmembrane current (I_{trans}), which depends on ionic current (I_{ion}) and capacitive current according to

$$I_{trans} = \chi(C_{mem}\frac{dV_{mem}}{dt} + I_{ion}), \tag{8.2}$$

where χ is the ratio of membrane area to tissue volume and C_{mem} represents membrane capacitance. Currents are expressed per unit of tissue volume in $\mu A/cm^3$. Assuming $C_{mem} = 1\ \mu F/cm^2$, ionic current is expressed in pA/pF and depends on V_{mem}, gating variables, and ion concentrations. To model I_{ion}, we extend the Courtemanche-Ramirez-Nattel model [37] with the stretch-activated current I_{sac}. The total ionic current is given by

$$I_{ion} = I_{Na} + I_{K1} + I_{to} + I_{Kur} + I_{Kr} + I_{Ks} + I_{Ca,L} + I_{p,Ca} + I_{NaK} + I_{NaCa} + I_{b,Na} + I_{b,Ca} + I_{sac}, \tag{8.3}$$

where I_{Na} is fast inward Na^+ current, I_{K1} is inward rectifier K^+ current, I_{to} is transient outward K^+ current, I_{Kur} is ultrarapid delayed rectifier K^+ current, I_{Kr} is rapid delayed rectifier K^+ current, I_{Ks} is slow delayed rectifier K^+ current, $I_{Ca,L}$ is L-type Ca^{2+} current, $I_{p,Ca}$ is Ca^{2+} pump current, I_{NaK} is Na^+-K^+ pump current, I_{NaCa} is Na^+/Ca^{2+} exchanger current, and $I_{b,Na}$ and $I_{b,Ca}$ are background Na^+ and Ca^{2+} currents [37].

I_{sac} is modeled as a nonselective cation current with a linear current-voltage relation [112]. The current size depends on the membrane potential V_{mem} and stretch ratio λ by

$$I_{sac} = \frac{G_{sac}(V_{mem} - E_{sac})}{1 + K_{sac}\exp(-\alpha_{sac}(\lambda - 1))}, \tag{8.4}$$

where G_{sac} is the maximum membrane conductance, E_{sac} is the reversal potential, K_{sac} is a parameter to define the amount of current when $\lambda = 1.0$, and α_{sac} is a parameter to describe the sensitivity to stretch. Parameters K_{sac} and α_{sac} are from Zabel *et al.* [230] (Table 8.1). The influence of I_{sac} on intracellular Na^+, K^+, and Ca^{2+} concentrations is modeled as described in Chapter 6.
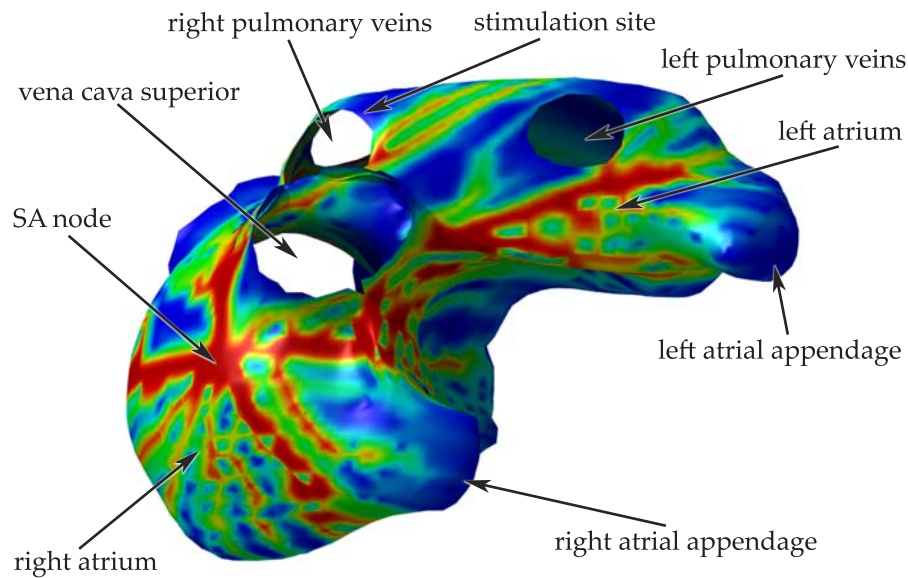
Figure 8.1: Thickness variation in atrial geometry. Red is thick tissue, green is tissue of medium thickness, and blue is thin tissue. The stimulation site is located near the right pulmonary veins.

8.2.2 Atrial mechanics

The mechanical behavior of a single segment is modeled by a series elastic, a contractile, and a parallel elastic element [112]. As in Chapter 6, active force generated by the contractile element is described by *model 4* of Rice *et al.* [158] and is related to intracellular Ca^{2+} concentration and sarcomere length (Appendix C).

To simulate atrial dilatation, it is assumed that the same amount of force is applied to each segment. During the simulation, the amount of force applied to the atria is adjusted, such that the overall stretch ratio remains constant (isometric simulation). Contraction of early activated regions may lead to increased stretch in late activated regions. To incorporate bundles, thickness of the tissue is varied as shown in Figure 8.1. Since thicker tissue is harder to deform, variation in thickness will lead to differences in local stretch and, hence, influences I_{sac}.

8.2.3 Simulation set-up

To investigate the effect of stretch on impulse propagation, we performed simulations using a single fiber as described in Chapter 6. The mesh rep-
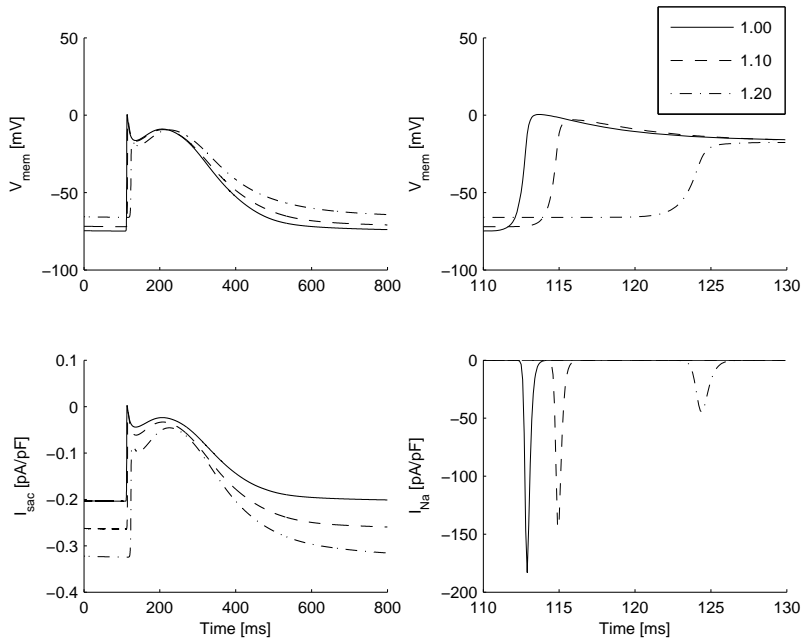
Figure 8.2: Effect of stretch on the action potential (AP) and impulse propagation. Left: membrane potential (V_mem) and stretch-activated current (I_sac). Right: V_mem and fast Na$^+$ current (I_Na) during AP upstroke. A stimulus current was applied at 100 ms. Data are plotted for stretch ratio $\lambda = 1.00$, 1.10, and 1.20 for a segment located 0.5 cm from the stimulation site.

resenting the human atria was refined as described in Chapter 3. Two levels of coarseness were distinguished. Mechanics computation was performed on the coarsest level (3800 nodes), while electrophysiology was simulated on the finer level (33754 nodes). The average distance between two connected nodes on the coarsest level was 0.27 cm and on the finest level 0.09 cm. To obtain accurate simulation results, the heuristic method introduced in Section 3.2.5 was applied with $\alpha = 0.3$. Under the assumption that the same amount of force is applied to each segment, computation of the mechanical state was performed as if all segments were part of one single fiber (isometric simulation; Appendix D). Simulation time steps to compute the ionic membrane currents were varied between 0.02 and 0.1 ms as described in Section 3.2.3, while the simulation time step to compute the mechanics was 0.1 ms.

8.3 Results

8.3.1 Influence of I_{sac} on impulse propagation

In Figure 8.2, the effect of stretch on the propagating action potential is illustrated. For increasing λ, the action potential duration (APD) increases, while I_{Na} decreases. The reduced I_{Na} is explained by inactivation of Na$^+$ channels as a consequence of the depolarized V_{mem} during diastole [112]. As can be observed in Figure 8.2, the smaller I_{Na} current size leads to a lower maximum upstroke velocity. For increasing λ, the segment located 0.5 cm from the stimulation site is excited at a later point in time, which indicates a reduced impulse propagation.

8.3.2 Influence of I_{sac} on the vulnerability to AF

To investigate the effect of I_{sac} on the vulnerability to AF, simulations were performed using the mesh of the human atria. Ectopic activity was simulated by applying a stimulus current near the pulmonary veins with a stimulation interval of 0.6 s. Overall stretch was varied between 0% and 20%.

In Figure 8.3, depolarization of the atria is shown after the fourth stimulation without stretch, with 10% stretch, and with 12% stretch. While conduction was normal without stretch, conduction slowing and local conduction block was observed with 10% stretch. With 12% stretch, conduction was normal after the first, third, and fifth stimulation, while conduction was blocked after the second and fourth stimulation due to an increased refractory period. Conduction was completely blocked with 20% stretch (not shown).

Due to conduction slowing and local conduction block with 10% stretch, a reentrant depolarization wave developed after 3 s. The path of the depolarization wave changed over time and the arrhythmia stopped after 14 s. In Figure 8.4, the atrial arrhythmia is shown after 12 s of simulation time. In Figure 8.5, V_{mem}, I_{sac}, intracellular Ca^{2+} concentration ([Ca^{2+}]$_i$), and stretch ratio (λ) are shown for a segment near the sino-atrial (SA) node and a segment near the pulmonary veins (PV) between 8 and 13 s. λ changes due to contraction of the segment and is influenced by contraction of other parts of the atria. Changes in λ affect I_{sac}, V_{mem}, and [Ca^{2+}]$_i$, and add to the irregular electrical activity of the atria.

8.3.3 Influence of contraction on AF

To investigate the effect of atrial contraction on arrhythmic behavior, we continued the simulation after 13 s with contraction enabled and with contraction disabled. Disabled contraction was implemented by assuming that [Ca^{2+}]$_i$

time [ms]	normal conduction without stretch	slow conduction with 10% stretch	conduction block with 12% stretch
0			
50			
100			
150			
200			
250			
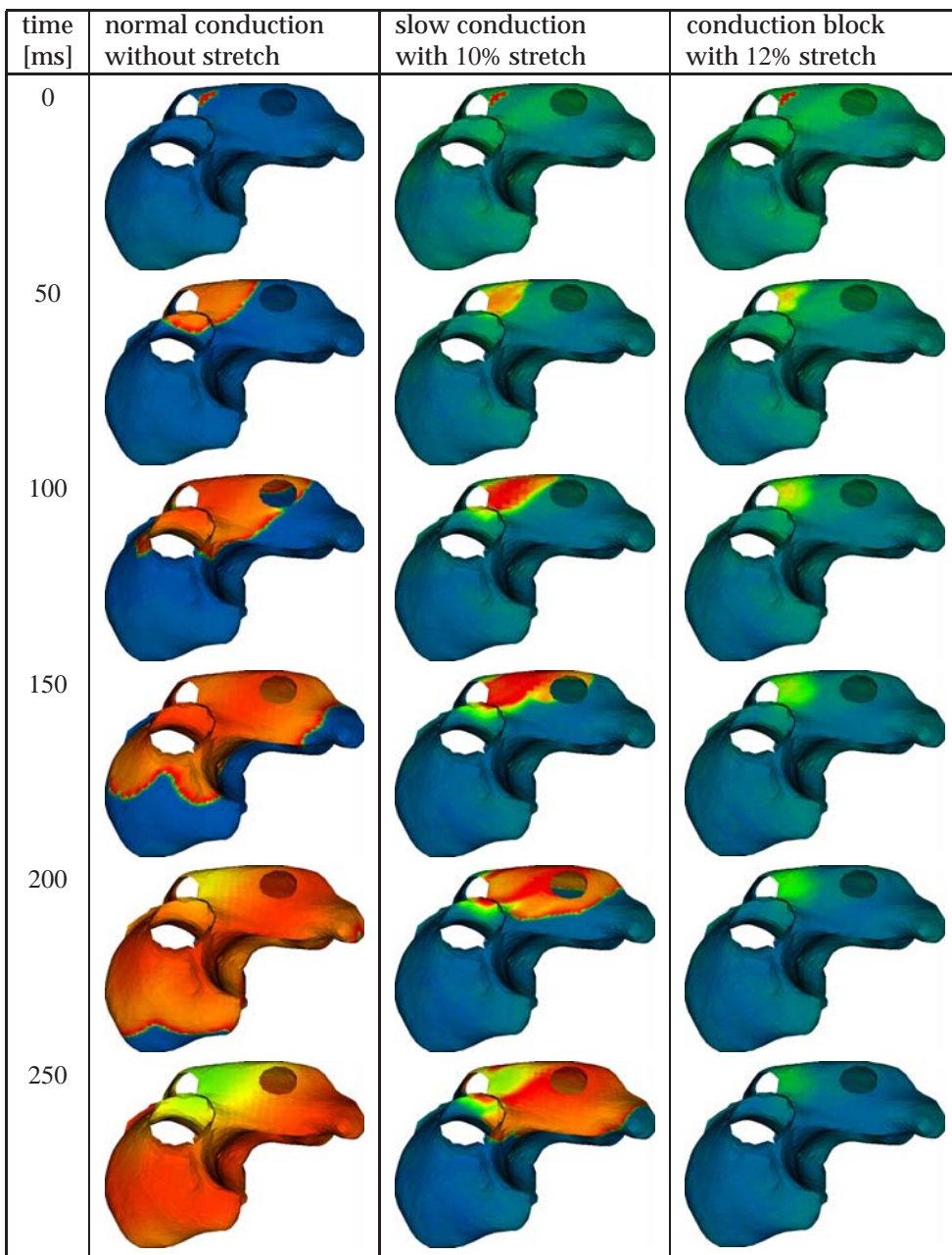
Figure 8.3: Atrial depolarization after the fourth stimulation near the pulmonary veins. Left: normal conduction when no stretch is applied. Center: slow conduction with 10% stretch. Right: conduction block with 12% stretch. Membrane potential (V_{mem}) is shown after stimulation at 0 ms with intervals of 50 ms. Red is depolarized tissue, green is tissue with increased V_{mem}, and blue is recovered tissue.
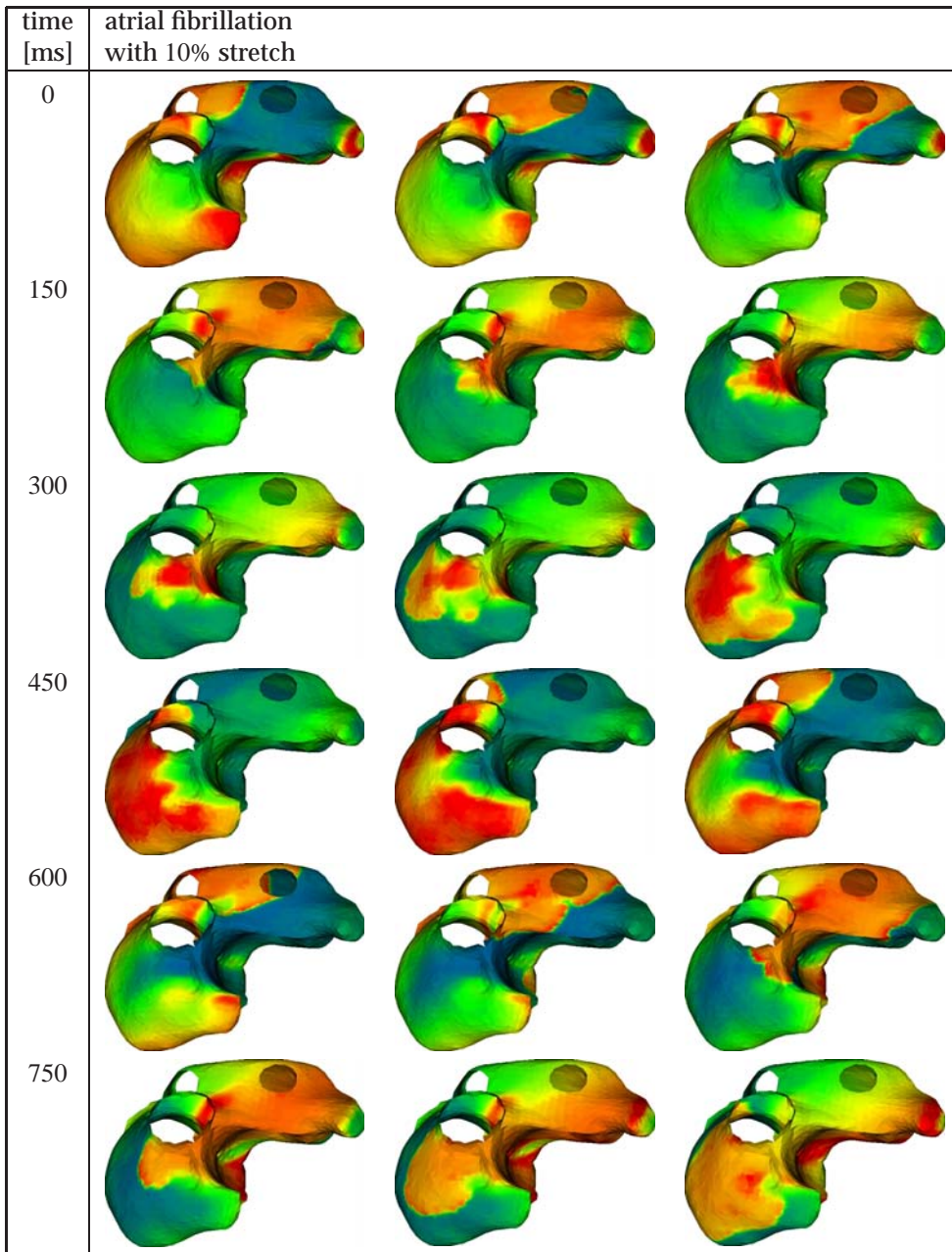
Figure 8.4: Atrial fibrillation with 10% stretch. Membrane potential (V_{mem}) is shown after 12 s of simulation with intervals of 50 ms. Red is depolarized tissue, green is tissue with increased V_{mem}, and blue is recovered tissue.
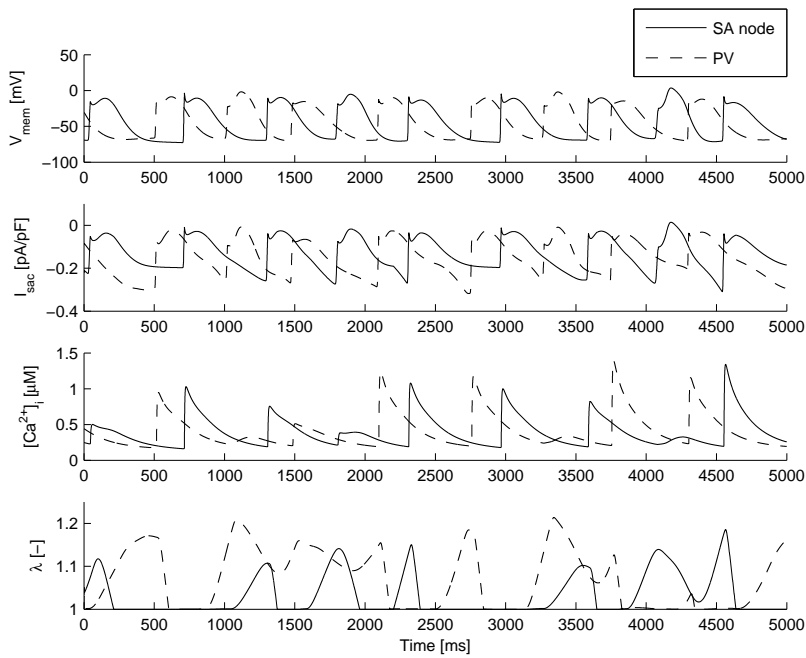
Figure 8.5: Membrane potential (V_{mem}), stretch-activated current (I_{sac}), intracellular Ca^{2+} concentration ([Ca^{2+}]$_i$), and stretch ratio (λ) for a segment near the sino-atrial node (SA node) and a segment near the pulmonary veins (PV) during an episode of atrial fibrillation with 10% stretch (simulation time 8-13 s).

was equal to its resting value of $0.0102\ \mu$M [37] when the contractile force was computed. In Figure 8.6, it is shown how the arrhythmia stops after 600 ms with contraction enabled, while it continues for another second if contraction is disabled. In the case that contraction is enabled, V_{mem} is depolarized at 600 ms in the thin region near the pulmonary veins due to an increase in λ. The depolarized V_{mem} leads to block of the reentrant depolarization wave. In the case that contraction is disabled, the depolarization wave is not blocked and continues to reenter.

8.4   Discussion

Atrial dilatation is simulated by the application of overall stretch to the atria. Variation in thickness leads to an inhomogeneous distribution of stretch, which influences impulse propagation, action potential duration (APD), and effective refractory period (ERP). Dispersion in APD and ERP is further enhanced
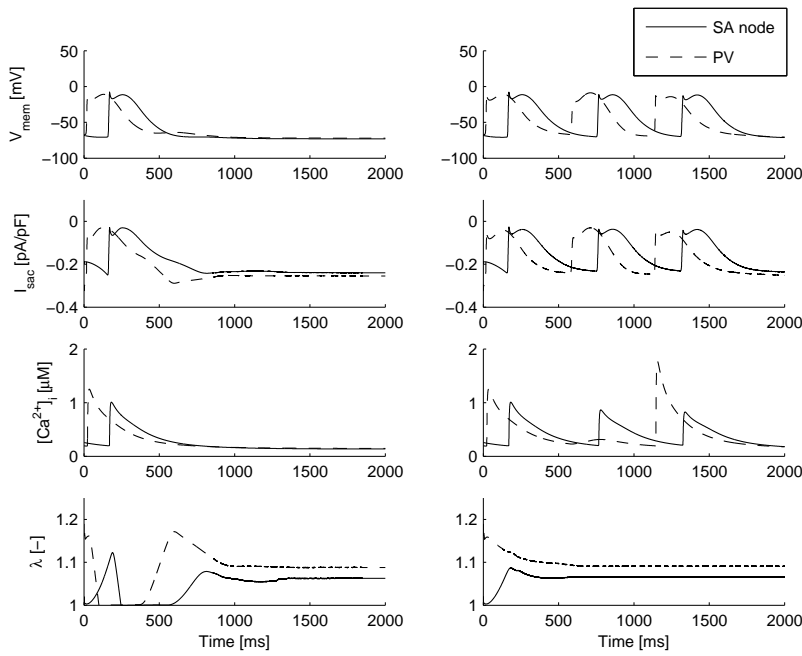
Figure 8.6: V_{mem}, I_{sac}, $[\mathrm{Ca}^{2+}]_i$, and λ for a segment near the sino-atrial node (SA node) and a segment near the pulmonary veins (PV) during an episode of atrial fibrillation with 10% stretch (simulation time 13-15 s). Left: contraction enabled. Right: contraction disabled.

by the contraction of active parts of the atria and can influence both the onset and the termination of atrial arrhythmia.

Conduction slowing and block in our model is explained by a decreased membrane excitability caused by the stretch-activated current I_{sac}. In an experimental study, Eijsbouts *et al.* [54] reported a decreased conduction velocity and local conduction block when the right atrium of a rabbit was acutely dilated. Satoh and Zipes [166] measured an increased ERP both in the thin atrial free wall and in the crista terminalis under stretch. The ERP of the thin free wall was increased more than the ERP in the thicker crista terminalis, which they explain by the assumption that the thin free wall is more stretched compared with the thicker bundles [166]. These experimental observations are in agreement with our simulation results and explain the vulnerability to AF under acute stretch. Bode *et al.* [16] report that SAC blocker gadolinium reduces the stretch-induced vulnerability to AF, confirming that I_{sac} plays a significant role in the vulnerability to AF in acutely dilated atria.

8.4.1 Model validity and limitations

To our best knowledge, our model is the first to integrate cardiac electrophysiology and cardiomechanics with physiological details such as ionic membrane currents, intracellular Ca^{2+} handling, and cross-bridge formation. In our model, changes in impulse propagation under stretch are related to I_{sac} and to a reduced conductivity. We do not consider other mechanisms that could influence impulse propagation, such as the stretch-related function of other membrane channels, autonomic reflexes, and metabolic changes.

The validity of our model largely depends on the validity of the underlying models and parameters. Validity and limitations of the models for the ionic membrane currents, cross-bridge formation, and cardiomechanics are extensively discussed elsewhere [37, 112, 158, 176, 230]. Validity and limitations of the integrated cell model and the model of I_{sac} is discussed in Chapter 6.

A limitation of our model with respect to mechanics is the assumption of a uniaxial state in the atrial wall, i.e., the segments are only stretched in the direction of the fiber. In reality, the segments will also experience force in the direction perpendicular to the fiber axis in the plane of the atrial wall. This force tends to reduce the strain along the fiber direction, which results in an overestimation of the stretch in our model.

8.5 Conclusion

Conduction slowing and block is related to the amount of stretch and is enhanced by contraction of early activated areas and inhomogeneity in the atrial wall. Variation in thickness increases the dispersion in refractory period and is proarrhythmic. Our observations are in agreement with experimental results and provide an explanation for the increased inducibility of atrial fibrillation observed in acutely dilated atria.

Acknowledgements

9

General discussion

In this thesis, we introduced the Cellular Bidomain Model and discussed various aspects of the model, including a numerical integration scheme and methods to save computation time and memory. The model was applied in five different simulation studies to cardiac electrophysiology and mechano-electric feedback. Here, we discuss the model, its applications, and possible further improvements.

9.1 The Cellular Bidomain Model

In Chapters 2 and 3, we introduced a mathematical framework to model cardiac electrophysiology. This framework is well-suited to simulate electrophysiological behavior at the cellular level and to combine different cell types into one simulation. An important aspect of our model is that conductances between the segments are explicitly modeled. Since our numerical scheme does not require matrix inversions, our approach can be applied in situations where conductivity changes during the simulation run. For example, in Chapter 6, we describe how local conductivity changes due to stretch or contraction.

Although our model allows for modeling at the level of individual cardiac myocytes, in our applications a single node represents a small portion of tissue containing multiple cells. On the other hand, the same mathematical framework can be applied to model cardiac tissue at the subcellular level as described in Refs. [118, 169, 179, 186]. In that case, multiple nodes of the simulation graph represent a single myocyte and the intracellular conductance of an edge either represents the conductance within the myoplasm or the conductance through the gap junctions. A model at the subcellular level in which the intracellular and extracellular spaces are spatially distinct is the model constructed by Stinstra *et al.* [187, 188].

An important aspect of our model is the strong coupling between cardiac electrophysiology and cardiomechanics, which has proved its value when in-

vestigating the role of stretch-activated currents in the onset and perpetuation of atrial fibrillation and the role of mechanoelectric feedback in remodeling of ionic membrane currents.

9.2 Applications of the Cellular Bidomain Model

In this thesis, we applied the Cellular Bidomain Model to investigate both normal and abnormal cardiac electrophysiology and mechanoelectric feedback. In particular, we investigated the success and failure of defibrillation, the onset of atrial fibrillation in relation to ectopic activity and stretch, and electrical remodeling that occurs after the implantation of a pacemaker.

9.2.1 Defibrillation

In Chapter 4, we investigated virtual electrode polarization (VEP) in uniform, decoupled, and nonuniform cardiac tissue. We found that fast depolarization and more or less synchronous repolarization may lead to successful termination of spiral waves. We concluded that the success of defibrillation in clinical practice is explained by nonconducting obstacles and nonuniform cellular coupling present in normal and in pathological hearts. A possible future application of our model of defibrillation would be the quantification of success rates of defibrillation protocols such as monophasic and biphasic shocks [59, 61, 127].

9.2.2 Ectopic activity

In Chapter 5, we extended our model of cardiac electrophysiology with the pacemaker current I_f. To model the kinetics of I_f, we used the formulation by DiFrancesco [43] for pacemaker channels in the rabbit SA node. With these kinetics, the half activation potential is -95 mV and only a small fraction of the I_f channels is open in diastolic range. To obtain spontaneous action potentials, we used a relatively large maximum conductance G_f, which corresponds to a large number of channels in the membrane.

At present, it is unclear whether human atrial myocytes are capable of pacemaker activity related to I_f. Spontaneous activity in the human atria under pathological conditions, such as heart failure, may be related to both an increase in I_f and a decrease in the rectifying K^+ current I_{K1} [76, 140]. Michels *et al.* [128] observed that the half activation potential for I_f in human atrial myocytes is about -68 mV, which is well within the diastolic voltage range of human atrial myocytes. Although the experimental results of

Michels *et al.* are subject of debate [44], their findings support a possible contribution of I_f to arrhythmia in working myocardium under pathological conditions [128].

9.2.3 Atrial fibrillation in relation to stretch

In Chapter 6, we extended our model of cardiac electrophysiology with mechanics and investigated the effect of the stretch-activated current I_sac on impulse propagation. We found that conduction slowing and block are related to a reduced maximum upstroke velocity $(\mathrm{d}V_\mathrm{mem}/\mathrm{d}t)_\mathrm{max}$, which is explained by a reduced number of available I_Na channels due to an increased resting membrane potential. Another effect of I_sac is the lengthening of the effective refractory period (ERP), which may be inhomogeneously distributed over the fiber when thickness is varied. An inhomogeneous distribution of ERP due to variation in thickness may explain the increased vulnerability to atrial fibrillation when the atria are acutely dilated [16, 54, 166].

In Chapter 8, we observed that after repetitively stimulating the atria near the pulmonary veins, a reentrant depolarization wave developed, which lead to arrhythmic behavior. Both the initiation and the termination of the arrhythmia were related to local conduction block and differences in ERP, confirming that the vulnerability to AF under stretch may be related to the characteristic inhomogeneity of atrial tissue. By comparing the results of simulations with and without contraction, we found that contraction of activated tissue may influence impulse propagation in other parts of the atria, and may either enhance arrhythmic behavior or terminate it.

9.2.4 Electrical remodeling in the ventricles

In Chapter 7, we investigated the hypothesis that the deviation from normal mechanical work with ventricular pacing functions as a trigger for electrical remodeling. By adaptation of the kinetics of the L-type Ca^{2+} current $I_\mathrm{Ca,L}$ such that a more homogeneous distribution of stroke work is obtained, we found more homogeneous shortening and an increased inhomogeneity in APD. In particular, we found reversal of the repolarization wave, which is a well-known phenomenon that occurs after several weeks of pacing [36, 120]. Our results indicate that electrical remodeling is a possible mechanism to reduce heterogeneity in mechanics after changing the activation sequence.

Since models of cardiac electromechanics are frequently applied to investigate medical interventions such as cardiac resynchronization therapy (CRT) [100, 204], incorporation of electrical remodeling into these models may lead to more accurate predictions of cardiac electromechanics with and

without pacing. These models can then be applied to investigate the effects of placing the pacemaker lead at different locations in the ventricular wall.

9.3   Model limitations and possible improvements

Our model of cardiac electrophysiology and mechanoelectric feedback is a large-scale model in which cardiac impulse propagation is influenced by mechanical deformation. In addition, the adaptation of ionic membrane currents is triggered by changes in mechanical load. The validity of our model largely depends on the validity of underlying models and parameters. Validity and limitations of the models for the ionic membrane currents, cross-bridge formation, and cardiomechanics are extensively discussed elsewhere [37, 158, 176]. Here, we discuss the limitations and possible improvements of our model with respect to intracellular ion concentrations, Ca^{2+}-force relation, calcium handling, ventricular membrane behavior, cardiac cycle simulation, and geometry.

Intracellular ion concentrations   A possible limitation of our model is that the effect of the stimulus current and intracellular currents on the intracellular concentrations of Na^+, K^+, and Ca^{2+} is not taken into account. Indeed, a drift in the ionic balance between $[Na^+]_i$ and $[K^+]_i$ was observed during longer simulation runs. Since long runs were needed to simulate electrical remodeling, we solved this problem in Chapter 7 by assuming constant $[Na^+]_i$ and $[K^+]_i$ during the entire simulation. A more elegant way to overcome this problem is to stimulate the cardiac tissue through the extracellular space and explicitly model the flow of ions between the cells.

Ca^{2+}-force relation   To describe contractile forces generated by the sarcomeres, we apply *model 4* of Rice *et al.* [158]. In contrast with *model 5*, *model 4* does not describe a feedback mechanism of force on the intracellular Ca^{2+} concentration. The choice between *model 4* and *model 5* is motivated by the fact that we found better agreement between the Ca^{2+}-force relation obtained by *model 4* and experimental observations [86, 98] (Appendix C). In experiments, Lab *et al.* [115] observed that a decreased mechanical load during shortening leads to an increased $[Ca^{2+}]_i$ and a longer APD. Since force-feedback is not part of *model 4*, these observations cannot be reproduced by the current version of our model. For future applications, it is recommended to incorporate force-feedback on intracellular calcium handling as described by Rice *et al.* [156, 157].

Calcium handling   Throughout this thesis, we used the Courtemanche-Ramirez-Nattel model of the human atrial action potential [37] to describe the ionic membrane currents and calcium handling for atrial myocytes. Calcium handling in this model is based on the ventricular model by Luo and Rudy [125, 126]. Since an accurate representation of the atrial Ca^{2+} transient is important when considering atrial excitation-contraction coupling, a possible improvement of our model would be to model atrial Ca^{2+} handling based on recent experiments with atrial myocytes. To incorporate force-feedback on $[Ca^{2+}]_i$, we recommend integration of the model describing the ionic membrane currents and Ca^{2+} handling with the model describing the Ca^{2+}-force relation.

Ventricular membrane behavior   In Chapter 7, we used the Courtemanche-Ramirez-Nattel model [37] to investigate electrical remodeling in the ventricles. Simulation results of ventricular electrical remodeling would be more accurate if a model of ionic membrane currents would be applied that is targeted at the ventricles. A recent model of human ventricular membrane behavior is the model by Ten Tusscher *et al.* [194, 197]. Application of this model would significantly improve accuracy when considering human ventricular electromechanics.

Cardiac cycle simulation   In Chapter 7, we simulated the cardiac cycle by an extended preload-afterload experiment [21, 81]. A more accurate simulation of the cardiac cycle may be achieved by considering hemodynamics part of the model. A possible improvement of our model would be to replace the preload-afterload work loop by a model of hemodynamics such as the CircAdapt model developed by Arts *et al.* [9].

Geometry   To model the geometry of the human atria, we used a triangular mesh obtained from MRI data [207, 208]. In Chapter 8, we introduced thickness variation in the geometry by introducing bundles. Accuracy of the model would be improved if thickness variations were directly obtained from measurements. Also when modeling ventricular electromechanics, the use of a human ventricular geometry should be considered.

9.4   Conclusion

Our model is well-suited to describe cardiac electrophysiology and mechano-electric feedback. For future applications, the model may be improved by

taking into account new insights from cellular physiology, a more accurate geometry, and hemodynamics.

A

Ionic membrane currents

In this thesis, we apply the Courtemanche-Ramirez-Nattel model of the human atrial action potential [37] to describe the ionic membrane currents and the handling of intracellular Ca^{2+} by the sarcoplasmic reticulum (SR). Here, we present the entire model.

A.1 Model formulation

In the model of Courtemanche *et al.* [37], ionic and pump currents are considered as well as intracellular Ca^{2+} handling by the sarcoplasmic reticulum (SR). The total ionic current is given by

$$I_{ion} = I_{Na} + I_{K1} + I_{to} + I_{Kur} + I_{Kr} + I_{Ks} + I_{Ca,L} + I_{p,Ca} + I_{NaK} + I_{NaCa} + I_{b,Na} + I_{b,Ca}, \quad (A.1)$$

where I_{Na} is fast inward Na^+ current, I_{K1} is inward rectifier K^+ current, I_{to} is transient outward K^+ current, I_{Kur} is ultrarapid delayed rectifier K^+ current, I_{Kr} is rapid delayed rectifier K^+ current, I_{Ks} is slow delayed rectifier K^+ current, $I_{Ca,L}$ is L-type Ca^{2+} current, $I_{p,Ca}$ is Ca^{2+} pump current, I_{NaK} is Na^+-K^+ pump current, I_{NaCa} is Na^+/Ca^{2+} exchanger current, and $I_{b,Na}$ and $I_{b,Ca}$ are background Na^+ and Ca^{2+} currents [37].

The model keeps track of the intracellular concentrations of Na^+, K^+, and Ca^{2+}, which are denoted by $[Na^+]_i$, $[K^+]_i$, and $[Ca^{2+}]_i$, respectively. The extracellular concentrations of Na^+, K^+, and Ca^{2+} are denoted by $[Na^+]_e$, $[K^+]_e$, and $[Ca^{2+}]_e$, and are kept constant (Table A.1). Intracellular Ca^{2+} handling by the SR is described by considering three compartments: myoplasm, SR release compartment (junctional SR or JSR), and SR uptake compartment (network SR or NSR). The model also describes Ca^{2+} buffering within the cytoplasm mediated by troponin and by calmodulin as well as Ca^{2+} buffering within the release compartment mediated by calsequestrin. It is assumed that a single cell has length and diameter 100 and 16 μm, respectively, and that the membrane capacitance C_m is equal to 100 pF.

Table A.1: Constants of Courtemanche-Ramirez-Nattel model

Parameter	Definition	Value
R	Gas constant	$8.3143 \, \text{J·K}^{-1}\text{·mol}^{-1}$
T	Temperature	$310 \, \text{K}$
F	Faraday's constant	$96.4867 \, \text{C/mmol}$
C_m	Membrane capacitance	$100 \, \text{pF}$
V_cell	Cell volume	$20100 \, \mu\text{m}^3$
V_up	SR uptake compartment volume	$1109.52 \, \mu\text{m}^3$
V_rel	SR release compartment volume	$96.48 \, \mu\text{m}^3$
$[\text{Na}^+]_\text{e}$	Extracellular Na^+ concentration	$140 \, \text{mM}$
$[\text{K}^+]_\text{e}$	Extracellular K^+ concentration	$5.4 \, \text{mM}$
$[\text{Ca}^{2+}]_\text{e}$	Extracellular Ca^{2+} concentration	$1.8 \, \text{mM}$

Ion concentrations

The influence of the ionic membrane currents on $[\text{Na}^+]_\text{i}$, $[\text{K}^+]_\text{i}$, and $[\text{Ca}^{2+}]_\text{i}$ is described by

$$\frac{\text{d}[\text{Na}^+]_\text{i}}{\text{d}t} = C_\text{m}\frac{-3I_\text{NaK} - 3I_\text{NaCa} - I_\text{b,Na} - I_\text{Na}}{F\,V_\text{i}}, \tag{A.2}$$

$$\frac{\text{d}[\text{K}^+]_\text{i}}{\text{d}t} = C_\text{m}\frac{2I_\text{NaK} - I_\text{K1} - I_\text{to} - I_\text{Kur} - I_\text{Kr} - I_\text{Ks}}{F\,V_\text{i}}, \tag{A.3}$$

$$\frac{\text{d}[\text{Ca}^{2+}]_\text{i}}{\text{d}t} = \frac{B1}{B2}, \tag{A.4}$$

$$B1 = C_\text{m}\frac{2I_\text{NaCa} - I_\text{p,Ca} - I_\text{Ca,L} - I_\text{b,Ca}}{2F\,V_\text{i}} + \frac{V_\text{up}(I_\text{up,leak} - I_\text{up}) + I_\text{rel}V_\text{rel}}{V_\text{i}}, \tag{A.5}$$

$$B2 = 1 + \frac{[\text{Trpn}]_\text{max}\,K_\text{m,Trpn}}{([\text{Ca}^{2+}]_\text{i} + K_\text{m,Trpn})^2} + \frac{[\text{Cmdn}]_\text{max}\,K_\text{m,Cmdn}}{([\text{Ca}^{2+}]_\text{i} + K_\text{m,Cmdn})^2}, \tag{A.6}$$

where, C_m is the membrane capacitance of a single atrial myocyte, F is Faraday's constant, V_i is the intracellular volume, and V_up and V_rel are the volumes of the SR uptake and release compartments, respectively (Table A.1); $I_\text{up,leak}$, I_up, and I_rel represent the SR currents, $[\text{Trpn}]$ is troponin concentration, $[\text{Cmdn}]$ is calmodulin concentration, and K_m is the half-saturation constant. Equation (A.6) represents the influence of Ca^{2+} buffering in the cytoplasm mediated by troponin ($[\text{Ca}^{2+}]_\text{Trpn}$) and calmodulin ($[\text{Ca}^{2+}]_\text{Cmdn}$) on $[\text{Ca}^{2+}]_\text{i}$.

Equilibrium potential

The equilibrium potential for ion species *ion* (Na^+, K^+ or Ca^{2+}) is given by the Nernst equation

$$E_{ion} = \frac{RT}{z_{ion}F} \ln\left(\frac{[ion]_e}{[ion]_i}\right), \tag{A.7}$$

where R is the universal gas constant, T is the absolute temperature, z_{ion} is the valence of *ion*, F is Faraday's constant, and $[ion]_e$ and $[ion]_i$ are the extracellular and intracellular concentrations of *ion*.

A.2 Ionic membrane currents

Fast inward Na^+ current

Fast inward Na^+ current (I_{Na}) is defined by

$$I_{Na} = G_{Na}\, m^3\, h\, j\, (V_{mem} - E_{Na}), \tag{A.8}$$

where G_{Na} is the maximum I_{Na} conductance (7.8 nS/pF), E_{Na} is the equilibrium potential for Na^+, m is the fast activation variable, and h and j are the fast and slow inactivation variables. Opening rate constant α_m and closing rate constant β_m are defined by

$$\alpha_m = \begin{cases} 3.2 & \text{if } V_{mem} = -47.13 \text{ mV} \\ 0.32\,\dfrac{V_{mem} + 47.13}{1 - \exp(-0.1(V_{mem} + 47.13))} & \text{otherwise} \end{cases} \tag{A.9}$$

$$\beta_m = 0.08 \exp\left(-\frac{V_{mem}}{11}\right) \tag{A.10}$$

For $V_{mem} < -40$ mV, α_h, β_h, α_j, and β_j are defined by

$$\alpha_h = 0.135 \exp\left(-\frac{V_{mem} + 80}{6.8}\right) \tag{A.11}$$

$$\beta_h = 3.56 \exp(0.079 V_{mem}) + 3.1 \times 10^5 \exp(0.35 V_{mem}) \tag{A.12}$$

$$\alpha_j = (-127140 \exp(0.2444 V_{mem}) - 3.474 \times 10^{-5} \exp(-0.04391 V_{mem})) \cdot \frac{V_{mem} + 37.78}{1 + \exp(0.311(V_{mem} + 79.23))} \tag{A.13}$$

$$\beta_j = 0.1212 \frac{\exp(-0.01052 V_{mem})}{1 + \exp(-0.1378(V_{mem} + 40.14))} \tag{A.14}$$

For $V_{\text{mem}} \geq -40$ mV, α_h, β_h, α_j, and β_j are defined by

$$\alpha_h = 0 \tag{A.15}$$

$$\beta_h = \left(0.13\left(1 + \exp\left(-\frac{V_{\text{mem}} + 10.66}{11.1}\right)\right)\right)^{-1} \tag{A.16}$$

$$\alpha_j = 0 \tag{A.17}$$

$$\beta_j = 0.3\frac{\exp(-2.535 \times 10^{-7} V_{\text{mem}})}{1 + \exp(-0.1(V_{\text{mem}} + 32))} \tag{A.18}$$

$\tau_\phi = (\alpha_\phi + \beta_\phi)^{-1}$ and $\phi_\infty = \alpha_\phi \tau_\phi$, for $\phi = m, h, j$.

Time-independent K$^+$ current

Time-independent K$^+$ current (I_{K1}) is defined by

$$I_{\text{K1}} = \frac{G_{\text{K1}}(V_{\text{mem}} - E_{\text{K}})}{1 + \exp(0.07(V_{\text{mem}} + 80))}, \tag{A.19}$$

where G_{K1} is the maximum I_{K1} conductance (0.09 nS/pF) and E_{K} is the equilibrium potential for K$^+$.

Transient outward K$^+$ current

Transient outward K$^+$ current (I_{to}) is defined by

$$I_{\text{to}} = G_{\text{to}} o_a^3 o_i (V_{\text{mem}} - E_{\text{K}}), \tag{A.20}$$

where G_{to} is the maximum I_{to} conductance (0.1652 nS/pF), o_a and o_i are the activation and inactivation gating variables, and E_{K} is the equilibrium potential for K$^+$. The dynamics of o_a and o_i are defined by

$$\alpha_{o_a} = 0.65\left(\exp\left(-\frac{V_{\text{mem}} + 10}{8.5}\right) + \exp\left(-\frac{V_{\text{mem}} - 30}{59.0}\right)\right)^{-1} \tag{A.21}$$

$$\beta_{o_a} = 0.65\left(2.5 + \exp\left(-\frac{V_{\text{mem}} + 82}{17.0}\right)\right)^{-1} \tag{A.22}$$

$$\tau_{o_a} = ((\alpha_{o_a} + \beta_{o_a})K_{Q10})^{-1} \tag{A.23}$$

$$o_{a(\infty)} = \left(1 + \exp\left(-\frac{V_{\text{mem}} + 20.47}{17.54}\right)\right)^{-1} \tag{A.24}$$

$$\alpha_{o_i} = \left(18.53 + \exp\left(\frac{V_{\text{mem}} + 113.7}{10.95}\right)\right)^{-1} \tag{A.25}$$

$$\beta_{o_i} = \left(35.56 + \exp\left(-\frac{V_{\text{mem}} + 1.26}{7.44}\right)\right)^{-1} \tag{A.26}$$

$$\tau_{o_i} = \left((\alpha_{o_i} + \beta_{o_i})K_{Q_{10}}\right)^{-1} \tag{A.27}$$

$$o_{i(\infty)} = \left(1 + \exp\left(\frac{V_{\text{mem}} + 43.1}{5.3}\right)\right)^{-1} \tag{A.28}$$

$K_{Q_{10}} = 3$ is a temperature scaling factor for I_{to} and I_{Kur} kinetics.

Ultrarapid delayed rectifier K$^+$ current

Ultrarapid delayed rectifier K$^+$ current (I_{Kur}) is defined by

$$I_{\text{Kur}} = G_{\text{Kur}} u_a^3 u_i (V_{\text{mem}} - E_K), \tag{A.29}$$

where G_{Kur} is the maximum I_{Kur} conductance, u_a and u_i are the activation and inactivation gating variables, and E_K is the equilibrium potential for K$^+$. G_{Kur} is voltage-dependent and is defined by

$$G_{\text{Kur}} = 0.005 + \frac{0.05}{1 + \exp\left(-\frac{V_{\text{mem}} - 15}{13}\right)}. \tag{A.30}$$

The dynamics of u_a and u_i are defined by

$$\alpha_{u_a} = 0.65\left(\exp\left(-\frac{V_{\text{mem}} + 10}{8.5}\right) + \exp\left(-\frac{V_{\text{mem}} - 30}{59.0}\right)\right)^{-1} \tag{A.31}$$

$$\beta_{u_a} = 0.65\left(2.5 + \exp\left(-\frac{V_{\text{mem}} + 82}{17.0}\right)\right)^{-1} \tag{A.32}$$

$$\tau_{u_a} = \left((\alpha_{u_a} + \beta_{u_a})K_{Q_{10}}\right)^{-1} \tag{A.33}$$

$$u_{a(\infty)} = \left(1 + \exp\left(-\frac{V_{\text{mem}} + 30.3}{9.6}\right)\right)^{-1} \tag{A.34}$$

$$\alpha_{u_i} = \left(21 + \exp\left(-\frac{V_{\text{mem}} - 185}{28}\right)\right)^{-1} \tag{A.35}$$

$$\beta_{u_i} = \exp\left(\frac{V_{\text{mem}} - 158}{16}\right) \tag{A.36}$$

$$\tau_{u_i} = \left((\alpha_{u_i} + \beta_{u_i})K_{Q_{10}}\right)^{-1} \tag{A.37}$$

$$u_{i(\infty)} = \left(1 + \exp\left(\frac{V_{\text{mem}} - 99.45}{27.48}\right)\right)^{-1} \tag{A.38}$$

As before, $K_{Q_{10}} = 3$ is a temperature scaling factor for I_{to} and I_{Kur} kinetics.

Rapid delayed outward rectifier K$^+$ current

Rapid delayed outward rectifier K$^+$ current (I_{Kr}) is defined by

$$I_{Kr} = \frac{G_{Kr}\,x_r\,(V_{mem} - E_K)}{1 + \exp\left(\frac{V_{mem} + 15}{22.4}\right)}, \tag{A.39}$$

where G_{Kr} is the maximum I_{Kr} conductance (0.0294 nS/pF), x_r is the activation gating variable, and E_K is the equilibrium potential for K$^+$. The dynamics of x_r are defined by

$$\alpha_{x_r} = 0.0003\,\frac{V_{mem} + 14.1}{1 - \exp\left(-\frac{V_{mem} + 14.1}{5}\right)} \tag{A.40}$$

$$\beta_{x_r} = 7.3898 \times 10^{-5}\,\frac{V_{mem} - 3.3328}{\exp\left(\frac{V_{mem} - 3.3328}{5.1237}\right) - 1} \tag{A.41}$$

$$\tau_{x_r} = \left(\alpha_{x_r} + \beta_{x_r}\right)^{-1} \tag{A.42}$$

$$x_{r(\infty)} = \left(1 + \exp\left(-\frac{V_{mem} + 14.1}{6.5}\right)\right)^{-1} \tag{A.43}$$

Slow delayed outward rectifier K$^+$ current

Slow delayed outward rectifier K$^+$ current (I_{Ks}) is defined by

$$I_{Ks} = G_{Ks}\,x_s^2\,(V_{mem} - E_K), \tag{A.44}$$

where G_{Ks} is the maximum I_{Ks} conductance (0.129 nS/pF), x_s is the activation gating variable, and E_K is the equilibrium potential for K$^+$. The dynamics of x_s are defined by

$$\alpha_{x_s} = 4 \times 10^{-5}\,\frac{V_{mem} - 19.9}{1 - \exp\left(-\frac{V_{mem} - 19.9}{17}\right)} \tag{A.45}$$

$$\beta_{x_s} = 3.5 \times 10^{-5}\,\frac{V_{mem} - 19.9}{\exp\left(\frac{V_{mem} - 19.9}{9}\right) - 1} \tag{A.46}$$

$$\tau_{x_s} = \tfrac{1}{2}\left(\alpha_{x_s} + \beta_{x_s}\right)^{-1} \tag{A.47}$$

$$x_{s(\infty)} = \left(1 + \exp\left(-\frac{V_{mem} - 19.9}{12.7}\right)\right)^{-\frac{1}{2}} \tag{A.48}$$

L-type Ca^{2+} current

L-type Ca^{2+} current ($I_{Ca,L}$) is defined by

$$I_{Ca,L} = G_{Ca,L}\, d\, f\, f_{Ca}\, (V_{mem} - 65), \tag{A.49}$$

where $G_{Ca,L}$ is the maximum $I_{Ca,L}$ conductance (0.1238 nS/pF), d is the activation gating variable, f is the voltage-dependent inactivation gating variable, and f_{Ca} is the Ca^{2+}-dependent inactivation gating variable. The dynamics of d, f, and f_{Ca} are defined by

$$\tau_d = \frac{1 - \exp\left(-\dfrac{V_{mem} + 10}{6.24}\right)}{0.035\,(V_{mem} + 10)\left(1 + \exp\left(-\dfrac{V_{mem} + 10}{6.24}\right)\right)} \tag{A.50}$$

$$d_\infty = \left(1 + \exp\left(-\frac{V_{mem} + 10}{8}\right)\right)^{-1} \tag{A.51}$$

$$\tau_f = \frac{9}{0.0197 \exp\left(-0.0337^2(V_{mem} + 10)^2\right) + 0.02} \tag{A.52}$$

$$f_\infty = \left(1 + \exp\left(\frac{V_{mem} + 28}{6.9}\right)\right)^{-1} \tag{A.53}$$

$$\tau_{f_{Ca}} = 2 \tag{A.54}$$

$$f_{Ca(\infty)} = \left(1 + \frac{[Ca^{2+}]_i}{0.00035}\right)^{-1} \tag{A.55}$$

Na^{+}-K^{+} pump current

Na^{+}-K^{+} pump current (I_{NaK}) is defined by

$$I_{NaK} = I_{NaK(max)}\, f_{NaK}\, \frac{1}{1 + (K_{m,Na(i)}/[Na^{+}]_i)^{1.5}}\, \frac{[K^{+}]_e}{[K^{+}]_e + K_{m,K(o)}}, \tag{A.56}$$

where $I_{NaK(max)}$ is maximum I_{NaK} (0.60 pA/pF), f_{NaK} is a voltage-dependent parameter, $K_{m,Na(i)}$ is the $[Na^{+}]_i$ half-saturation constant (10 mM), and $K_{m,K(o)}$ is the $[K^{+}]_e$ half-saturation constant (1.5 mM). f_{NaK} is defined by

$$f_{NaK} = \left(1 + 0.1245 \exp\left(-0.1\frac{FV_{mem}}{RT}\right) + 0.0365\,\sigma \exp\left(-\frac{FV_{mem}}{RT}\right)\right)^{-1}, \tag{A.57}$$

where F is Faraday's constant, R is the universal gas constant, T is the absolute temperature, and σ is the $[Na^{+}]_e$-dependence parameter defined by

$$\sigma = \frac{1}{7}\left(\exp\left(\frac{[Na^{+}]_e}{67.3}\right) - 1\right). \tag{A.58}$$

Na$^+$/Ca^{2+} exchanger current

Na$^+$/Ca^{2+} exchanger current (I_{NaCa}) is defined by

$$I_{NaCa} = I_{NaCa(max)} \cdot \tag{A.59}$$
$$\frac{\exp(\gamma F V_{mem}/(RT))[Na^+]_i^3[Ca^{2+}]_e - \exp((\gamma - 1)F V_{mem}/(RT))[Na^+]_e^3[Ca^{2+}]_i}{(K_{m,Na}^3 + [Na^+]_e^3)(K_{m,Ca} + [Ca^{2+}]_e)(1 + k_{sat}\exp((\gamma - 1)F V_{mem}/(RT)))},$$

where $I_{NaCa(max)}$ is maximum I_{NaCa} (1600 pA/pF), γ is the voltage-dependent parameter (0.35), $K_{m,Na}$ is the $[Na^+]_e$ half-saturation constant (87.5 mM), $K_{m,Ca}$ is the $[Ca^{2+}]_e$ half-saturation constant (1.38), and k_{sat} is a saturation factor (0.1).

Na$^+$ background current

Na$^+$ background current ($I_{b,Na}$) is defined by

$$I_{b,Na} = G_{b,Na}(V_{mem} - E_{Na}), \tag{A.60}$$

where $G_{b,Na}$ is the maximum $I_{b,Na}$ conductance (0.000674 nS/pF) and E_{Na} is the equilibrium potential for Na$^+$.

Ca^{2+} background current

Ca^{2+} background current ($I_{b,Ca}$) is defined by

$$I_{b,Ca} = G_{b,Ca}(V_{mem} - E_{Ca}), \tag{A.61}$$

where $G_{b,Ca}$ is the maximum $I_{b,Ca}$ conductance (0.00113 nS/pF) and E_{Ca} is the equilibrium potential for Ca^{2+}.

Ca^{2+} pump current

Ca^{2+} pump current ($I_{p,Ca}$) is defined by

$$I_{p,Ca} = I_{p,Ca(max)}\frac{[Ca^{2+}]_i}{0.0005 + [Ca^{2+}]_i}, \tag{A.62}$$

where $I_{p,Ca(max)}$ is maximum $I_{p,Ca}$ (0.275 pA/pF).

A.3 Calcium storage and release

Ca^{2+} release current from JSR

Ca^{2+} release current from JSR (I_{rel}) is defined by

$$I_{rel} = k_{rel}\, u^2\, v\, w\, ([Ca^{2+}]_{rel} - [Ca^{2+}]_i), \tag{A.63}$$

where k_{rel} is the maximum release rate (30 ms^{-1}), u is the activation gating variable, v is the Ca^{2+} flux-dependent inactivation gating variable, w is the voltage-dependent inactivation gating variable, and $[Ca^{2+}]_{rel}$ is the Ca^{2+} concentration in the release compartment. The dynamics of u, v, and w are defined by

$$\tau_u = 8.0 \tag{A.64}$$

$$u_\infty = \left(1 + \exp\left(-\frac{F_n - 3.4175 \times 10^{-13}}{13.67 \times 10^{-16}}\right)\right)^{-1} \tag{A.65}$$

$$\tau_v = 1.91 + 2.09\left(1 + \exp\left(-\frac{F_n - 3.4175 \times 10^{-13}}{13.67 \times 10^{-16}}\right)\right)^{-1} \tag{A.66}$$

$$v_\infty = 1 - \left(1 + \exp\left(-\frac{F_n - 6.835 \times 10^{-14}}{13.67 \times 10^{-16}}\right)\right)^{-1} \tag{A.67}$$

$$\tau_w = 6.0\,\frac{1 - \exp\left(-\frac{V_{mem} - 7.9}{5}\right)}{\left(1 + 0.3\exp\left(-\frac{V_{mem} - 7.9}{5}\right)\right)(V_{mem} - 7.9)} \tag{A.68}$$

$$w_\infty = 1 - \left(1 + \exp\left(-\frac{V_{mem} - 40}{17}\right)\right)^{-1} \tag{A.69}$$

$$F_n = 10^{-12}\, V_{rel}\, I_{rel} - \frac{5 \times 10^{-13}}{F}\left(\tfrac{1}{2} I_{Ca,L} - \tfrac{1}{5} I_{NaCa}\right), \tag{A.70}$$

where F_n is the sarcoplasmic Ca^{2+} flux signal, V_{rel} is the volume of the SR release compartment (96.48 μm^3), and F is Faraday's constant.

Transfer current from NSR to JSR

Transfer current from NSR to JSR (I_{tr}) is defined by

$$I_{tr} = \frac{[Ca^{2+}]_{up} - [Ca^{2+}]_{rel}}{\tau_{tr}}, \tag{A.71}$$

where τ_{tr} is the Ca^{2+} transfer time constant (180 ms).

Ca²⁺ uptake current by the NSR

Ca^{2+} uptake current by the NSR (I_{up}) is defined by

$$I_{up} = \frac{I_{up(max)}}{1 + (K_{up}/[Ca^{2+}]_i)}, \tag{A.72}$$

where $I_{up(max)}$ is maximum I_{up} (0.005 mM/ms) and K_{up} is the $[Ca^{2+}]_i$ half-saturation constant (0.00092 mM).

Ca²⁺ leak current by the NSR

Ca^{2+} leak current by the NSR ($I_{up,leak}$) is defined by

$$I_{up,leak} = \frac{[Ca^{2+}]_{up}}{[Ca^{2+}]_{up(max)}} I_{up(max)}, \tag{A.73}$$

where $[Ca^{2+}]_{up}$ is Ca^{2+} concentration in the uptake compartment, $[Ca^{2+}]_{up(max)}$ is maximum $[Ca^{2+}]_{up}$ (15 mM), and $I_{up(max)}$ is maximum I_{up} (0.005 mM/ms).

A.4   Ca²⁺ buffering

Ca^{2+} buffering within the cytoplasm is mediated by troponin and calmodulin and Ca^{2+} buffering in the release compartment is mediated by calsequestrin. It is assumed that the buffers are at equilibrium at all times. Ca^{2+} buffering by troponin is modeled by

$$[Ca^{2+}]_{Trpn} = [Trpn]_{max} \frac{[Ca^{2+}]_i}{[Ca^{2+}]_i + K_{m,Trpn}}, \tag{A.74}$$

where $[Ca^{2+}]_{Trpn}$ is Ca^{2+}-bound troponin concentration, $[Trpn]_{max}$ is total troponin concentration in the myoplasm (0.07 mM), and $K_{m,Trpn}$ is the $[Ca^{2+}]_i$ half-saturation constant for troponin (0.0005 mM).

Ca^{2+} buffering by calmodulin is modeled by

$$[Ca^{2+}]_{Cmdn} = [Cmdn]_{max} \frac{[Ca^{2+}]_i}{[Ca^{2+}]_i + K_{m,Cmdn}}, \tag{A.75}$$

where $[Ca^{2+}]_{Cmdn}$ is Ca^{2+}-bound calmodulin concentration, $[Cmdn]_{max}$ is total calmodulin concentration in the myoplasm (0.05 mM), and $K_{m,Cmdn}$ is the $[Ca^{2+}]_i$ half-saturation constant for calmodulin (0.00238 mM).

Ca^{2+} buffering by calsequestrin is modeled by

$$[\text{Ca}^{2+}]_{\text{Csqn}} = [\text{Csqn}]_{\text{max}} \frac{[\text{Ca}^{2+}]_{\text{rel}}}{[\text{Ca}^{2+}]_{\text{rel}} + K_{\text{m,Csqn}}}, \tag{A.76}$$

where $[\text{Ca}^{2+}]_{\text{Csqn}}$ is Ca^{2+}-bound calsequestrin concentration, $[\text{Csqn}]_{\text{max}}$ is total calsequestrin concentration in the SR release compartment (10 mM), and $K_{\text{m,Csqn}}$ is the $[\text{Ca}^{2+}]_{\text{rel}}$ half-saturation constant for calsequestrin (0.8 mM).

A.5 Model initialization

In our simulations, the state variables of the Courtemanche-Ramirez-Nattel model are initialized with the steady-state values listed in Table A.2 [37].

Table A.2: State variables of Courtemanche-Ramirez-Nattel model at rest

Variable	Definition	Initial value
V_{mem}	Membrane potential	-81.2 mV
$[\text{Na}^+]_i$	Intracellular Na$^+$ concentration	11.2 mM
$[\text{K}^+]_i$	Intracellular K$^+$ concentration	139 mM
$[\text{Ca}^{2+}]_i$	Intracellular Ca^{2+} concentration	1.02×10^{-4} mM
m	Activation gating variable for I_{Na}	2.91×10^{-3}
h	Fast inactivation gating variable for I_{Na}	9.65×10^{-1}
j	Slow inactivation gating variable for I_{Na}	9.78×10^{-1}
o_a	Activation gating variable for I_{to}	3.04×10^{-2}
o_i	Inactivation gating variable for I_{to}	9.99×10^{-1}
u_a	Activation gating variable for I_{Kur}	4.96×10^{-3}
u_i	Inactivation gating variable for I_{Kur}	9.99×10^{-1}
x_r	Activation gating variable for I_{Kr}	3.29×10^{-5}
x_s	Activation gating variable for I_{Ks}	1.87×10^{-2}
d	Activation gating variable for $I_{\text{Ca,L}}$	1.37×10^{-4}
f	Voltage-dependent inactivation gating var. for $I_{\text{Ca,L}}$	9.99×10^{-1}
f_{Ca}	Ca^{2+}-dependent inactivation gating var. for $I_{\text{Ca,L}}$	7.75×10^{-1}
$[\text{Ca}^{2+}]_{\text{up}}$	Ca^{2+} concentration in uptake compartment	1.49 mM
$[\text{Ca}^{2+}]_{\text{rel}}$	Ca^{2+} concentration in release compartment	1.49 mM
u	Activation gating variable for I_{rel}	0.00
v	Ca^{2+} flux-dependent inactivation gating var. for I_{rel}	1.00
w	Voltage-dependent inactivation gating var. for I_{rel}	9.99×10^{-1}
$[\text{Ca}^{2+}]_{\text{Trpn}}$	Ca^{2+}-bound troponin concentration	1.18×10^{-2} mM
$[\text{Ca}^{2+}]_{\text{Cmdn}}$	Ca^{2+}-bound calmodulin concentration	2.05×10^{-3} mM
$[\text{Ca}^{2+}]_{\text{Csqn}}$	Ca^{2+}-bound calsequestrin concentration	6.51 mM

B

Mathematical aspects of the computational scheme

B.1 Consistency of the equations

In Chapter 2, we introduced the Cellular Bidomain Model. In matrix notation, the model is represented by equations (3.8) and (3.9), which are repeated below:

$$C_{\text{mem}} \frac{d\mathbf{V}_{\text{mem}}}{dt} + S_{\text{mem}} \mathbf{I}_{\text{ion}} = -D_{\text{ext}} \mathbf{V}_{\text{ext}}, \tag{B.1}$$

$$(D_{\text{int}} + D_{\text{ext}})\mathbf{V}_{\text{ext}} = -D_{\text{int}} \mathbf{V}_{\text{mem}}. \tag{B.2}$$

The system of differential equations (B.1) describes the time evolution of the membrane potentials $\mathbf{V}_{\text{mem}}$. The extracellular potentials $\mathbf{V}_{\text{ext}}$ occur in the right hand side of (B.1) and must be found by solving the linear system of equations (B.2). Since the Kirchhoff matrices D_{int} and D_{ext} have vanishing row sums, they are both singular, which also holds for the matrix $D_{\text{int}} + D_{\text{ext}}$. Hence, it is not a priori clear that the system (B.2) has a unique solution for $\mathbf{V}_{\text{ext}}$. We study systems of the form (B.2) in more detail.

Consider the system of equations

$$D\mathbf{V} = \mathbf{I}, \tag{B.3}$$

where D is the matrix $D_{\text{int}} + D_{\text{ext}}$. Each row sum of matrix D vanishes, hence the product $D\mathbf{n} = \mathbf{0}$, where $\mathbf{n} = (1, \ldots, 1)^{\mathsf{T}}$. In Ref. [38], it is shown that, for a connected simulation graph, the null space of D is the one-dimensional space spanned by $\mathbf{n}$. For a symmetric matrix, the range is perpendicular to the null space. Hence, the range of D consists of all vectors $\mathbf{y}$ with $(\mathbf{y}, \mathbf{n}) = 0$ or, equivalently, all vectors $\mathbf{y}$ with $\sum_{j=1}^{N} y_j = 0$. The same considerations hold for the matrices D_{int} and D_{ext}. Hence, all three matrices D_{int}, D_{ext}, and $D_{\text{int}} + D_{\text{ext}}$ have the same range and the same null space.

For the system of equations (B.3), we conclude that there can only be a solution if the right hand side $\mathbf{I}$ is in the range of D, i.e., $\sum_{j=1}^{N} I_j = 0$. Moreover,

if that condition holds, the solution $\mathbf{V}$ is only determined up to a multiple of the vector $\mathbf{n}$. In electrical terms, these conditions mean that there can only be a solution if the total current that enters the system vanishes and that the potentials in a solution can be shifted by a constant.

In the original system (B.2), the right hand side is the vector $-D_{\text{int}} V_{\text{mem}}$. This vector is by construction an element of the range of D_{int}, and thus an element of the range of D. Hence, the system (B.2) always has a solution. This solution $\mathbf{V}_{\text{ext}}$ is only determined up to a vector $\mu\mathbf{n}$, where μ is a real number. Solution $\mathbf{V}_{\text{ext}}$ is used again in (B.1) to describe the dynamics of the membrane potential. However, since $D_{\text{int}}\,\mathbf{n} = \mathbf{0}$, the value of μ does not influence the dynamics of $\mathbf{V}_{\text{mem}}$.

In Chapter 3, we introduced the forward Euler scheme defined by equations (3.10) and (3.11) to solve the equations of the Cellular Bidomain Model. This scheme is repeated below:

$$\mathbf{V}_{\text{mem}}^{k+1} = \mathbf{V}_{\text{mem}}^{k} - \Delta t \, C_{\text{mem}}^{-1}(D_{\text{ext}}\mathbf{V}_{\text{ext}}^{k} + S_{\text{mem}}\,\mathbf{I}_{\text{ion}}^{k}), \tag{B.4}$$

$$(D_{\text{int}}+D_{\text{ext}})\mathbf{V}_{\text{ext}}^{k+1} = -D_{\text{int}}\mathbf{V}_{\text{mem}}^{k+1}. \tag{B.5}$$

Using the same considerations as above, it can be shown that the numerical scheme (B.4) and (B.5) is correctly defined. The solution $\mathbf{V}_{\text{ext}}^{k+1}$ of system (B.5) exists and is, as before, determined up to a vector $\mu\mathbf{n}$. In the next time step, $\mathbf{V}_{\text{ext}}^{k+1}$ occurs in (B.4) in the matrix-vector product $D_{\text{ext}}\mathbf{V}_{\text{ext}}^{k+1}$, which means that the value of μ is not relevant. In Chapter 3, the solution of (B.5) is fixed by equation (3.12), which states that for all k it holds

$$\sum_{j=1}^{N}\mathbf{V}_{\text{ext}}^{j,k} = 0. \tag{B.6}$$

B.2 Numerical solution of the linear system

We discuss matrix inversion and Jacobi's iteration method to solve the system of linear equations (B.5) at each time step.

B.2.1 Matrix inversion

Since the matrix $D = D_{\text{int}} + D_{\text{ext}}$ is singular, we cannot compute the inverse of D to solve the system. By replacing the last row of D by a row with only elements 1, and replacing the last element of the right hand side by 0, we impose the additional condition (B.6). The modified version of matrix D is not singular and the system can be solved by computing the inverse of D.

Since, in general, the system is large and the conductivities may change during the simulation, this method may require recomputing the inverse of a large matrix each time step. Since this is computationally expensive, we use an iterative method to solve the system (B.5).

B.2.2   Jacobi's iteration method

Let matrix P be the diagonal part of D, with reversed sign. Hence, the elements of P are defined by

$$P^{n,n} = \sum_{(n,a)\in\mathcal{E}} \left(\sigma_{int}^{(n,a)} + \sigma_{ext}^{(n,a)} \right). \tag{B.7}$$

Since the simulation graph is connected, each node n is connected to at least one other node, which implies that all elements $P^{n,n}$ are positive. Hence, the matrix P is not singular. Using the definition of matrix P, equation (B.5) can be reformulated as

$$P\,\mathbf{V}_{ext}^{k+1} = (D + P)\mathbf{V}_{ext}^{k+1} + D_{int}\,\mathbf{V}_{mem}^{k+1}. \tag{B.8}$$

Jacobi's iteration method to solve this system is formulated by

$$\mathbf{V}_{ext}^{k+1,i+1} = R\mathbf{V}_{ext}^{k+1,i} + \mathbf{b}, \tag{B.9}$$

where the R is the matrix $P^{-1}(D + P)$, $\mathbf{b}$ is the vector $P^{-1}D_{int}\mathbf{V}_{mem}^{k+1}$, and $\mathbf{V}_{ext}^{k+1,i}$ denotes the approximation of $\mathbf{V}_{ext}^{k+1}$ after i iterations. As a first approximation of $\mathbf{V}_{ext}^{k+1}$, the value of $\mathbf{V}_{ext}$ at time $k\Delta t$ is chosen, i.e.,

$$\mathbf{V}_{ext}^{k+1,0} = \mathbf{V}_{ext}^{k}. \tag{B.10}$$

The iteration process defined by (B.9) converges if the absolute values of all eigenvalues of the matrix R are smaller than 1.

Eigenvalues of R

The eigenvalues and eigenvectors of R are the same as those of the generalized eigenvalueproblem

$$(D + P)\,\mathbf{y} = \lambda P\,\mathbf{y}. \tag{B.11}$$

Both matrices $(D + P)$ and P are symmetric and, since all elements on the diagonal are positive, P is a positive matrix. Since P is positive, there are N

real eigenvalues $\lambda_1, \ldots, \lambda_N$, with corresponding linearly independent eigen-vectors $\mathbf{w}_1, \ldots, \mathbf{w}_N$. Moreover, these eigenvectors are "P orthogonal", i.e.

$$\mathbf{w}_j{}^\mathsf{T} P \mathbf{w}_k = \begin{cases} 0 & \text{if} \quad j \neq k \\ c_j & \text{if} \quad j = k \end{cases}, \tag{B.12}$$

where the c_j are positive normalization constants.

Using Gershgorin's theorem, it can be shown that all eigenvalues λ_i of R satisfy $|\lambda_i| \leq 1$. This leaves the possibility of eigenvalues 1 and -1, which will prevent convergence of Jacobi's iteration method.

First, we assume that R has no eigenvalue -1. Since $R\mathbf{y} = \mathbf{y}$ is equivalent with $D\mathbf{y} = 0$, matrix R indeed has an eigenvalue $\lambda_1 = 1$ with eigenvector $\mathbf{w}_1 = \mathbf{n}$. To analyze the convergence of (B.9), we expand the vector $\mathbf{V}_{\text{ext}}^{k+1,i}$ and the right hand side $\mathbf{b}$ in the eigenbasis of R:

$$\mathbf{V}_{\text{ext}}^{k+1,i} = \sum_{j=1}^{N} \alpha_j^i \mathbf{w}_j$$

$$\mathbf{b} = \sum_{j=1}^{N} \beta_j \mathbf{w}_j. \tag{B.13}$$

We obtain from (B.9)

$$\alpha_j^{i+1} = \lambda_j \alpha_j^i + \beta_j. \tag{B.14}$$

For all j with $|\lambda_j| < 1$, this process converges. However, since $\lambda_1 = 1$, this iteration process converges only for $j = 1$ if $\beta_1 = 0$. To compute β_1, we multiply (B.13) on the left with row vector $\mathbf{w}_1{}^\mathsf{T} P$. The "$P$ orthogonality" of the eigenvectors yields

$$\mathbf{w}_1{}^\mathsf{T} P \mathbf{b} = \beta_1 c_1. \tag{B.15}$$

To compute the left hand side, we use the definition of $\mathbf{b}$, the symmetry of matrix D_{int}, and the fact that $D_{\text{int}} \mathbf{n} = 0$.

$$\begin{aligned} \mathbf{w}_1{}^\mathsf{T} P \mathbf{b} &= \mathbf{w}_1{}^\mathsf{T} P P^{-1} D_{\text{int}} \mathbf{V}_{\text{mem}}^{k+1} \\ &= \mathbf{w}_1{}^\mathsf{T} D_{\text{int}} \mathbf{V}_{\text{mem}}^{k+1} \\ &= \mathbf{V}_{\text{mem}}^{k+1\,\mathsf{T}} D_{\text{int}} \mathbf{w}_1 \\ &= \mathbf{V}_{\text{mem}}^{k+1\,\mathsf{T}} D_{\text{int}} \mathbf{n} \\ &= 0. \end{aligned}$$

Consequently, $\beta_1 = 0$ and iteration process (B.14) converges for all j. This means that Jacobi's iteration method defined by (B.9) converges to a solution of the original system of equations (B.5). To obtain a unique solution, the V_{ext} must be shifted such that extra requirement (B.6) is satisfied.

So far, we have assumed that R does not have an eigenvalue -1. In general, R may have an eigenvalue -1. However, any eigenvalue -1 can be removed by replacing (B.9) with the iteration process

$$\mathbf{V}_{ext}^{k+1,i+1} = R'\mathbf{V}_{ext}^{k+1,i} + \mathbf{b}, \tag{B.16}$$

where R' is defined by

$$R' = (1 - \gamma)R + \gamma E. \tag{B.17}$$

Here E is the $N \times N$ identity matrix and γ is a real number with $0 < \gamma < 1$. It is easily verified that a fixed point of this iteration process also yields a solution of (B.5). Moreover, R' has the same eigenvectors as R, and R' has eigenvalues $\mu_j = (1 - \gamma)\lambda_j + \gamma$. Consequently, if $-1 \leq \lambda_j \leq 1$, then $-1 < \mu_j \leq 1$. Hence, a possible eigenvalue -1 in R is not present in R'. Similar to R, the modified matrix R' also has an eigenvalue 1. However, it is easily verified that the previous considerations on the convergence of Jacobi's iteration process also hold for the modified process defined by (B.16).

To avoid a possible eigenvalue -1 in R, we use R' as defined by equation (B.17) with $\gamma = 0.2$ in our computations.

Ca^{2+}-force relation

To model the Ca^{2+}-force relation, we apply *model 4* from Rice *et al.* [158]. The model is based on a functional unit of troponin, tropomyosin, and actin. Troponin can be in one of two states, indicating whether it is unbound or bound to Ca^{2+}. Tropomyosin can be in one of six states of which two represent the non-permissive states with 0 and 1 cross bridges, and the other four the permissive states with 0, 1, 2, and 3 cross bridges [158]. Transitions between the states are governed by rate functions that depend on the intracellular Ca^{2+} concentration ([Ca^{2+}]$_i$) and the sarcomere length (l_s). The force generated by the sarcomeres depends on the fraction of tropomyosin in the states that represent cross-bridge formation. In this thesis, we do not consider a direct feedback mechanism that influences the Ca^{2+} transient through a change in the affinity of troponin for Ca^{2+} binding as in *model 5* from Rice *et al.* [157, 158].

Here, we present *model 4* and discuss the differences between *model 4* and *model 5*. The notation is adopted from Rice *et al.* [157]. Model parameters and initial values of the state variables are given in Table C.1 and in Table C.2.

C.1 Troponin

Ca^{2+} binding to troponin is represented by the states T and T_{Ca}. T represents troponin with no Ca^{2+} bound to the regulatory (low affinity) site; T_{Ca} represents troponin with Ca^{2+} bound to the regulatory site. All functional units are in one of these two states, yielding $T + T_{Ca} = 1$. The concentration of Ca^{2+} bound to low-affinity troponin sites is denoted by [LTRPNCa] and the dynamics are given by

$$\frac{d[LTRPNCa]}{dt} = k_{ltrpn}^+ [Ca^{2+}]_i ([LTRPN]_{tot} - [LTRPNCa]) - k_{ltrpn}^- [LTRPNCa],$$

(C.1)

where [LTRPN]$_{tot}$ represents the total troponin low-affinity site concentration, and k_{ltrpn}^+ and k_{ltrpn}^- are the Ca^{2+} on and off-rate for troponin low-affinity sites.

Table C.1: Model parameters for Ca^{2+}-force relation

Parameter	Definition	Value
$[LTRPN]_{tot}$	Total troponin low-affinity site concentration	$70.0\,\mu M$
$[HTRPN]_{tot}$	Total troponin high-affinity site concentration	$140.0\,\mu M$
k^+_{ltrpn}	Ca^{2+} on-rate for troponin low-affinity sites	$20\,M^{-1}{\cdot}s^{-1}$
k^-_{ltrpn}	Ca^{2+} off-rate for troponin low-affinity sites	$40\,s^{-1}$
k^+_{htrpn}	Ca^{2+} on-rate for troponin high-affinity sites	$1.0\times10^8\,M^{-1}{\cdot}s^{-1}$
k^-_{htrpn}	Ca^{2+} off-rate for troponin high-affinity sites	$0.33\,s^{-1}$
k^{trop}_{pn}	Tropomyosin rate from permissive to non-perm.	$40\,s^{-1}$
ζ	Factor to convert F_{norm} to physiological force	$0.1\,N\,mm^{-2}$
f_{XB}	Basic transition rate from weak to strong binding	$10\,s^{-1}$
g^*_{XB}	Min. transition rate from strong to weak binding	$30\,s^{-1}$

The concentration of Ca^{2+} bound to high-affinity troponin sites is denoted by [HTRPNCa] and the dynamics are given by

$$\frac{d[HTRPNCa]}{dt} = k^+_{htrpn}\,[Ca^{2+}]_i\,([HTRPN]_{tot} - [HTRPNCa]) - k^-_{htrpn}\,[HTRPNCa],$$

$$(C.2)$$

where $[HTRPN]_{tot}$ represents the total troponin high-affinity site concentration, and k^+_{htrpn} and k^-_{htrpn} are the Ca^{2+} on and off-rate for troponin high-affinity sites.

C.2 Tropomyosin/cross bridges

To incorporate the cooperative mechanism that the rates of cross-bridge formation increase progressively as more cross bridges are formed, the formation rates $f_{0,1}$, $f_{1,2}$, and $f_{2,3}$ are defined by

$$
\begin{aligned}
f_{0,1} &= 3\,f_{XB}, & (C.3)\\
f_{1,2} &= 10\,f_{XB}, & (C.4)\\
f_{2,3} &= 7\,f_{XB}, & (C.5)
\end{aligned}
$$

Table C.2: Initial conditions for Ca^{2+}-force relation

Variable	Definition	Initial value
[LTRPNCa]	Conc. of Ca^{2+} bound to low affinity troponin sites	$6.46\ \mu M$
[HTRPNCa]	Conc. of Ca^{2+} bound to high affinity troponin sites	$135.5\ \mu M$
N0	Non-perm. tropomyosin with 0 cross bridges	0.99999027
N1	Non-perm. tropomyosin with 1 cross bridge	3.88506×10^{-06}
P0	Permissive tropomyosin with 0 cross bridges	1.46758×10^{-06}
P1	Permissive tropomyosin with 1 cross bridge	1.47026×10^{-06}
P2	Permissive tropomyosin with 2 cross bridges	1.83527×10^{-06}
P3	Permissive tropomyosin with 3 cross bridges	1.06786×10^{-06}

where f_{XB} denotes the basic transition rate from weak to strong cross bridge. The reverse rates $g_{1,0}$, $g_{2,1}$, and $g_{3,2}$ are not cooperative and are given by

$$g_{1,0} = 1\, g_{XB}(l_s), \tag{C.6}$$
$$g_{2,1} = 2\, g_{XB}(l_s), \tag{C.7}$$
$$g_{3,2} = 3\, g_{XB}(l_s), \tag{C.8}$$

where $g_{XB}(l_s)$ represents the variable off rate which is dependent on the sarcomere length l_s. $g_{XB}(l_s)$ is defined by

$$g_{XB}(l_s) = g_{XB}^* \left(1 + (1 - l_{s,norm})^{1.6}\right), \tag{C.9}$$

where g_{XB}^* is the minimum transition rate from strong to weak cross bridge and $l_{s,norm}$ is the normalized sarcomere length defined by

$$l_{s,norm} = (l_s - 1.7\ \mu m)/0.6\ \mu m. \tag{C.10}$$

Here, it is assumed that for sarcomere length l_s it holds $1.7\ \mu m \leq l_s \leq 2.3\ \mu m$.

The tropomyosin rate from non-permissive to permissive is denoted by k_{np}^{trop} and is influenced by the concentration of Ca^{2+} bound to low-affinity troponin sites [LTRPNCa]. k_{np}^{trop} is defined by

$$k_{np}^{trop} = k_{pn}^{trop} \left(\frac{[LTRPNCa]/[LTRPN]_{tot}}{K_{\frac{1}{2}}^{trop}} \right)^{N^{trop}}, \tag{C.11}$$

where $k_{\text{pn}}^{\text{trop}}$ is a model parameter representing the tropomyosin rate from permissive to non-permissive. N^{trop} is defined by

$$N^{\text{trop}} = 5 + 3\,l_{s,\text{norm}}, \tag{C.12}$$

and $K_{\frac{1}{2}}^{\text{trop}}$ by

$$K_{\frac{1}{2}}^{\text{trop}} = \left(1 + \frac{K_{\text{Ca}}^{\text{trop}}}{1.5 - l_{s,\text{norm}}}\right)^{-1}. \tag{C.13}$$

Here, $K_{\text{Ca}}^{\text{trop}}$ is defined by

$$K_{\text{Ca}}^{\text{trop}} = k_{\text{ltrpn}}^{-}/k_{\text{ltrpn}}^{+}. \tag{C.14}$$

The dynamics of the two non-permissive states *N0* and *N1* and the permissive states *P0, P1, P2,* and *P3* are defined by differential equations as follows:

$$\frac{dN0}{dt} = -k_{\text{np}}^{\text{trop}}\,N0 + k_{\text{pn}}^{\text{trop}}\,P0 + g_{1,0}\,N1, \tag{C.15}$$

$$\frac{dN1}{dt} = -(k_{\text{np}}^{\text{trop}} + g_{1,0})\,N1 + k_{\text{pn}}^{\text{trop}}\,P1, \tag{C.16}$$

$$\frac{dP0}{dt} = -(k_{\text{pn}}^{\text{trop}} + f_{0,1})\,P0 + k_{\text{np}}^{\text{trop}}\,N0 + g_{1,0}\,P1, \tag{C.17}$$

$$\frac{dP1}{dt} = -(k_{\text{pn}}^{\text{trop}} + f_{1,2} + g_{1,0})\,P1 + k_{\text{np}}^{\text{trop}}\,N1 + f_{0,1}\,P0 + g_{2,1}\,P2, \tag{C.18}$$

$$\frac{dP2}{dt} = -(f_{2,3} + g_{2,1})\,P2 + f_{1,2}\,P1 + g_{3,2}\,P3, \tag{C.19}$$

$$\frac{dP3}{dt} = -g_{3,2}\,P3 + f_{2,3}\,P2. \tag{C.20}$$

C.3 Force computation

The physiological force F_{phys} generated by the sarcomeres is defined by

$$F_{\text{phys}} = \zeta\,F_{\text{norm}}, \tag{C.21}$$

where ζ is the conversion factor and F_{norm} the normalized force defined by

$$F_{\text{norm}} = \phi(l_s)\,\frac{P1 + N1 + 2\,P2 + 3\,P3}{F_{\text{max}}}, \tag{C.22}$$

where F_{max} is the maximum force defined below. $\phi(l_s)$ is included to describe the physical structure of thick and thin filaments within a sarcomere (see

Ref. [116]). When $\phi(l_s) = 1$, all myosin heads are able to interact with actin in the single overlap zone, whereas for $\phi(l_s) < 1$, some of the filaments are in the double or non-overlap zones. $\phi(l_s)$ is defined by

$$\phi(l_s) = \begin{cases} (l_s - 0.6\,\mu\mathrm{m})/1.4\,\mu\mathrm{m} & \text{if } 1.7\,\mu\mathrm{m} \le l_s \le 2.0\,\mu\mathrm{m} \\ 1 & \text{if } 2.0\,\mu\mathrm{m} < l_s \le 2.2\,\mu\mathrm{m} \\ (3.6\,\mu\mathrm{m} - l_s)/1.4\,\mu\mathrm{m} & \text{if } 2.2\,\mu\mathrm{m} < l_s \le 2.3\,\mu\mathrm{m} \end{cases} \tag{C.23}$$

The maximum force $F_{\max}$ is defined by

$$F_{\max} = P1_{\max} + 2\,P2_{\max} + 3\,P3_{\max}, \tag{C.24}$$

where $P1_{\max}$, $P2_{\max}$, and $P3_{\max}$ are found using the King-Altman rule [102] as follows

$$P1_{\max} = \frac{f_{0,1}\,2g_{\mathrm{XB}}^*\,3g_{\mathrm{XB}}^*}{\Sigma\mathrm{paths}}, \tag{C.25}$$

$$P2_{\max} = \frac{f_{0,1}\,f_{1,2}\,3g_{\mathrm{XB}}^*}{\Sigma\mathrm{paths}}, \tag{C.26}$$

$$P3_{\max} = \frac{f_{0,1}\,f_{1,2}\,f_{2,3}}{\Sigma\mathrm{paths}}, \tag{C.27}$$

where

$$\Sigma\mathrm{paths} = g_{\mathrm{XB}}^*\,2g_{\mathrm{XB}}^*\,3g_{\mathrm{XB}}^* + f_{0,1}\,2g_{\mathrm{XB}}^*\,3g_{\mathrm{XB}}^* + f_{0,1}\,f_{1,2}\,3g_{\mathrm{XB}}^* + f_{0,1}\,f_{1,2}\,f_{2,3}. \tag{C.28}$$

C.4   Differences between model 4 and model 5

In *model 5*, the off rate of Ca^{2+} from troponin is a function of the total force developed. In Ref. [158], two versions of *model 5* are presented, one with a modest degree of feedback ($\frac{1}{2} \cdot F_{\mathrm{norm}}$) and one with a stronger feedback ($\frac{3}{4} \cdot F_{\mathrm{norm}}$). Here, we present the version of *model 5* with an intermediate feedback of $\frac{2}{3} \cdot F_{\mathrm{norm}}$ introduced in Ref. [157].

The Ca^{2+} off-rate for troponin low-affinity site k_{ltrpn}^- in equation (C.1) is replaced with

$$k_{\mathrm{ltrpn}}^- \left(\tfrac{1}{3} + \tfrac{2}{3}(1 - F_{\mathrm{norm}}) \right), \tag{C.29}$$

where k_{ltrpn}^- is unchanged and F_{norm} is calculated as in *model 4*. Since cooperativity increases with this modification, the tropomyosin shifting has been made less sensitive to Ca^{2+}. Decreased sensitivity is incorporated by changing equation (C.12) to

$$N^{\mathrm{trop}} = 3.5 + 2.5 \cdot l_{s,\mathrm{norm}}, \tag{C.30}$$
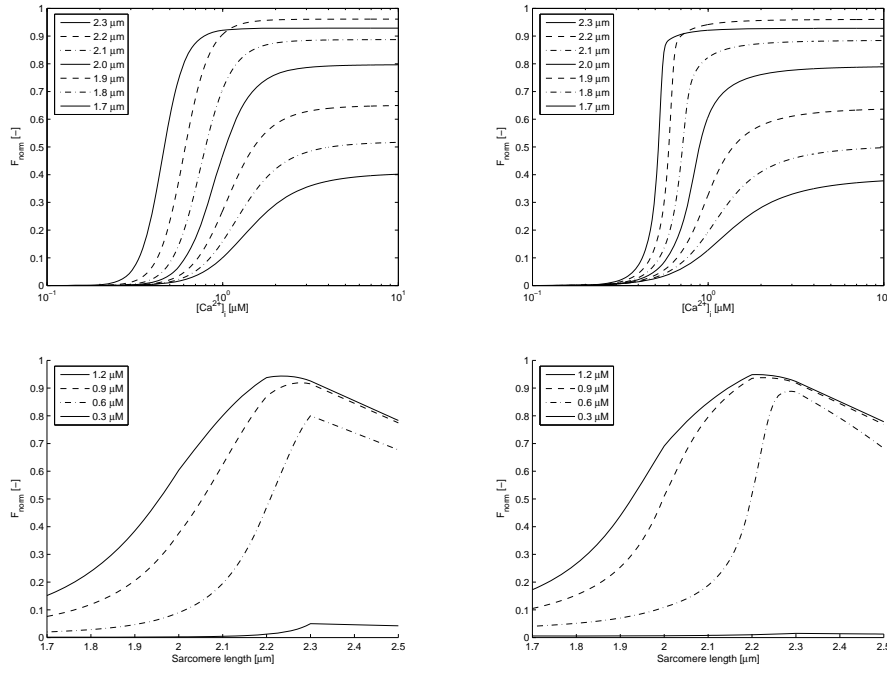
Figure C.1: Comparison between *model 4* (left) and *model 5* (right) from Rice *et al.* [157, 158]. Top: F_{norm} versus $[Ca^{2+}]_i$ for sarcomere length between 1.7 μm and 2.3 μm. Bottom: F_{norm} versus sarcomere length for $[Ca^{2+}]_i = 0.3, 0.6, 0.9,$ and $1.2\,\mu$M.

and equation (C.13) to

$$
K_{\frac{1}{2}}^{trop} = \left(1 + \frac{K_{Ca}^{trop}}{1.7 - 0.9 \cdot l_{s,norm}} \right)^{-1}. \tag{C.31}
$$

Here, K_{Ca}^{trop} is defined as in equation (C.14) and $l_{s,norm}$ is defined as in equation (C.10).

In Figure C.1, F_{norm} is presented for various intracellular Ca^{2+} concentrations and sarcomere lengths. These plots were obtained by computing the steady-state values of F_{norm}. The force-Ca^{2+} relations obtained by *model 4* correspond better to the experimental results of Kentish *et al.* [98], especially for sarcomere lengths above 1.9 μm. The steady-state Ca^{2+}-force relation for *model 4* is also presented in Figure 6.2.

In Figure C.2, traces of F_{norm} for *model 4* and *model 5* are presented for various sarcomere lengths after application of a stimulus current. Compared with *model 4*, the peak force is lower and the latency to peak force increases for larger sarcomere lengths for *model 5*. Compared with the experimental data

measured by Janssen and Hunter [86], the latency to peak force increases too much with sarcomere length for *model 5*.

Our findings confirm the finding by Rice *et al.* [158] that the hypothesis that cross-bridge binding increases the affinity of troponin for Ca^{2+} is not crucial to reproduce the experimental results. Since the traces obtained by *model 4* better resemble the experimental results from Janssen and Hunter [86], we have chosen *model 4* to compute F_{norm} in our model.
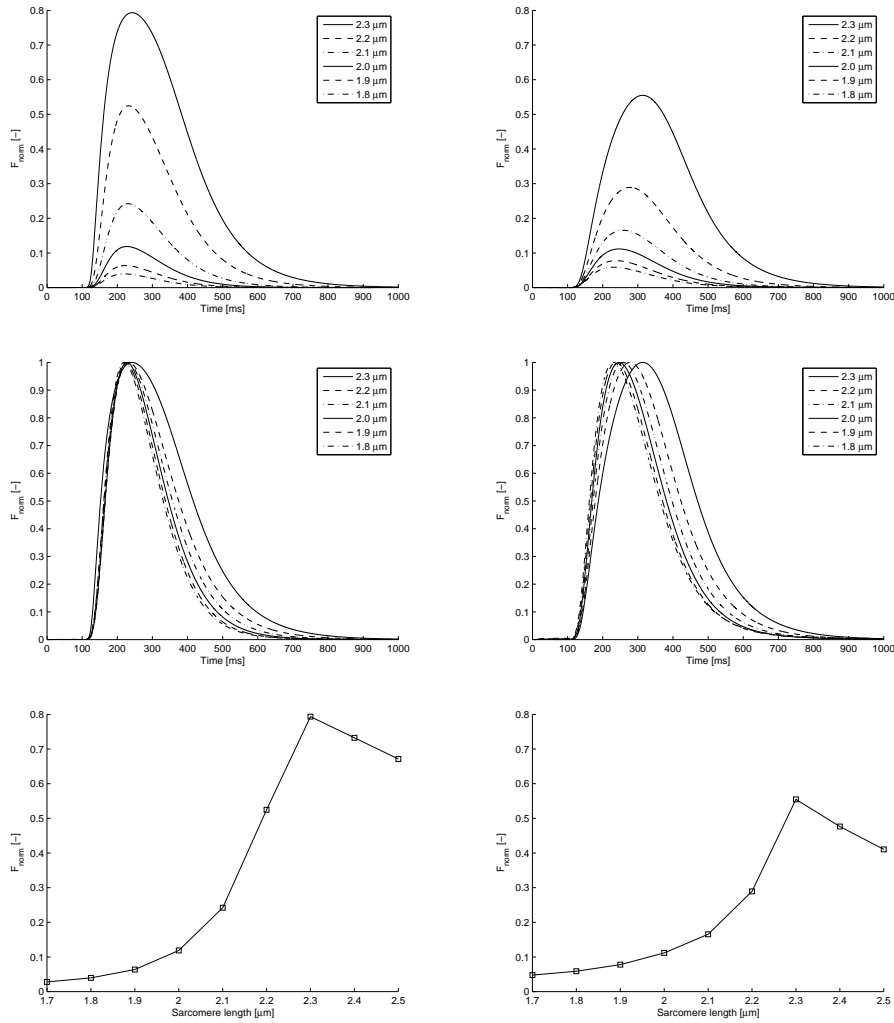
Figure C.2: Comparison between *model 4* (left) and *model 5* (right) from Rice *et al.* [157, 158]. Top: trace of F_{norm}. Center: trace of F_{norm} individually normalized. Bottom: Peak F_{norm} versus sarcomere length. A stimulus current was applied at 100 ms.

D

Mechanics computation

In Chapters 6 and 7, we introduced the model equations to describe the mechanics of a single segment and the mechanics of a cardiac fiber. Here, we repeat the model and describe the numerical integration scheme to solve the model equations.

D.1 Single-segment mechanics

The mechanical behavior of a single segment is modeled by the classical three-element rheological scheme. Active force is generated by the contractile element (CE) together with the series elastic element (SE) and passive force is generated in the parallel elastic element (PE). The PE describes the force-length relation when the segment is not stimulated (Figure 6.3).

Contractile force (F_{CE}) generated by the CE depends on intracellular Ca^{2+} concentration ($[Ca^{2+}]_i$), sarcomere length (l_{CE}), and the velocity of sarcomere shortening $v = -\frac{dl_{CE}}{dt}$. F_{CE} is defined by

$$F_{CE} = f_{CE}\, f_v(v)\, F_{norm}([Ca^{2+}]_i, l_{CE}), \tag{D.1}$$

where f_{CE} is a scaling factor, $f_v(v)$ is Hill's force-velocity relation, and F_{norm} ($[Ca^{2+}]_i, l_{CE}$) is the normalized force generated by the sarcomeres. Function $f_v(v)$ is defined by

$$f_v(v) = \frac{1 - \frac{v}{v_{max}}}{1 + c_v \frac{v}{v_{max}}}, \tag{D.2}$$

where v_{max} is the maximum velocity of sarcomere shortening and c_v is a constant describing the shape of the hyperbolic relationship.

Forces generated in the SE and in the PE are exponentially related to their respective lengths l_{SE} and l_{PE}, and are defined by

$$F_{SE} = f_{SE}\, (\exp(k_{SE}\, (l_{SE} - l_{SE0})) - 1) \tag{D.3}$$

and

$$F_{PE} = f_{PE} \left(\exp(k_{PE} (l_{PE} - l_{PE0})) - 1 \right), \qquad\qquad\qquad\qquad (D.4)$$

where l_{SE0} and l_{PE0} denote the reference element lengths and f_{SE}, k_{SE}, f_{PE}, and k_{PE} are material constants describing the elasticity of the elements.

Total force generated by the segment ($F_{segment}$) is the sum of passive force (F_{PE}) and active force (F_{SE}). In summary, it holds for the three-element model (Figure 6.3):

$$
\begin{aligned}
F_{CE} &= F_{SE}, & (D.5)\\
F_{segment} &= F_{SE} + F_{PE}, & (D.6)\\
l_{PE} &= l_{CE} + l_{SE}. & (D.7)
\end{aligned}
$$

For segment n, the reference length l_{n0} is defined by

$$l_{n0} = \xi_n \, l_{PE0}^n \qquad\qquad\qquad\qquad\qquad\qquad\qquad (D.8)$$

and the actual length l_n by

$$l_n = \xi_n \, l_{PE}^n, \qquad\qquad\qquad\qquad\qquad\qquad\qquad (D.9)$$

where ξ_n is a scaling factor. The stretch ratio (λ_n) for segment n is then defined by

$$\lambda_n = \frac{l_n}{l_{n0}} = \frac{l_{PE}^n}{l_{PE0}^n}. \qquad\qquad\qquad\qquad\qquad\qquad (D.10)$$

The numerical scheme to solve the equations for the three-element model is based on the scheme described by Solovyova *et al.* [176]. The forces and lengths of CE, SE, and PE are computed by introducing $l_1 = l_{CE} - l_{CE0}$ and $l_2 = l_{PE} - l_{PE0}$. Furthermore, it is assumed that $l_{PE0} = l_{CE0}$, from which it follows that $l_{SE0} = l_{PE0} - l_{CE0} = 0\,\mu\text{m}$. Equations (D.3) and (D.4) can be rewritten as

$$F_{SE} = f_{SE} \left(\exp(k_{SE} (l_2 - l_1)) - 1 \right) \qquad\qquad\qquad (D.11)$$

and

$$F_{PE} = f_{PE} \left(\exp(k_{PE} \, l_2) - 1 \right). \qquad\qquad\qquad\qquad (D.12)$$

The mechanical state of each segment is now defined by l_1, l_2, $\frac{dl_1}{dt}$, $\frac{dl_2}{dt}$, and $F_{norm}([Ca^{2+}]_i, l_{CE})$. Each simulation time step, F_{norm} is computed using $[Ca^{2+}]_i$ obtained from the model of Courtemanche *et al.* [37] and l_{CE} of the former time step. Next, l_1 and l_2 are updated using a forward Euler step and $\frac{dl_1}{dt}$ and

$\frac{dl_2}{dt}$ of the former time step. New values of $\frac{dl_1}{dt}$ and $\frac{dl_2}{dt}$ are then computed as follows. Using equations (D.1) and (D.2), we obtain

$$\frac{1 - \frac{v}{v_{max}}}{1 + c_v \frac{v}{v_{max}}} = \frac{F_{CE}}{f_{CE} \, F_{norm}([Ca^{2+}]_i, l_{CE})}, \qquad (D.13)$$

from which sarcomere shortening velocity v can be obtained by

$$v = \frac{f_{CE} \, F_{norm}([Ca^{2+}]_i, l_{CE}) - F_{CE}}{F_{CE} \, c_v + f_{CE} \, F_{norm}([Ca^{2+}]_i, l_{CE})} v_{max}. \qquad (D.14)$$

F_{CE} can be obtained from equations (D.5) and (D.11) by

$$F_{CE} = F_{SE} = f_{SE} \, (\exp(k_{SE} \, (l_2 - l_1)) - 1). \qquad (D.15)$$

Since $l_1 = l_{CE} - l_{CE0}$, we obtain for sarcomere shortening velocity v

$$v = -\frac{dl_{CE}}{dt} = -\frac{dl_1}{dt}, \qquad (D.16)$$

from which $\frac{dl_1}{dt}$ follows immediately.

For isometric single-segment simulations, $\frac{dl_2}{dt} = 0$ and the generated force can be directly computed from equations (D.11) and (D.12). For isotonic simulations, $\frac{dl_2}{dt}$ can be obtained from $\frac{dF_{segment}}{dt}$ as follows. Using $F_{segment} = F_{SE} + F_{PE}$ and equations (D.11) and (D.12), we obtain

$$F_{segment} = f_{SE} \, (\exp(k_{SE} \, (l_2 - l_1)) - 1) + f_{PE} \, (\exp(k_{PE} \, l_2) - 1) \qquad (D.17)$$

and, by taking the derivative,

$$\frac{dF_{segment}}{dt} = f_{SE} \, k_{SE} \, \exp(k_{SE} \, (l_2 - l_1)) \left(\frac{dl_2}{dt} - \frac{dl_1}{dt} \right) + f_{PE} \, k_{PE} \, \exp(k_{PE} \, l_2) \frac{dl_2}{dt}, \qquad (D.18)$$

from which $\frac{dl_2}{dt}$ can be computed by

$$\frac{dl_2}{dt} = \frac{\frac{dF_{segment}}{dt} + f_{SE} \, k_{SE} \, \exp(k_{SE} \, (l_2 - l_1)) \frac{dl_1}{dt}}{f_{SE} \, k_{SE} \, \exp(k_{SE} \, (l_2 - l_1)) + f_{PE} \, k_{PE} \, \exp(k_{PE} \, l_2)}. \qquad (D.19)$$

Note that during isotonic contraction $\frac{dF_{segment}}{dt} = 0$.

D.2   Cardiac fiber mechanics

In Section 6.2.6, a cardiac fiber is modeled as a string of segments that are coupled in series. From mechanical equilibrium, it follows that the force F^n_{segment} generated by a single segment n, $n \in \mathcal{N}$, is equal to the force generated by the fiber (F_{fiber}), i.e.,

$$F^n_{\text{segment}} = F_{\text{fiber}}. \tag{D.20}$$

If we take into account that l_{n0} may be different for each segment n, $n \in \mathcal{N}$, the stretch ratio of the fiber (λ_{fiber}) is defined by

$$\lambda_{\text{fiber}} = \frac{L}{L_0} = \frac{\sum_{n \in \mathcal{N}} l_n}{\sum_{n \in \mathcal{N}} l_{n0}}, \tag{D.21}$$

where L denotes the actual fiber length and L_0 is the reference length.

To obtain a solution for a multiple-segment simulation, we define α and β by

$$\alpha = \frac{1}{f_{\text{SE}}\, k_{\text{SE}}\, \exp(k_{\text{SE}}\,(l_2 - l_1)) + f_{\text{PE}}\, k_{\text{PE}}\, \exp(k_{\text{PE}}\, l_2)} \tag{D.22}$$

and

$$\beta = \frac{f_{\text{SE}}\, k_{\text{SE}}\, \exp(k_{\text{SE}}\,(l_2 - l_1))\, \frac{\mathrm{d}l_1}{\mathrm{d}t}}{f_{\text{SE}}\, k_{\text{SE}}\, \exp(k_{\text{SE}}\,(l_2 - l_1)) + f_{\text{PE}}\, k_{\text{PE}}\, \exp(k_{\text{PE}}\, l_2)}. \tag{D.23}$$

Equation (D.19) can be formulated for each segment n by

$$\frac{\mathrm{d}l^n_2}{\mathrm{d}t} = \alpha_n \frac{\mathrm{d}F^n_{\text{segment}}}{\mathrm{d}t} + \beta_n, \tag{D.24}$$

where α_n and β_n denote α and β for segment n. Using $l^n_2 = l^n_{\text{PE}} - l^n_{\text{PE0}}$ and $l_n = \xi_n\, l^n_{\text{PE}}$, we obtain for fiber length L

$$\frac{\mathrm{d}L}{\mathrm{d}t} = \sum_{n \in \mathcal{N}} \frac{\mathrm{d}l_n}{\mathrm{d}t} = \sum_{n \in \mathcal{N}} \xi_n \frac{\mathrm{d}l^n_2}{\mathrm{d}t} = \sum_{n \in \mathcal{N}} \xi_n \alpha_n \frac{\mathrm{d}F^n_{\text{segment}}}{\mathrm{d}t} + \sum_{n \in \mathcal{N}} \xi_n \beta_n. \tag{D.25}$$

Using $F^n_{\text{segment}} = F_{\text{fiber}}$ for each segment n, $n \in \mathcal{N}$, and introducing a and b, we obtain

$$\frac{\mathrm{d}L}{\mathrm{d}t} = \sum_{n \in \mathcal{N}} \xi_n \alpha_n \frac{\mathrm{d}F_{\text{fiber}}}{\mathrm{d}t} + \sum_{n \in \mathcal{N}} \xi_n \beta_n = a \frac{\mathrm{d}F_{\text{fiber}}}{\mathrm{d}t} + b, \tag{D.26}$$

where a and b are defined by

$$a = \sum_{n \in \mathcal{N}} \xi_n \alpha_n \tag{D.27}$$

and

$$b = \sum_{n \in \mathcal{N}} \xi_n \beta_n. \tag{D.28}$$

Finally, using the definition of fiber stretch $\lambda_{\text{fiber}} = \frac{L}{L_0}$ and equation (D.26), we obtain

$$\frac{\mathrm{d}\lambda_{\text{fiber}}}{\mathrm{d}t} = \frac{a \frac{\mathrm{d}F_{\text{fiber}}}{\mathrm{d}t} + b}{L_0}, \tag{D.29}$$

from which follows

$$\frac{\mathrm{d}F_{\text{fiber}}}{\mathrm{d}t} = \frac{\frac{\mathrm{d}\lambda_{\text{fiber}}}{\mathrm{d}t} L_0 - b}{a}. \tag{D.30}$$

For isotonic simulations, F_{fiber} is constant and $\frac{\mathrm{d}F_{\text{fiber}}}{\mathrm{d}t} = 0$. Using $F_{\text{segment}}^n = F_{\text{fiber}}$, $\frac{\mathrm{d}l_2^n}{\mathrm{d}t}$ can be obtained from equation (D.19) for each segment n, $n \in \mathcal{N}$. For isometric simulations, λ_{fiber} is constant and $\frac{\mathrm{d}\lambda_{\text{fiber}}}{\mathrm{d}t} = 0$. In the isometric case, F_{fiber} and its derivative $\frac{\mathrm{d}F_{\text{fiber}}}{\mathrm{d}t}$ can be obtained from equation (D.30).

In summary, the mechanical state of segment n is described by l_1^n, l_2^n, $\frac{\mathrm{d}l_1^n}{\mathrm{d}t}$, $\frac{\mathrm{d}l_2^n}{\mathrm{d}t}$, and F_{norm}^n. F_{norm}^n is dependent on $[\text{Ca}^{2+}]_i$ and $l_{\text{CE}} = l_{\text{CE0}} + l_1^n$. For each time step, l_1^n and l_2^n are computed using a forward Euler step and $\frac{\mathrm{d}l_1^n}{\mathrm{d}t}$ and $\frac{\mathrm{d}l_2^n}{\mathrm{d}t}$, respectively. However, initial values for l_1^n and l_2^n remain to be defined. Initially, it is assumed that the electrophysiological state of all segments is resting, i.e., the membrane potential is −81 mV and $[\text{Ca}^{2+}]_i$ is 0.102 μM [37]. For such low $[\text{Ca}^{2+}]_i$, F_{norm} is small and we assume $F_{\text{norm}}^n = 0$ for each segment n. Thus, $F_{\text{CE}}^n = 0$ and, since $F_{\text{SE}}^n = F_{\text{CE}}^n$, the force generated by the segment must come from the parallel elastic element, i.e., $F_{\text{PE}}^n = F_{\text{segment}}^n$. Since $F_{\text{SE}}^n = F_{\text{CE}}^n = 0$, it follows from equation (D.11) that $l_1^n = l_2^n$. For homogeneous tissue, the material properties k_{PE} and f_{PE} are equal for all segments. For isotonic simulations, l_2^n can be obtained from equation (D.12) by

$$l_2^n = \frac{1}{k_{\text{PE}}} \ln \left(\frac{F_{\text{segment}}^n + f_{\text{PE}}}{f_{\text{PE}}} \right). \tag{D.31}$$

For isometric simulations, l_2^n can be directly obtained from the initial stretch ratio λ_{fiber} by

$$l_2^n = l_{\text{PE}}^n - l_{\text{PE0}}^n = l_{\text{PE0}}^n (\lambda_{\text{fiber}} - 1). \tag{D.32}$$

For inhomogeneous tissue, it is assumed that, initially, $\lambda_{\text{fiber}} = 1$ and $F_{\text{fiber}} = 0$. In that case, $l_1^n = l_2^n = 0$ for all segments n. During the simulation, stretch (isometric simulation) or force (isotonic simulation) are slowly increased until the desired values are reached. This process typically requires 200 ms of simulation. Finally, it is assumed that, initially

$$\frac{\mathrm{d}l_1^n}{\mathrm{d}t} = \frac{\mathrm{d}l_2^n}{\mathrm{d}t} = 0 \tag{D.33}$$

for homogeneous and inhomogeneous tissue.

[1] E. A. Accili, C. Proenza, M. Baruscotti, and D. DiFrancesco, *From funny current to HCN channels: 20 years of excitation*, News Physiol Sci **17**: 32–37 (2002)

[2] F. Aguel, K. A. Debruin, W. Krassowska, and N. A. Trayanova, *Effects of electroporation on the transmembrane potential distribution in a two-dimensional bidomain model of cardiac tissue*, J Cardiovasc Electrophysiol **10**: 701–714 (1999)

[3] A. Al-Khadra, V. Nikolski, and I. R. Efimov, *The role of electroporation in defibrillation*, Circ Res **87**: 797–804 (2000)

[4] D. G. Allen and J. C. Kentish, *The cellular basis of the length-tension relation in cardiac muscle*, J Mol Cell Cardiol **17**: 821–840 (1985)

[5] M. Allessie, J. Ausma, and U. Schotten, *Electrical, contractile and structural remodeling during atrial fibrillation*, Cardiovasc Res **54**: 230–246 (2002)

[6] M. A. Allessie, P. A. Boyden, J. A. Camm, A. G. Kléber, M. J. Lab, M. J. Legato, M. R. Rosen, P. J. Schwartz, P. M. Spooner, D. R. Van Wagoner, and A. L. Waldo, *Pathophysiology and prevention of atrial fibrillation*, Circulation **103**: 769–777 (2001)

[7] E. P. Anyukhovsky, E. A. Sosunov, A. Plotnikov, R. Z. Gainullin, J. S. Jhang, C. C. Marboe, and M. R. Rosen, *Cellular electrophysiologic properties of old canine atria provide a substrate for arrhythmogenesis*, Cardiovasc Res **54**: 462–469 (2002)

[8] T. Arts, P. Bovendeerd, T. Delhaas, and F. W. Prinzen, *Modeling the relation between cardiac pump fuction and myofiber mechanics*, J Biomech **36**: 731–736 (2003)

[9] T. Arts, T. Delhaas, P. Bovendeerd, X. Verbeek, and F. W. Prinzen, *Adaptation to mechanical load determines shape and properties of heart and circulation: the CircAdapt model*, Am J Physiol Heart Circ Physiol **288**: H1943–H1954 (2005)

[10] H. Ashikaga, B. A. Coppola, B. Hopenfeld, E. S. Leifer, E. R. McVeigh, and J. H. Omens, *Transmural dispersion of myofiber mechanics*, J Am Coll Cardiol **49**: 909–916 (2007)

[11] J. Ausma, H. M. W. van der Velden, M. H. Lenders, E. P. van Ankeren, H. J. Jongsma, F. C. S. Ramaekers, M. Borgers, and M. A. Allessie, *Reverse structural and gap-junctional remodeling after prolonged atrial fibrillation in the goat*, Circulation **107**: 2051–2058 (2003)

[12] O. Axelsson, *Iterative Solution Methods*, Cambridge University Press, Cambridge, UK (1994)

[13] A. Bauer, R. Becker, C. Karle, K. D. Schreiner, J. C. Senges, F. Voss, P. Kraft, W. Kuebler, and W. Schoels, *Effects of the I_{Kr}-blocking agent dofetilide and of the I_{Ks}-blocking agent chromanol 293b on regional disparity of left ventricular repolarization in the intact canine heart*, J Cardiovasc Pharmacol **39**: 460–467 (2002)

[14] C. S. Beck, W. H. Pritchard, and H. S. Feil, *Ventricular fibrillation of long duration abolished by electric shock*, JAMA **135**: 985–986 (1947)

[15] G. W. Beeler and H. Reuter, *Reconstruction of the action potential of ventricular myocardial fibers*, J Physiol **268**: 177–210 (1977)

235

[16] F. Bode, A. Katchman, R. L. Woosley, and M. R. Franz, *Gadolinium decreases stretch-induced vulnerability to atrial fibrillation*, Circulation **101**: 2200–2205 (2000)

[17] F. Bode, F. Sachs, and M. R. Franz, *Tarantula peptide inhibits atrial fibrillation*, Nature **409**: 35–36 (2001)

[18] R. F. Bosch and S. Nattel, *Cellular electrophysioly of atrial fibrillation*, Cardiovasc Res **54**: 259–269 (2002)

[19] M. R. Boyett, A. Clough, J. Dekanski, and A. V. Holden, *Modelling cardiac excitation and excitability* pp. 1–47 (1997)

[20] F. Brette, J. Leroy, J. Y. Le Guennec, and L. Sallé, *Ca^{2+} currents in cardiac myocytes: old story, new insights*, Progr Biophys Mol Biol **91**: 1–82 (2006)

[21] D. L. Brutsaert and E. H. Sonnenblick, *Nature of the force-velocity relation in heart muscle*, Cardiovasc Res **1: suppl 1**: 18–33 (1971)

[22] A. Burashnikov and C. Antzelevitch, *Reinduction of atrial fibrillation immediately after termination of the arrhythmia is mediated by late phase 3 early afterdepolarization-induced triggered activity*, Circulation **107**: 2355–2360 (2003)

[23] D. Cai, R. L. Winslow, and D. Noble, *Effects of gap junction conductance on dynamics of sinoatrial node cells: two-cell and large-scale network models*, IEEE Trans Biomed Eng **41**: 217–231 (1994)

[24] S. C. Calaghan and E. White, *The role of calcium in the response to cardiac muscle to stretch*, Progr Biophys Mol Biol **71**: 59–90 (1999)

[25] E. Carmeliet, *Existence of pacemaker current I_f in human atrial appendage fibres*, J Physiol (Lond) **357**: 125P (1984)

[26] E. Cerbai, M. Barbieri, and A. Mugelli, *Characterization of the hyperpolarization-activated current, I_f, in ventricular myocytes isolated from hypertensive rats*, J Physiol (Lond) **481**: 585–591 (1994)

[27] E. Cerbai, M. Barbieri, and A. Mugelli, *Occurrence and properties of the hyperpolarization-activated current I_f in ventricular myocytes from normotensive and hypertensive rats during aging*, Circulation **94**: 1674–1681 (1996)

[28] E. Cerbai, R. Pino, F. Porciatti, G. Sani, M. Toscano, M. Maccherini, G. Giunti, and A. Mugelli, *Characterization of the hyperpolarization-activated current, I_f, in ventricular myocytes from human failing heart*, Circulation **95**: 568–571 (1997)

[29] E. Cerbai, R. Pino, L. Sartiani, and A. Mugelli, *Influence of postnatal-development on I_f occurence and properties in neonatal rat ventricular myocytes*, Cardiovasc Res **42**: 416–423 (1999)

[30] R. A. Chapman and C. H. Fry, *An analysis of the cable properties of frog ventricular myocardium*, J Physiol **283**: 263–282 (1978)

[31] Y. J. Chen, S. A. Chen, Y. C. Chen, H. I. Yeh, P. Chan, M. S. Chang, and C. I. Lin, *Effects of rapid atrial pacing on the arrhythmogenic activity of single cardiomyocytes from pulmonary veins: implication in initiation of atrial fibrillation*, Circulation **104**: 2849–2854 (2001)

[32] F. J. Chorro, S. Egea, L. Mainar, J. Canoves, J. Sanchis, E. Llavador, V. Lopez-Merino, and L. Such, *Acute changes in wavelength of the process of auricular activation induced by stretching. Experimental study*, Rev Esp Cardiol **51**: 874–883 (1998)

[33] L. Clerc, *Directional differences of impulse spread in trabecular muscle from mammalian heart*, J Physiol **255**: 335–346 (1976)

[34] S. L. Cloherty, N. H. Lovell, B. G. Celler, and S. Dokos, *Inhomogeneity of action potential waveshape assists frequency entrainment of cardiac pacemaker cells*, IEEE Trans Biomed Eng **48**: 1108–1115 (2001)

[35] J. M. Cordeiro, L. Greene, C. Heilmann, D. Antzelevitch, and C. Antzelevitch, *Transmural heterogeneity of calcium activity and mechanical function in the canine left ventricle*, Am J Physiol Heart Circ Physiol **286**: H1471–H1479 (2004)

[36] A. Costard-Jäckle, B. Goetsch, M. Antz, and M. R. Franz, *Slow and long-lasting modulation of myocardial repolarization produced by ectopic activation in isolated rabbit hearts. Evidence for cardiac "memory"*, Circulation **80**: 1412–1420 (1989)

[37] M. Courtemanche, R. J. Ramirez, and S. Nattel, *Ionic mechanisms underlying human atrial action potential properties: insights from a mathematical model*, Am J Physiol Heart Circ Physiol **275**: H301–H321 (1998)

[38] E. B. Curtis and J. A. Morrow, *Inverse problems for electrical networks*, World Scientific, Singapore (2000)

[39] J. M. T. de Bakker, S. Y. Ho, and M. Hocini, *Basic and clinical electrophysiology of pulmonary vein ectopy*, Cardiovasc Res **54**: 287–294 (2002)

[40] P. P. de Tombe and H. E. ter Keurs, *Force and velocity of sarcomere shortening in trabeculae from rat heart. Effects of temperature*, Circ Res **66**: 1239–1254 (1990)

[41] T. Delhaas, T. Arts, F. W. Prinzen, and R. S. Reneman, *Regional fibre stress - fibre strain area as an estimate of regional blood flow and oxygen demand in the canine heart*, J Physiol (Lond) **477**: 481–496 (1994)

[42] D. DiFrancesco, *Pacemaker mechanisms in cardiac tissue*, Annu Rev Physiol **55**: 455–472 (1993)

[43] D. DiFrancesco, *Dual allosteric modulation of pacemaker (f) channels by cAMP and voltage in rabbit SA node*, Journal of Physiology **515**: 367–376 (1999)

[44] D. DiFrancesco, *Letter regarding article by Michels et al, "Single-channel properties support a potential contribution of hyperpolarization-activated cyclic nucleotide-gated channels and I_f to cardiac arrhythmias"*, Circulation **112**: e72–e73 (2005)

[45] D. DiFrancesco and D. Noble, *A model of cardiac electrical activity incorporating ionic pumps and concentration changes*, Phil Trans R Soc Lond B Biol Sci **307**: 353–398 (1985)

[46] J. Eason and N. Trayanova, *Phase singularities and termination of spiral wave reentry*, J Cardiovasc Electrophysiol **13**: 672–679 (2002)

[47] K. A. P. Edman, *Mechanical deactivation induced by active shortening in isolated muscle fibres of the frog*, J Physiol **246**: 255–275 (1975)

[48] I. R. Efimov, F. Aguel, Y. Cheng, B. Wollenzier, and N. Trayanova, *Virtual electrode polarization in the far field: Implications for external defibrillation*, Am J Physiol Heart Circ Physiol **279**: H1055–H1070 (2000)

[49] I. R. Efimov, Y. Cheng, D. R. Van Wagoner, T. Mazgalev, and P. J. Tchou, *Virtual electrode-induced phase singularity: A basic mechanism of defibrillation failure*, Circ Res **82**: 918–925 (1998)

[50] I. R. Efimov, Y. N. Cheng, Y. Yamanouchi, and P. J. Tchou, *Direct evidence of the role of virtual electrode-induced phase singularity in success and failure of defibrillation*, J Cardiovasc Electrophysiol **11**: 861–868 (2000)

[51] J. R. Ehrlich, T. J. Cha, L. Zhang, D. Chartier, P. Melnyk, S. H. Hohnloser, and S. Nattel, *Cellular electrophysiology of canine pulmonary vein cardiomyocytes: action potential and ionic current properties*, J Physiol **551**: 801–813 (2003)

[52] J. R. Ehrlich, T. J. Cha, L. Zhang, D. Chartier, L. Villeneuve, T. E. Hébert, and S. Nattel, *Characterization of a hyperpolarization-activated time-dependent potassium current in canine cardiomyocytes from pulmonary vein myocardial sleeves and left atrium*, J Physiol **557**: 583–597 (2004)

[53] S. C. M. Eijsbouts, R. P. M. Houben, Y. Blaauw, U. Schotten, and M. A. Allessie, *Synergistic action of atrial dilation and sodium channel blockade on conduction in rabbit atria*, J Cardiovasc Electrophysiol **15**: 1453–1461 (2004)

[54] S. C. M. Eijsbouts, M. Majidi, M. van Zandvoort, and M. A. Allessie, *Effects of acute atrial dilation on heterogeneity in conduction in the isolated rabbit heart*, J Cardiovasc Electrophysiol **14**: 269–278 (2003)

[55] V. G. Fast and A. G. Kléber, *Block of impulse propagation at an abrupt tissue expansion: evaluation of the critical strand diameter in 2- and 3-dimensional computer models*, Cardiovasc Res **30**: 449–459 (1995)

[56] V. G. Fast, S. Rohr, A. M. Gillis, and A. G. Kléber, *Activation of cardiac tissue by extracellular electrical shocks*, Circ Res **82**: 375–385 (1998)

[57] J. Feng, L. Yue, Z. Wang, and S. Nattel, *Ionic mechanisms of regional action potential heterogeneity in the canine right atrium*, Circ Res **83**: 541–551 (1998)

[58] F. H. Fenton, E. M. Cherry, H. M. Hastings, and S. J. Evans, *Multiple mechanisms of spiral wave breakup in a model of cardiac electrical activity*, Chaos **12**: 852–892 (2002)

[59] M. G. Fishler, *Spatiotemporal effects of syncytial heterogeneities on cardiac far-field excitations during monophasic and biphasic shocks*, J Cardiovasc Electrophysiol **9**: 1310–1324 (1998)

[60] M. G. Fishler, *Syncytial heterogeneity as a mechanism underlying cardiac far-field stimulation during defibrillation-level shock*, J Cardiovasc Electrophysiol **9**: 384–394 (1998)

[61] M. G. Fishler, *Theoretical predictions of the optimal monophasic and biphasic defibrillation waveshapes*, IEEE Trans Biomed Eng **47**: 59–67 (2000)

[62] M. R. Franz, *Mechano-electrical feedback in ventricular myocardium*, Cardiovasc Res **32**: 15–24 (1996)

[63] M. R. Franz, K. Bargheer, R. W, A. Haverich, and P. R. Lichtlen, *Monophasic action potential mapping in human subjects with normal electrocardiograms: direct evidence for the genesis of the T wave*, Circulation **75**: 379–386 (1987)

[64] A. M. Gillis, V. G. Fast, S. Rohr, and A. G. Kléber, *Spatial changes in transmembrane potential during extracellular electrical shocks in cultured monolayers of neonatal rat ventricular myocytes*, Circ Res **79**: 676–690 (1996)

[65] J. L. Greenstein, R. Wu, S. Po, G. F. Tomaselli, and R. L. Winslow, *Role of the calcium-independent transient outward current I_{to1} in shaping action potential morphology and duration*, Circ Res **87**: 1026–1033 (2000)

[66] M. Haïssaguerre, P. Jaïs, D. C. Shah, A. Takahashi, M. Hocini, G. Quiniou, S. Garrigue, A. Le Mouroux, P. Le Métayer, and J. Clémenty, *Spontaneous initiation of atrial fibrillation by ectopic beats originating in the pulmonary veins*, New Engl J Med **339**: 659–666 (1998)

[67] D. M. Harrild and C. S. Henriquez, *A computer model of normal conduction in the human atria*, Circ Res **87**: 25–36 (2000)

[68] S. N. Healy and A. D. McCulloch, *An ionic model of stretch-activated and stretch-modulated currents in rabbit ventricular myocytes*, Europace **7**: S128–S134 (2005)

[69] C. S. Henriquez, *Simulating the electrical behavior of cardiac tissue using the bidomain model*, Crit Rev Biomed Eng **21**: 1–77 (1993)

[70] B. Herweg, F. Chang, P. Chandra, P. Danilo Jr, and M. R. Rosen, *Cardiac memory in canine atrium: identification and implications*, Circulation **103**: 455–461 (2001)

[71] A. V. Hill, *The heat of shortening and the dynamic constants in muscle*, Proc Roy Soc London **126**: 136–195 (1938)

[72] M. G. Hillebrenner, J. C. Eason, and N. A. Trayanova, *Mechanistic inquiry into decrease in probability of defibrillation success with increase in complexity of preshock reentrant activity*, Am J Physiol Heart Circ Physiol **286**: H909–H917 (2004)

[73] M. Hocini, S. Y. Ho, T. Kawara, A. C. Linnenbank, M. Potse, D. Shah, P. Jaïs, M. J. Janse, M. Haïssaguerre, and J. M. T. de Bakker, *Electrical conduction in canine pulmonary veins: electrophysiological and anatomic correlation*, Circulation **105**: 2442–2448 (2002)

[74] A. V. Holden and A. V. Panfilov, *Modelling propagation in excitable media*, in A. V. Panfilov and A. V. Holden, editors, *Computational Biology of the Heart*, pp. 65–99, John Wiley & Sons Ltd, Chichester, UK (1997)

[75] D. A. Hooks, K. A. Tomlinson, S. G. Marsden, I. J. LeGrice, B. H. Smaill, A. J. Pullan, and P. J. Hunter, *Cardiac microstructure implications for electrical propagation and defibrillation in the heart*, Circ Res **91**: 331–338 (2002)

[76] U. C. Hoppe and D. J. Beuckelmann, *Characterization of the hyperpolarization-activated inward current in isolated human atrial myocytes*, Cardiovasc Res **38**: 788–801 (1998)

[77] U. C. Hoppe, E. Jansen, M. Südkamp, and D. J. Beuckelmann, *Hyperpolarization-activated inward current in ventricular myocytes from normal and failing human hearts*, Circulation **97**: 55–65 (1998)

[78] H. Hu and F. Sachs, *Stretch-activated ion channels in the heart*, J Mol Cell Cardiol **29**: 1511–1523 (1997)

[79] J. L. Huang, C. T. Tai, J. T. Chen, C. T. Ting, Y. T. Chen, M. S. Chang, and S. A. Chen, *Effect of atrial dilatation on electrophysiologic properties and inducibility of atrial fibrillation*, Basic Res Cardiol **98**: 16–24 (2003)

[80] P. J. Hunter, A. D. McCulloch, and H. E. D. J. ter Keurs, *Modelling the mechanical properties of cardiac muscle*, Progr Biophys Mol Biol **69**: 289–331 (1998)

[81] G. Iribe, M. Helmes, and P. Kohl, *Force-length relations in isolated intact cardiomyocytes subjected to dynamic changes in mechanical load*, Am J Physiol Heart Circ Physiol **292**: H1487–H1497 (2007)

[82] V. Jacquemet, *A biophysical model of atrial fibrillation and electrograms: formulation, validation and applications*, Ph.D. thesis, EPFL, Lausanne, Switzerland (2005)

[83] V. Jacquemet, N. Virag, Z. Ihara, L. Dang, O. Blanc, S. Zozor, J. M. Vesin, L. Kappenberger, and C. Henriquez, *Study of unipolar electrogram morphology in a computer model of atrial fibrillation*, J Cardiovasc Electrophysiol **14**: S172–S179 (2003)

[84] V. Jacquemet, N. Virag, and L. Kappenberger, *Wavelength and vulnerability to atrial fibrillation: insights from a computer model of human atria*, Europace **7**: S83–S92 (2005)

[85] P. Jaïs, M. Hocini, L. Macle, K. J. Choi, I. Deisenhofer, R. Weerasooriya, D. C. Shah, S. Garrigue, F. Raybaud, C. Scavee, P. Le Metayer, J. Clémenty, and M. Haïssaguerre, *Distinctive electrophysiological properties of pulmonary veins in patients with atrial fibrillation*, Circulation **106**: 2479–2485 (2002)

[86] P. M. L. Janssen and W. C. Hunter, *Force, not sarcomere length, correlates with prolongation of isosarcometric contraction*, Am J Physiol Heart Circ Physiol **269**: H676–H685 (1995)

[87] D. Jeyaraj, L. D. Wilson, J. Zhong, C. Flask, J. E. Saffitz, I. Deschênes, X. Yu, and D. S. Rosenbaum, *Mechanoelectric feedback as novel mechanism of cardiac electrical remodeling*, Circulation **115**: 3145–3155 (2007)

[88] H. J. Jongsma and R. Wilders, *Gap junctions in cardiovascular disease*, Circ Res **86**: 1193–1197 (2000)

[89] S. Kääb, B. Nuss, N. Chiamvimonvat, B. O'Rourke, P. H. Pak, D. A. Kass, E. Marban, and G. F. Tomaselli, *Ionic mechanisms of action potential prolongation in ventricular myocytes from dogs with pacing-induced heart failure*, Circ Res **78**: 262–273 (1996)

[90] Y. Kagiyama, J. L. Hill, and L. S. Gettes, *Interaction of acidosis and increased extracellular potassium on action potential characteristics and conduction in guinea pig ventricular muscle*, Circ Res **51**: 614–623 (1982)

[91] A. Kamkin, I. Kiseleva, K. D. Wagner, J. Bohm, H. Theres, J. Gunther, and H. Scholz, *Characterization of stretch-activated ion currents in isolated atrial myocytes from human hearts*, Pflügers Arch - Eur J Physiol **446**: 339–346 (2003)

[92] W. B. Kannel, P. A. Wolf, E. J. Benjamin, and D. Levy, *Prevalence, incidence, prognosis, and predisposing conditions for atrial fibrillation: populaton-based estimates*, Am J Cardiol **82**: 2N–9N (1998)

[93] T. Kawara, R. Derksen, J. de Groot, R. Coronel, S. R. T. Tasseron, A. C. Linnenbank, R. N. W. Hauer, H. Kirkels, M. J. Janse, and J. M. T. de Bakker, *Activation delay after premature stimulation in chronically diseased human myocardium relates to the architecture of interstitial fibrosis*, Circulation **104**: 3069–3075 (2001)

[94] J. P. Keener and K. Bogar, *A numerical method for the solution of the bidomain equations in cardiac tissue*, Chaos **8**: 234–241 (1998)

[95] J. P. Keener and E. Cytrynbaum, *The effect of spatial scale of resistive inhomogeneity on defibrillation of cardiac tissue*, J Theor Biol **223**: 233–248 (2003)

[96] J. P. Keener and A. V. Panfilov, *A biophysical model for defibrillation of cardiac tissue*, Biophys J **71**: 1335–1345 (1996)

[97] J. P. Keener and J. Sneyd, *Mathematical Physiology*, Springer-Verlag, New York (1998)

[98] J. C. Kentish, H. E. D. J. ter Keurs, L. Ricciardi, J. J. J. Bucx, and M. I. M. Noble, *Comparison between the sarcomere length-force relations of intact and skinned trabeculae from rat right ventricle*, Circ Res **58**: 755–768 (1986)

[99] R. C. P. Kerckhoffs, P. H. M. Bovendeerd, J. C. S. Kotte, F. W. Prinzen, K. Smits, and T. Arts, *Homogeneity of cardiac contraction despite physiological asynchrony of depolarization: a model study*, Ann Biomed Eng **31**: 536–547 (2003)

[100] R. C. P. Kerckhoffs, O. P. Faris, P. H. M. Bovendeerd, F. W. Prinzen, K. Smits, E. R. McVeigh, and T. Arts, *Electromechanics of paced left ventricle simulated by straightforward mathematical model: comparison with experiments*, Am J Physiol Heart Circ Physiol **289**: H1889–H1897 (2005)

[101] D. Kim, *Novel cation-selective mechanosensitive ion channel in the atrial cell membrane*, Circ Res **72**: 225–231 (1993)

[102] E. L. King and C. Altman, *A schematic method of deriving the rate laws for enzyme-catalyzed reactions*, J Am Chem Soc **60**: 1375–1378 (1956)

[103] A. G. Kléber and Y. Rudy, *Basic mechanisms of cardiac impulse propagation and associated arrhythmias*, Physiol Rev **84**: 431–488 (2004)

[104] J. Kneller, R. Zou, E. J. Vigmond, Z. Wang, L. J. Leon, and S. Nattel, *Cholinergic atrial fibrillation in a computer model of a two-dimensional sheet of canine atrial cells with realistic ionic properties*, Circ Res **90**: e73–e87 (2002)

[105] P. Kohl and F. Sachs, *Mechanoelectric feedback in cardiac cells*, Phil Trans R Soc Lond **359**: 1173–1185 (2001)

[106] W. Krassowska, *Effects of electroporation on transmembrane potential induced by defibrillation shocks*, PACE **18**: 1644–1660 (1995)

[107] W. Krassowska, *Field stimulation of cardiac fibers with random spatial structure*, IEEE Trans Biomed Eng **50**: 33–40 (2003)

[108] W. Krassowska and J. C. Neu, *Response of a single cell to an external electric field*, Biophys J **66**: 1768–1776 (1994)

[109] N. H. L. Kuijpers, R. H. Keldermann, T. Arts, and P. A. J. Hilbers, *Computer simulations of successful defibrillation in decoupled and non-uniform cardiac tissue*, Europace **7**: S166–S177 (2005)

[110] N. H. L. Kuijpers, R. H. Keldermann, H. M. M. ten Eikelder, T. Arts, and P. A. J. Hilbers, *The role of the hyperpolarization-activated inward current I_f in arrhythmogenesis: a computer model study*, IEEE Trans Biomed Eng **53**: 1499–1511 (2006)

[111] N. H. L. Kuijpers, R. J. Rijken, H. M. M. ten Eikelder, and P. A. J. Hilbers, *Vulnerability to atrial fibrillation under stretch can be explained by stretch-activated channels*, Comput Cardiol **34**: 237–240 (2007)

[112] N. H. L. Kuijpers, H. M. M. ten Eikelder, P. H. M. Bovendeerd, S. Verheule, T. Arts, and P. A. J. Hilbers, *Mechanoelectric feedback leads to conduction slowing and block in acutely dilated atria: a modeling study of cardiac electromechanics*, Am J Physiol Heart Circ Physiol **292**: H2832–H2853 (2007)

[113] M. J. Lab, *Mechano-electric feedback (transduction) in heart: concepts and implications*, Cardiovasc Res **32**: 3–14 (1996)

[114] M. J. Lab, *Mechanosensitivity as an integrative system in heart: an audit*, Progr Biophys Mol Biol **71**: 7–27 (1998)

[115] M. J. Lab, D. G. Allen, and C. H. Orchard, *The effects of shortening on myoplasmic calcium concentration an on the action potential in mammalian ventricular muscle*, Circ Res **55**: 825–829 (1984)

[116] A. Landesberg and S. Sideman, *Mechanical regulation of cardiac muscle by coupling calcium kinetics with cross-bridge cycling: a dynamic model*, Am J Physiol Heart Circ Physiol **267**: H779–H795 (1994)

[117] K. R. Laurita, R. Katra, B. Wible, X. Wan, and M. H. Koo, *Transmural heterogeneity of calcium handling in canine*, Circ Res **92**: 668–675 (2003)

[118] L. J. Leon and F. A. Roberge, *Structural complexity effects on transverse propagation in a two-dimensional model of myocardium*, IEEE Trans Biomed Eng **38**: 997–1009 (1991)

[119] W. Li, P. Kohl, and N. Trayanova, *Myocardial ischemia lowers precordial thump efficacy: An inquiry into mechanisms using three-dimensional simulations*, Heart Rhythm **3**: 179–186 (2006)

[120] I. Libbus and D. S. Rosenbaum, *Remodeling of cardiac repolarization: mechanisms and implications of memory*, Cardiac Electrophysiology Review **6**: 302–310 (2002)

[121] I. Libbus and D. S. Rosenbaum, *Transmural action potential changes underlying ventricular electrical remodeling*, J Cardiovasc Electrophysiol **14**: 394–402 (2003)

[122] I. Libbus, X. Wan, and D. S. Rosenbaum, *Electrotonic load triggers remodeling of repolarizing current I_{to} in ventricle*, Am J Physiol Heart Circ Physiol **286**: H1901–H1909 (2004)

[123] D. W. Liu and C. Antzelevitch, *Characteristics of the delayed rectifier current (I_{Kr} and I_{Ks}) in canine ventricular epicardial, midmyocardial, and endocardial myocytes: a weaker I_{Ks} contributes to the longer action potential of the M cell*, Circ Res **76**: 351–365 (1995)

[124] A. Ludwig, X. Zong, J. Stieber, R. Hullin, F. Hofmann, and M. Biel, *Two pacemaker channels from human heart with profoundly different activation kinetics*, Embo J **18**: 2323–2329 (1999)

[125] C. H. Luo and Y. Rudy, *A dynamic model of the cardiac ventricular action potential. I. Simulations of ionic currents and concentration changes*, Circ Res **74**: 1071–1096 (1994)

[126] C. H. Luo and Y. Rudy, *A dynamic model of the cardiac ventricular action potential. II. Afterdepolarizations, triggered activity, and potentiation*, Circ Res **74**: 1097–1113 (1994)

[127] R. A. Malkin, S. R. Jackson, J. Nguyen, Z. Yang, and D. Guan, *Experimental verification of theoretical predictions concerning the optimum defibrillation waveform*, IEEE Trans Biomed Eng **53**: 1492–1498 (2006)

[128] G. Michels, F. Er, I. Khan, M. Südkamp, S. Herzig, and U. C. Hoppe, *Single-channel properties support a potential contribution of hyperpolarization-activated cyclic nucleotide-gated channels and I_f to cardiac arrhythmias*, Circulation **111**: 399–404 (2005)

[129] A. Moroni, A. Barbuti, C. Altomare, C. Viscomi, J. Morgan, M. Baruscotti, and D. DiFrancesco, *Kinetic and ionic properties of the human HCN2 pacemaker channel*, Pflügers Arch - Eur J Physiol **439**: 618–626 (2000)

[130] M. P. Nash and A. V. Panfilov, *Electromechanical model of excitable tissue to study reentrant cardiac arrhythmias*, Progr Biophys Mol Biol **85**: 501–522 (2004)

[131] S. Nattel, *Newer developments in the management of atrial fibrillation*, Am Heart J **130**: 1094–1106 (1995)

[132] S. Nattel, *Experimental evidence for proarrhythmic mechanisms of antiarrhythmic drugs*, Cardiovasc Res **37**: 567–577 (1998)

[133] S. Nattel, *New ideas about atrial fibrillation 50 years on*, Nature **415**: 219–226 (2002)

[134] S. Nattel, A. Shiroshita-Takeshita, S. Cardin, and P. Pelletier, *Mechanisms of atrial remodeling and clinical relevance*, Curr Opin Cardiol **20**: 21–25 (2005)

[135] S. A. Nazir and M. J. Lab, *Mechanoelectric feedback and atrial arrhythmias*, Cardiovasc Res **32**: 52–61 (1996)

[136] J. C. Newton, S. B. Knisley, X. Zhou, A. E. Pollard, and R. E. Ideker, *Review of mechanisms by which electrical stimulation alters the transmenbrane potential*, J Cardiovasc Electrophysiol **10**: 234–243 (1999)

[137] D. Nickerson, N. Smith, and P. Hunter, *New developments in a strongly coupled cardiac electromechanical model*, Europace **7**: S118–S127 (2005)

[138] M. N. Obreztchikova, K. W. Patberg, A. N. Plotnikov, N. Ozgen, I. N. Shlapakova, A. V. Rybin, E. A. Sosunov, P. Danilo Jr, E. P. Anyukhovsky, R. B. Robinson, and M. R. Rosen, *I_{Kr} contributes to the altered ventricular repolarization that determines long-term cardiac memory*, Cardiovasc Res **71**: 88–96 (2006)

[139] T. Ohara, Z. Qu, M. H. Lee, K. Ohara, C. Omichi, W. J. Mandel, P. S. Chen, and H. S. Karagueuzian, *Increased vulnerability to inducible atrial fibrillation caused by*

partial cellular uncoupling with heptanol, Am J Physiol Heart Circ Physiol **283**: H1116–H1122 (2002)

[140] T. Opthof, *The membrane current (I_f) in human atrial cells: implications for atrial arrhythmias*, Cardiovasc Res **38**: 537–540 (1998)

[141] A. V. Panfilov, R. H. Keldermann, and M. P. Nash, *Self-organized pacemakers in a coupled reaction-diffusion-mechanics system*, Phys Rev Lett **95**: 258104 (2005)

[142] K. W. Patberg, A. N. Plotnikov, A. Quamina, R. Z. Gainullin, A. Rybin, P. Danilo Jr, L. S. Sun, and M. R. Rosen, *Cardiac memory is associated with decreased levels of the transcriptional factor CREB modulated by angiotensin II and calcium*, Circ Res **93**: 472–478 (2003)

[143] C. Philips and B. Cornelius, *Computational Numerical Methods*, Ellis Horwood Limited, West Sussex, UK (1986)

[144] G. Plank, L. J. Leon, S. Kimber, and E. J. Vigmond, *Defibrillation depends on conductivity fluctuations and the degree of disorganization in reentry patterns*, J Cardiovasc Electrophysiol **16**: 205–216 (2005)

[145] A. N. Plotnikov, H. Yu, J. C. Geller, R. Z. Gainullin, P. Chandra, K. W. Patberg, S. Friezema, P. Danilo Jr, I. S. Cohen, S. J. Feinmark, and M. R. Rosen, *Role of L-type calcium channels in pacing-induced short-term and long-term cardiac memory in canine heart*, Circulation **107**: 2844–2849 (2003)

[146] F. Porciatti, B. Pelzmann, E. Cerbai, P. Shaffer, R. Pino, E. Bernhart, B. Koidl, and A. Mugelli, *The pacemaker current I_f in single human atrial myocytes and the effect of β-adrenoceptor and A1-adenosine receptor stimulation*, Br J Pharmacol **122**: 963–969 (1997)

[147] W. H. Press, S. A. Teukolsky, W. T. Vetterling, and B. P. Flannery, *Numerical Recipes in C: The Art of Scientific Computing 2nd ed*, Cambridge University Press, Cambridge, UK (1992)

[148] F. W. Prinzen, C. H. Augustijn, T. Arts, M. A. Allessie, and R. S. Reneman, *Redistribution of myocardial fiber strain and blood flow by asynchronous activation*, Am J Physiol **259**: H300–H308 (1990)

[149] F. W. Prinzen, W. C. Hunter, B. T. Wyman, and E. R. McVeigh, *Mapping of regional myocardial strain and work during ventricular pacing: experimental study using magnetic resonance imaging tagging*, J Am Coll Cardiol **33**: 1735–1742 (1999)

[150] B. M. Psaty, T. A. Manolio, L. H. Kuller, R. A. Kronmal, M. Cushman, L. P. Fried, R. White, C. D. Furberg, and P. M. Rautaharju, *Incidence of and risk factors for atrial fibrillation in older adults*, Circulation **96**: 2455–2461 (1997)

[151] S. Puwal and B. J. Roth, *Forward Euler stability of the bidomain model of cardiac tissue*, IEEE Trans Biomed Eng **54**: 951–953 (2007)

[152] F. Ravelli, *Mechano-electric feedback and atrial fibrillation*, Progr Biophys Mol Biol **82**: 137–149 (2003)

[153] F. Ravelli and M. Allessie, *Effects of atrial dilatation on refractory period and vulnerability to atrial fibrillation in the isolated Langendorff-perfused rabbit heart*, Circulation **96**: 1686–1695 (1997)

[154] F. Ravelli, M. Disertori, F. Cozzi, R. Antolini, and M. A. Allessie, *Ventricular beats induce variations in cycle length of rapid (type II) atrial flutter in humans: evidence of leading circle reentry*, Circulation **89**: 2107–2116 (1994)

[155] P. L. Rensma, M. A. Allessie, W. J. Lammers, F. I. Bonke, and M. J. Schalij, *Length of excitation wave and susceptibility to reentrant atrial arrhythmias in normal conscious dogs*, Circ Res **62**: 395–410 (1988)

[156] J. J. Rice and P. P. de Tombe, *Approaches to modeling crossbridges and calcium-dependent activation in cardiac muscle*, Progr Biophys Mol Biol **85**: 179–195 (2004)

[157] J. J. Rice, M. S. Jafri, and R. L. Winslow, *Modeling short-term interval-force relations in cardiac muscle*, Am J Physiol Heart Circ Physiol **278**: H913–H931 (2000)

[158] J. J. Rice, R. L. Winslow, and W. C. Hunter, *Comparison of putative cooperative mechanisms in cardiac muscle: length dependence and dynamic responses*, Am J Physiol Heart Circ Physiol **276**: H1734–H1754 (1999)

[159] B. Rodríguez and N. Trayanova, *Upper limit of vulnerability in a defibrillation model of the rabbit ventricles*, J Electrocardiol **36**: 51–56 (2003)

[160] M. B. Rosenbaum, H. H. Blanco, M. V. Elizari, J. O. Lazzari, and J. M. Davidenko, *Electrotonic modulation of the T wave and cardiac memory*, Am J Cardiol **50**: 213–222 (1982)

[161] B. J. Roth and J. P. Wikswo Jr, *Electrical stimulation of cardiac tissue: a bidomain model with active membrane properties*, IEEE Trans Biomed Eng **41**: 232–240 (1994)

[162] M. Rubart, J. C. Lopshire, N. S. Fineberg, and D. P. Zipes, *Changes in left ventricular repolarization and ion channel currents following a transient rate increase superimposed on bradycardia in anesthetized dogs*, J Cardiovasc Electrophysiol **11**: 652–664 (2000)

[163] F. Sachs, *Modeling mechanical-electrical transduction in the heart*, in V. C. Mow, F. Guliak, R. Tran-Son-Tay, and R. M. Hochmuth, editors, *Cell Mechanics and Cellular Engineering*, pp. 308–328, Springer Verlag, New York (1994)

[164] R. Sah, R. J. Ramirez, G. Y. Oudit, D. Gidrewicz, M. G. Trivieri, C. Zobel, and P. H. Backx, *Regulation of cardiac excitation-contraction coupling by action potential repolarization: role of the transient outward potassium current (I_{to})*, J Physiol **546**: 5–18 (2003)

[165] L. Sartiani, P. Bochet, E. Cerbai, A. Mugelli, and R. Fischmeister, *Functional expression of the hyperpolarization-activated, non-selective cation current I_f in immortalized HL-1 cardiomyocytes*, J Physiol **545**: 81–92 (2002)

[166] T. Satoh and D. P. Zipes, *Unequal atrial stretch in dogs increases dispersion of refractoriness conducive to developing atrial fibrillation*, J Cardiovasc Electrophysiol **7**: 833–842 (1996)

[167] U. Schotten, M. Duytschaever, J. Ausma, S. Eijsbouts, H. R. Neuberger, and M. A. Allessie, *Electrical and contractile remodeling during the first days of atrial fibrillation go hand in hand*, Circulation **107**: 1433–1439 (2003)

[168] U. Schotten, H. R. Neuberger, and M. A. Allessie, *The role of atrial dilation in the domestication of atrial fibrillation*, Progr Biophys Mol Biol **82**: 151–162 (2003)

[169] R. M. Shaw and Y. Rudy, *The vulnerable window for unidirectional block in cardiac tissue*, J Cardiovasc Electrophysiol **6**: 115–131 (1995)

[170] R. M. Shaw and Y. Rudy, *Electrophysiologic effects of acute myocardial ischemia: a mechanistic investigation of action potential conduction and conduction failure*, Circ Res **80**: 124–138 (1997)

[171] R. M. Shaw and Y. Rudy, *Ionic mechanisms of propagation in cardiac tissue: roles of the sodium and L-type calcium currents during reduced excitability and decreased gap junction coupling*, Circ Res **81**: 727–741 (1997)

[172] A. Shimizu and O. A. Centurion, *Electrophysiological properties of the human atrium in atrial fibrillation*, Cardiovasc Res **54**: 302–314 (2002)

[173] A. Shvilkin, P. Danilo Jr, J. Wang, D. Burkhoff, E. P. Anyukhovsky, E. A. Sosunov, M. Hara, and M. R. Rosen, *Evolution and resolution of long-term cardiac memory*, Circulation **97**: 1810–1817 (1998)

[174] D. Sideris, S. Toumanidis, M. Thodorakis, K. Kostopoulos, E. Tselepatiotis, C. Langoura, T. Stringli, and S. Moulopoulos, *Some observations on the mechanism of pressure related atrial fibrillation*, Eur Heart J **15**: 1585–1589 (1994)

[175] K. Skouibine, N. Trayanova, and P. Moore, *A numerically efficient model for simulation of defibrillation in an active bidomain sheet of myocardium*, Math Biosci **166**: 85–100 (2000)

[176] O. Solovyova, L. Katsnelson, S. Guriev, L. Nikitina, Y. Protsenko, S. Routkevitch, and V. Markhasin, *Mechanical inhomogeneity of myocardium studied in parallel and serial cardiac muscle duplexes: experiments and models*, Chaos, Solitons and Fractals **13**: 1685–1711 (2002)

[177] F. Solti, T. Vecsey, V. Kekési, and A. Juhász-Nagy, *The effect of atrial dilatation on the genesis of atrial arrhythmias*, Cardiovasc Res **23**: 882–886 (1989)

[178] E. A. Sosunov, E. P. Anyukhovsky, and M. R. Rosen, *Altered ventricular stretch contributes to initiation of cardiac memory*, Heart Rhythm **5**: 106–113 (2008)

[179] M. S. Spach and J. P. Boineau, *Microfibrosis produces electrical load variations due to loss of side-to-side cell connections: a major mechanism of structural heart disease arrhythmias*, PACE **20[Pt. II]**: 397–413 (1997)

[180] M. S. Spach and P. C. Dolber, *Relating extracellular potentials and their derivatives to anisotropic propagation at a microscopic level in human cardiac muscle: evidence for electrical uncoupling of side-to-side fiber connections with increasing age*, Circ Res **58**: 356–371 (1986)

[181] M. S. Spach, P. C. Dolber, and P. A. Anderson, *Multiple regional differences in cellular properties that regulate repolarization and contraction in the right atrium of adult and newborn dogs*, Circ Res **65**: 1594–1611 (1989)

[182] M. S. Spach, P. C. Dolber, and J. F. Heidlage, *Interaction of inhomogeneities of repolarization with anisotropic propagation in dog atria: a mechanism for preventing and initiating reentry*, Circ Res **65**: 1612–1631 (1989)

[183] M. S. Spach and J. F. Heidlage, *The stochastic nature of cardiac propagation at a microscopic level: electrical description of myocardial architecture and its application to conduction*, Circ Res **76**: 366–380 (1995)

[184] M. S. Spach, J. F. Heidlage, P. C. Dolber, and R. C. Barr, *Extracellular discontinuities in cardiac muscle: evidence for capillary effects on the action potential foot*, Circ Res **83**: 1144–1164 (1998)

[185] M. S. Spach, W. T. Miller III, E. Miller-Jones, R. B. Warren, and R. C. Barr, *Extracellular potentials related to intracellular action potentials during impulse conduction in anisotropic canine cardiac muscle*, Circ Res **45**: 188–204 (1979)

[186] N. Sperelakis and K. McConnell, *Electric field interactions between closely abutting excitable cells*, IEEE Eng Med Biol Mag **21**: 77–89 (2002)

[187] J. G. Stinstra, S. Poelzing, R. S. MacLeod, and C. S. Henriquez, *A model for estimating the anisotropy of the conduction velocity in cardiac tissue based on the tissue morphology*, Comput Cardiol **34**: 129–132 (2007)

[188] J. G. Stinstra, S. F. Roberts, J. B. Pormann, R. S. MacLeod, and C. S. Henriquez, *A model of 3D propagation in discrete cardiac tissue*, Comput Cardiol **33**: 41–44 (2006)

[189] A. M. Street and R. Plonsey, *Propagation in cardiac tissue adjacent to connective tissue: two-dimensional modeling studies*, IEEE Trans Biomed Eng **46**: 19–25 (1999)

[190] H. Suga, *Total mechanical energy of a ventricle model and cardiac oxygen consumption*, Am J Physiol Heart Circ Physiol **236**: H498–H505 (1979)

[191] J. Sundnes, G. T. Lines, X. Cai, B. F. Nielsen, K. A. Mardal, and A. Tveito, *Computing the Electrical Activity in the Heart*, Springer, New York (2006)

[192] D. Sung, R. W. Mills, J. Schettler, S. M. Narayan, J. H. Omens, and A. D. McCulloch, *Ventricular filling slows epicardial conduction and increases action potential duration in an optical mapping study of the isolated rabbit heart*, J Cardiovasc Electrophysiol **14**: 739–749 (2003)

[193] P. Tavi, C. Han, and M. Weckstrom, *Mechanisms of stretch-induced changes in* $[Ca^{2+}]_i$ *in rat atrial myocytes: role of increased troponin C affinity and stretch-activated ion channels*, Circ Res **83**: 1165–1177 (1998)

[194] K. H. W. J. ten Tusscher, D. Noble, P. J. Noble, and A. V. Panfilov, *A model for human ventricular tissue*, Am J Physiol Heart Circ Physiol **286**: H1573–H1589 (2004)

[195] K. H. W. J. ten Tusscher and A. V. Panfilov, *Reentry in heterogeneous cardiac tissue described by the luo-rudy ventricular action potential model*, Am J Physiol Heart Circ Physiol **284**: H542–H548 (2002)

[196] K. H. W. J. ten Tusscher and A. V. Panfilov, *Influence of nonexcitable cells on spiral breakup in two-dimensional and three-dimensional excitable media*, Phys Rev E **68**: 062902 (2003)

[197] K. H. W. J. ten Tusscher and A. V. Panfilov, *Alternans and spiral breakup in a human ventricular tissue model*, Am J Physiol Heart Circ Physiol **291**: H1088–H1100 (2006)

[198] J. W. Thomas, *Numerical Partial Differential Equations: Finite Difference Methods*, Springer-Verlag, New York (1995)

[199] N. Trayanova, *Discrete versus syncytial tissue behavior in a model of cardiac stimulation - II: results of simulation*, IEEE Trans Biomed Eng **43**: 1141–1150 (1996)

[200] N. Trayanova, W. Li, J. Eason, and P. Kohl, *Effect of stretch-activated channels on defibrillation efficacy*, Heart Rhythm **1**: 67–77 (2004)

[201] N. Trayanova and K. Skouibine, *Modeling defibrillation: effects of fiber curvature*, J Electrocardiol **31**: 23–29 (1998)

[202] N. Trayanova, K. Skouibine, and F. Aguel, *The role of cardiac tissue structure in defibrillation*, Chaos **8**: 221–233 (1998)

[203] L. Tung, *A bi-domain model for describing ischemic myocardial D-C potentials*, Ph.D. thesis, MIT, Cambridge, Massachusetts, USA (1978)

[204] T. P. Usyk and A. D. McCulloch, *Electromechanical model of cardiac resynchronization in the dilated failing heart with left bundle branch block*, J Electrocardiol **36**: 57–61 (2003)

[205] T. P. Usyk and A. D. McCulloch, *Relationship between regional shortening and asynchronous electrical activation in a three-dimensional model of ventricular electromechanics*, J Cardiovasc Electrophysiol **14**: S196–S202 (2003)

[206] M. Uzzaman, H. Honjo, Y. Takagishi, L. Emdad, A. Magee, N. Severs, and I. Kodama, *Remodeling of gap-junctional coupling in hypertrophied right ventricles of rats with monocrotaline-induced pulmonary hypertension*, Circ Res **86**: 871–878 (2000)

[207] P. M. van Dam and A. van Oosterom, *Atrial excitation assuming uniform propagation*, J Cardiovasc Electrophysiol **14 (10 Suppl)**: S166–S171 (2003)

[208] P. M. van Dam and A. van Oosterom, *Volume conductor effects involved in the genesis of the P wave*, Europace **7**: S30–S38 (2005)

[209] H. M. W. van der Velden, J. Ausma, M. B. Rook, A. J. C. G. M. Hellemons, T. A. A. B. van Veen, M. A. Allessie, and H. J. Jongsma, *Gap junctional remodeling in relation to stabilization of atrial fibrillation in the goat*, Cardiovasc Res **46**: 476–486 (2000)

[210] H. M. W. van der Velden and H. J. Jongsma, *Cardiac gap junctions and connexins: their role in atrial fibrillation and potential as therapeutic targets*, Cardiovasc Res **54**: 270–279 (2002)

[211] A. Varghese and G. R. Sell, *A conservation principle and its effect on the formulation of Na-Ca exchanger current in cardiac cells*, J Theor Biol **189**: 33–40 (1997)

[212] S. M. Vaziri, M. G. Larson, E. J. Benjamin, and D. Levy, *Echocardiographic predictors of nonrheumatic atrial fibrillation. The Framingham Heart Study*, Circulation **89**: 724–730 (1994)

[213] E. Vigmond, R. Ruckdeschel, and N. Trayanova, *Reentry in a morphologically realistic atrial model*, J Cardiovasc Electrophysiol **12**: 1046–1054 (2001)

[214] E. J. Vigmond, V. Tsoi, S. Kuo, H. Arevalo, J. Kneller, S. Nattel, and N. Trayanova, *The effect of vagally induced dispersion of action potential duration on atrial arrhythmogenesis*, Heart Rhythm **3**: 334–344 (2004)

[215] N. Virag, V. Jacquemet, C. S. Henriquez, S. Zozor, O. Blanc, J. M. Vesin, E. Pruvot, and L. Kappenberger, *Study of atrial arrhythmias in a computer model based on magnetic resonance images of human atria*, Chaos **12**: 754–763 (2002)

[216] P. G. A. Volders, K. R. Sipido, R. L. H. M. G. Spätjens, H. J. J. Wellens, and M. A. Vos, *Repolarizing K^+ currents I_{to1} and I_{Ks} are larger in right than left canine ventricular midmyocardium*, Circulation **99**: 206–210 (1999)

[217] D. Vollmann, Y. Blaauw, H. R. Neuberger, U. Schotten, and M. Allessie, *Long-term changes in sequence of atrial activation and refractory periods: no evidence for "atrial memory"*, Heart Rhythm **2**: 155–161 (2005)

[218] M. B. Wagner, R. Kumar, R. W. Joyner, and Y. Wang, *Induced automaticity in isolated rat atrial cells by incorporation of a stretch-activated conductance*, Pflügers Arch - Eur J Physiol **447**: 819–829 (2004)

[219] H. S. Wang and I. S. Cohen, *Calcium channel heterogeneity in canine left ventricular myocytes*, J Physiol **547**: 825–833 (2003)

[220] J. B. White, G. P. Walcott, A. E. Pollard, and R. E. Ideker, *Myocardial discontinuities: a substrate for producing virtual electrodes that directly excite the myocardium by shocks*, Circulation **97**: 1738–1745 (1998)

[221] M. C. E. F. Wijffels, C. J. H. J. Kirchhof, R. Dorland, and M. A. Allessie, *Atrial fibrillation begets atrial fibrillation: a study in awake chronically instrumented goats*, Circulation **92**: 1954–1968 (1995)

[222] J. P. Wikswo Jr, S. F. Lin, and R. A. Abbas, *Virtual electrodes in cardiac tissue: a common mechanism for anodal and cathodal stimulation*, Biophys J **69**: 2195–210 (1995)

[223] R. Wilders, M. B. Wagner, D. A. Golod, R. Kumar, Y. G. Wang, W. N. Goolsby, R. W. Joyner, and H. J. Jongsma, *Effects of anisotropy on the development of cardiac arrhythmias associated with focal activity*, Pflügers Arch - Eur J Physiol **441**: 301:312 (2000)

[224] R. L. Winslow, D. Cai, A. Varghese, and Y. C. Lai, *Generation and propagation of normal and abnormal pacemaker activity in network models of cardiac sinus node and atrium*, Chaos, Solitons and Fractals **5**: 491–512 (1995)

[225] R. L. Winslow, J. J. Rice, M. S. Jafri, E. Marbán, and B. O'Rourke, *Mechanisms of altered excitation-contraction coupling in canine tachycardia-induced heart failure, II: model studies*, Circ Res **84**: 571–586 (1999)

[226] J. Y. Wu, J. Vereecke, E. Carmeliet, and S. L. Lipsius, *Ionic currents activated during hyperpolarization of single right atrial myocytes from cat heart*, Circ Res **68**: 1059–1069 (1991)

[227] F. Xie, Z. Qu, A. Garfinkel, and J. N. Weiss, *Electrical refractory period restitution and spiral wave reentry in simulated cardiac tissue*, Am J Physiol Heart Circ Physiol **283**: H448–H460 (2002)

[228] H. Yu, F. Chang, and I. S. Cohen, *Pacemaker current exists in ventricular myocytes*, Circ Res **72**: 232–236 (1993)

[229] H. Yu, D. McKinnon, J. E. Dixon, J. Gao, R. Wymore, I. S. Cohen, P. Danilo Jr, A. Shvilkin, E. P. Anyukhovsky, E. A. Sosunov, M. Hara, and M. R. Rosen, *Transient outward current, I_{to1}, is altered in cardiac memory*, Circulation **99**: 1898–1905 (1999)

[230] M. Zabel, B. S. Koller, F. Sachs, and M. R. Franz, *Stretch-induced voltage changes in the isolated beating heart: importance of timing of stretch and implications for stretch-activated ion channels*, Cardiovasc Res **32**: 120–130 (1996)

[231] T. Zeng, G. C. L. Bett, and F. Sachs, *Stretch-activated whole cell currents in adult rat cardiac myocytes*, Am J Physiol Heart Circ Physiol **278**: H548–H557 (2000)

[232] X. Zhou, R. E. Ideker, T. F. Blitchington, W. M. Smith, and S. B. Knisley, *Optical transmembrane potential measurements during defibrillation-strength shocks in perfused rabbit hearts*, Circ Res **77**: 593–602 (1995)

[233] A. C. Zygmunt, R. J. Goodrow, and C. Antzelevitch, I_{NaCa} *contributes to electrical heterogeneity within the canine ventricle*, Am J Physiol Heart Circ Physiol **278**: H1671–H1678 (2000)

Cardiac Electrophysiology and Mechanoelectric Feedback

Modeling and Simulation

Cardiac arrhythmia such as atrial and ventricular fibrillation are characterized by rapid and irregular electrical activity, which may lead to asynchronous contraction and a reduced pump function. Besides experimental and clinical studies, computer simulations are frequently applied to obtain insight in the onset and perpetuation of cardiac arrhythmia. In existing models, the excitable tissue is often modeled as a continuous two-phase medium, representing the intracellular and interstitial domains, respectively. A possible drawback of continuous models is the lack of flexibility when modeling discontinuities in the cardiac tissue. We introduce a discrete bidomain model in which the cardiac tissue is subdivided in segments, each representing a small number of cardiac cells. Active membrane behavior as well as intracellular coupling and interstitial currents are described by this model. Compared with the well-known continuous bidomain equations, our Cellular Bidomain Model is better aimed at modeling the structure of cardiac tissue, in particular anisotropy, myofibers, fibrosis, and gap junction remodeling.

An important aspect of our model is the strong coupling between cardiac electrophysiology and cardiomechanics. Mechanical behavior of a single segment is modeled by a contractile element, a series elastic element, and a parallel elastic element. Active force generated by the sarcomeres is represented by the contractile element together with the series elastic element. The parallel elastic element describes mechanical behavior when the segment is not electrically stimulated. Contractile force is related to the intracellular calcium concentration, the sarcomere length, and the velocity of sarcomere shortening. By incorporating the influence of mechanical deformation on electrophysiology, mechanoelectric feedback can be studied. In our model, we consider the immediate influence of stretch on the action potential by modeling a stretch-activated current. Furthermore, we consider the adap-

251

tation of ionic membrane currents triggered by changes in mechanical load. The strong coupling between cardiac electrophysiology and cardiac mechanics is a unique property of our model, which is reflected by its application to obtain more insight in the cause and consequences of mechanical feedback on cardiac electrophysiology.

In this thesis, we apply the Cellular Bidomain Model in five different simulation studies to cardiac electrophysiology and mechanoelectric feedback. In the first study, the effect of field stimulation on virtual electrode polarization is studied in uniform, decoupled, and nonuniform cardiac tissue. Field stimulation applied on nonuniform tissue results in more virtual electrodes compared with uniform tissue. Spiral waves can be terminated in decoupled tissue, but not in uniform, homogeneous tissue. By gradually increasing local differences in intracellular conductivities, the amount and spread of virtual electrodes increases and spiral waves can be terminated. We conclude that the clinical success of defibrillation may be explained by intracellular decoupling and spatial heterogeneity present in normal and in pathological cardiac tissue.

In the second study, the role of the hyperpolarization-activated inward current I_f is investigated on impulse propagation in normal and in pathological tissue. The effect of diffuse fibrosis and gap junction remodeling is simulated by reducing cellular coupling nonuniformly. As expected, the conduction velocity decreases when cellular coupling is reduced. In the presence of I_f, the conduction velocity increases both in normal and in pathological tissue. In our simulations, ectopic activity is present in regions with high expression of I_f and is facilitated by cellular uncoupling. We also found that an increased I_f may facilitate propagation of the action potential. Hence, I_f may prevent conduction slowing and block. Overexpression of I_f may lead to ectopic activity, especially when cellular coupling is reduced under pathological conditions.

In the third study, the influence of the stretch-activated current I_{sac} is investigated on impulse propagation in cardiac fibers composed of segments that are electrically and mechanically coupled. Simulations of homogeneous and inhomogeneous cardiac fibers have been performed to quantify the relation between conduction velocity and I_{sac} under stretch. Conduction slowing and block are related to the amount of stretch and are enhanced by contraction of early-activated segments. Our observations are in agreement with experimental results and explain the large differences in intra-atrial conduction, as well as the increased inducibility of atrial fibrillation in acutely dilated atria.

In the fourth study, we investigate the hypothesis that electrical remodel-

ing is triggered by changes in mechanical work. Stroke work is determined for each segment by simulating the cardiac cycle. Electrical remodeling is simulated by adapting the L-type Ca^{2+} current $I_{Ca,L}$ such that a homogeneous distribution of stroke work is obtained. With electrical remodeling, a more homogeneous shortening of the fiber is obtained, while heterogeneity in APD increases and the repolarization wave reverses. These results are in agreement with experimentally observed distributions of strain and APD and indicate that electrical remodeling leads to more homogeneous shortening during ejection.

In the fifth study, we investigate the effect of stretch on the vulnerability to AF. The human atria are represented by a triangular mesh obtained from MRI data. To model acute dilatation, overall stretch is applied to the atria. In the presence of I_{sac}, the membrane potential depolarizes, which causes inactivation of the sodium channels and results in conduction slowing or block. Inducibility of AF increases under stretch, which is explained by an increased dispersion in refractory period, conduction slowing, and local conduction block. Our observations explain the large differences in intra-atrial conduction measured in experiments and provide insight in the vulnerability to AF in dilated atria.

In conclusion, our model is well-suited to describe cardiac electrophysiology and mechanoelectric feedback. For future applications, the model may be improved by taking into account new insights from cellular physiology, a more accurate geometry, and hemodynamics.

Het hart is een holle spier die de bloedsomloop in stand houdt. Het hart bestaat uit twee helften. De rechterhelft pompt het bloed naar de longen (kleine bloedsomloop) en de linkerhelft pompt het bloed naar de overige delen van het lichaam (grote bloedsomloop). De twee helften zijn ieder opgebouwd uit twee holtes: de boezem en de kamer. Het bloed uit de aders wordt opgevangen in de boezems. Tijdens een hartcyclus trekken eerst de boezems samen om het bloed in de kamers te pompen. Vervolgens trekken de kamers samen en wordt het bloed in de slagaders gepompt. Deze cyclus wordt ongeer 70 keer per minuut herhaald. De gemiddelde "hartslag" is dus ongeveer 70 keer per minuut.

Het samentrekken van de hartspier wordt vooraf gegaan door een elektrische prikkel. Normaal gesproken begint de prikkel in de sinusknoop en gaat dan via de boezems naar de kamers. Verstoring van de prikkelvoortgeleiding kan leiden tot een onregelmatige hartslag en een verslechtering van de pompfunctie. Hartritmestoornissen kunnen zowel in de boezems als in de kamers voorkomen. De meest bekende geleidingsstoornis in de boezems is boezemfibrilleren, waarbij de hartslag in de boezems kan oplopen tot wel 600 "slagen" per minuut. Boezemfibrilleren komt vaak voor bij oudere mensen en bij mensen die een hartoperatie hebben ondergaan. Deze mensen hebben doorgaans last van kortademigheid en raken sneller vermoeid, maar ondervinden verder weinig hinder. Hoewel boezemfibrilleren soms ook met medicijnen wordt behandeld, wordt tegenwoordig vaak een operatieve ingreep toegepast waarbij een gedeelte van het weefsel wordt geïsoleerd van de rest van de boezems.

Stoornissen kunnen ook voorkomen in het geleidingssysteem van de kamers. Omdat dergelijke stoornissen veel invloed hebben op de pompfunctie van het hart, wordt vaak een pacemaker geïmplanteerd. Het inbrengen van een pacemaker leidt tot een onmiddelijke verbetering van de pompfunctie. Een neveneffect van pacen is dat het hart zich aanpast aan de nieuwe omstandigheden. Zowel de dikte van de hartwand als de geleidingseigenschappen van het hartweefsel kunnen dan veranderen. In extreme gevallen kunnen deze veranderingen leiden tot fibrilleren van de kamers. Kamerfibrilleren is de meest bekende hartritmestoornis en kan voorkomen bij mensen met bijvoorbeeld een hartinfarct. Er zijn echter ook gevallen van kamerfibrilleren bekend bij mensen zonder hartproblemen, bijvoorbeeld bij jonge sporters. Als er niet snel wordt ingegegrepen met een zogenaamde defibrillator, kan kamerfibrilleren de dood tot gevolg hebben. Om deze reden zien we steeds vaker een semi-automatische defibrillator (AED) in openbare gebouwen en op andere plaatsen waar veel mensen samenkomen.

Om inzicht te verkrijgen in het onstaan van hartritmestoornissen en de

255

mogelijke gevolgen voor de patiënt op langere termijn, wordt veel onderzoek gedaan. Naast (dier)experimenteel en klinisch onderzoek wordt meer en meer gebruik gemaakt van computermodellen. Doordat computers steeds krachtiger worden is het mogelijk om de werking van het hart te simuleren met steeds nauwkeuriger modellen. In dit proefschrift wordt een wiskundig model geïntroduceerd waarbij zowel de elektrische als de mechanische eigenschappen tot op het detail van een enkele cel worden beschreven. Hoewel een echt hart uit miljoenen cellen is opgebouwd, laten we zien dat door een slimme elektrische en mechanische koppeling van slechts enkele tienduizenden van onze gesimuleerde cellen het toch mogelijk is om hartritmestoornissen zoals boezemfibrilleren in detail te bestuderen.

Om een efficiënte prikkelvoortgeleiding mogelijk te maken zijn de hartcellen elektrisch met elkaar verbonden. In het hartweefsel vindt elektrische geleiding langs twee wegen plaats: via de zogenaamde *gap junctions* die het binnenste van de cellen met elkaar verbinden en via het zogenaamde *interstitium*, de omgeving waarin de cellen zich bevinden. In ons Cellular Bidomain Model maken wij onderscheid tussen deze twee vormen van elektrische geleiding. Dat is met name van belang om defibrilleren te kunnen simuleren. In dit proefschrift worden alle facetten van het Cellular Bidomain Model in detail beschreven. Daarnaast wordt het model toegepast in een vijftal simulatiestudies. Hieronder volgt een korte beschrijving van deze studies.

In de eerste studie wordt het effect onderzocht van het toedienen van een elektroshock op het hartweefsel zoals dat bij defibrilleren gebeurt. Door toepassing van ons model laten we zien dat defibrilleren mogelijk is door het feit dat de geleidingseigenschappen in het hart niet overal gelijk zijn. Als we namelijk regelmatige geleidingseigenschappen veronderstellen in ons model lukt het niet om een spiraalgolf te defibrilleren, terwijl dit wel mogelijk is als we de geleidingseigenschappen variëren. Hiermee kunnen we meer inzicht verkrijgen in de levensreddende functie van bijvoorbeeld een automatische defibrillator.

In de tweede studie wordt de rol van het zogenaamde pacemakerstroompje in de boezems onderzocht. Deze stroom door het celmembraan komt normaal gesproken alleen voor in de sinusknoop en draagt ertoe bij dat de sinusknoop zo'n 70 keer per minuut een elektrische prikkel afgeeft. Wanneer dit stroompje ook in andere delen van de boezem voorkomt, kan dit de normale prikkelvoortgeleiding beïnvloeden of er kan, naast de sinusknoop, een tweede pacemaker ontstaan. Dat laatste kan uiteindelijk leiden tot boezemfibrilleren. Met behulp van ons model onderzoeken we de invloed van het pacemakerstroompje op de prikkelvoortgeleiding en de omstandigheden waaronder een tweede pacemaker kan ontstaan. Zoals wellicht te verwach-

ten kan het pacemakerstroompje in een ziek hart inderdaad tot een tweede pacemaker leiden. Echter, we hebben ook ontdekt dat het pacemakerstroompje een rol kan spelen om normale prikkelvoortgeleiding in stand te houden als de geleidingseigenschappen in het hartweefsel verminderd zijn door ziekte of ouderdom.

In de derde studie wordt de invloed van rek van het hartweefsel op de prikkelvoortgeleiding onderzocht. Uit (dier)experimentele studies is gebleken dat door rek geactiveerde membraanstromen de prikkelvoortgeleiding vertraagd wordt of zelfs geblokkeerd kan worden. Door het modelleren van een door rek geactiveerde membraanstroom laten we zien dat de prikkelvoortgeleiding geblokkeerd kan worden door het samentrekken van eerder geactiveerde gebieden in het hart. Onze simulaties komen overeen met de resultaten van experimentele studies en geven een verklaring voor het feit dat boezemfibrilleren makkelijker kan ontstaan wanneer de druk in de boezems tijdelijk is toegenomen.

In de vierde studie wordt de hypothese onderzocht dat veranderingen in elektrische eigenschappen na het implanteren van een pacemaker worden veroorzaakt door veranderingen in mechanisch gedrag. In deze studie nemen we aan dat de elektrische en mechanische eigenschappen van het hart zich voortdurend aanpassen zodat de hartspier optimaal blijft functioneren. Op basis van deze aanname blijkt uit ons model dat een meer gelijkmatige samentrekking van de hartspier samengaat met grotere verschillen in elektrische eigenschappen. Onze simulatieresultaten komen overeen met metingen aan elektrische en mechanische eigenschappen in harten waarin een pacemaker is geplaatst en bevestigen onze oorspronkelijke hypothese.

In de vijfde studie wordt het effect van rek op het ontstaan van boezemfibrilleren onderzocht. In deze studie wordt gebruik gemaakt van een natuurgetrouwe vorm van de menselijke boezems. Door de druk in de boezems te laten variëren, onderzoeken we onder welke omstandigheden boezemfibrilleren kan ontstaan. Uit onze simulatieresultaten blijkt dat, door lokale verschillen in de wanddikte van de boezems, slechts een geringe toename van de druk voldoende is om normale prikkelvoortgeleiding te verstoren. In één van de simulaties heeft dit geleid tot een steeds terugkerende geleidingsgolf met boezemfibrilleren tot gevolg.

Samengevat kunnen we concluderen dat het Cellular Bidomain Model toepasbaar is als methode om inzicht te verkrijgen in het ontstaan van hartritmestoornissen en de effecten van medisch ingrijpen.

Langs deze weg wil ik iedereen bedanken die op de een of andere manier betrokken is geweest bij de totstandkoming van dit proefschrift. In de eerste plaats zijn dat de voormalige decaan en opleidingsdirecteur van de faculteit Biomedische Technologie, Jan Janssen en Fons Sauren. Samen met mijn promotor Peter Hilbers hebben jullie ervoor gezorgd dat ik het onderzoek beschreven in dit proefschrift aan de TU/e heb mogen uitvoeren. Peter, jij bent degene die mij naar de TU/e heeft gehaald en ervoor gezorgd heeft dat ik voldoende tijd heb gekregen om het onderzoek naar behoren uit te voeren. Verder gaat mijn dank uit naar mijn beide copromotoren, Huub ten Eikelder en Theo Arts. Huub, jij hebt mij bijgestaan bij het wiskundige ontwerp van het model en de numerieke oplossingsmethoden. Door jouw bijdrage is de betrouwbaarheid van het model aanzienlijk verbeterd en is toepassing mogelijk geworden. Jij was steeds de eerste die mijn hoofdstukken gelezen heeft. Ik ben je zeer dankbaar voor jouw commentaar en suggesties voor verbetering, maar bovenal ben je heel fijne collega om mee samen te werken. Theo, jij hebt mij geïntroduceerd in de wereld van het hartmodelleren. Niet alleen heb je me kennis laten maken met relevante literatuur, maar ook heb je me kennis laten maken met de onderzoekers die in het hartonderzoek werkzaam zijn. Steeds heb je me gewezen op nieuwe mogelijke toepassingen van mijn model.

Naast mijn promotor en copromoteren hebben diverse mede-auteurs hun bijdrage geleverd aan mijn proefschrift. Dit zijn Rikkert Keldermann, Peter Bovendeerd, Sander Verheule en Roel Rijken. Rikkert, jij was mijn eerste afstudeerder van BMT op het gebied van hartmodelleren. Samen met jou heb ik de fysiologie bestudeerd die onontbeerlijk is gebleken voor dit onderzoek. Met veel plezier kijk ik terug op de jaren 2003 en 2004 waarin we veel hebben samengewerkt. Een groot deel van jouw afstudeerwerk is terug te vinden in de hoofdstukken 2, 4 en 5 van dit proefschrift. Peter, jij hebt een belangrijke bijdrage geleverd aan de totstandkoming van het hartmechanica gedeelte van mijn model. De afgelopen jaren hebben wij vele interessante discussies gevoerd waar wij beide veel van geleerd hebben: jij van elektrofysiologie en ik van hartmechanica. Sander, jouw bijdrage zit vooral in de fysiologische aspecten van mechanoelectric feedback. De afgelopen jaren hebben we de basis gelegd voor een nog veel intensievere samenwerking in de nabije toekomst. Ik kijk hier heel erg naar uit. Roel, jij hebt tijdens je afstuderen gewerkt aan het simuleren van boezemfibrilleren. Met veel plezier kijk ik terug op het afgelopen jaar waarin wij veel hebben samengewerkt. Naast de vele interessante gesprekken tijdens de koffie zijn wij er samen in geslaagd een mooie simulatie van boezemfibrilleren te maken. Het resultaat van onze samenwerking is niet alleen terug te vinden in de binnenkant van dit proefschrift, maar

ook op de kaft.

Naast Rikkert en Roel zijn er nog vele andere studenten die met hun project, stage of afstudeerwerk hebben bijgedragen aan het onderzoek beschreven in dit proefschrift. Met name wil ik Chris Delnooz, Marije Mulder, Pamela de Jong, Wilco Kroon, Frans Kremers, Sandra Loerakker en Gijs Huisman noemen. Graag wil ik jullie bedanken voor de prettige samenwerking. Hoewel jullie werk slechts gedeeltelijk of soms helemaal niet is terug te vinden in dit proefschrift, heeft het mij zeker geholpen om meer inzicht te verkrijgen in het vakgebied. Daarnaast zijn er door jullie werk verschillende deuren geopend voor mogelijke toekomstige toepassingen van het model.

Hoewel het modelleren en simuleren van hartritmestoornissen als een rode draad door mijn werk heeft gelopen, heb ik ook aan andere onderzoeksgebieden gewerkt. In het bijzonder wil ik vier studenten noemen die ik heb mogen begeleiden bij hun afstudeerwerk in de gebieden beeldbewerking en neuronale netwerken. Dit zijn Saskia van Engeland, Marije Mulder, Sandra Sherwood en Floor Klijn. Met veel plezier kijk ik terug op de periode van afstuderen waarin we intensief hebben samengewerkt. Na jullie afstuderen is het kontakt gebleven en daar hecht ik heel veel waarde aan.

Tot slot wil ik nog mijn collega's, vrienden, familie en gezin bedanken voor de belangstelling en morele ondersteuning die zij mij de afgelopen jaren hebben gegeven. In het bijzonder wil ik mijn ouders en schoonouders bedanken voor de warme belangstelling en het opvangen van de kinderen. Veel steun heb ik mogen ontvangen van mijn vrouw en kinderen. Lieve Heleen, jij hebt al die jaren voor me klaar gestaan en begrip getoond wanneer het tegenzat. In diezelfde tijd heb je het leven mogen schenken aan onze twee jongens. Joris en Guus, jullie zijn het mooiste wat er is!

Bedankt!

Nico Kuijpers

Nico Kuijpers was born on March 15, 1971, in Bergen op Zoom, The Netherlands. In 1989, he received his Gymnasium diploma from Juvenaat H. Hart in Bergen op Zoom. He studied Computer Science from 1989 till 1993 and received his M.Sc. degree from Eindhoven University of Technology. In 1995, he received his Master of Technological Design (MTD) in Software Technology, also from Eindhoven University of Technology. He worked at TNO Physics and Electronics Laboratory (TNO-FEL) from 1995 till 1998, where he was the project leader of several collaborative projects in the areas of Collaborative Virtual Environments and Distributed Simulation. In 1999, he became an assistant professor in the Parallel Systems group of the Department of Mathematics and Computer Science at Eindhoven University of Technology. Since September 2001, he is assistant professor in the Biomodeling and Bioinformatics group of the Department of Biomedical Engineering at Eindhoven University of Technology.

Refereed journal publications

1. N.H.L. Kuijpers, H.M.M. ten Eikelder, P.H.M. Bovendeerd, S. Verheule, T. Arts, and P.A.J. Hilbers, *Mechanoelectric feedback as a trigger mechanism for cardiac electrical remodeling: a model study*, submitted

2. N.H.L. Kuijpers, H.M.M. ten Eikelder, P.H.M. Bovendeerd, S. Verheule, T. Arts, and P.A.J. Hilbers, *Mechanoelectric feedback leads to conduction slowing and block in acutely dilated atria: a modeling study of cardiac electromechanics*, Am J Physiol Heart Circ Physiol **292**: H2832-H2853 (2007)

3. N.H.L. Kuijpers, R.H. Keldermann, H.M.M. ten Eikelder, T. Arts, and P.A.J. Hilbers, *The role of the hyperpolarization-activated current I_f in arrhythmogenesis: a computer model study*, IEEE Trans Biomed Eng **53**: 1499-1511 (2006)

4. N.H.L. Kuijpers, R.H. Keldermann, T. Arts, and P.A.J. Hilbers, *Computer simulations of successful defibrillation in decoupled and non-uniform cardiac tissue*, Europace **7**: S166-S177 (2005)

5. T. Delhaas, S. van Engeland, J.L.V. Broers, C.V.C. Bouten, N.H.L. Kuijpers, F. Ramaekers, and L.H.E.H. Snoeckx, *Quantification of cytoskeletal deformation in living cells based on hierarchical featur vector matching*, Am J Physiol Cell Physiol **283**: C639-C645 (2002)

6. V. Normand, C. Babski, S.D. Benford, A.N. Bullock, S. Carion, N. Farcet, E. Frécon, J. Harvey, N.H.L. Kuijpers, N. Magnenat-Thalmann, S. Raupp-Musse, T. Rodden, M. Slater, G. Smith, A. Steed, D. Thalmann, J. Tromp, M. Usoh, G. Van Liempd, N. Kladias, *The COVEN Project: Exploring Applicative, Technical, and Usage Dimensions of Collaborative Virtual Environments*, Presence: Teleoperators and Virtual Environments **8**: 218-236 (1999)

7. C.M. Greenhalgh, S.D. Benford, A.N. Bullock, N.H.L. Kuijpers, K. Donkers, *Predicting Network Traffic for Collaborative Virtual Environments*, Computer Networks **30**: 1677-1685 (1998)

Refereed proceedings

8. N.H.L. Kuijpers, R.J. Rijken, H.M.M. ten Eikelder, and P.A.J. Hilbers, *Vulnerability to Atrial Fibrillation under Stretch Can Be Explained by Stretch-Activated Channels*, Computers in Cardiology **34**: 237-240 (2007)

9. N.H.L. Kuijpers, H.M.M. ten Eikelder, P.H.M. Bovendeerd, and P.A.J. Hilbers, *Conduction slowing and block in acutely dilated atria can be explained by stretch-activated currents*, in Proc 1st Dutch Conference on Bio-Medical Engineering BME 2007; Egmond aan Zee, The Netherlands, 86 (2007)

10. M.J. Mulder, M.N. Steijaert, N.H.L. Kuijpers, H.M.M. ten Eikelder, and P.A.J. Hilbers, *A computational model of the retina*, in Proc 1st Dutch Conference on Bio-Medical Engineering BME 2007; Egmond aan Zee, The Netherlands, 44 (2007)

11. R.H. Keldermann, N.H.L. Kuijpers, and P.A.J. Hilbers, *Computer simulations of the initiation of atrial fibrillation*, in Proc 14th World Congress in Electrophysiology and Cardiac Techniques (CARDIOSTIM); Editors: R. Sutton and L. Jordaens, Nice, France, 138P/7 (2004)

12. T. Delhaas, S. van Engeland, N.H.L. Kuijpers, C.V.C. Bouten, J. Broers, F. Ramaekers, and L. Snoeckx, *Cytoskeletal deformation measurement in GFP-vimentin transfected fibroblasts*, in Proc 5th Int Conf Cellular Engineering; Editors: G. Artman and H. Merk, Aachen, Germany, S11-5 (2001)

13. N.H.L. Kuijpers and P.A.J. Hilbers, *Simulation of Atrium Electrical Activity*, in Proc EUROSIM 2001; Delft, The Netherlands (2001)

14. M. Brassé and N.H.L. Kuijpers, *Realizing a Platform for Collaborative Virtual Environments based on the High Level Architecture*, in Proc 2000 Spring Simulation Interoperability Workshop; Orlando, Florida, USA (2000)

15. N.H.L. Kuijpers, J.J. Lukkien, B. Huijbrechts, M. Brassé, *Applying Data Distribution Management and Ownership Management Services of the HLA Interface Specification*, in Proc 1999 Fall Simulation Interoperability Workshop; Orlando, Florida, USA (1999)

16. C.M. Greenhalgh, S.D. Benford, A.N. Bullock, N.H.L. Kuijpers, and K. Donkers, *Predicting Network Traffic for Collaborative Virtual Environments*, in Proc TERENA networking conference '98; Editors: P.H. Enslow, Jr., Dresden, Germany, 1677-1685 (1998)

17. N.H.L. Kuijpers, P. van Gool, and H. Jense, *A Component Architecture for Simulator Development*, in Proc 1998 Spring Simulation Interoperability Workshop; Orlando, Florida, USA (1998)

18. H. Jense, N.H.L. Kuijpers, and A.C.M. Dumay, *DIS an HLA: Connecting People, Simulations and Simulators in the Military, Space and Civil Domains*, in Proc 48th International Astronautical Congress; Turin, Italy (1997)

19. H. Jense, N.H.L. Kuijpers, and R.J.D. Elias, *Electronic Battlespace Facility for Research, Develoment and Engineering*, in Proc 1997 Fall Simulation Interoperability Workshop; Orlando, Florida, USA (1997)

20. N.H.L. Kuijpers and H. Jacobs, *Teleconferencing and Collaboration in Virtual Environments*, in Proc HPCN Europe 1997; Editors: L.O. Hertzberger and P.M.A. Sloot, Vienna, Austria, 165-174 (1997)

21. N.H.L. Kuijpers and H. Jense, *Collaborative Engineering in Distributed Virtual Environments*, in Proc 1997 Spring Simulation Interoperability Workshop; Orlando, Florida, USA (1997)

22. H. Jense and N.H.L. Kuijpers, *DIS - The Next Generation: A Perspective for European Space Programmes*, in Proc 4th Workshop on Simulators for European Space Programmes; ESTEC, Noordwijk, The Netherlands (1996)

23. G. Paar, N.H.L. Kuijpers, and C. Gasser, *Stereo Vision and 3D Reconstruction on a Processor Network*, in Proc IAPR TC-8 Workshop on Machine Perception Applications; Editors: A. Pinz and W. Pölzleitner, Graz, Austria, 97-111 (1996)

24. N.H.L. Kuijpers, G. Paar, and J.J. Lukkien, *Stereo Vision and 3D Reconstruction on a Distributed Memory System*, in Proc International Conference on Parallel and Distributed Processing Techniques and Applications (PDPTA 1996); Sunnyvale, California, USA (1996)

25. N.H.L. Kuijpers, R.J.D. Elias, and R.G.W. Gouweleeuw, *Electronic Battlefield Facility*, in Proc Battlefield Systems International 1996; Chertsey, Surrey, UK (1996)

Professional publications

26. S. van Engeland and N.H.L. Kuijpers, *Quantification of cytoskeletal deformation in living cells*, Xootic Magazine **8**: 17-22 (2001)

27. M. Brassé and N.H.L. Kuijpers, *Standardising Distributed Simulations: The High Level Architecture*, Xootic Magazine **7**: 16-24 (1999)

Posters presented at conferences

28. N.H.L. Kuijpers, R.H. Keldermann, T. Arts, and P.A.J. Hilbers, *How the 'funny' current can lead to ectopic foci*, 4th International Workshop on Computer Simulation and Experimental Assessment of Electrical Cardiac Function; Cap d'Ail, France (2004)

29. R.H. Keldermann, N.H.L. Kuijpers, and P.A.J. Hilbers, *Computer simulations of the initiation of atrial fibrillation*, 14th World Congress in Electrophysiology and Cardiac Techniques (CARDIOSTIM); Nice, France (2004)

Other

30. N.H.L. Kuijpers, *Parallel Implementation of Stereo Vision on a Distributed Memory System*, Thesis Postmaster's Programme Software Technology; Eindhoven University of Technology and Joanneum Research, Supervisors: J.J. Lukkien and G. Paar, ISBN 90-5282-503-3 (1995)

31. N.H.L. Kuijpers, *Feature Matching Algorithms for Stereo Vision on a Distributed Memory System*, Master's Thesis Computer Science; Eindhoven University of Technology and ESTEC, Supervisor: M. Rem, Advisors: P.A.J. Hilbers, J.J. Lukkien, and P.S.E. Plancke (1993)